UNIVERSITY OF COPENHAGEN

DOCTORAL THESIS

Investigation of azimuthal anisotropy using multi-particle correlations of identified hadrons at the LHC with ALICE detector

Author:
Vojtěch PACÍK

Supervisor:
prof. Jens Jørgen GAARDHØJE

Co-Supervisor:
Dr. You ZHOU

High Energy Heavy-Ion Group
Niels Bohr Institute

This PhD thesis has been submitted to the PhD School of the Faculty of Science, University of Copenhagen on January 17, 2020.

Abstract

The primary goal of ultra-relativistic heavy-ion physics is the study of the created strongly-interacting quark-gluon plasma (sQGP). Measurements of the azimuthal anisotropy of created particles, quantified by anisotropic flow v_n coefficients, compared to hydrodynamic calculations, can be used to investigate this unique state of nuclear matter and its properties.

Due to the absence of the QGP-like medium, small collision systems have been considered as a baseline for the heavy-ion measurements. However, high-multiplicity pp and pPb collisions have revealed similar collective behaviour traditionally associated with the expanding medium. The origin of such features is not yet understood and is a focus point of the present work.

This work presents the analysis of azimuthal correlations of inclusive charged hadrons and identified $\pi^{\pm}$, $\mathrm{K}^{\pm}$, $\mathrm{K}^{0}_{\mathrm{S}}$, $\mathrm{p}(\bar{\mathrm{p}})$, $\Lambda(\bar{\Lambda})$, and ϕ meson in Pb-Pb and p-Pb collisions at $\sqrt{s_{\mathrm{NN}}} = 5.02$ TeV recorded by ALICE detector at the Large Hadron Collider. Besides the v_n measurement obtained for the first time using the 4-particle cumulants, more advanced observables such as flow fluctuations and non-linear flow response are studied in Pb-Pb collisions. The presented results exhibit an explicit mass ordering consistent with radial expansion with universal velocity, as described by hydrodynamical calculations based on the iEBE-VISHNU model for low $p_{\mathrm{T}} < 3$ GeV/c, and baryon/meson grouping at intermediate p_{T} region.

Non-flow correlations, arising from jet fragmentation and resonance decays, present a challenge as they generally dominate in small collision systems. In order to reduce such contamination, a pseudo-rapidity separation between correlated particles is applied as well as subtraction of remaining non-flow estimate based on a measurement of minimum-bias pp collisions at $\sqrt{s} = 13$ TeV. Motivated by Pb-Pb measurements, an initial attempt for extracting v_2 using the 4-particle cumulant is made. The mass-related features observed in Pb-Pb collisions are also apparent in non-flow subtracted p-Pb measurement.

Overall, these differential measurements of v_n coefficients present challenges for theoretical calculations further constraining the medium properties as well as initial conditions of the collision. In addition to the inclusive particles, the measurements using identified hadrons provide unique insights into particle production mechanisms. The results presented here mark a starting point for potential future development in investigating the obscure origin of the collectivity by analysing high-multiplicity pp collisions.

Dansk resumé

Det primære mål for den ultra-relativistiske tungionfysik er studiet af det skabte stærkt interagerende quark-gluon-plasma. Målingerne af den azimutale anisotropi af skabte partikler, kvantificeret ved anisotropisk strømning v_n-koefficienter og sammenlignet med de hydrodynamiske beregninger, kan bruges til at undersøge en så unik tilstand af nukleare stoffer og dens egenskaber. På grund af fraværet af det QGP-lignende medium betragtes små kollisionssystemer som en basislinje for tungionmålingerne. Imidlertid afslørede observationen af høj-multiplicitet pp- og p-Pb-kollisioner en lignende kollektiv adfærd, der traditionelt er forbundet med det ekspanderende medium. Oprindelsen af sådanne funktioner er endnu ikke forstået.

Dette arbejde præsenterer analysen af azimuthalkorrelationer af inkluderende ladede hadroner og identificerede $\pi^{\pm}$, $\mathrm{K}^{\pm}$, K^0_S, $\mathrm{p}(\bar{\mathrm{p}})$, $\Lambda(\bar{\Lambda})$, og ϕ meson i Pb-Pb og p-Pb kollisioner på $\sqrt{s_{\mathrm{NN}}} = 5.02$ TeV optaget af ALICE-detektor ved Large Hadron Collider. Udover den v_n-måling, der blev opnået for første gang ved anvendelse af 4-partikel-kumulanter, studeres mere avancerede observerbare ting såsom strømningsfluktuationer og ikke-lineær strømningsrespons i Pb-Pb-kollisioner. De præsenterede resultater udviser en eksplicit masseordre, der er konsistent med radial ekspansion med universalhastighed beskrevet ved hydrodynamiske beregninger baseret på iEBE-VISHNU-model til lav $p_{\mathrm{T}} < 3$ GeV/c og baryon/meson-gruppering ved mellemliggende p_{T}-region.

En sammenhæng uden strømning, der stammer fra jetfragmentering og resonansforfald, udgør en udfordring, da det generelt dominerer i små kollisionssystemer. For at reducere en sådan kontaminering anvendes en pseudo-hurtighedsadskillelse mellem korrelerede partikler samt subtraktion af resterende ikke-strømningsestimat baseret på en måling $\sqrt{s} = 13$ TeV. Motiveret af Pb-Pb-målinger gøres et første forsøg på at ekstrahere v_2 ved hjælp af kumulanten med 4 partikler. De masserelaterede funktioner, der er observeret i Pb-Pb-kollisioner, er også tydelige i ikke-flow subtraherede p-Pb-måling.

Samlet set udgør disse differentielle målinger af v_n-koefficienter overhængende udfordringer til teoretiske beregninger, der yderligere begrænser de middelegenskaber såvel som de indledende betingelser for kollisionen. Foruden de inkluderende partikler tilvejebringer målingerne ved hjælp af identificerede hasroner unik indsigt i mekanismer til produktion af partikler. De rapporterede resultater markerer et udgangspunkt for potentiel fremtidig udvikling i at undersøge den uklare oprindelse af kollektiviteten ved at analysere pp-kollisioner med høj multiplicitet.

List of Publications

1. **Elliptic flow of identified hadrons in small collisional systems measured with ALICE**
   Vojtěch Pacík (for the ALICE Collaboration)
   Nucl. Phys. A982 (2019), 451-454, arXiv:1807.04538 [nucl-ex]

2. **Non-linear flow modes of identified particles in Pb-Pb collisions at $\sqrt{s_{\mathrm{NN}}} = 5.02$ TeV**
   ALICE Collaboration [PC: N. Mohammadi (chair), V. Pacík, Y. Zhou]
   submitted to JHEP, arXiv:1912.00740 [nucl-ex]

3. **Investigations of Anisotropic Flow Using Multiparticle Azimuthal Correlations in pp, p-Pb, Xe-Xe, and Pb-Pb Collisions at the LHC**
   ALICE Collaboration [PC: K. Gajdošová Krížková (chair), C. Loizides, V. Pacík, Y. Zhou]
   Phys. Rev. Lett. 123 (2019) no.14, 142301, arXiv:1903.01790 [nucl-ex]

4. **Anisotropic flow and flow fluctuations of identified hadrons in Pb-Pb collisions at $\sqrt{s_{\mathrm{NN}}} = 5.02$ TeV**
   ALICE Collaboration [PC: Z. Moravcová, V. Pacík, Y. Zhou, Y. Zhu]
   in preparation

List of Contributions

1. **Investigation of collectivity in small collision systems with ALICE**
   Parallel talk at 5th International Conference on the Initial Stages in High-Energy Nuclear Collisions (IS 2019)
   24-28 June 2019, New York, USA

2. **Elliptic flow coefficients of identified hadrons in pp and p-Pb collisions measured with ALICE**
   Parallel talk at 27th International Conference on Ultra-relativistic Nucleus-Nucleus Collisions (Quark Matter 2018)
   13-19 May 2018, Venice, Italy

3. **Anisotropic azimuthal correlations of identified hadrons in p-Pb collisions at $\sqrt{s_{\mathrm{NN}}} = 5.02$ TeV**
   Poster awarded with EPJ Young Scientist Award at 17th International Conference on Strangeness in Quark Matter (SQM 2017)
   10-15 July, 2017, Utrecht, the Netherlands

Acknowledgements

Throughout my PhD, I have been fortunate to encounter so many interesting and inspiring people. Without them, this thesis would not have been possible.

I would like to express my deepest gratitude to both of my supervisors. To Jens Jørgen Gaardøje, for his unrelenting support and helpful advice in the professional matters but also in personal life. To You Zhou, for his day-to-day guidance; for all the discussions; for profound belief in my abilities, and for motivating me when it was needed.

I have greatly benefited from the whole HEHI group: Børge Nielsen, Christian Holm, Ian Bearden, Kristjan Gulbrandsen, and Hans Bøggild. I thank you for providing me with invaluable expertise and extra opinions; for the fruitful discussions by the coffee-machine and within the meeting room; and for keeping me up to speed with the current political situation around the globe while sustaining the regular dosage of pizza. I would also like to thank Anette Uhl, who was always very kind and helpful, and capable of dealing with all the inevitable non-scientific business in science with elegance.

I am very grateful to share this part of my life with my friends and colleagues: Christian, Helene, Fabian, Freja, Jean-Loup, Lais, Meera, Ya, and Zlatko. I thank you all, for the time we spent together inside (but more notably outside) the NBI walls; for all the dinners, gaming nights, simple chats over beer, and for all attempts of rekindling my social life from time to time. I want to thank Christian Bierlich for the remarkable memories, from the kayaking trip in Utrecht to the midnight pizza at Manhattan. I also thank Zuzana, the recent addition to the HEHI troupe, who will carry the flag from now on. I wish you the very best in the coming years.

Special thanks go to Katarina who helped me from the very first day of my PhD. For her advice, cooperation, and her ability to listen to whatever I had to say whenever I felt like it. Simply for preserving a little piece of home in the heart of Copenhagen. I want to extend the special thanks to my "brother-in-arms", Vytautas, who was always very supportive, and who played an instrumental role on countless extraordinary occasions.

My most profound appreciation goes to my better half, Tereza, who stood by me unconditionally and supported me in my decisions (and bravely endured the consequences). For reminding me that there is a life besides the piles of work, and for showing me the fantastic places around the world that we have seen together, and also those still ahead of us.

Last, but not least, I am very grateful for my family and my friends, without whom I would have never been where I am today. For providing me with a safe harbour and distractions from the every-day routine, and for always having my back.

Needless to say, my thanks go to you, who opened this book and decided to read through the rest of my thesis. I wish you an exciting reading and thank you all for the last couple of crazy and unforgettable years!

Contents

Dedicated to my most beloved Tereza.

1 Introduction

During its evolution, just moments after the Big Bang the Universe existed for a very brief moment in the extremely hot and dense form composed of almost-free quarks and gluons. Roughly 13.4 billion years later, this unique state of nuclear matter, called quark-gluon plasma (QGP), can be recreated by colliding heavy (e.g. Pb) ions within the most powerful particle accelerators.

Analysis of the particles produced in such collisions provides a suitable tool to investigate the properties of the created medium. Measurements of anisotropic flow v_n coefficients of inclusive charged hadrons, extracted from azimuthal correlations, showed that the QGP behaves similarly to an almost perfect liquid. Surprisingly, a similar fluid-related collectivity was also observed in proton-proton and proton-nucleus collisions where QGP formation is not expected. Consequently, many studies aiming to investigate the collective nature recently emerged, although its origin remains unclear.

In this work, the azimuthal anisotropy quantified by the anisotropic flow v_n coefficients. Specifically, the measurement of inclusive charged hadrons as well as identified $\pi^{\pm}$, $\mathrm{K}^{\pm}$, $\mathrm{K}^0_{\mathrm{S}}$, $\mathrm{p}(\bar{\mathrm{p}})$, $\Lambda(\bar{\Lambda})$, and ϕ using 2- and 4-particle cumulant technique in Pb-Pb and p-Pb collisions at $\sqrt{s_{\mathrm{NN}}} = 5.02$ TeV is presented.

In the rest of Chapter 1, a brief introduction to the physics of ultra-relativistic collisions is discussed including the evolution of strongly-interacting QGP, phase diagram of nuclear matter, as well as the development of anisotropy in azimuthal distribution of emitted particles. Moreover, observation of collectivity in p-Pb and pp collisions will is discussed together with an overview of measurement focusing on recent development of anisotropic flow. In Chapter 2, a description of some of the azimuthal correlation techniques, such as the Event Plane method, before moving towards the so-called Generic Framework implementation of multi-particle cumulants used in the analysis reported here. In addition, some more advanced aspects related to anisotropic flow are reported there, namely flow fluctuations, non-linear flow mode, and the non-flow contamination. The technical description of the ALICE apparatus and the corresponding detectors essential for this measurement is provided in Chapter 3. An entire analysis procedure is described in Chapter 4, starting from the data sample and event selection, followed by the selection of inclusive charged hadrons, particle identification procedure and reconstruction of shortly-lived hadrons, and concluding with correlation-related data-driven techniques. Finally, the results of this work are presented in Chapter 5, while the summary of important findings is given in Chapter 6.

1.1 Standard Model and Strong interaction

The Standard Model is a theory of Particle Physics describing the elementary particles of matter, *quarks* and *leptons*, as well as their universal behaviour conveyed by three fundamental forces: *electromagnetic*, *strong*, and *weak*.

Overall, there are six quarks and six leptons. Both groups are characterised by their *flavour*. In case of quarks, we distinguish six flavours (one for each quark type): up (u), down (d), strange (s), charm (c), bottom (b), and top (t). On the other hand, the three lepton flavours are consisting of a given lepton and a corresponding *neutrino*: electron (e), muon (μ), and tau (τ). The elementary particles are commonly grouped into three *generations* (also known as families). They are made up of two quarks and a lepton-neutrino pair.

The fundamental forces act via an exchange of force carriers referred to as *gauge bosons*. Specifically, the electromagnetic (EM) force is carried by γ photons exchanged between electrically-charged particles. The weak force is mediated by $W^{\pm}$ and Z bosons accountable for nuclear decays due to the ability to change the flavour of both quarks and leptons. Finally, the strong interaction, moderated by gluons g carrying a *colour* charge, which binds the quarks (and gluons) within composite particles, generally referred to as *hadrons*. Last, but not least, there is a Higgs boson (H) which is responsible for giving the mass (inertia) to all massive particles by its interaction with a scalar Higgs field permeating the entire Universe. An overview of the elementary particles of the Standard Model is provided in Fig. 1.1, including some of their characteristic quantities.

The strong interaction is described by a theory of Quantum Chromodynamics (QCD). The name is derived from the associated charge, the colour, carried by quarks and gluons. In analogy with the visible light, the colour-charge has three types: red, green, and blue. In addition, for each colour, there is a corresponding anti-colour, i.e. anti-red, anti-green, and anti-blue, giving together six different states. The colour is only carried by either quarks or gluons. While quark can carry only one (anti-)charge, gluons carry one colour and one anti-colour at the same time. It allows gluons to interact with themselves, contrary to EM interaction where γ does not carry the electric charge. On the other hand, the hadrons are "white", i.e. colour-neutral (in terms of light analogy). This can be achieved in two ways resulting in two different types of hadrons: *mesons* composed from a quark and an anti-quark of the same colour, or *baryons* made up of three quarks with exclusive colours (i.e. one green, one blue, and one red). In general, both quarks and gluons are considered as hadron constituents (as gluons bind quarks together) and are commonly referred to as *partons*.

The strength of the interaction is characterised by a *coupling constant*. For instance, the coupling constant of Quantum Electrodynamics (QED) describing the EM interaction, α_{QED} is strongest at the shortest distances while decreasing as the distance increases.

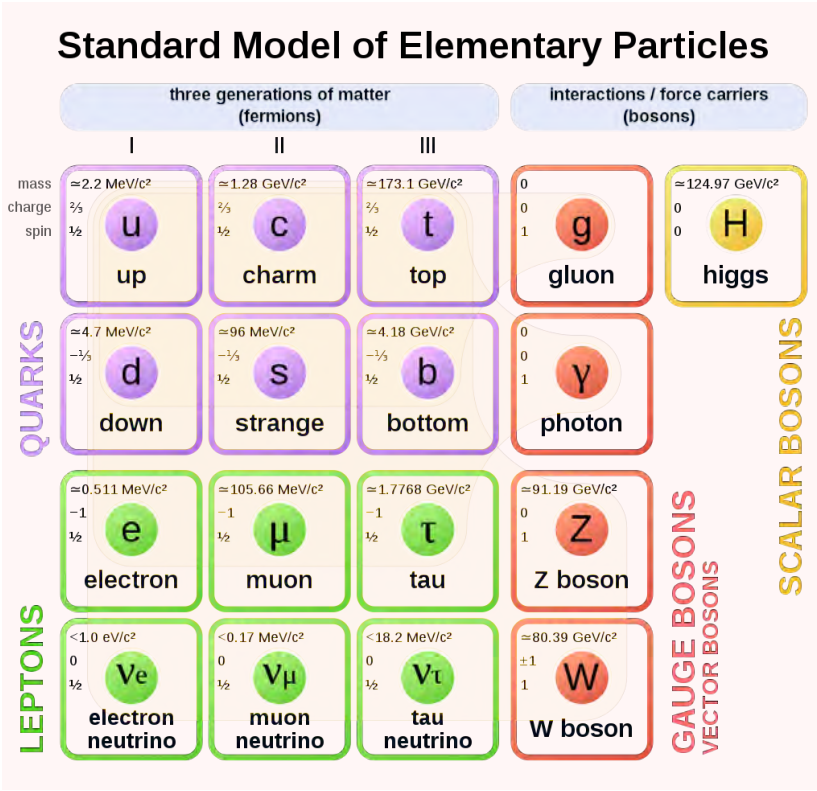

FIGURE 1.1: An overview of elementary particles according to the Standard Model of particle physics. Figure taken from [1].

The coupling constant of QCD, α_{QCD}, exhibits an opposite behaviour: on relatively long distances or low energies[1], the strong force is (as the name suggest) strong. However, with decreasing length or increasing energy, it gets rapidly weaker. Such behaviour is illustrated in Fig. 1.2. Consequently, there are two distinct features related to such behaviour: *colour confinement* and *asymptotic freedom*.

The colour confinement is a phenomenon that holds the quark bound within the composite hadrons. As the distance between the quarks increases, more and more energy is needed to pull them further as the interaction grow stronger. At a certain point where the potential energy is large enough, energy grows no longer, but a new pair of quark–anti-quark is created instead. Consequently, no free quark can be observed under normal conditions.

On the other hand, at very low distances or extremely high energies, a binding between quarks is so small that they are no longer confined within hadrons but instead

[1]Please note, that these two quantities are related via the uncertainty principle.

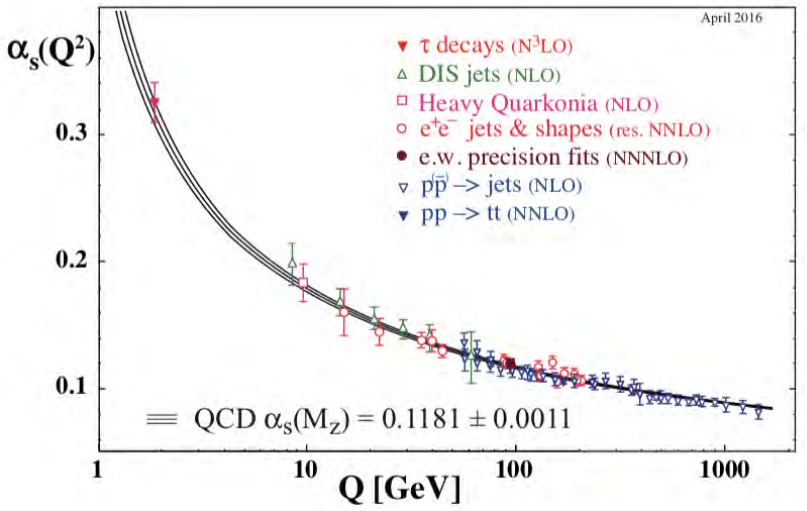

FIGURE 1.2: Overview of experimental measurements of α_{QCD} (here denoted as α_s) as a function of transferred momentum Q from various physical processes. Figure taken from [2].

behave as quasi-free particles. This regime is called asymptotic freedom. In extremely harsh conditions few microseconds after the Big Bang, the Universe was in a state of de-confined hadronic matter, consisting of these almost free quarks and gluons, called Quark-Gluon Plasma (QGP).

In the regime where α_{QCD} is small, *hard processes* (i.e. those with large momentum transfer Q) can be approximated using perturbation theory techniques called *perturbative QCD (pQCD)* framework. This is done by setting a cut-off of an infinite series expanded in powers of α_{QCD}. Based on the number of included terms, one distinguishes calculation in leading order (LO), next-to-leading order (NLO), next-to-next-to-leading order (NNLO), etc. In contrast, the *soft processes* producing particles with momentum of $\mathcal{O}(100\,\mathrm{MeV})$ cannot be calculated using pQCD. Instead, the well-established *lattice QCD (lQCD)* is used, where the phase-space is discretised into a finite grid. The calculation is then performed on the crossing points and subsequently extrapolated for infinitely small grid size.

To summarise the various stages of QCD matter, a phase diagram is presented in Fig. 1.3. In analogy to the well-known phase diagram of water, it depicts different steps in the evolution of nuclear matter depending on its conditions characterised by its temperature T and baryon chemical potential μ_B. While the latter reflects the abundance of matter over anti-matter present in the system (with perfect balance between the two at $\mu_B = 0$, and dominance of the matter at $\mu_B > 0$), it can be simply considered as the net

density of the baryons. As the water boils into vapour or freezes into ice, it changes its structure and dynamics significantly. And so does the nuclear matter.

In the region of low T and μ_B, the matter consists of tightly-bound hadrons. At $\mu_B \approx 900$ MeV the hadrons are in a state of "ordinary" nuclear matter forming atomic nuclei and by extension the matter around us. However, when the temperature reaches a critical value, the hadron gas undergoes a phase transition. Afterwards, the matter is in a state of de-confined QGP as described above.

For low μ_B, a rapid cross-over transition is expected [4, 5]. Based on the recent lQCD calculations, such transition happens at the critical temperature $T_c = (156.5 \pm 1.5)$ MeV [6] and critical energy density within $0.18 < \epsilon_c < 0.5\,\mathrm{GeV/fm^3}$ [7]. On the other hand, a first-order phase transition happens for larger values of μ_B [8]. The two types of transition are likely separated by the presence of a *critical point* where the liquid and gaseous phase are nearly non-distinguishable [9, 10]. It should be noted that the phase transition is not yet completely understood. Similarly, the presence, as well as the potential location of the critical point, is currently under heavy investigation. Specifically, this is the ultimate goal of a so-called Beam Energy Scan programme conducted at RHIC by colliding different nuclei at various energies [11] as illustrated in Fig. 1.3.

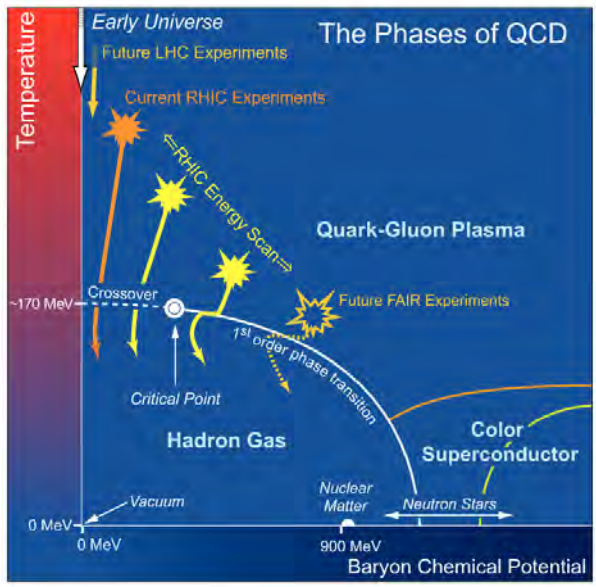

FIGURE 1.3: Schematic phase diagram of QCD matter.
Figure taken from [3].

For completeness, at low T and very high μ_B, the matter enters a regime present within the core of extremely dense neutron stars. Needless to say, the current understanding of the dynamics of such celestial bodies is very limited and very little is known about the physical processes involved.

After the Big Bang, the Universe was created in a state of extremely high temperature and $\mu_B \to 0$ (indicated by white arrow). When its temperature decreased to the critical value, the above-described phase transition happened. Since then, it is in the state of confined nuclear matter.

Luckily, the unique and rare state of QGP can be re-created for a brief moment at large colliders which will be discussed later in Chapter 3. This is achieved by accelerating nuclei of heavy elements at unprecedented energy and let them subsequently collide with each other. As the collision happens, the system is in the condition close to that of Early Universe (denoted by the orange arrow in Fig. 1.3). Because of that, such heavy-ion collision is often called the *Little Bang* [12].

1.2 Ultra-relativistic heavy-ion collision

Before the collision, the circulating nuclei are accelerated to a velocity very close to the speed of light. At such extremely high velocities, the projectiles are greatly affected by relativistic effects as the *Lorentz factor* is very large ($\gamma \gg 1$). This regime is often referred to as ultra-relativistic, thus ultra-relativistic collision. Due to Lorentz contraction, the two incoming nuclei resemble narrow disks rather than spherical objects. Because of that, they are commonly called "pancakes". Consequently, the system exhibits high nucleon density as well as gluon occupancy.

As the collision occurs, the nucleons which do not collide with any nucleon of the other nuclei pass by unscathed. These are called *spectators*. On the other hand, the nucleons which undergo at least one nucleon-nucleon interaction are called *participants*. The progress of a heavy-ion collision is schematically illustrated in Fig. 1.4, where b denotes the *impact parameter*. This quantity is defined as a distance in a transverse plane between the geometrical centres of the two nuclei. It characterises the level of the overlap.

Based on the impact parameter, one can distinguish central collisions with $b \approx 0$, semi-central collisions when $b > 0$, and peripheral collisions in case of $b \lesssim 2R$, where R represents the radius of the nucleus. So-called ultra-peripheral collisions with $b > 2R$ provides a unique environment to study particle production strictly via EM interaction as there is no overlap between the two nuclei and thus no physical collision between the nucleons occur.

As the projectiles pass through each other, they leave behind a system with an extremely high density and temperature. If the conditions are sufficiently harsh, the QGP is

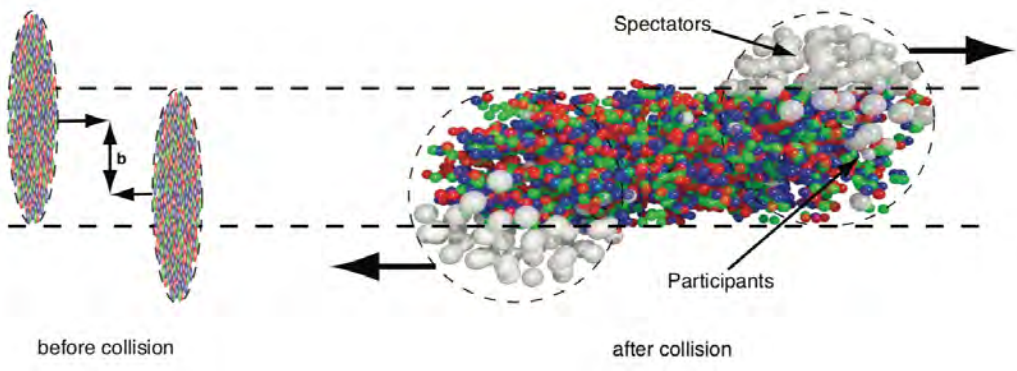

FIGURE 1.4: Schematic illustration of two colliding heavy-ion nuclei before (left) and after the collision (right). See the text for details. See the text for details. Figure taken from [13].

formed as discussed in the previous section. Due to a large amount of energy deposited by the tightly-packed participants, the created medium tends to return to its equilibrium state. Therefore, it expands and cools down. The evolution of the expanding nuclear matter is illustrated by light-cone diagram shown in Fig. 1.5 described by longitudinal direction z and time. The hyperbolas reflect the space-time coordinates with the same proper time $\tau = \sqrt{t^2 - z^2}$ and by extension temperature T. In general, the medium undergoes the following successive stages during its evolution [15] which are described further in the following.

1. Formation of QGP
2. Thermal equilibrium
3. Phase transition
4. Chemical freeze-out
5. Kinetic freeze-out

The formation of the QGP is typically described in the framework of Colour-Glass Condensate (CGC) [16, 17]. Since the nuclei (and thus the nucleons) are accelerated to the ultra-relativistic energy, they are in the regime of small Bjorken x denoting the fraction of hadron momentum carried by individual partons. Under such conditions, the nucleons ought no longer be treated as being composed of three valence quarks, but instead densely packed with gluons. This can be seen by looking at the parton distribution function depicted in Fig. 1.6, representing the probability of finding a specific parton with a given momentum fraction x of the collided proton. In can be seen, that while the

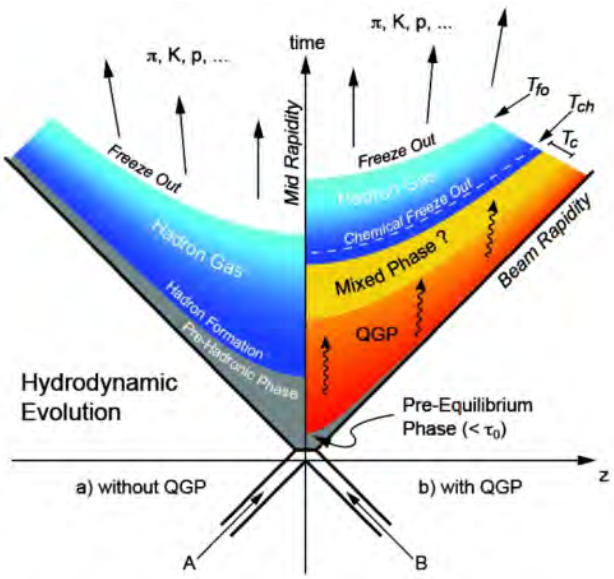

FIGURE 1.5: Schematic space-time evolution of ultra-relativistic collision with the formation of QGP (right side) and without it (left side). Figure taken from [14].

valence u and d quarks are most significant under normal conditions (i.e. high x), the gluons clearly dominates in low x region. According to the effective field theory of CGC, the number of gluons increases with decreasing x until it saturates at certain saturation energy scale Q_s due to limited space (thus the name colour condensate). As the time dilatation takes place, the lifetime of gluons is much longer than the overall time frame of the collision. Consequently, they appear as almost static objects (similarly to slowly moving glass). In the moment of the collision, the two ions create a very strong electric and magnetic fields. Afterwards, the gluon-saturated nucleons passes through each other forming a prolongated colour-flux tubes (*strings*) as illustrated in Fig. 1.7. This stage of the QCD medium is referred to as Glasma [16]. At this very early stage of the collision, hard processes with large momentum transfer Q occur, such as the production of heavy-flavour quarks and high-p_{T} partons which undergo fragmentation (i.e. a sequential QCD radiation) resulting in a collimated sprays of particles called *jets*.

When the Glasma is formed, the partons interact with each other. As a result, the thermal equilibrium is reached, and the QGP is created after $\tau_0 \sim 1$ fm/c. Such short thermalisation time indicates that the created medium is strongly-coupled. Therefore, it is commonly referred to as sQGP. Since the system expands, the equilibrium is only local as the temperature is not uniform within the whole volume. In this stage, the viscous

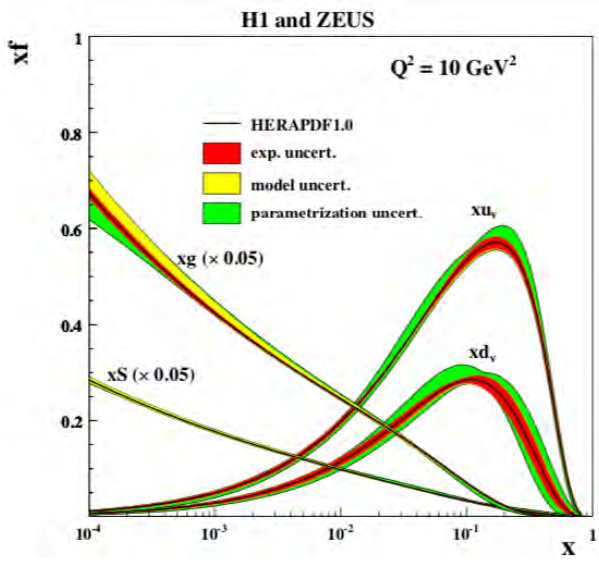

FIGURE 1.6: Parton distribution for gluons (xg), valence u and d quarks (xu_v and xu_d), and sea quarks (xS) within a proton as a function of Bjorken x measured for energy scale of $Q^2 = 10$ GeV^2 as measured by H1 and Zeus experiments. Figure taken from [18].

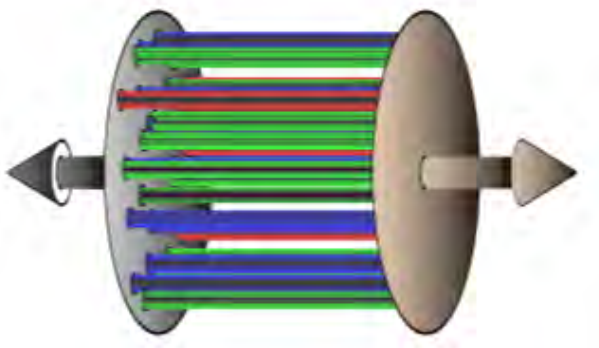

FIGURE 1.7: Illustration of Glasma composed of longitudinal colour-flux tubes in the ultra-relativistic collision of two heavy-ion nuclei. Figure taken from [15].

hydrodynamic description is used [19, 20]. By doing so, the system evolution is governed by local conservation of energy-momentum tensor $T^{\mu\nu}$ and conserving currents N_i^μ such as, e.g. electric charge or baryon number. Moreover, an additional set of parameters known as transport coefficients are present: namely the *shear viscosity* η and *bulk viscosity* ξ characterising the resistance to the flow of the fluid and its deformation due

to the expansion of the system, respectively.

On the other hand, if the interaction is small or absent at all, the individual partons would be quickly separated from each other. Subsequently, they would form the hadrons via fragmentation process (colloquially known as string breaking) as described by Lund String Model [21]. This hadron production mechanism is expected to take place in case of QGP absence such as in proton-proton (pp) or proton-nucleus (pA) collisions. Such a scenario is illustrated in the left part of Fig. 1.5.

As the QGP expands and cools down, a phase transition happens when critical temperature T_c is reached. This process is called hadronisation as the quasi-free quarks and gluons become confined again within hadrons. When the transition is over, the system is in a state of hot and rather dense hadron gas.

Afterwards, the hadrons interact with each other via inelastic scattering. However, as the density decreases, the system becomes more dilute. Consequently, the interaction rate diminishes until the inelastic scatterings cease, and the chemical composition of the system is fixed. This is referred to as the chemical freeze-out, and the associated temperature is denoted as T_{ch}.

Following the chemical freeze-out, the system continues to interact only elastically. In addition, the short-lived heavy particles decay into the lighter and more stable species. When the density decreases to the point that the mean-free path of the hadrons is large enough (approximately comparable to the system size), the elastic scatterings stop as well, and the kinetic freeze-out at temperature T_{kin} (or T_{fo}) occurs fixing the particle momentum.

Finally, the individual particles leave the system and continue their journey towards the detectors. This final stage of the evolution of QCD matter is called the free-streaming.

1.3 Azimuthal anisotropy and anisotropic flow

Due to finite sizes of the colliding nuclei, the initial geometry of the overlapping region varies from one collision to another. In non-central collisions, the overlapping region exhibits an elliptical shape. Such anisotropy creates non-uniform pressure gradients. This leads to different expansion rates depending on the azimuthal angle. The largest is along the minor axis while it decreases towards the major axis. Due to strong interaction among the constituents of QGP, such initial spatial anisotropy is transferred to the final momentum anisotropy. Consequently, more emitted particles are observed in the preferred direction. This phenomenon is known as *anisotropic flow*, and it presents one of the most prominent probes of the QGP properties. The evolution of the expanding system created in semi-central collision is depicted in Fig. 1.8.

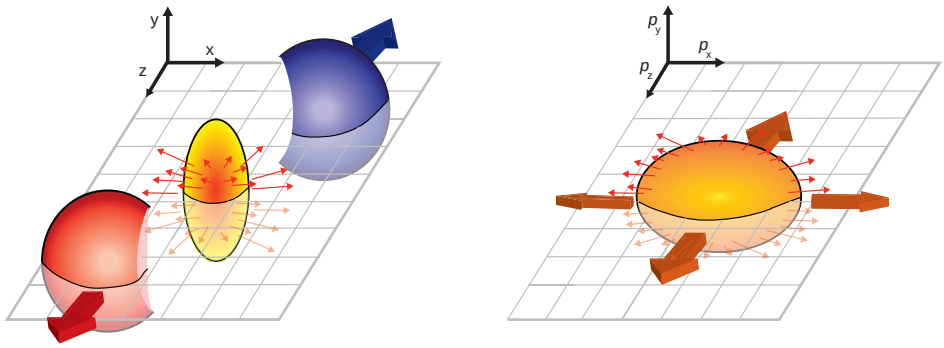

FIGURE 1.8: Schematic illustration of QGP expansion in semi-central heavy-ion collision. Figure taken from [22] (courtesy of Boris Hippolyte).

To quantify the final-state anisotropies, one can decompose the measured azimuthal distribution of detected particles into a Fourier series with respect to the common symmetry plane [23]:

$$\frac{\mathrm{d}N}{\mathrm{d}\varphi} \propto 1 + 2\sum_{n=1}^{\infty} v_n \cos\left[n(\varphi - \Psi_n)\right], \tag{1.1}$$

where φ is the azimuthal angle of the emitted particle, and Ψ_n and v_n represent the symmetry plane angle and anisotropic flow coefficient corresponding the to n-th harmonic, respectively. The later is defined as

$$v_n = \left\langle \cos\left[n(\varphi - \Psi_n]\right\rangle\right., \tag{1.2}$$

where the angle brackets, $\langle\cdot\rangle$, represent an average of all particles. Related to that, a n-th order complex anisotropic flow vector V_n can be constructed as

$$V_n \equiv v_n e^{in\Psi_n}, \tag{1.3}$$

such that v_n coefficients can be interpreted as its magnitude, i.e. $v_n = |V_n|$. A brief overview of selected methods used to extract the v_n coefficients are described in Chapter 2.

In general, the v_n coefficients are dependent on the collision centrality due to their connection to initial spatial anisotropy vectors $\mathcal{E}_n$ which can be quantified by the corresponding coefficient ϵ_n as follows [24]:

$$\mathcal{E}_n \equiv \epsilon_n e^{in\Phi_n} \equiv \frac{\left\langle r^n e^{in\phi}\right\rangle}{\left\langle r^n\right\rangle}, \quad n > 1, \tag{1.4}$$

where r is a radial position in transverse plane and ϕ is the azimuthal angle of participant nucleons. Besides collision geometry, v_n coefficients exhibit additional dependency on particle properties, such as p_{T}, η, as well as particle mass (provided by analysing individual species) which will be discussed later.

Given the afore-mentioned eccentricity (characterised by a significant ϵ_2) of the initial geometry, the corresponding second harmonic of anisotropic flow v_2, often referred to as *elliptic flow*, is dominant in the non-central heavy-ion collisions. However, as the position of the nucleons within the two projectiles changes from one collision to another, so does the the overlapping region dictated by the participants Consequently, these event-by-event fluctuations generate non-negligible contribution of higher harmonics to the total anisotropy of the system [24]. With respect to the corresponding geometrical resemblance of ϵ_n components, these are commonly called *triangular flow* v_3, *rectangular flow* v_4, etc. For comparison, an illustration of a non-central heavy-ion collision with significant elliptic and triangular component is shown in Fig. 1.9.

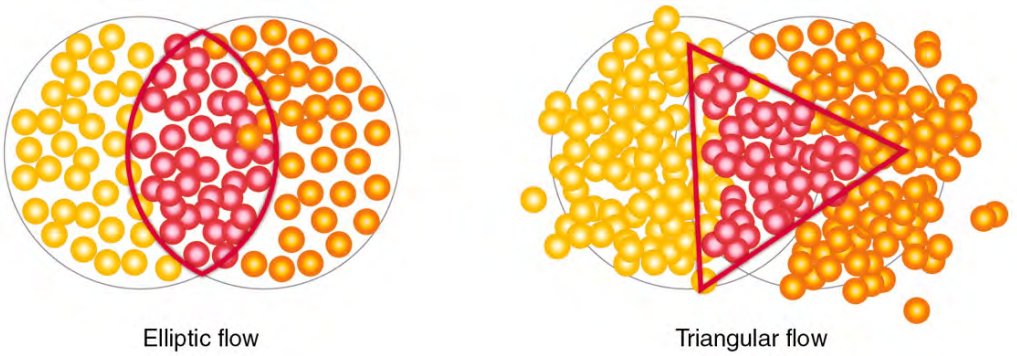

FIGURE 1.9: Illustration of spatial distribution of participating nucleons (red) and the resulting geometry of the overlapping region in semi-central heavy-ion collision with clear elliptic (left) and triangular (right) shape. Figure taken from [25].

1.4 Collectivity in small systems

The collective behaviour demonstrated as long-range azimuthal correlations quantified by anisotropic flow coefficients is typically associated with the presence of expanding QGP created in the heavy-ion collision. Over the years, heavy-ion collisions were extensively studied by comparing the measurement with various theoretical models which further supported such a statement.

On the other hand, a QGP-like medium is not expected to be formed in the proton-proton (pp) or proton-nucleus (p-A) collisions as discussed in Section 1.2 (and as illustrated by the left-hand side of Fig. 1.5). Therefore, the partons created right after the collision are not affected by the presence of the strongly-interacting medium. Consequently, the pp and p-A collisions, generally referred to as *small nucleonic systems*, serve as a baseline for comparison with the heavy-ion measurements used to study the properties of the QGP. Besides the nuclear modification, the p-A are also used to characterise so-called Cold Nuclear Matter (CNM) effects connected with the gluon interaction within the nuclei during the early stage of the collision.

However, such picture of small collision systems have been challenged recently as the correlation studies in both pp and p-A collisions seem to mimic the features which are traditionally associated with QGP-like collectivity. Since then, the small collision systems attracted much attention representing a potential paradigm shift in the current understanding of the collective phenomena in the heavy-ion collisions.

To identify which aspects are essential to establish a potential presence of collectivity, let us start with its definition. Based on the observation in heavy-ion collisions, the medium-induced collectivity exhibits two features. First, as the medium expands in the longitudinal direction, the emitted particles are correlated across wide range of rapidity. Second, the correlations should persist even for a high number of correlated particles as opposed to local collective behaviour affecting only a handful of particles. Such local collectivity can be caused by several processes, e.g. resonance decays (which are correlated through the original mother particle), jet fragmentation of the initial hard parton, or local momentum conservation. Therefore, in the "working" definition of the collectivity is that it is characterised by long-range and multi-particle correlations [26].

These characteristic aspects are illustrated in Fig. 1.10 depicting the di-hadron angular correlations measured in most-central Pb-Pb collisions at $\sqrt{s_{\mathrm{NN}}} = 2.76$ TeV [27]. In this 3-dimensional plot, a two-particle correlation function $C(\Delta\phi, \Delta\eta)$ is plotted as a function of the azimuthal angle $\Delta\phi$ and pseudorapidity $\Delta\eta$ difference between the triggered and the associated particles. The angular correlation measurements in heavy-ion collisions typically exhibit the following distinct features. Firstly, a significant correlation in the so-called *jet-peak* region at $(\Delta\phi, \Delta\eta) \approx (0, 0)$ left by (as the name suggests) jet constituents which are typically located close to each other. Secondly, the double-ridge structure spanning the whole $\Delta\eta$ region. The so-called *away-side ridge* at $\Delta\phi \approx \pi$ is caused by the particles from the associated "second" jet (as the jets are typically created in pairs known as di-jets due to the momentum conservation and nature of QCD). More importantly, the *near-side ridge* at $\Delta\phi \approx 0$ is understood as a result of the anisotropic flow in accordance with the above-mentioned definition of collectivity. Based on this method, the correlation function is projected into the $\Delta\phi$ plane (while rejecting the jet

peak region). Subsequently, the corresponding v_n coefficients are extracted by fitting the projection direction by a Fourier series.

Moving to the small systems, similar di-hadron correlation measurements performed in pp [28] and then also later in p-Pb collisions [29]. The results are shown in Fig. 1.11 and 1.12 for pp and p-Pb collisions, respectively, for collisions with low (left plot) and very high (right plot) number of detected charged particles N_{ch}. The jet peak, as well as the away-side jet ridge, is present for both low- and high-multiplicity pp and p-Pb collisions. While being absent in the low-multiplicity events, a significant near-side ridge, which is usually related to fluid-like collectivity, only appears in the collisions with a vast number of produced (detected) particles.

This striking and initially unexpected resemblance of high-multiplicity pp and p-Pb collisions with the heavy-ion counterpart was the afore-mentioned spark which ignited the interest in small collision system within the heavy-ion community. Consequently, the possibility of the collective behaviour in the absence of QGP-like medium started a discussion leading to further studies of such a collectivity and as well as the investigation of its origin.

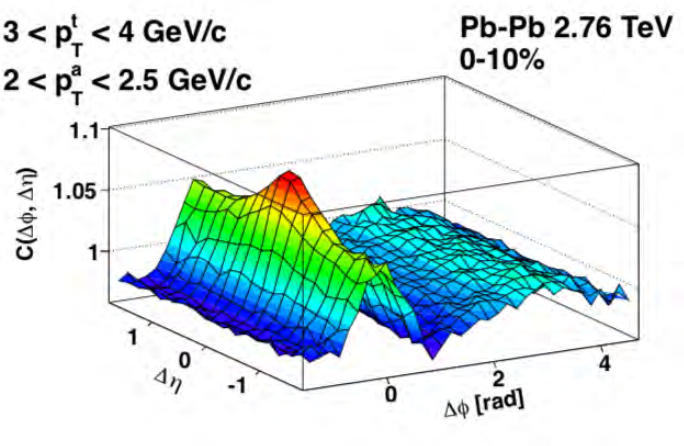

FIGURE 1.10: Di-hadron angular correlations as a function of $\Delta\eta$ and $\Delta\phi$ in 0-10% most-central Pb-Pb collisions. Figure taken from [27].

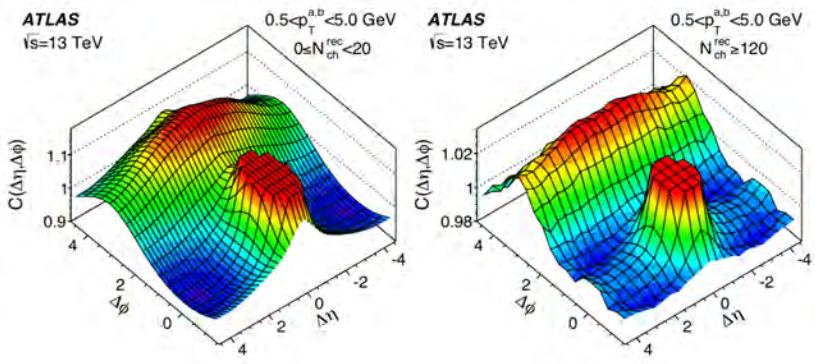

FIGURE 1.11: Di-hadron angular correlations as a function of $\Delta\eta$ and $\Delta\phi$ in low-multiplicity (left) and high-multiplicity (right) pp collisions at $\sqrt{s} = 13$ TeV. Figure taken from [30].

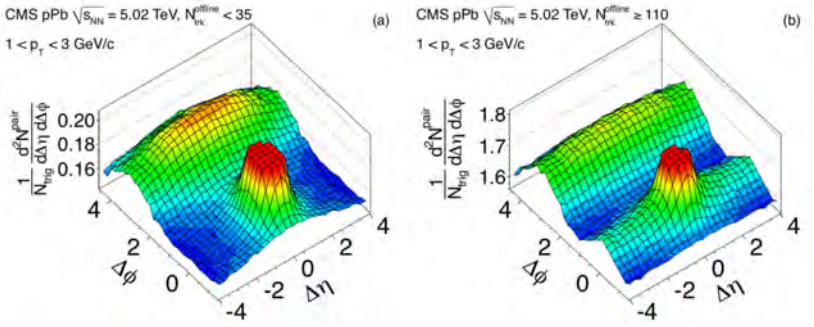

FIGURE 1.12: Di-hadron angular correlations as a function of $\Delta\eta$ and $\Delta\phi$ in low-multiplicity (left) and high-multiplicity (right) p-Pb collisions at $\sqrt{s_{\mathrm{NN}}} = 5.02$ TeV. Figure taken from [29].

1.5 Overview of recent v_n measurements

The aim of the measurements of anisotropic flow, introduced in the previous section, is to extract the information about the hot and dense QGP created in the heavy-ion collisions. Besides others, transport properties such as shear viscosity over entropy density ratio, η/s, attract great interest. This observable characterises the ability (or resistance) of the system to flow, and it is used as a correction to the initial ideal hydrodynamic description.

Motivated by the success of viscous hydrodynamics, a great amount of effort was devoted to a more precise determination of η/s [31]. An overview of the developments on

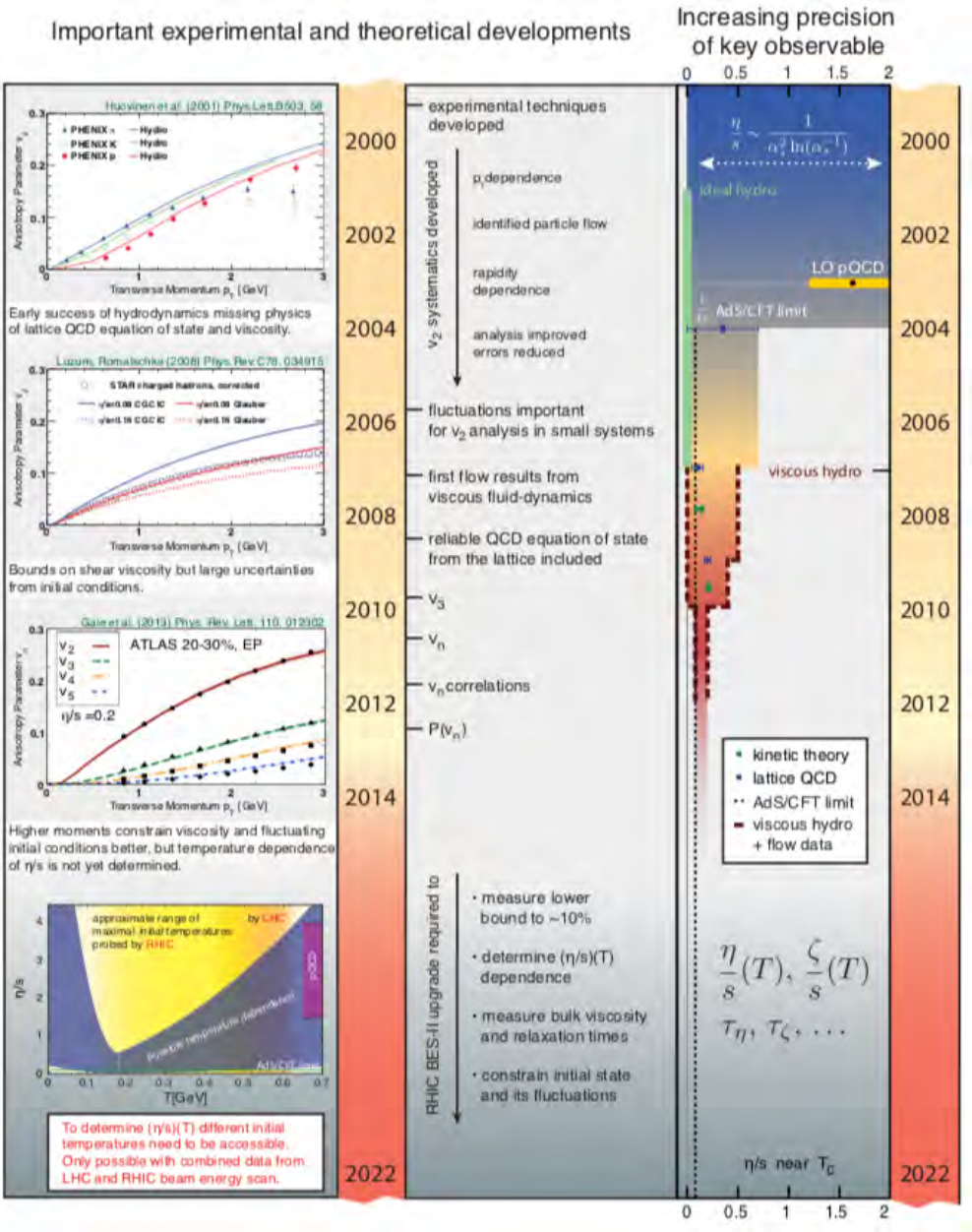

FIGURE 1.13: A time-line overview of important experimental and theoretical developments leading to more precise determination of the medium properties of the QGP, especially the ratio of shear viscosity over entropy density η/s. Figure taken from [31].

both experimental and theoretical fronts in recent years is shown in Fig. 1.13. There, selected milestones marking substantial improvements are shown in the form of time-line together with the corresponding estimates of η/s at the time. According to our current understanding, the value of η/s is rather low, close to the quantum limit of $1/4\pi$ provided by AdS/CFT correspondence [32]. Consequently, based on such observation, the QGP behaves as the "nearly perfect" liquid [33]. A brief overview of the recent state-of-the-art measurements of anisotropic flow, related to the context of this thesis, is discussed in the rest of this section.

The anisotropic flow v_n coefficients can be extracted from the correlation measurement (as will be described in detail in Section 2). The compendium summarising the available results of reference (p_{T}-integrated) v_n of inclusive charged hadrons in Pb-Pb collisions as a function of centrality percentile measured by ALICE is shown in Fig. 1.14. These results are obtained by a two- and multi-particle cumulant method, which is related to different moments of v_n distribution. The order of the cumulant (denoted by a number in curly brackets) can be understood as a number of correlated particles.

Moving from most-central (corresponding to the low values of percentiles) toward semi-central (with higher percentiles) collisions, the values of v_n coefficients increases. Such a centrality dependence is the most pronounced for the second harmonic v_2, i.e. the elliptic flow, as a result of increasing ellipticity of the "almond-shaped" overlapping region. Then, the v_2 decreases again due to the lack of interactions in the peripheral collisions. Moreover, the non-zero values of higher harmonics ($n > 2$) indicate the presence of higher-order azimuthal asymmetries due to the event-by-event fluctuations of the nucleon position, as discussed in Section 1.3. When comparing different harmonics, a clear hierarchy of v_n coefficients is apparent such that $v_2 > v_3 > v_4$.

As can be seen in Fig. 1.14, the elliptic flow coefficient obtained with 2-particle cumulants (while using large pseudorapidity separation), i.e. $v_2\{2, |\Delta\eta| > 1\}$, is systematically higher than values obtained with multi-particle cumulants. Moreover, these higher-order cumulants are in agreement among themselves, i.e. $v_2\{4\} \approx v_2\{6\} \approx v_2\{8\}$. This is due to their lower sensitivity to a so-called *non-flow* (which can be described as correlations mimicking global collective behaviour) and the opposite contribution of fluctuations of underlying v_n distribution. Both of these aspects are discussed further in Section 2.5 and 2.3.

Last but not least, the experimental results are compared to the theoretical calculations (predictions) using hydrodynamic models [34, 35] with different parameterisations, such as constant or temperature-dependent η/s. Based on a rather good agreement, the viscous hydrodynamics provides a suitable description of the azimuthal anisotropy of the system.

In order to provide tighter constraints on the theoretical models, more detailed and

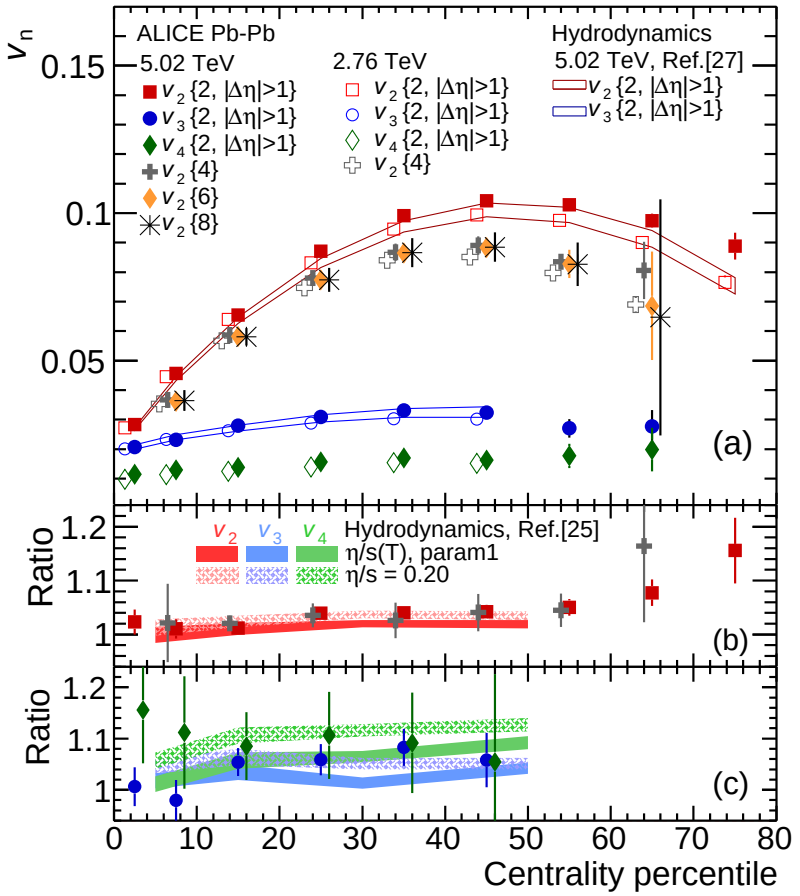

FIGURE 1.14: Measurements integrated (reference) anisotropic flow v_n coefficients as a function of event centrality in Pb-Pb collisions at $\sqrt{s_{\mathrm{NN}}} = 2.76$ TeV and $\sqrt{s_{\mathrm{NN}}} = 5.02$ TeV using two- and multi-particle cumulant method. In addition, a comparison with hydrodynamic calculation [34] (a) and [35] (b,c) is performed. Figure taken from [36].

challenging measurements are needed. This is illustrated by the measurement of p_{T}-differential v_n coefficients of charged particles in Pb-Pb collisions shown in Fig. 1.15. There, the results of presented hydrodynamic models with varying initial conditions (for details, see [37] and the references therein) are capable to reasonably describe the data only in the low p_{T} region up to ~ 1 GeV/c. For a higher p_{T}, the viscous hydrodynamics fails to reproduce the measurements. On the other hand, the experimental results are compared to the models based on path-length L dependent energy-loss of parton passing through the QGP at the very high $p_{\mathrm{T}} > 10$ GeV/c. The measurement of v_2 tends to

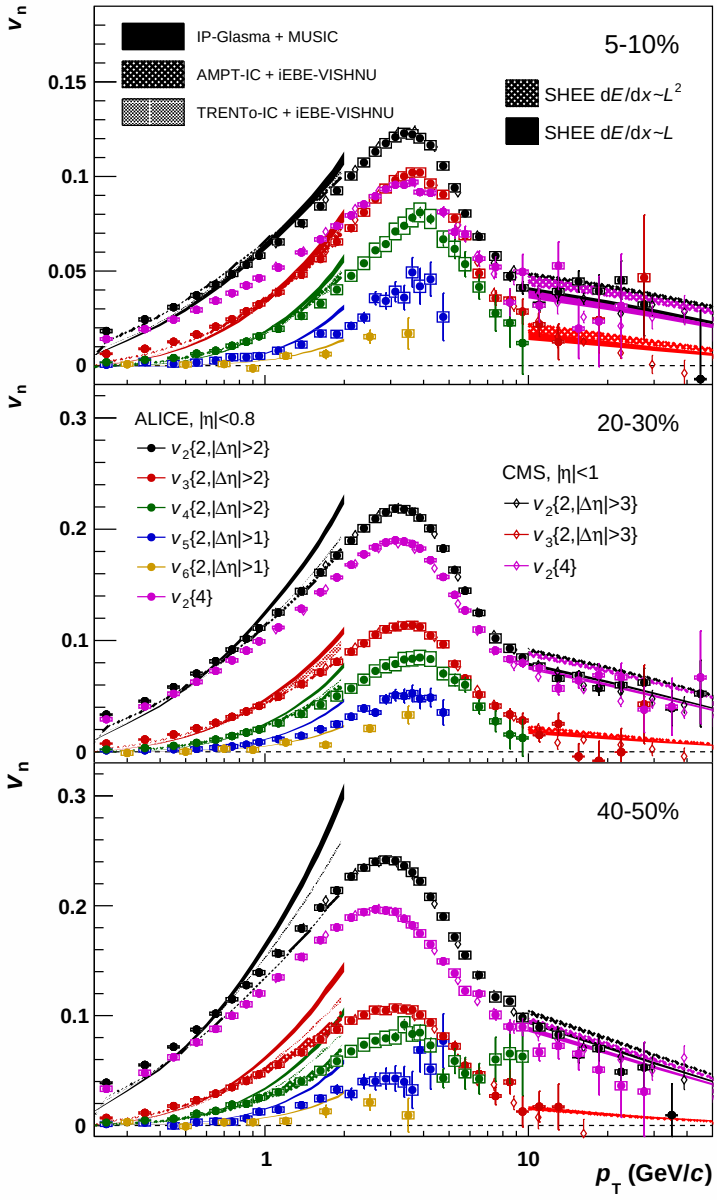

FIGURE 1.15: Measurements p_{T}-differential anisotropic flow v_n coefficients for selected centrality classes of Pb-Pb collisions at $\sqrt{s_{\mathrm{NN}}} = 5.02$ TeV using 2- and 4-particle correlations including various calculations based on hydrodynamic model (low p_{T}) and parton energy-loss (high p_{T}). Figure taken from [37].

prefer the linear dependence, while the case of v_3 provides no firm conclusion, as the two calculations are compatible.

As a next step in this direction, the measurement can be extended by studying the individual particle species separately in contrast of inclusive (un-identified) charged hadrons discussed altogether so far. The results of such study of p_{T}-differential v_2 coefficients of identified $\pi^{\pm}$, $\mathrm{K}^{\pm}$, $\mathrm{K}^0_{\mathrm{S}}$, $\mathrm{p}(\bar{\mathrm{p}})$, $\Lambda(\bar{\Lambda})$, and ϕ meson determined via using 2-particle correlation in Pb-Pb collisions is presented in Fig. 1.16.

In general, all species exhibit similar p_{T} dependence as inclusive charged hadrons: a steep increase in low p_{T}, reaching a maximum value followed by a gradual decrease at high p_{T}. However, interesting features emerge as the slope in low p_{T}, as well as the momentum corresponding to the peak v_n value, varies for different species. As a consequence, a clear mass ordering of v_n coefficients is apparent in $p_{\mathrm{T}} < 2 - 3$ GeV/c. At a higher p_{T}, the individual species form two distinct groups based on the hadron type resulting in a so-called baryon/meson grouping effect. Such behaviour, which will be further discussed in Chapter 5, is typically associated with the interplay of radial flow (at low p_{T}) and parton recombination (at high p_{T}). To illustrate its distinguishing power, the v_2, v_3, and v_4 measurements of identified $\mathrm{K}^{\pm}$are presented in Fig. 1.17. A comparison to the same set of hydrodynamic models with different initial conditions is also shown as in the case of the inclusive charged hadrons.

Motivated by the observed similarities between small and large collision systems, discussed in Section 1.4, measurements of v_2 coefficients of both inclusive and identified $\pi^{\pm}$, $\mathrm{K}^{\pm}$, and $\mathrm{p}(\bar{\mathrm{p}})$ was performed in p-Pb collisions at $\sqrt{s_{\mathrm{NN}}} = 2.76$ TeV. The results of such analysis using di-hadron angular and 2-particle azimuthal correlations, denoted as 2PC and SP, respectively, are shown in Fig. 1.18 for various event multiplicity classes. Even with a limited precision caused by a smaller data sample, a slight hint of mass dependence emerges, similar to the heavy-ion case, in low p_{T} region of 0-20% event class.

From the historical point of view, the observed correlations were considered as a manifestation of the non-flow presence. Subsequently, an attempt for its removal was performed by subtracting the non-flow estimate - specifically, the v_2 signal in collisions with a low number of produced particles corresponding to 60-100% event class. The details of the non-flow subtraction is further discussed in Section 2.5.2. The results of such exercise is presented in Fig. 1.19, where the subtracted v_2 closer resemble the measurement observed in collisions of Pb-Pb collisions. However, it is not clear whether such correlations are similar to the ones caused by medium-induced collectivity as observed in the heavy-ion collision, manifestation of initial stage effects, or it is an artefact of the residual non-flow presence.

In order to shed some light into this puzzling question about the possible origin of the

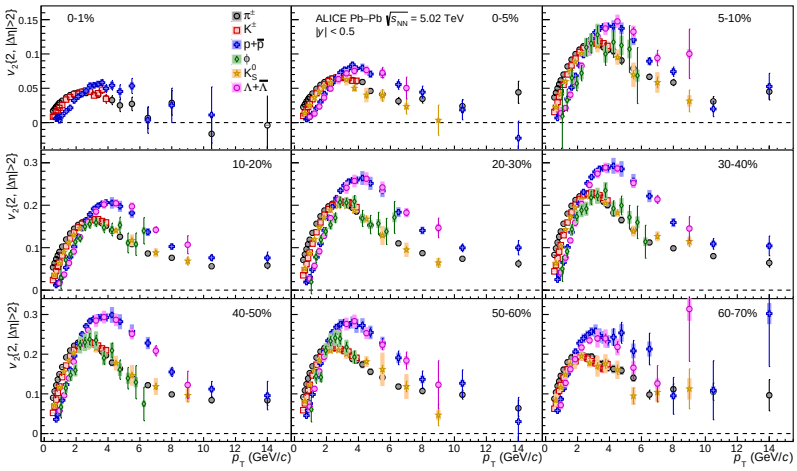

FIGURE 1.16: Measurements p_T-differential v_2 coefficients of identified hadrons for various centrality classes of Pb-Pb collisions at $\sqrt{s_{NN}} = 5.02$ TeV using 2-particle correlation with large η separation. Figure taken from [38].

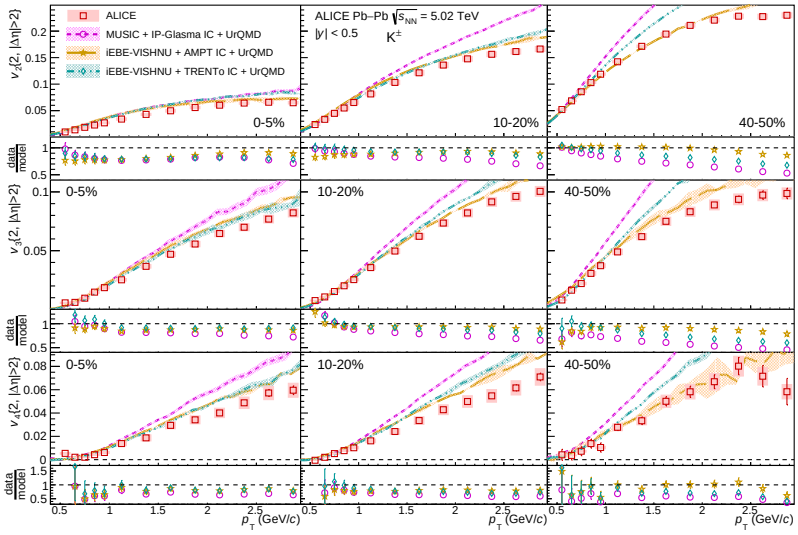

FIGURE 1.17: Measurements p_T-differential v_n coefficients of identified $K^{\pm}$ for selected centrality classes of Pb-Pb collisions at $\sqrt{s_{NN}} = 5.02$ TeV compared to hydrodynamic models with various initial conditions. Figure taken from [38].

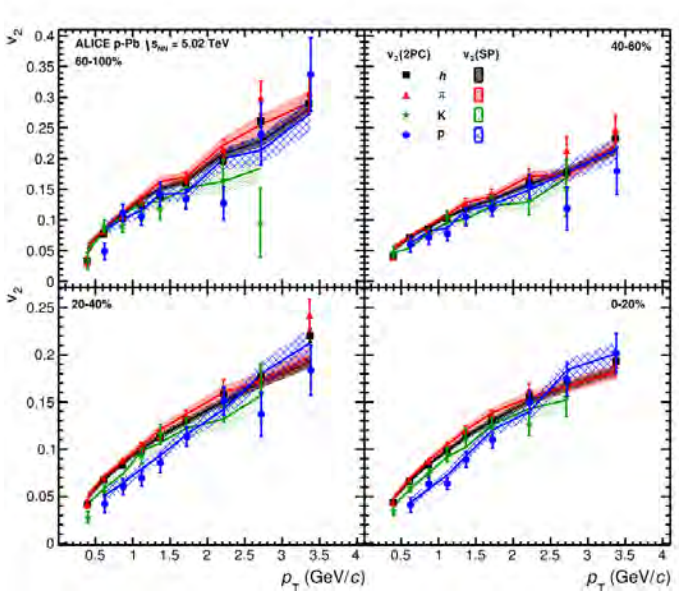

FIGURE 1.18: Measurements p_{T}-differential v_2 coefficients of inclusive and identified hadrons for various centrality classes of p-Pb collisions at $\sqrt{s_{\mathrm{NN}}} = 5.02$ TeV using di-hadron angular (2PC) and 2-particle azimuthal (SP) correlation. Figure taken from [39].

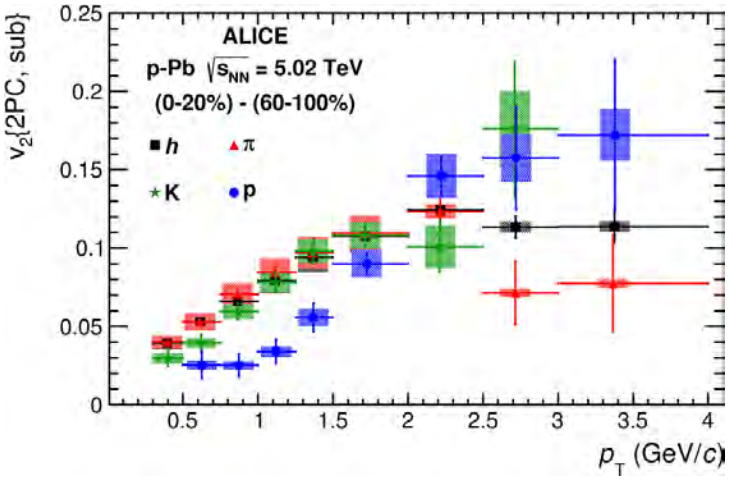

FIGURE 1.19: Measurements p_{T}-differential v_2 coefficients of inclusive and identified hadrons using di-hadron angular correlations in p-Pb collisions at $\sqrt{s_{\mathrm{NN}}} = 5.04$ TeV within 0-20% event class after the non-flow subtraction by estimate from 60-100% event class. Figure taken from [39].

collective behaviour, a plethora of correlation measurement of inclusive charged hadrons in small collision systems emerged. Based on the experience with heavy-ion collisions and due to the insensitivity to non-flow, the multi-particle cumulants are considered as a decisive benchmark for the presence of collectivity [40, 41, 42, 43]. More recently, a comprehensive measurement of multiplicity dependence of v_n coefficients using multi-particle cumulants ranging from 20 to 3000 charged particles was performed [26]. Summarising system-size comparison encapsulating both small and large systems (including Xe-Xe collisions) are depicted in Fig. 1.20. There, the non-zero values of v_n coefficients are observed not only in case of Pb-Pb and Xe-Xe, but also in pp and p-Pb collisions. In addition, the extracted finite v_n coefficients in small systems cannot be explained solely by the non-flow contamination. This is due to the discrepancy between the data and PYTHIA calculation [44] which does not include any final state collective effects and thus represents a rough estimate of the non-flow level. But what is probably the most surprising, is the consistency of the v_n values across all systems in low multiplicity region. This results in a rather smooth transition between small and large systems further supporting initially unexpected similarity between them.

In summary, the development in the recent measurements of higher-order cumulants indicates that the collective behaviour in terms of long-range and multi-particle correlations is indeed present in the small collision systems. However, its origin still represents one of the biggest open questions which continue to attract keen interest in the field of heavy-ion physics [45].

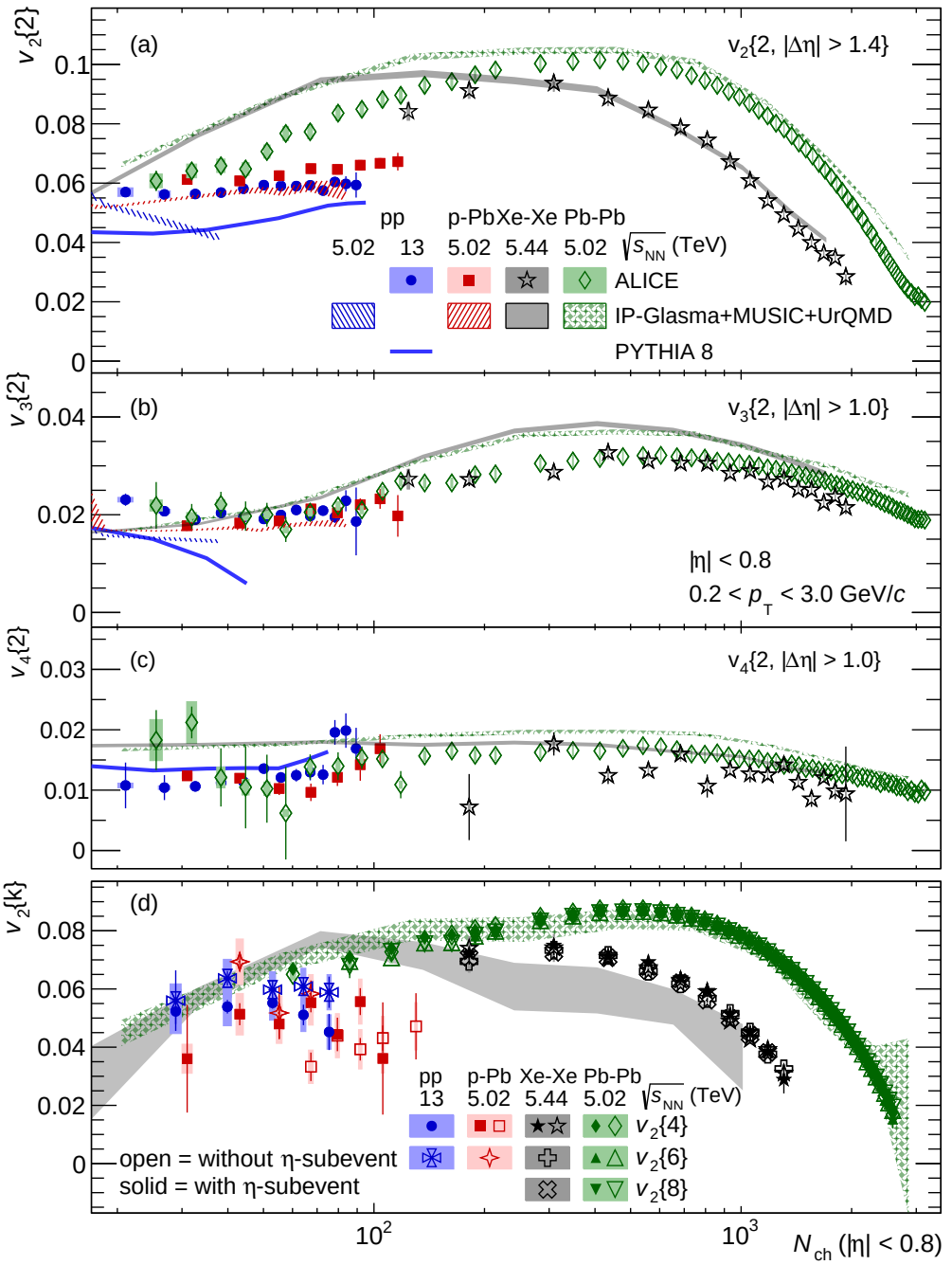

FIGURE 1.20: Multiplicity dependence of anisotropic flow v_n coefficients using two- and multi-particle cumulants in pp, p-Pb, Pb-Pb, and Xe-Xe collisions with various theoretical calculations. Figure taken from [26].

2 Anisotropic flow

2.1 Event plane method

Historically, the event plane (EP) method [46] represented of the common approach used to quantify the anisotropy observed in heavy-ion collisions. This method assumes that the flow symmetry plane angle Ψ_n can be approximated by an experimentally obtained event plane angle Ψ_n^{EP}.

Similarly to (1.2), the extracted anisotropic flow v_n coefficient for a given harmonic n can be expressed as

$$v_n^{\mathrm{obs}} \equiv \left\langle \cos\left[n(\varphi - \Psi_n^{\mathrm{EP}}\right] \right\rangle . \tag{2.1}$$

Since it would require the knowledge of the exact position of all nucleons participating in the collision, the symmetry plane Ψ_n cannot be measured directly. On the other hand, the event plane Ψ_n^{EP} can be determined from the azimuthal angle of all particles detected in a single collision as follows:

$$\Psi_n \simeq \Psi_n^{\mathrm{EP}} \equiv \frac{1}{n} \arctan \frac{\sum_i \sin\left(n\varphi_i\right)}{\sum_i \cos\left(n\varphi_i\right)}. \tag{2.2}$$

In the ideal case, this method requires an infinite number of particles for a proper determination of the event plane. However, such numbers are obviously not available in reality. Consequently, the event plane method suffers from a limited resolution resulting from a finite number of detected particles in a single collision. The EP resolution R_n^{EP} for a given harmonic can be expressed by (2.3) and parametrised using modified Bessel function [46]. In practice, it is experimentally extracted from two (or more) subsets of detected particles within the collision (denoted by A and B).

$$R_n^{\mathrm{EP}} \equiv \left\langle \cos\left[n(\Psi_n^{\mathrm{EP}} - \Psi_n\right] \right\rangle \equiv \sqrt{\left\langle \cos\left[n(\Psi_n^{\mathrm{EP,A}} - \Psi_n^{\mathrm{EP,B}}\right] \right\rangle} \tag{2.3}$$

In order to obtain the final estimate of v_n coefficient using the EP method, the observed v_n^{obs} defined by (2.1) has to be corrected using the extracted event plane resolution, R_n^{EP} (2.3), as follows:

$$v_n\{\mathrm{EP}\} \equiv \frac{v_n^{\mathrm{obs}}}{R_n^{\mathrm{EP}}}. \tag{2.4}$$

Moreover, there is even more serious disadvantage of using EP method. The final $v_n\{\mathrm{EP}\}$ yields a value lying somewhere in between the mean and the RMS of v_n distribution, i.e. $\langle v_n \rangle \leq v_n\{\mathrm{EP}\} \leq \langle v_n^2 \rangle^{1/2}$, depending on the resolution R_n^{EP} itself [47].

2.2 Two- and multi-particle cumulants

The main drawback of estimation of the v_n coefficients is the unavailability to extract the flow symmetry plane experimentally. Although it can be determined from detected particles, as illustrated by the event plane method, such an approach is only an approximation with its limitations as discussed in the previous section.

Alternatively, one can circumvent the necessary knowledge of the flow symmetry plane by measuring event-averaged 2-particle azimuthal correlations. These are related to the anisotropic flow coefficient v_n via (1.2) as can be seen from (2.5). The $\langle\langle\cdot\rangle\rangle$ represents the averaging firstly over correlations between all particles and then over all studied events. Contrary to the previously discussed EP method, estimation of v_n coefficient utilising 2-particle correlation technique is possible without explicit knowledge of symmetry (or event) plane angle Ψ_n.

$$\langle\langle 2\rangle\rangle \equiv \left\langle\left\langle e^{\mathrm{i}n(\varphi_i-\varphi_j)}\right\rangle\right\rangle = \left\langle\left\langle e^{\mathrm{i}n(\varphi_i-\Psi_n)}\right\rangle\left\langle e^{-\mathrm{i}n(\varphi_j-\Psi_n)}\right\rangle\right\rangle = \left\langle v_n^2\right\rangle \tag{2.5}$$

This is generally true for any higher-order correlation of an even number of particles, such as 4-particle correlation expressed by:

$$\begin{aligned}\langle\langle 4\rangle\rangle &\equiv \left\langle\left\langle e^{\mathrm{i}n(\varphi_i+\varphi_j-\varphi_k-\varphi_l)}\right\rangle\right\rangle \\ &= \left\langle\left\langle e^{\mathrm{i}n(\varphi_i-\Psi_n)}\right\rangle\left\langle e^{\mathrm{i}n(\varphi_j-\Psi_n)}\right\rangle\left\langle e^{-\mathrm{i}n(\varphi_k-\Psi_n)}\right\rangle\left\langle e^{-\mathrm{i}n(\varphi_l-\Psi_n)}\right\rangle\right\rangle \\ &= \left\langle v_n^4\right\rangle,\end{aligned} \tag{2.6}$$

and also higher-even-number correlations.

To obtain such event-averaged quantities, one starts by estimating average correlations within a single event. For a given event e with a total of M detected particles, a single-event-averaged 2-particle correlation $\langle 2\rangle_e$ is extracted by averaging over all pairs of M particles as defined by the following:

$$\langle 2\rangle_e = \frac{(M-2)!}{M!}\sum_{\substack{i,j=1\\(i\neq j)}}^{M} e^{\mathrm{i}n(\varphi_i-\varphi_j)}, \tag{2.7}$$

where contributions of individual pairs are summed first and then divided by a number of all possible particle pairs. Similarly for a single-event-averaged 4-particle correlation:

$$\langle 4 \rangle_e = \frac{(M-4)!}{M!} \sum_{\substack{i,j,k,l=1 \\ (i \neq j \neq k \neq l)}}^{M} e^{\mathrm{i}n(\varphi_i + \varphi_j - \varphi_k - \varphi_l)}. \tag{2.8}$$

It should be noted that in order to remove trivial autocorrelation arising from correlating particles with themselves, the terms with identical indices are removed from the sums. Thus $i \neq j$ and $i \neq j \neq k \neq l$ constraints are presented in the summations above.

Afterwards, the single event quantities are averaged over all analysed events as already mentioned. The average is done independently of the actual number of correlated particles. Therefore it can be illustrated for a general m-particle correlation as follows:

$$\langle \langle m \rangle \rangle \equiv \frac{\sum_{e=1}^{N} W_e^{\langle m \rangle} \langle m \rangle_e}{\sum_{e=1}^{N} W_e^{\langle m \rangle}}, \tag{2.9}$$

where N is the total number of studied events, and $W_e^{\langle m \rangle}$ is a specific weight for a e-th event corresponding to the given m-particle correlation.

In order to account for the effects of varying multiplicity of correlated particles in individual events of the overall analysed sample, the following weights considering the total number of combinations is used [48, 49]:

$$W_e^{\langle m \rangle} = \frac{M!}{(M-m)!}, \tag{2.10}$$

where M is total number of correlated particles present in the e-th event, and m is the order of correlation (i.e. number of particles being correlated). Explicitly, the following event weights are used in case of $\langle 2 \rangle$ and $\langle 4 \rangle$, respectively:

$$W_e^{\langle 2 \rangle} = \frac{M!}{(M-2)!} = M(M-1), \tag{2.11}$$

$$W_e^{\langle 4 \rangle} = \frac{M!}{(M-4)!} = M(M-1)(M-2)(M-3). \tag{2.12}$$

Finally, the individual cumulants of v_n coefficients are obtained from event-averaged 2- and 4-particle correlations. The 2-particle cumulant $c_n\{2\}$ is merely equal to $\langle \langle 2 \rangle \rangle$ expressed by (2.13), while the 4-particle cumulant, $c_n\{4\}$, is a combination of both $\langle \langle 2 \rangle \rangle$ and $\langle \langle 4 \rangle \rangle$ as given by (2.14), which makes it "a genuine 4-particle correlation" [50].

$$c_n\{2\} = \langle \langle 2 \rangle \rangle \tag{2.13}$$

$$c_n\{4\} = \langle\langle 4\rangle\rangle - 2\langle\langle 2\rangle\rangle^2 \tag{2.14}$$

These cumulants provide the independent estimates for the anisotropic flow coefficient shown by (2.15) and (2.16). There, v_n coefficients obtained from 2- and 4-particle cumulants are denoted as $v_n\{2\}$ and $v_n\{4\}$, respectively.

$$v_n\{2\} = \sqrt{c_n\{2\}} \tag{2.15}$$

$$v_n\{4\} = \sqrt[4]{-c_n\{4\}} \tag{2.16}$$

So far, only the integrated flow, also called reference flow, was discussed. In the following, a differential flow will be discussed. The following statement can summarise the difference between the two. While the reference flow provides an estimate for a "typical" or "average" value of v_n coefficient for a given sample of collisions (typically defined as a class of collisions, e.g. within a narrow interval of centrality percentiles), a differential flow explores the flow of a subset of correlated particles typically related to a narrower phase-space. This specific subset is generally called particles of interest (POI) in contrast to unbiased[1] inclusive reference flow particles (RFP) used for reference flow estimation discussed in the previous section. Common examples of POIs are particles restricted to a narrow transverse momentum interval, a finite pseudo-rapidity window, or particles belonging to a specific species. In the following, the azimuthal angle of the POI is denoted by ϕ instead of φ, which is used for RFPs, for distinction of the two groups of particles.

A differential correlations are obtained in a very similar way as reference counterparts, with the only difference being that a POI substitutes one of the RPFs. By doing so, one obtains an event-averaged differential 2- and 4-particle correlations:

$$\langle\langle 2'\rangle\rangle = \left\langle\left\langle e^{in(\phi_i - \varphi_j)}\right\rangle\right\rangle, \tag{2.17}$$

$$\langle\langle 4'\rangle\rangle = \left\langle\left\langle e^{in(\phi_i + \varphi_j - \varphi_k - \varphi_l)}\right\rangle\right\rangle, \tag{2.18}$$

where the asterisk is used to distinguish between differential and integrated quantities. These are obtained from corresponding single-event correlations defined as:

$$\langle 2'\rangle_e = \frac{1}{m_p M - m_s}\sum_{i=1}^{m_p}\sum_{j=1}^{M} e^{in(\phi_i - \varphi_j)}, \tag{2.19}$$

[1] The RFPs are not completely unbiased since one typically selects only particles with relatively small p_T. This is done to reduce the contribution from high p_T ones mostly originating from hard processes such as jets which are not related to common symmetry plane, i.e. non-flow (discussed in Section 2.5).

$$\langle 4' \rangle_e = \frac{1}{(m_p M - 3m_s)(M-1)(M-2)} \sum_{i=1}^{m_p} \sum_{\substack{j,k,l=1 \\ (j \neq k \neq l)}}^{M} e^{in(\phi_i + \varphi_j - \varphi_k - \varphi_l)}, \tag{2.20}$$

where m_p represents a number of POIs and m_s denotes the number of particles that are tagged as both POI and RFP in a given event e. The latter is used for subtracting the contribution of autocorrelation caused by correlating identical particles.

Next, the average of such single-event correlations is done as prescribed by (2.9) by substituting integrated quantities with differential ones. However, as the number of combinations of correlating particles changes, so does the corresponding event weight given by (2.21) and (2.12) for 2- and 4-particle correlation, respectively.

$$W_e^{\langle 2' \rangle} \equiv m_p M - m_s \tag{2.21}$$

$$W_e^{\langle 4' \rangle} \equiv (m_p M - 3m_s)(M-1)(M-2) \tag{2.22}$$

Afterwards, the 2- and 4-particle differential cumulants are calculated from the differential correlations:

$$d_n\{2\} \equiv \langle\langle 2' \rangle\rangle, \tag{2.23}$$

$$d_n\{4\} \equiv \langle\langle 4' \rangle\rangle - 2\langle\langle 2' \rangle\rangle \langle\langle 2 \rangle\rangle. \tag{2.24}$$

Finally, the differential flow coefficients v_n' are estimated as given by (2.25) and (2.26). Since the differential correlations contain information not only about differential coefficient but also reference one, as indicated in (2.17) and (2.18), a combination of both cumulants is needed for the evaluation.

$$v_n'\{2\} = \frac{d_n\{2\}}{\sqrt{c_n\{2\}}}, \tag{2.25}$$

$$v_n'\{4\} = \frac{-d_n\{4\}}{(-c_n\{4\})^{3/4}}. \tag{2.26}$$

2.2.1 Q-cumulants

As discussed in the beginning of the previous section, using multi-particle correlations dispense with knowing the exact angle of the experimental symmetry plane. However, such useful feature does not come for free. To obtain a simple $\langle 2 \rangle$, one has to evaluate a difference in azimuthal angle between two correlated particles for each pair in a given event. Although this might seem innocent at first, in fact, it presents a severe issue which complexity can be illustrated in the following example.

Let there be a single event with N particles. Single iteration over all of them requires N operations. In order to iterate over all pairs, a total of $N(N-1)$ operations is needed.

Therefore the complexity of this problem is $\mathcal{O}(N^2)$. Now, imagine that one is also interested in higher-order correlations such as $\langle 4 \rangle$. In such a case, the total number of combinations is $N(N-1)(N-2)(N-3)$. Thus the complexity is $\mathcal{O}(N^4)$. This example can be simply generalised for m-particle correlations $\langle m \rangle$ which calculation would require $\mathcal{O}(N^m)$ operations for each collision. Even with modern CPU architectures and the growing availability of computing capacity, this still poses a problem from the point of view of algorithm complexity. It can even prevent higher-number correlation from being calculated at all, as already complexity of $\mathcal{O}(N^3)$ is considered unbearable within the field of high-energy physics [51] given the overall number of recorded collisions and number of particles produced per such event.

Instead of evaluating the contribution of each combination of correlated particles, an alternative approach was proposed in [52] utilising a complex flow vector Q_n constructed from all RFPs in a given event as illustrated by (2.27). This method was further developed in [48] and is commonly referred to as Q-cumulants (QC).

$$Q_n = \sum_{i=1}^{M} e^{\mathrm{i}n\varphi_i} = \left(\sum_{i=1}^{M} \cos n\varphi_i ; \mathrm{i} \sum_{i=1}^{M} \sin n\varphi_i \right) \tag{2.27}$$

With this new quantity, one can express the relation for $\langle 2 \rangle$ and $\langle 4 \rangle$ given by (2.7) and (2.8), respectively, in terms of Q_n vectors as follows[2]:

$$\langle 2 \rangle = \frac{|Q_n|^2 - M}{M(M-1)}, \tag{2.28}$$

$$\langle 4 \rangle = \frac{|Q_n|^4 + |Q_{2n}|^2 - 4(M-2)|Q_n|^2 - 2\,\mathrm{Re}(Q_{2n}Q_n^*Q_n^*) + 2M(M-3)}{M(M-1)(M-2)(M-3)}. \tag{2.29}$$

Since only Q_n quantities are needed for evaluating 2- and 4-particle correlations (hence the name Q-cumulants) without actual iteration over all combination, only a single pass over all particles is necessary. This effectively reduces the complexity from $\mathcal{O}(N^m)$ to $\mathcal{O}(N)$, which presents a tremendous improvement.

For the differential correlations, another flow vector p_n is built from all particles selected as POIs in a similar fashion, as illustrated by (2.30). In addition to that, in case of overlap, an additional flow vector, s_n, given by (2.31) is constructed from all particles labelled as both POI and RFP[3]. This is done to account for autocorrelations terms present in the sums, i.e. to avoid double counting of contributions from correlating particles with themselves. Therefore it substitutes the conditions for unique indexes used in (2.7),

[2] Note, the M subtracted in a nominator is related to autocorrelation terms in the summation (i.e. terms where $i = j$).

[3] For clarity, here the notation deviates from the original publication where q_n is used instead of s_n.

etc.

$$p_n = \sum_{i=1}^{m_p} e^{in\phi_i}, \quad i \in \text{POI} \tag{2.30}$$

$$s_n = \sum_{i=1}^{m_s} e^{in\phi_i}, \quad i \in \text{POI} \cap \text{RFP} \tag{2.31}$$

When all particles are correctly labelled, and the corresponding flow vectors are constructed, single event 2-particle $\langle 2' \rangle$ and 4-particle $\langle 4' \rangle$ differential correlations are determined by (2.32) and (2.33), respectively.

$$\langle 2' \rangle = \frac{p_n Q_n^* - m_s}{m_p M - m_s} \tag{2.32}$$

$$\begin{aligned} \langle 4' \rangle = \Big(& p_n Q_n Q_n^* Q_n^* - s_{2n} Q_n^* Q_n^* - p_n Q_n Q_{2n}^* - 2M p_n Q_n^* \\ & - 2m_s |Q_n|^2 + 7 s_n Q_n^* - Q_n s_n^* + s_{2n} Q_{2n}^* + 2 p_n Q_n^* \\ & + 2m_s M - 6m_s \Big) / \left[(m_p M - 3m_s)(M-1)(M-2) \right] \end{aligned} \tag{2.33}$$

2.2.2 Generic Framework

While addressing the issue of algorithm complexity and thus significantly reducing the amount of computing resources required, the QCs are "very tedious to compute analytically" [53].

The implementation of Generic Framework (GF) [53] provides a universal prescription for calculating correlations of any arbitrary number of particles and any combination of flow harmonics. For example, m-particle azimuthal correlation with a general combination of harmonics n_i can be determined using the relation:

$$\langle m \rangle_{n_1, n_2, \ldots, n_m} \equiv \frac{\mathrm{N} \langle m \rangle_{n_1, n_2, \ldots, n_m}}{\mathrm{D} \langle m \rangle_{n_1, n_2, \ldots, n_m}}, \tag{2.34}$$

where numerator $\mathrm{N}\langle m \rangle$ provides total m-particle correlation, while denominator $\mathrm{D}\langle m \rangle$ generally counts all pairs within a given event. The numerator and denominator terms are defined by (2.35) and (2.36), respectively. It should also be noted that the denominator term is equivalent to numerator term with all harmonic indices equal to zero as explicitly shown in (2.36).

$$\mathrm{N} \langle m \rangle_{n_1, n_2, \ldots, n_m} \equiv \sum_{\substack{k_1, k_2, \ldots, k_m = 1 \\ (k_1 \neq k_2 \neq \cdots \neq k_m)}}^{M} w_{k_1} w_{k_2} \ldots w_{k_m} e^{n_1 \varphi_{k_1} + n_2 \varphi_{k_2} + \cdots + n_m \varphi_{k_m}} \tag{2.35}$$

$$\mathrm{D}\left\langle m\right\rangle_{n_1,n_2,\ldots,n_m} \equiv \sum_{\substack{k_1,k_2,\ldots,k_m=1 \\ (k_1\neq k_2\neq\cdots\neq k_m)}}^{M} w_{k_1} w_{k_2} \ldots w_{k_m} = \mathrm{N}\left\langle m\right\rangle_{0,0,\ldots,0} \tag{2.36}$$

The GF formalism allows for more robust treatment of corrections for systematic biases arising from various detector inefficiencies. In order to do that, single-particle weights w_i are introduced to all complex flow vectors discussed in the previous section[4]:

$$Q_{n,p} = \sum_{\substack{i=1 \\ (i\in\mathrm{RFP})}}^{M} w_i^p e^{\mathrm{i}n\varphi_i}, \tag{2.37}$$

$$p_{n,p} = \sum_{\substack{i=1 \\ (i\in\mathrm{POI})}}^{m_p} w_i^p e^{\mathrm{i}n\phi_i}, \tag{2.38}$$

$$s_{n,p} = \sum_{\substack{i=1 \\ (i\in\mathrm{POI}\cap\mathrm{RFP})}}^{m_s} w_i^p e^{\mathrm{i}n\phi_i}. \tag{2.39}$$

For illustration, 2-particle correlation $\langle 2\rangle$ is given by the ratio of the following terms:

$$\mathrm{N}\left\langle 2\right\rangle_{n_1,n_2} = Q_{n_1,1}Q_{n_2,1} - Q_{n_1+n_2,2}, \tag{2.40}$$

$$\mathrm{D}\left\langle 2\right\rangle_{n_1,n_2} = \mathrm{N}\left\langle 2\right\rangle_{0,0} = Q_{0,1}^2 - Q_{0,2}. \tag{2.41}$$

In a case of opposite harmonic indices, i.e. $n_1 = -n_2$, and that all particles are weighted the same, i.e. $\forall i, w_i = 1$ (therefore $\sum w_i = M$) relations (2.40) and (2.41) are identical to numerator and denominator of (2.28), respectively[5]. Similarly, for 2-particle differential correlation $\langle 2'\rangle$, the following terms:

$$\mathrm{N}\left\langle 2'\right\rangle_{\underline{n_1},n_2} = p_{n_1,1}Q_{n_2,1} - s_{n_1+n_2,2}, \tag{2.42}$$

$$\mathrm{D}\left\langle 2'\right\rangle_{\underline{n_1},n_2} = \mathrm{N}\left\langle 2'\right\rangle_{\underline{0},0} = p_{0,1}Q_{0,1} - s_{0,2}, \tag{2.43}$$

[4] It should be noted, that the concept of particle weights was already mentioned in the Appendix of Ref. [48], although in a different context.

[5] The underscore indicates which harmonic index corresponds to the differential flow vector.

are equal to numerator and denominator of (2.32), respectively. The equivalency between GF and QC formalism is also valid for 4-particle correlations, as shown in relations (2.44)-(2.47) under the same condition.

$$\begin{aligned}\mathrm{N}\langle 4\rangle_{n_1,n_2,n_3,n_4} &= Q_{n_1,1}Q_{n_2,1}Q_{n_3,1}Q_{n_4,1} - Q_{n_1+n_2,2}Q_{n_3,1}Q_{n_4,1} \\ &- Q_{n_1+n_3,2}Q_{n_2,1}Q_{n_4,1} - Q_{n_1,1}Q_{n_2+n_3,2}Q_{n_4,1} \\ &+ 2Q_{n_1+n_2+n_3,3}Q_{n_4,1} - Q_{n_2,1}Q_{n_3,1}Q_{n_1+n_4,2} \\ &+ Q_{n_2+n_3,2}Q_{n_1+n_4,2} - Q_{n_1,1}Q_{n_3,1}Q_{n_2+n_4,2} \\ &+ Q_{n_1+n_3,2}Q_{n_2+n_4,2} + 2Q_{n_3,1}Q_{n1+n_2+n_4,3} \\ &- Q_{n_1,1}Q_{n_2,1}Q_{n_3+n_4,2} + Q_{n_1+n_2,2}Q_{n_3+n_4,2} \\ &+ 2Q_{n_2,1}Q_{n1+n_3+n_4,3} + 2Q_{n_1,1}Q_{n_2+n_3+n_4,3} \\ &- 6Q_{n_1+n_2+n_3+n_4,4}\end{aligned} \tag{2.44}$$

$$\begin{aligned}\mathrm{D}\langle 4\rangle_{n_1,n_2,n_3,n_4} &= \mathrm{N}\langle 4\rangle_{0,0,0,0} \\ &= Q_{0,1}^4 - 6Q_{0,1}^2Q_{0,2} + 3Q_{0,2}^2 + 8Q_{0,1}Q_{0,3} - 6Q_{0,4}\end{aligned} \tag{2.45}$$

$$\begin{aligned}\mathrm{N}\langle 4'\rangle_{\underline{n_1},n_2,n_3,n_4} &= p_{n_1,1}Q_{n_2,1}Q_{n_3,1}Q_{n_4,1} - s_{n_1+n_2,2}Q_{n_3,1}Q_{n_4,1} \\ &- s_{n_1+n_3,2}Q_{n_2,1}Q_{n_4,1} - p_{n_1,1}Q_{n_2+n_3,2}Q_{n_4,1} \\ &+ 2s_{n_1+n_2+n_3,3}Q_{n_4,1} - Q_{n_2,1}Q_{n_3,1}s_{n_1+n_4,2} \\ &+ Q_{n_2+n_3,2}s_{n_1+n_4,2} - p_{n_1,1}Q_{n_3,1}Q_{n_2+n_4,2} \\ &+ s_{n_1+n_3,2}Q_{n_2+n_4,2} + 2Q_{n_3,1}s_{n1+n_2+n_4,3} \\ &- p_{n_1,1}Q_{n_2,1}Q_{n_3+n_4,2} + s_{n_1+n_2,2}Q_{n_3+n_4,2} \\ &+ 2Q_{n_2,1}s_{n1+n_3+n_4,3} + 2p_{n_1,1}Q_{n_2+n_3+n_4,3} \\ &- 6s_{n_1+n_2+n_3+n_4,4}\end{aligned} \tag{2.46}$$

$$\begin{aligned}\mathrm{D}\langle 4'\rangle_{\underline{n_1},n_2,n_3,n_4} &= \mathrm{N}\langle 4'\rangle_{\underline{0},0,0,0} \\ &= p_{0,1}Q_{0,1}^3 - 3s_{0,2}Q_{0,1}^2 - 3p_{0,1}Q_{0,1}Q_{0,2} + 3s_{0,2}Q_{0,1} \\ &+ 6s_{0,3}Q_{0,1} + 2p_{0,1}Q_{0,3} - 6s_{0,4}\end{aligned} \tag{2.47}$$

Besides the previously discussed measurement of the v_n coefficient using 2- and 4-particle cumulants, the GF allows for a variety of new multi-particle azimuthal observables utilising a combination of multiple harmonics, such as a study of so-called symmetric cumulants [53] or non-linear flow modes [54] (discussed further in Section 2.4).

For determination of the latter, the following relations for integrated 3-particle correlations are essential:

$$\begin{aligned} \mathrm{N}\langle 3\rangle_{n_1,n_2,n_3} &= Q_{n_1,1}Q_{n_2,1}Q_{n_3,1} - Q_{n_3,1}Q_{n_1+n_2,2} \\ &\quad - Q_{n_2,1}Q_{n_1+n_3,2} - Q_{n_1,1}Q_{n_2+n_3,2} + 2Q_{n_1+n_2+n_3,3}, \end{aligned} \tag{2.48}$$

$$\begin{aligned} \mathrm{D}\langle 3\rangle_{n_1,n_2,n_3} &= \mathrm{N}\langle 3\rangle_{0,0,0} \\ &= Q_{0,1}^3 - 3Q_{0,1}Q_{0,2} + 2Q_{0,3}, \end{aligned} \tag{2.49}$$

as well as differential equivalents:

$$\begin{aligned} \mathrm{N}\langle 3'\rangle_{\underline{n_1},n_2,n_3} &= p_{n_1,1}Q_{n_2,1}Q_{n_3,1} - Q_{n_3,1}s_{n_1+n_2,2} \\ &\quad - Q_{n_2,1}s_{n_1+n_3,2} - p_{n_1,1}Q_{n_2+n_3,2} + 2s_{n_1+n_2+n_3,3}, \end{aligned} \tag{2.50}$$

$$\begin{aligned} \mathrm{D}\langle 3'\rangle_{\underline{n_1},n_2,n_3} &= \mathrm{N}\langle 3'\rangle_{0,0,0} \\ &= p_{0,1}Q_{0,1}^2 - 2Q_{0,1}s_{0,2} - p_{0,1}Q_{0,2} + 2s_{0,3}. \end{aligned} \tag{2.51}$$

As one can see from equations above, while relations for 2- and 3-particle correlations are rather compact, already 4-particle correlation requires a lot more terms to be evaluated. In fact, the number of unique terms per correlator follows a steeply-growing sequence of Bell numbers counting possible partitions for a given set [53]:

$$1, 2, 5, 15, 52, 203, 877, 4120, 21147, \ldots. \tag{2.52}$$

According to this sequence (2.52), an analytical solution for the next even correlator $\langle 6\rangle$ involves 203 terms, which would no longer fit on a single page and thus are not explicitly written here.

Fortunately, GF formalism allows to use a recursive algorithm which calculates higher-number correlations from previously obtained lower-number ones as illustrated by the pseudocode below[6].

[6] Please note, that the recursive algorithm is mentioned here for completeness and to satisfy reader's curiosity and it was not used in the analysis described in this thesis.

Algorithm Calculate $\mathrm{N}\langle m\rangle_{n_1,n_2,\ldots,n_m}$

if $m = 1$ **then**
  return $Q_{n_1,1}$
else
  $C \leftarrow 0$
  for $k \leftarrow (m-1)$ **to** 1 **do**
    for each combination $c = \{c_1, \ldots c_k\}$ of $\{n_1, \ldots, n_{m-1}\}$ **do**
      $q \leftarrow \sum_{j \notin c} n_j$
      $C \leftarrow C + (-1)^{m-k}(m-k-1)! \times \mathrm{N}\langle k\rangle_{c_1,\ldots,c_k} \times Q_{q,m-k}$
    end for each c
  end for k
  return C
end if

2.3 Flow fluctuations

Being the dominant component in non-central heavy-ion collisions, the initial eccentricity $\mathcal{E}_2$ (1.4), characterised by the overlapping region of the two projectiles, drives the elliptic flow v_2 coefficient [55, 56]. However, as the geometry itself fluctuates on an event-by-event basis, so does the magnitude of the v_n coefficients. Therefore, there are additional features of the system affecting the measurement of v_n coefficients besides the non-flow component: flow fluctuations. These are mainly a result of fluctuations of the position of individual nucleons within the two nuclei and finite spread of impact parameters within a given event class (centrality bin) [57].

It was shown that for a Bessel-Gaussian distribution in a limit of small fluctuations (i.e. $\sigma_n \ll \langle v_n\rangle$), v_n from 2- and 4-particle cumulants have opposite contribution from flow fluctuations σ_n [58, 59], as expressed by

$$v_n\{2\}^2 = \langle v_n\rangle^2 + \sigma_n^2 + \delta_n^2, \tag{2.53}$$

$$v_n\{4\}^2 \approx \langle v_n\rangle^2 - \sigma_n^2, \tag{2.54}$$

where δ_n denotes the contribution of non-flow component described in the previous section. By measuring 2- and 4-particle cumulants, one can effectively learn about the collision dynamics in terms of level of fluctuations as well as the mean value of v_n Probability Density Function (PDF).

Assuming that the non-flow contribution is suppressed in 2- and 4-particle correlations, the mean value, $\langle v_n\rangle$, as well as the fluctuations, σ_n, can be extracted using (2.53)-(2.54) as follows:

$$\langle v_n\rangle = \sqrt{\frac{v_n\{2\}^2 + v_n\{4\}^2}{2}}, \tag{2.55}$$

$$\sigma_n = \sqrt{\frac{v_n\{2\}^2 - v_n\{4\}^2}{2}}. \tag{2.56}$$

Besides these absolute quantities, the relative fluctuations of v_n coefficients, $F(v_n)$, can be estimated as a ratio of the σ_n and $\langle v_n \rangle$:

$$F(v_n) \equiv \frac{\sigma_n}{\langle v_n \rangle} = \sqrt{\frac{v_n\{2\}^2 - v_n\{4\}^2}{v_n\{2\}^2 + v_n\{4\}^2}}. \tag{2.57}$$

The flow fluctuations take a vital part in the studies of anisotropic flow. Their significance grew even more after the observation that triangular flow v_3 (and its corresponding initial eccentricity $\mathcal{E}_3$) is primarily driven by such fluctuations of the initial geometry [24, 60].

2.4 Linear and non-linear response

As already mentioned, the lower-order (i.e. $n \leq 3$) v_n coefficients are primarily determined by the corresponding initial anisotropy vectors $\mathcal{E}_n$ [55, 56, 24] as defined by (1.4). However, it was shown that for higher harmonics (i.e. $n > 3$), v_n coefficients scale with a cumulant-based anisotropy vector $\mathcal{E}'_n$ instead [61, 62]. For example, fourth-order cumulant-based anisotropy $\mathcal{E}'_4$, given by

$$\mathcal{E}'_4 = \epsilon'_4 e^{in\Phi'_4} = \epsilon_4 e^{in\Phi_4} + \frac{3\langle r^2 \rangle^2}{\langle r^4 \rangle} \epsilon_2^2 e^{in\Phi_2}, \tag{2.58}$$

is related to standard (momentum-based) anisotropy coefficients ϵ_4 and ϵ_2. This indicates that v_4 is not only linearly dependent on corresponding initial anisotropy coefficient ϵ_4 (similarly to lower harmonics), but also quadratically dependent on ϵ_2.

Such lower-order contributions (or their products) in higher-order flow is referred to as non-linear response [54, 63]. The higher-order complex flow vectors V_n, defined by (1.3), can be therefore decomposed into a linear V_n^{L} and a non-linear V_n^{NL} component, as expressed by the following relations:

$$V_4 = V_4^{\mathrm{L}} + V_4^{\mathrm{NL}} = V_4^{\mathrm{L}} + \chi_{4,22}(V_2)^2, \tag{2.59}$$

$$V_5 = V_5^{\mathrm{L}} + V_5^{\mathrm{NL}} = V_5^{\mathrm{L}} + \chi_{5,32} V_3 V_2, \tag{2.60}$$

$$V_6 = V_6^{\mathrm{L}} + V_6^{\mathrm{NL}} = V_6^{\mathrm{L}} + \chi_{6,33}(V_3)^2 + \chi_{6,222}(V_2)^3 + \chi_{6,42} V_4^L V_2, \tag{2.61}$$

where $\chi_{n,m_1,\ldots,m_k}$ referred as non-linear mode coefficients, quantify the contribution of lower order harmonics $(m_1, \ldots, m_k)$ to the overall V_n [64].

Similarly to v_n coefficients representing the magnitude of the flow vector V_n, the magnitude of the non-linear component is denoted as $v_{n,m_1,\ldots,m_k}$ for consistency and are given by the following relations:

$$v_{4,22} = \frac{\langle v_4 v_2^2 \cos\left(4\Psi_4 - 4\Psi_2\right)\rangle}{\sqrt{\langle v_2^4\rangle}} \approx \langle v_4 \cos\left(4\Psi_4 - 4\Psi_2\right)\rangle\,, \tag{2.62}$$

$$v_{5,32} = \frac{\langle v_5 v_3 v_2 \cos\left(5\Psi_5 - 3\Psi_3 - 2\Psi_2\right)\rangle}{\sqrt{\langle v_3^2 v_2^2\rangle}} \approx \langle v_5 \cos\left(5\Psi_5 - 3\Psi_3 - 2\Psi_2\right)\rangle\,, \tag{2.63}$$

$$v_{6,33} = \frac{\langle v_6 v_3^2 \cos\left(6\Psi_6 - 6\Psi_3\right)\rangle}{\sqrt{\langle v_3^4\rangle}} \approx \langle v_6 \cos\left(6\Psi_6 - 6\Psi_3\right)\rangle\,. \tag{2.64}$$

Note, that the approximation on the RHS of (2.62)-(2.65) is valid under the assumption of weak correlation between individual v_n coefficients [54].

In the case of differential study of the non-linear response, the integrated coefficient with the highest harmonics is substituted by a differential one. For example,

$$v_{5,32}(p_{\mathrm{T}}) \approx \langle v_5(p_{\mathrm{T}}) \cos\left(5\Psi_5 - 3\Psi_3 - 2\Psi_2\right)\rangle\,. \tag{2.65}$$

These coefficients are experimentally obtained as a ratio of 3- and 4-particle correlations[7]. Therefore, the multi-particle correlations techniques described earlier in this chapter can be used for its determination. Notably, the Generic Framework is a convenient tool due to its flexibility in terms or higher-order correlations and precise corrections, as discussed in Section 2.2.2.

2.5 Non-flow contribution

Azimuthal correlation techniques are useful tools to quantify the level of anisotropic flow. Only collective effects related to global symmetry plane were discussed in this chapter so far. However, there is an additional component encompassing all correlations not related to the expanding medium, generally referred to as non-flow. In the context of the analysis of the v_n coefficients aimed to probe the collective behaviour of collision dynamics, non-flow presents an undesired background biasing the results. Hence, the effort is made to eliminate (or at least reduce) the effects of non-flow to prevent such bias.

[7] It should be stressed here, that non-linear flow coefficients are not cumulants related to the corresponding observables contrary to previously discussed $v_n\{m\}$ observables.

Typical representatives of the non-flow are resonance decays and jet fragmentation. Such processes are characterised by creating localised clusters consisting of a limited number of particles. Consequently, especially short-range 2-particle correlations are very sensitive to non-flow contamination. A natural way of how to reduce the effect of such few-particle processes is to utilise multi-particle correlations. Already 4-particle cumulants are rather insensitive to such non-flow component since the lower-order correlations are removed by construction [50, 59, 48]. The sensitivity of the cumulant technique to non-flow can be summarised by the following relations where the non-flow contribution is denoted by δ_n:

$$v_n\{2\}^2 = \left\langle v_n^2 \right\rangle + \delta_n, \tag{2.66}$$

$$v_n\{4\}^2 = \left\langle v_n^2 \right\rangle. \tag{2.67}$$

Even though using the multi-particle cumulant method could effectively suppress the non-flow, it is not always accessible as it requires a higher number of correlated particles, which makes it quite statistically demanding. Currently, there are few experimental methods available on the market, providing an alternative approach for reducing the non-flow contamination in 2-particle correlations. The most commonly used ones are a sub-event method imposing separation between correlated particles, and subtraction of a suitable non-flow estimate from the correlation measurement. Both methods are used in this analysis, and their implementation is described in the following.

2.5.1 Sub-event method

When a measurement is performed using standard 2- (or multi-)particle correlation technique as described in Section 2.2, all possible combinations of pairs (or m-tuples) within the whole acceptance are taken into account. Concerning the flow vectors, all corresponding particles are used for their construction. This is illustrated in Fig. 2.1.

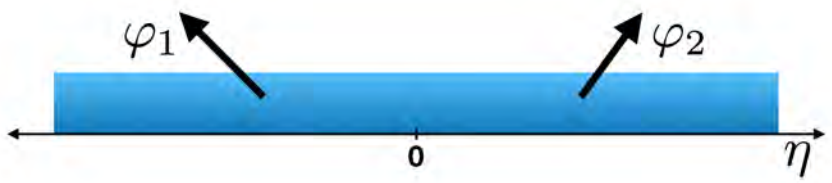

FIGURE 2.1: Illustration of standard correlation technique of particle pairs with azimuthal angles (φ_1, φ_2) within a single correlation region (blue rectangle) covering whole available detector η acceptance. Figure taken from [65].

As mentioned in the previous section, particles produced in non-flow processes are typically clustered close to each other. Consequently, by imposing the separation between the correlated particles, the non-flow contribution from these sources is significantly reduced. The original acceptance coverage is separated into two or more exclusive regions called sub-events. Specifically, all the particles within the symmetric region of $\pm\eta$ are excluded, and thus a pseudorapidity separation denoted as $|\Delta\eta| > 2\eta$ is created between the two newly formed sub-events. According to this notation, the smallest separation of $|\Delta\eta| > 0$ is possible when the two sub-events share a common boundary. Then, the full acceptance is covered, and no particles are excluded. Although the overall number of combinations of correlated pairs is reduced compared to the standard case without sub-events, to reduce short-range correlations further, a larger η separation ought to be imposed. With a larger $|\Delta\eta|$, the exclusion region is larger. As a smaller number of correlated pairs is used in the calculations, the statistical precision is reduced. An inherent trade-off takes place. Consequently, a delicate balance needs to be found between the number of correlated particles and the width of the applied gap.

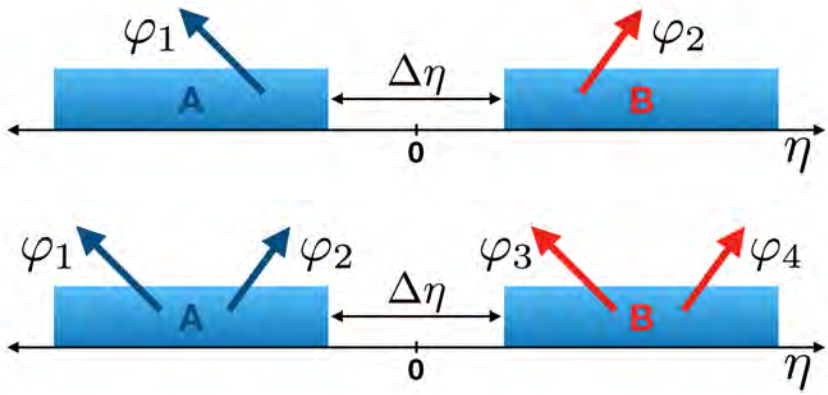

FIGURE 2.2: Illustration of 2- (top) and 4-particle (bottom) correlation using sub-event method where η separation is imposed between the particles located within the region A and those in B (blue rectangles) by excluding $|\Delta\eta|$ interval symmetrically arround 0 of the overall η detector acceptance. Figure taken from [65].

Similarly to (2.5) and (2.6), the event-averaged 2- and 4-particle correlations for a given harmonic n using the sub-event method are expressed by (2.68) and (2.69), respectively. Here, A and B denote the corresponding sub-events within which the correlated particles are located. This is depicted in Fig. 2.2. In case of $\langle\langle 4\rangle\rangle^{|\Delta\eta|}$, it is crucial that the azimuthal angle of particles taken from the same sub-event contributes by the same sign

in the exponent, i.e. particles from sub-event A positively, while those from B negatively.

$$\langle\langle 2\rangle\rangle^{|\Delta\eta|} = \left\langle\left\langle e^{in(\varphi_i^{\mathrm{A}}-\varphi_j^{\mathrm{B}})}\right\rangle\right\rangle \tag{2.68}$$

$$\langle\langle 4\rangle\rangle^{|\Delta\eta|} = \left\langle\left\langle e^{in(\varphi_i^{\mathrm{A}}+\varphi_j^{\mathrm{A}}-\varphi_k^{\mathrm{B}}-\varphi_l^{\mathrm{B}})}\right\rangle\right\rangle = \left\langle\left\langle e^{in(\varphi_i^{\mathrm{A}}-\varphi_k^{\mathrm{B}})}\right\rangle\left\langle e^{in(\varphi_j^{\mathrm{A}}-\varphi_l^{\mathrm{B}})}\right\rangle\right\rangle \tag{2.69}$$

However, the correlations are not evaluated directly through the correlated particles as expressed by (2.68) but via the flow vectors instead. New flow vectors are constructed from the corresponding particles within each sub-event separately. Hence, the value of $|\Delta\eta|$ does not represent the exact η difference among all individual correlated pairs but rather its lower limit. Since the separation between some of the particles is effectively larger than the width of the gap.

Using the Generic framework for an arbitrary combination of harmonics, the numerator of 2-, 3- and 4-particle[8] correlation with the sub-event method is calculated as follows:

$$\mathrm{N}\,\langle 2\rangle_{n_1,n_2}^{|\Delta\eta|} = Q_{n_1,1}^{\mathrm{A}} Q_{n_2,1}^{\mathrm{B}}, \tag{2.70}$$

$$\mathrm{N}\,\langle 3\rangle_{n_1,n_2,n_3}^{|\Delta\eta|} = Q_{n_1,1}^{\mathrm{A}} Q_{n_2,1}^{\mathrm{B}} Q_{n_3,1}^{\mathrm{B}} + Q_{n_1,1}^{\mathrm{A}} Q_{n_2+n_3,2}^{\mathrm{B}}, \tag{2.71}$$

$$\begin{aligned}\mathrm{N}\,\langle 4\rangle_{n_1,n_2,n_3,n_4}^{|\Delta\eta|} = {} & Q_{n_1,1}^{\mathrm{A}} Q_{n_2,1}^{\mathrm{A}} Q_{n_3,1}^{\mathrm{B}} Q_{n_4,1}^{\mathrm{B}} - Q_{n_1+n_2,2}^{\mathrm{A}} Q_{n_3,1}^{\mathrm{B}} Q_{n_4,1}^{\mathrm{B}} \\ & - Q_{n_1,1}^{\mathrm{A}} Q_{n_2,1}^{\mathrm{A}} Q_{n_3+n_4,2}^{\mathrm{B}} + Q_{n_1+n_2,2}^{\mathrm{A}} Q_{n_3+n_4,2}^{\mathrm{B}},\end{aligned} \tag{2.72}$$

where $Q_{n,p}^{\mathrm{A}}$ and $Q_{n,p}^{\mathrm{B}}$ denotes flow vectors from particles from sub-event A and B, respectively. Because of no overlap between the two sub-events, there are no autocorrelations present. Therefore, the difference between (2.70) and original (2.40) is in the missing terms accounting for this contribution.

For the case of differential correlations, the numerator is obtained in a similar fashion as in the case without sub-events. This is done by substituting one of the correlated RFPs with a POI. In terms of flow vectors, a single reference $Q_{n,p}$ vector is replaced by a differential $p_{n,p}$ one in each term (or $s_{n,p}$ in case of overlap in terms with $p > 1$ within the same sub-event) as indicated in (2.73)-(2.75) for 2-, 3- and 4-particle differential correlations, respectively.

$$\mathrm{N}\,\langle 2'\rangle_{\underline{n_1},n_2}^{|\Delta\eta|} = p_{n_1,1}^{\mathrm{A}} Q_{n_2,1}^{\mathrm{B}}, \tag{2.73}$$

$$\mathrm{N}\,\langle 3'\rangle_{\underline{n_1},n_2,n_3}^{|\Delta\eta|} = p_{n_1,1}^{\mathrm{A}} Q_{n_2,1}^{\mathrm{B}} Q_{n_3,1}^{\mathrm{B}} - p_{n_1,1}^{\mathrm{A}} Q_{n_2+n_3,2}^{\mathrm{B}}, \tag{2.74}$$

$$\begin{aligned}\mathrm{N}\,\langle 4'\rangle_{\underline{n_1},n_2,n_3,n_4}^{|\Delta\eta|} = {} & p_{n_1,1}^{\mathrm{A}} Q_{n_2,1}^{\mathrm{A}} Q_{n_3,1}^{\mathrm{B}} Q_{n_4,1}^{\mathrm{B}} - s_{n_1+n_2,2}^{\mathrm{A}} Q_{n_3,1}^{\mathrm{B}} Q_{n_4,1}^{\mathrm{B}} \\ & - p_{n_1,1}^{\mathrm{A}} Q_{n_2,1}^{\mathrm{A}} Q_{n_3+n_4,2}^{\mathrm{B}} + s_{n_1+n_2,2}^{\mathrm{A}} Q_{n_3+n_4,2}^{\mathrm{B}},\end{aligned} \tag{2.75}$$

[8] While $\langle 2\rangle$ and $\langle 4\rangle$ with a sub-event are symmetric for $A \leftrightarrow B$, $\langle 3\rangle$ is not in general. Therefore, both configurations are possible in this case.

Obviously, the replaced $Q_{n,p}$ vector can be associated with only one of the two sub-events. Because of that, the correlations are estimated in both configurations (one with POIs taken from sub-event A and one with POIs from B), and their average is used in the subsequent calculations.

In the case of measurement using the sub-event method, it is essential to use the same sub-event configuration for all the terms involved. For clarity, this is illustrated by (2.78) where the imposed η separation is denoted by the $|\Delta\eta|$ value in braces for both v_n coefficients and corresponding c_n and d_n cumulants given by (2.76) and (2.77), respectively.

$$c_n\{4, |\Delta\eta| > 0.8\} = \frac{\mathrm{N}\,\langle 4\rangle_{\underline{n},n,-n,-n}^{|\Delta\eta|>0.8}}{\mathrm{N}\,\langle 4\rangle_{\underline{0},0,0,0}^{|\Delta\eta|>0.8}} \tag{2.76}$$

$$d_n\{4, |\Delta\eta| > 0.8\} = \frac{\mathrm{N}\,\langle 4'\rangle_{\underline{n},n,-n,-n}^{|\Delta\eta|>0.8}}{\mathrm{N}\,\langle 4'\rangle_{\underline{0},0,0,0}^{|\Delta\eta|>0.8}} \tag{2.77}$$

$$v_n'\{4, |\Delta\eta| > 0.8\} = \frac{-d_n\{4, |\Delta\eta| > 0.8\}}{(-c_n\{4, |\Delta\eta| > 0.8\})^{3/4}} \tag{2.78}$$

To reduce the non-flow contamination even more (especially in pp or p-Pb collisions), one does not have to limit oneself to only two sub-events. However, splitting the acceptance into more regions impose a restriction for the correlated particles. Therefore, it reduces the overall number of pairs (or tuples) and consequently the precision of the measurement Due to that, a higher number of sub-events is not applied in this analysis, given the size of the available data sample. A study of integrated 4-particle correlations across all colliding system (i.e. pp, p-Pb, Pb-Pb, and event Xe-Xe) was performed within ALICE detector acceptance using three sub-events [26]. For technical details, see [65].

2.5.2 Subtraction method

While utilising multi-particle cumulants or applying large pseudorapidity separation in the form of sub-events are effective ways how to deal with the non-flow component, they are also very demanding on the size of the data sample (in terms of an average number of correlated pairs per collision and an overall number of recorded collisions). If the sample is not large enough, the non-flow subtraction method can be used as an alternative approach. The reason being that this method does not reduce the number of correlations (by limiting the acceptance regions or requiring a higher number of particles), contrary to the before-mentioned two methods. Especially for collision between small nuclei, where the average multiplicity of produced particles is considerably lower than the heavy-ion collisions.

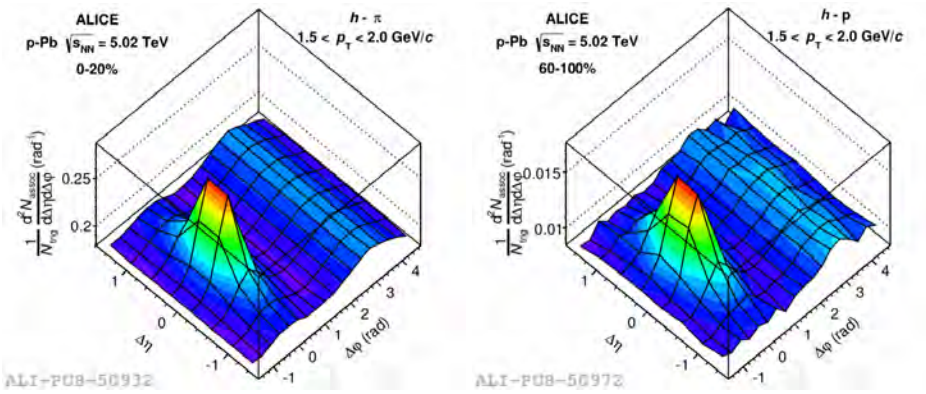

FIGURE 2.3: Associated yield normalised per trigger particle as a function of $\Delta\eta$ and $\Delta\varphi$ for h-π correlation within $1.5 < p_T < 2$ GeV/c in 0–20% (left) and 60–100% (right) event class of p-Pb collision at $\sqrt{s_{NN}} =$ 5.02 TeV [66].

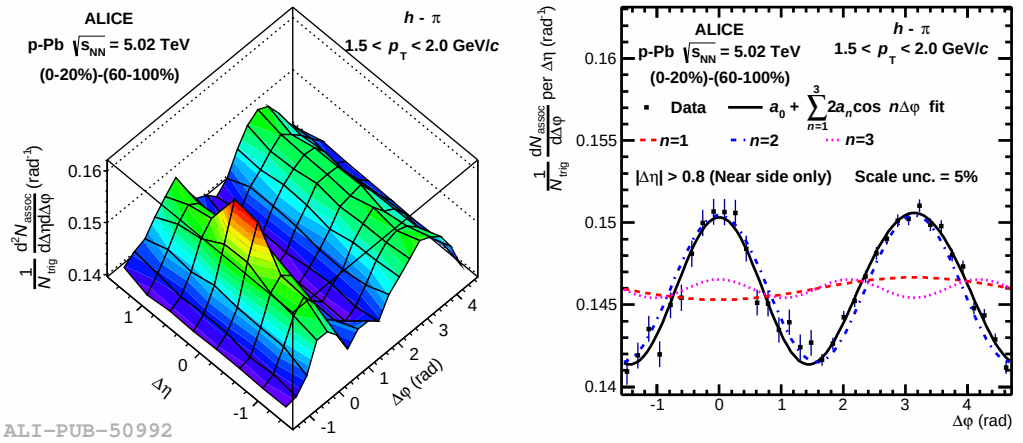

FIGURE 2.4: Left: Associated yield normalised per trigger particle as a function of $\Delta\eta$ and $\Delta\varphi$ for h-π correlation within $1.5 < p_T < 2$ GeV/c in 0–20% event class subtracted by associated yield in 60–100% event class of p-Pb collision at $\sqrt{s_{NN}} = 5.02$ TeV. Right: Corresponding projection onto $\Delta\varphi$ averaged over $|\Delta\eta| < 1.6$ ($0.8 < |\Delta\eta| < 1.6$ for the near-side peak) region; the results of the fit (solid line) are shown together with the individual components corresponding to different harmonics (dotted lines) where a_n coefficients are related to v_n magnitudes [66].

The non-flow subtraction method is based on the previous measurement of p_{T}-differential v_n coefficients of identified hadrons in p-Pb collisions published by the ALICE Collaboration [66]. Without elaborating too much on specifics (for more details see, e.g. [39]), this method based on di-hadron angular correlation measurement (already mentioned in Section 1.4) can be outlined as follows. First, the normalised particle yield $N(\Delta\eta, \Delta\varphi)$ is constructed from all pairs based on the relative difference in pseudorapidity $\Delta\eta$ and azimuthal angle $\Delta\varphi$ among the two correlated particles of each pair. Then, the azimuthal angle projection of $N(\Delta\eta, \Delta\varphi)$ is made by averaging over $\Delta\eta$ region. Lastly, the v_n coefficients are obtained by fitting such projection with a finite series of cosine terms according to the Fourier decomposition.

In the analysis mentioned above, the non-flow subtraction is done directly on the level of associated yields of correlated particles. The measurement of 60–100% event class generally corresponding to lower event multiplicities is used as an estimate for a level of non-flow contamination. The associated yields of correlations between inclusive charged hadrons and identified pions 0–20% and 60–100% p-Pb collisions at $\sqrt{s_{\mathrm{NN}}} = 5.02$ TeV are shown in Fig. 2.3. Once subtracted, the projection is made, and it is fitted similarly as described above for the case of raw (not subtracted) measurement. The outcome of the subtraction is presented by both subtracted yields and fitted projections in Fig. 2.4.

After the subtraction, an apparent double ridge structure is present (seen on the left panel of Fig. 2.4), which magnitude is more significantly pronounced when compared to associated yield before the subtraction (as seen in Fig. 2.3). More importantly, in the region of the near-side jet peak ($\Delta\varphi \approx 0$), the ridge structure spans multiple units of pseudorapidity. These observed long-range correlations are typically associated with collective behaviour such as the one induced by created medium (QGP) in case of heavy-ion collisions.

3 Experimental setup

3.1 the Large Hadron Collider (LHC)

The Large Hadron Collider (LHC) is the world's largest and the most powerful scientific apparatus in the field of high-energy physics of today [67, 68]. As the name suggests, it was designed and built to accelerate particles to unprecedented energies and to study the products of their subsequent collisions. The LHC is capable of colliding beams of protons at an energy of 7 TeV (corresponding to centre-of-mass energy of 14 TeV for pp collisions). Alternatively, it can also collide heavier elements, such as Pb ions at a beam energy of 2.7 TeV per nucleon (centre-of-mass energy of 5.4 TeV per nucleon for Pb-Pb collisions). The particles circulate within the collider as smaller groups called bunches separated in time by intervals of 25 ns. There can be up to 2808 bunches of protons with 10^{11} particle in each, or 592 bunches with 10^7 Pb ions in each. The LHC also accelerated Xe ions at a beam energy of 2.72 TeV for a single day in 2017 to extend its scientific reach to test potential system-size dependence [69].

The LHC is located at European Organization for Nuclear Research (CERN)[1] complex primarily based in Meyrin, a suburb of Geneva, Switzerland. Its construction started in 1998 and was finished after a construction period of approximately ten years in 2008. The overall cost of the machine is evaluated at 4.6 billion Swiss francs ($\approx$ €3.1bn) [70]. After an incident with the magnet system a few days after the circulation of the first beam in September 2008, it re-started its operation in November 2009 [71]. Since then it has completed two data taking campaigns referred to as Run 1 and Run 2. Currently, it is preparing to continue with its rich scientific programme planned up to 2038 known as the high-luminosity LHC era with data rates up to 50 kHz [45].

The LHC itself lies in a preexisting 26.7 km long circular tunnel beneath the Swiss-French borders at the depth ranging from 50 to 175 m which was previously used by the Large Electron-Positron Collider (LEP) [72]. It consists of two parallel pipes serving as conduits for two separated beams of particles travelling in opposite directions in each one. The collisions occur at the four out of eight locations where the beam pipes are crossing each other. There, the four major LHC experiments are situated: A Toroidal LHC Apparatus (ATLAS), Compact Muon Solenoid (CMS), Large Hadron Collider beauty (LHCb) and A Large Ion Collider Experiment (ALICE). The first two were

[1] Abbreviation is derived from French name *Conseil européen pour la recherche nucléaire*.

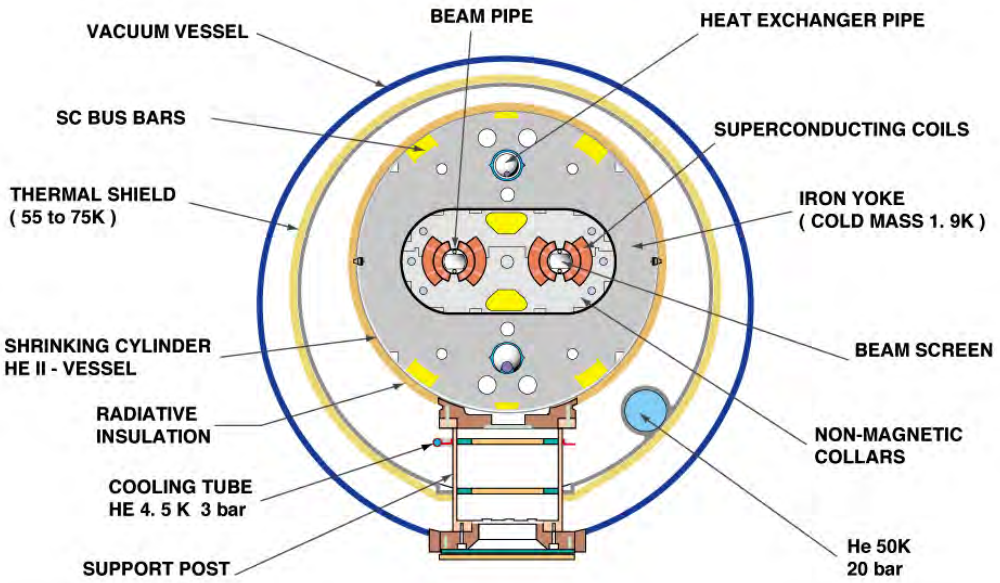

FIGURE 3.1: A scheme of LHC dipole magnet. Figure taken from [76].

designed for studying new and rare processes in proton-proton collisions, especially the observation of the Higgs boson. After finding the last missing piece of the Standard Model by discovering a Higgs-like particle [73, 74], the ATLAS and CMS experiments continue to probe its properties as well pushing the frontier of searches for so-called "Physics beyond the Standard Model". The LHCb experiment focuses on studying interactions of beauty-flavour quarks to investigate the violation of CP-symmetry. Last, but not least, ALICE is the only experiment originally dedicated to study the collisions of heavy ions with the ultimate aim to investigate the new extreme state of QCD matter, the quark-gluon plasma created in such collisions.

The pipes are surrounded by superconducting electromagnets used for keeping the beams stable on its fixed circular trajectory. The main body of the rather complicated setup [68, 75] consists of 1232 main dipoles magnets, each 15 m long and weighing 35 t. They generate magnetic fields of up to 8.3 T, bending the passing charged particles. The cross-section of the dipole magnet is schematically shown in Fig. 3.1. In addition, there are 394 quadrupoles magnets with length ranging from 5-7 m used to squeeze the beam both vertically and horizontally to keep it focused in the small transverse area to prevent losses of beam intensity. Besides that, there are also specialised magnets for correcting the imperfections of magnetic fields, insertion magnets used just before the collision to tighten the beam and thus focus the beam even further, and many more. Overall, more

than 50 types of magnets are needed for the LHC operation.

In order to sustain the superconductivity, the electromagnets need to be cooled down and operated at an extremely low temperature of 1.9 K (-271.3 °C) which is colder than the average temperature of the outer space of 2.7 K [77]. This is achieved by using niobium-titanium wires cooled by super-fluid liquid helium.

Contrary to common misconception, the electromagnets are not responsible for the acceleration process. Instead, a complex system of 16 metallic chambers known as radio-frequency cavities is used for this purpose. Each time the charged particles are passing through, they receive a specific electromagnetic impulse which accelerates them. The whole acceleration phase is reached after 20 minutes, during which the particles circulate within the LHC for more than 10 million revolutions [78]. Moreover, the acceleration within the LHC presents only the final step in which the particles traverse a chain of smaller and less-powerful accelerators, both circular and linear, and where they reach their final energy. For illustration, a scheme of the whole CERN accelerator complex including (but not limited to) machines "feeding" the LHC is shown in Fig. 3.2.

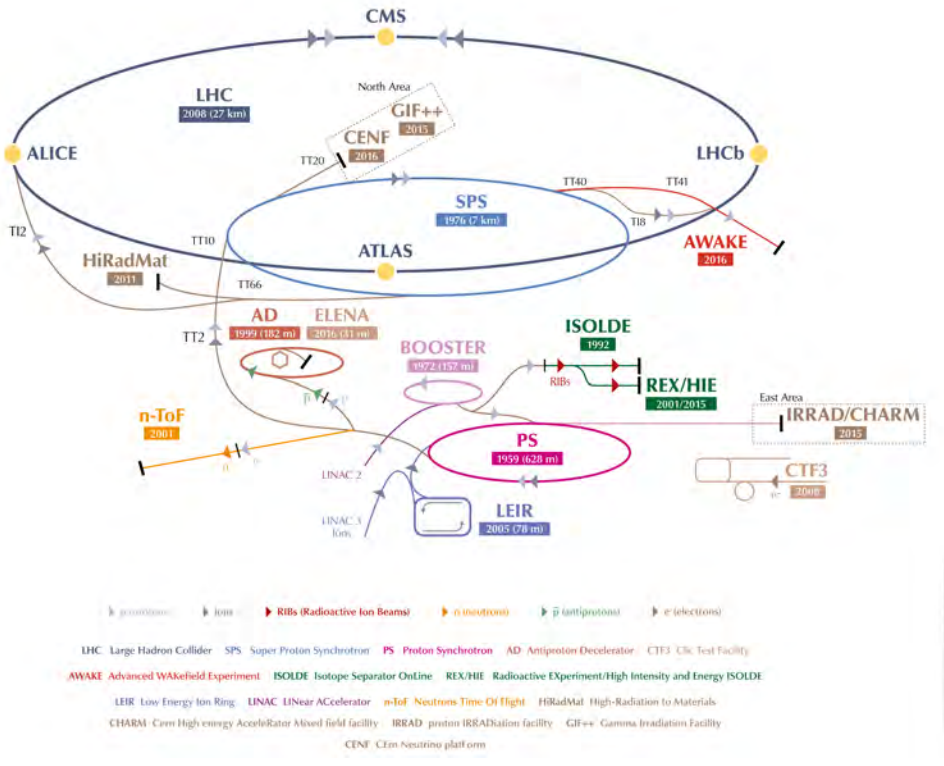

FIGURE 3.2: A scheme of the CERN accelerator complex. Figure taken from [79].

The pipes are kept at ultra-high vacuum reaching an impressive 10^{-11} mbar [80] to limit any undesired interaction of accelerated particles with anything but themselves (e.g. specks of dust or molecules of air). A less demanding vacuum system is also used as heat insulation for both cryogenically cooled electromagnets as well as a distribution line for liquid helium coolant.

3.2 A Large Ion Collider Experiment (ALICE)

A Large Ion Collider Experiment, ALICE, is one of the four major experiments of the LHC [81]. It is built, managed and maintained by the ALICE Collaboration, which brings together (by 2019) almost 2000 researchers and engineers from more than 170 institutes and 40 countries all around the globe [82].

The primary objective of ALICE, being the only experiment dedicated to studying the heavy-ion collisions, is to probe the properties of the strongly-interacting QGP. This is a unique state of nuclear matter where quarks and gluons are no longer confined within the nucleons. As such, it is optimised to detect extremely large multiplicities of charged particles reaching up to $\langle \mathrm{d}N_{\mathrm{ch}}/\mathrm{d}\eta \rangle \approx 1900$[2] in an average most-central Pb-Pb collision at $\sqrt{s_{\mathrm{NN}}} = 5.02$ TeV [83]. In addition, it has excellent particle identification (PID) capabilities, especially in the low momentum region. Combined with the great tracking performance for charged particle transverse momentum down to $p_{\mathrm{T}} \approx 100$ MeV/c, it makes ALICE a complementary and yet unique detector among other LHC experiments. Besides its heavy-ion programme, ALICE also records pp and p-Pb collisions to collect precision measurements serving as a baseline for comparison and to quantify the effects of cold-nuclear matter.

The schematic layout of the ALICE detector is shown in Fig. 3.3. The overall dimensions are $16 \times 16 \times 26$ m^3 with a gross weight of 10 000 tons. The detector consists of two main parts: the central barrel detector, and the forward arm with a muon spectrometer. The two components are separated by a sizeable composite absorber made of layers of both light and heavy elements to provide a clean muon signal.

The central barrel provides full azimuthal coverage and overall effective pseudorapidity acceptance of $|\eta| < 0.8$. It is enclosed within a big solenoid magnet generating a static magnetic field of $B = 0.5$ T formerly used by the L3 experiment at LEP. Charged particles created inside such a magnetic field are passing through it on a bent trajectory, separating positive and negative particles. The following systems are located within

[2] More specifically, this corresponds to a total number of charged particles produced per unit of pseudorapidity at mid-rapidity averaged over $|\eta| < 0.5$.

the central barrel: Inner Tracking System (ITS), Time-Projection Chamber (TPC), Transition Radiation Detector (TRD), Time-Of-Flight (TOF), High-Momentum Particle Identification Detector (HMPID), Electromagnetic Calorimeter (EMCal), Di-jet Calorimeter (DCal), Photon Spectrometer (PHOS) with Charged-Particle Veto (CPV), Forward Multiplicity Detector (FMD), V0 and T0 detectors.

Moreover, there are additional supporting forward detectors: Zero Degree Calorimeter (ZDC) for triggering and event characterisation, ALICE Diffractive detector (AD) for diffraction studies, and ALICE Cosmic Ray Detector (ACORDE) used for calibration and detector alignment.

The laboratory frame is defined as follows: x-axis is aligned horizontally pointing towards centre of the LHC ring, y-axis is aligned vertically pointing upwards, z-axis pointing from the muon arm along the beam direction [85], and the geometrical centre of the central barrel representing a point of origin $(x, y, z) = (0, 0, 0)$ referred to as Interaction Point (IP).

In the following sections, only the technical details of those detectors involved in the analysis discussed in this thesis are described[3]. Further information about the ALICE detector can be found in [81].

3.2.1 Inner Tracking System (ITS)

The ITS [81, 86] is the innermost ALICE detector in terms of radial distance from the beam pipe. It contains three distinct types of silicon semiconductor detectors: Silicon Pixel Detector (SPD), Silicon Drift Detector (SDD), and Silicon Strip Detector (SSD). Each of them consists of 2 layers forming in total six coaxial cylinders with increasing radii, as shown in Fig. 3.4 (and in the insert of Fig. 3.3). Even though each detecting subsystem differs in design, they share a universal principle of operation. Free electrons within n-type semiconductor are collected by applying a reversed-bias voltage. When a charged particle passes through the sensitive volume of the detector, it excites the valence electrons into the conductive band effectively creating electron-hole pair. Such electrons can drift through the volume towards collection anodes providing output signal for the read-out electronics.

The SPD forms the two innermost layers of the ITS located in a radial distance of 3.9 cm and 7.6 cm. Its design was chosen to achieve a high spatial resolution essential for the determination of the Primary Vertex (PV), i.e. an approximate point where the collision occurs. This is achieved by finding a common point of origin for the highest number of reconstructed tracks available. With such excellent spatial resolution (12 μm in $r\varphi$ and 100 μm in z [86]), the SPD can be used for measurement of impact parameter

[3] The description of each detector is based on the references provided on the beginning of each section (unless explicitly stated otherwise).

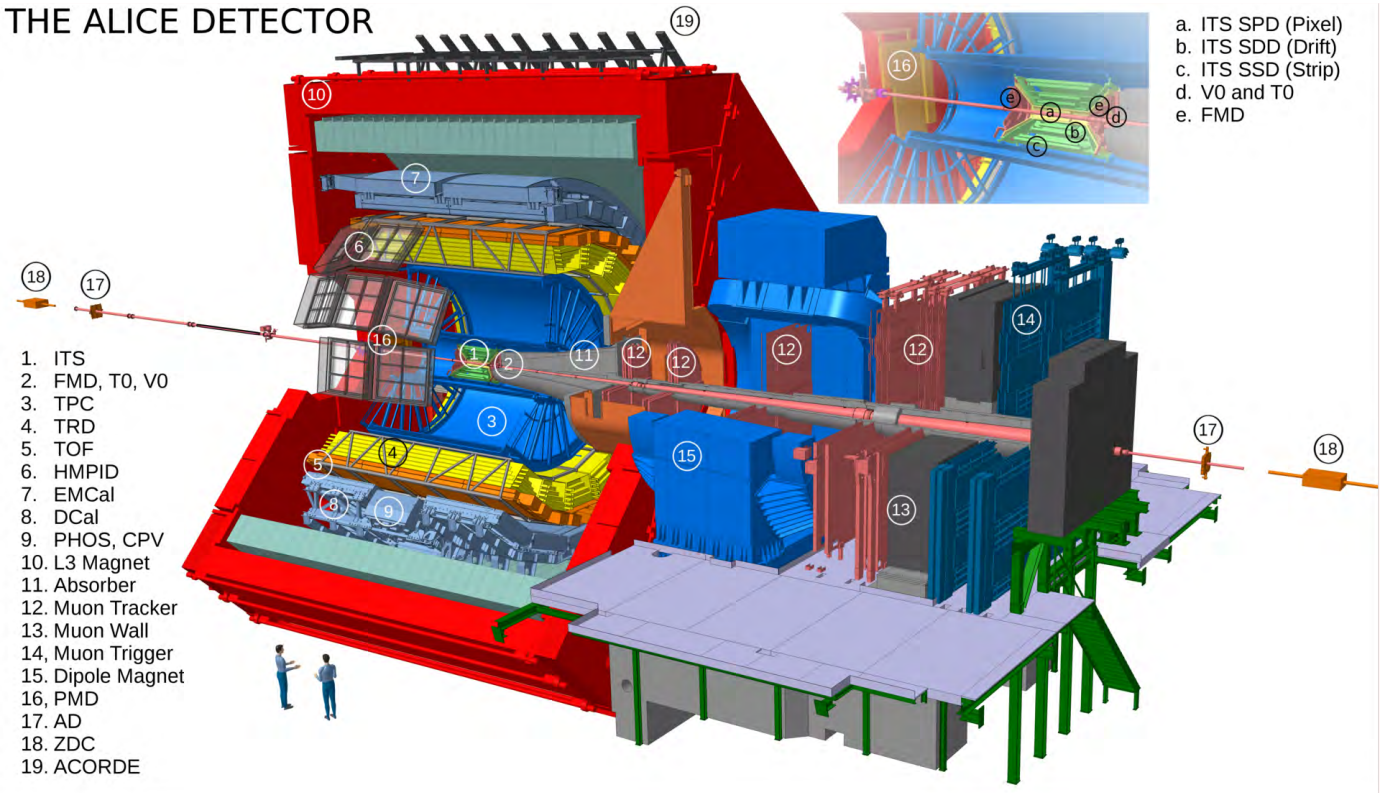

FIGURE 3.3: A layout of the ALICE detector during Run 2 data taking campaign. Figure taken from [84].

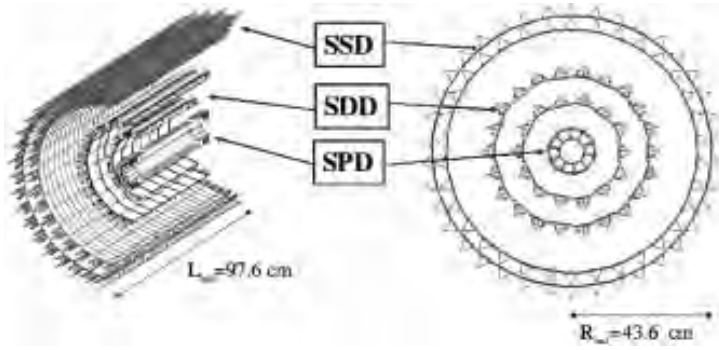

FIGURE 3.4: A scheme of the ITS detector. Figure taken from [87].

of secondary tracks (i.e. the distance of closest approach between PV and the secondary track) produced in decays of strange, charm and beauty hadrons.

It consists of a matrix of hybrid pixel cells each containing a sensitive area with dimensions of 50 μm (azimuthal) and 425 μm (along the z-axis), as well as its read-out. Such microscopic scales are suitable to ensure that each pixel can be hit by up to one particle only. This approach allows using a simple binary representation in which each pixel can be assigned with "1" if the registered signal is above a certain threshold indicating passing particle, or "0" otherwise. Moreover, each chip provides a fast Fast-OR digital pulse every time when one or more pixels are hit. In this way, SPD provides a rapid response and can be integrated into the lowest L0 trigger level. Overall, SPD consists of almost 10 million sensitive cells covering the total area of ≈ 0.2 m^2.

The SDD constitutes the two intermediate layers of the ITS located at 15 cm and 23.9 cm from the beam pipe and provides two-dimensional information about the position of the passing particle. The detector sensors have a sensitive area of 7.02×7.53 cm^2 divided into two equal drift areas. Each drift area consists of 291 cathode strips creating a drift field followed by a single row of 256 collection anodes at the edge of the sensor. As the particle interacts with the detector, the produced electrons drift towards the anodes. One coordinate is then extracted from the position of the charge collected by the anodes, while the perpendicular coordinate is determined from the drift time of the electrons.

Lastly, the two outer layers composed of the SSD are crucial for bridging the tracking information provided by ITS and TPC in order to secure a smooth connection of the final reconstructed tracks. The detector consists of double-sides sensors. Each sensor with an area of 74×40 mm^2 has 768 strips on each side oriented with a relative angle difference of 35 mrad. The position of the passing particle is determined as a crossing point where each side provides a single coordinate.

The four outer layers of ITS have analogue read-out allowing the measurement of

the actual amount of energy deposited by the particle into the detector. Such information about the energy loss $\mathrm{d}E/\mathrm{d}x$ of the passing particle can be used for PID. Together with its tracking capabilities, ITS can be used as a standalone low-p_{T} particle spectrometer. The PID performance of ITS is illustrated in Fig. 3.5 where the distribution of the measured energy loss per unit length $\mathrm{d}E/\mathrm{d}x$ is shown as a function of particle momentum p as measured in Pb-Pb collisions at $\sqrt{s_{\mathrm{NN}}} = 2.76$ TeV. A clear separation between low-p_{T} $\pi^{\pm}$, $\mathrm{K}^{\pm}$, and $\mathrm{p}(\bar{\mathrm{p}})$ is observed.

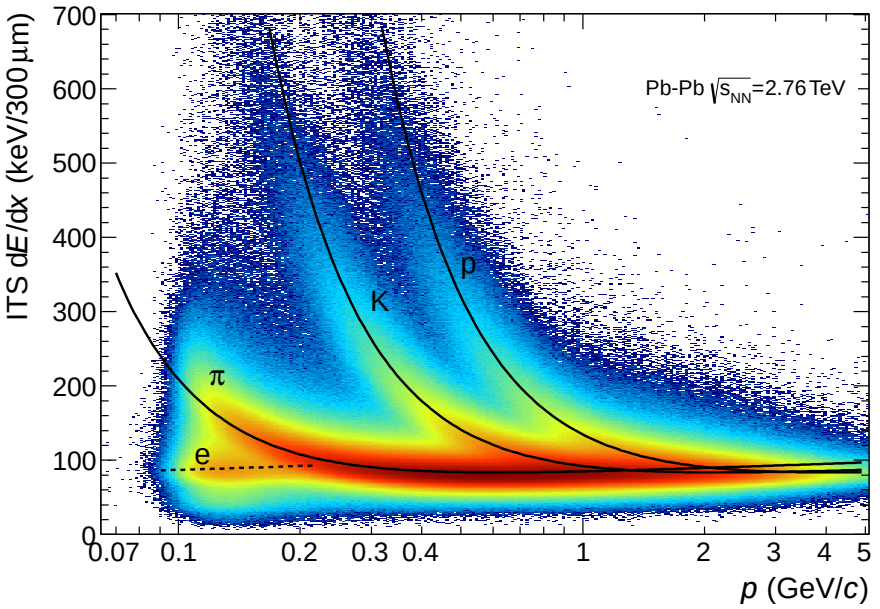

FIGURE 3.5: PID performance of ITS detector represented by the distribution of energy loss $\mathrm{d}E/\mathrm{d}x$ as a function of particle momentum p in Pb-Pb collision at $\sqrt{s_{\mathrm{NN}}} = 2.76$ TeV. the solid lines represent expected detector response for various particle species. Figure taken from [88].

3.2.2 Time-Projection Chamber (TPC)

The TPC [81, 89] serves as a primary detector used for reconstruction of charged-particle trajectories providing up to 159 space-points for each track with good two-track separation. Also, it is capable of determining particle transverse momentum in a wide range of $0.1 \lessapprox p_{\mathrm{T}} < 100$ GeV/c from the curvature of the corresponding track.

In addition, it provides PID information based on measurement of the characteristic ionisation energy loss $\mathrm{d}E/\mathrm{d}x$. The PID capability in terms of separation between various particle species is illustrated on the measurement of the distribution of energy

loss as a function of particle momentum in Pb-Pb collisions at $\sqrt{s_{\mathrm{NN}}} = 2.76$ TeV shown in Fig. 3.6. The solid lines represent the expected detector response to the corresponding species.

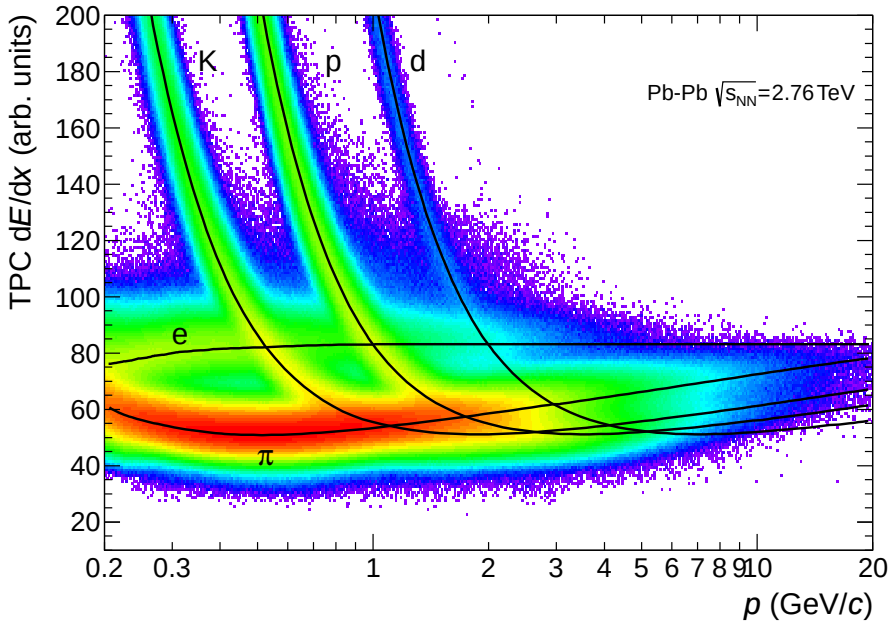

FIGURE 3.6: PID performance of TPC detector represented by distribution of energy loss $\mathrm{d}E/\mathrm{d}x$ as a function of particle momentum p in Pb-Pb collision at $\sqrt{s_{\mathrm{NN}}} = 2.76$ TeV. the solid lines represent expected detector response for various particle species. Figure taken from [88].

Together with other central barrel detectors, TPC is involved in primary vertex determination and triggering by providing a fast input for the High-Level Trigger (HLT). Overall, the above-mentioned features make TPC an essential detector system of the ALICE apparatus.

TPC is a large cylindrical chamber surrounding ITS consisting of large field cage, and two read-out endplates, each divided into 18 trapezoidal segments as illustrated by its cross-section in Fig. 3.7 In the middle, i.e. $z = 0$, the field cage is divided in two by a central electrode to provide the drift field. Given the overall length of 5 m and the inner and outer radius of 85 cm and 250 cm, respectively, its total active volume is approximately 90 m^3. It is filled with a mixture of Ne, CO_2, and N_2 gas while varying its composition for performance optimisation. It covers full azimuth and $|\eta| < 0.9$ units of pseudorapidity (and $|\eta| < 1.5$ for tracks with reduced length). The endplates contain 36 Multi-Wire Proportional Chambers (MWPC) with almost 560 000 readout pads.

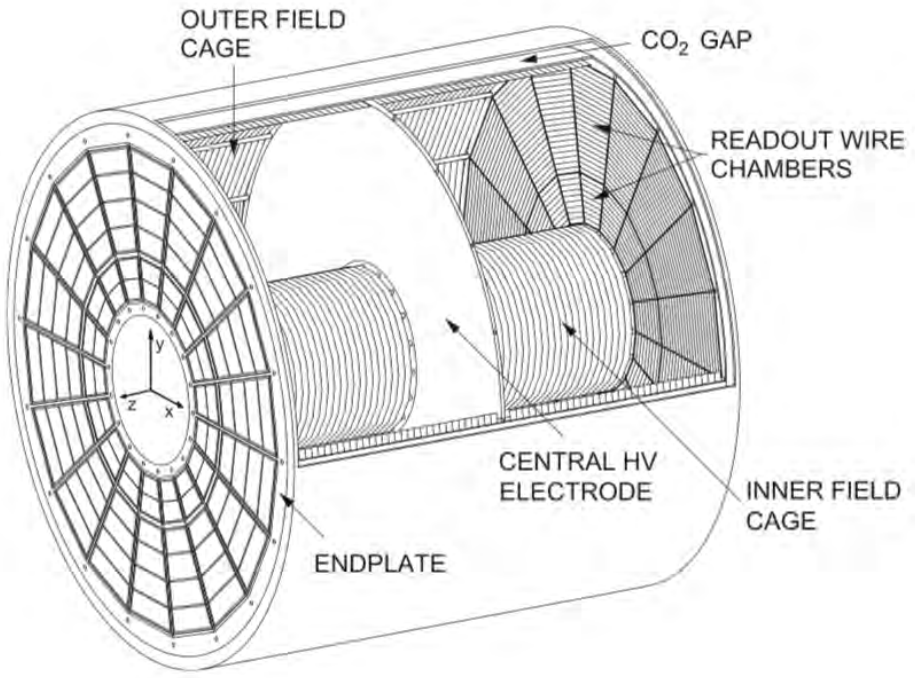

FIGURE 3.7: A 3D-cross-section of TPC. Figure taken from [90].

When a charged particle passes through the sensitive volume of TPC, it ionises the gas molecules present in the chamber creating free electrons and ions. These products of ionisations then drift towards the electrodes, which generate an electrostatic drift field of 400 V/cm: the central electrode collects the ions while the electrons drift towards the endplates as illustrated in Fig. 3.8. When arriving close to the anode plane, a high electric field gradients create an avalanche of electrons resulting in additional production of secondary electrons and ions. Working in the proportional mode, the number of secondary-produced electrons carry information about the number of primary-produced electrons and thus the energy loss of the passing particle. On the other hand, the secondary ions induce a signal in the pad rows giving the information about the position within transverse xy plane. Moreover, a gating plane is located in front of the MWPCs. By alternating its voltage between $\pm$100 V, it can be either open or closed. The gate is open for approximately 90 μs intervals which is a maximal drift time of electrons from the centre towards the endplate. When closed, primary electrons are collected by the gate wires and do not reach the anodes, while most of the secondary ions are prevented to entering the main body of the TPC which would result in distortions of the electrostatic field.

Outside of the LHC operation, the TPC is aligned and calibrated by using information about incoming cosmic radiation. Additional calibration is possible with a laser-emitting system [91] even when hadron beams are present. It is capable of shooting coherent laser rays into the TPC volume, providing a set of straight tracks used for precise online monitoring of position reconstruction and potential space-charge distortion.

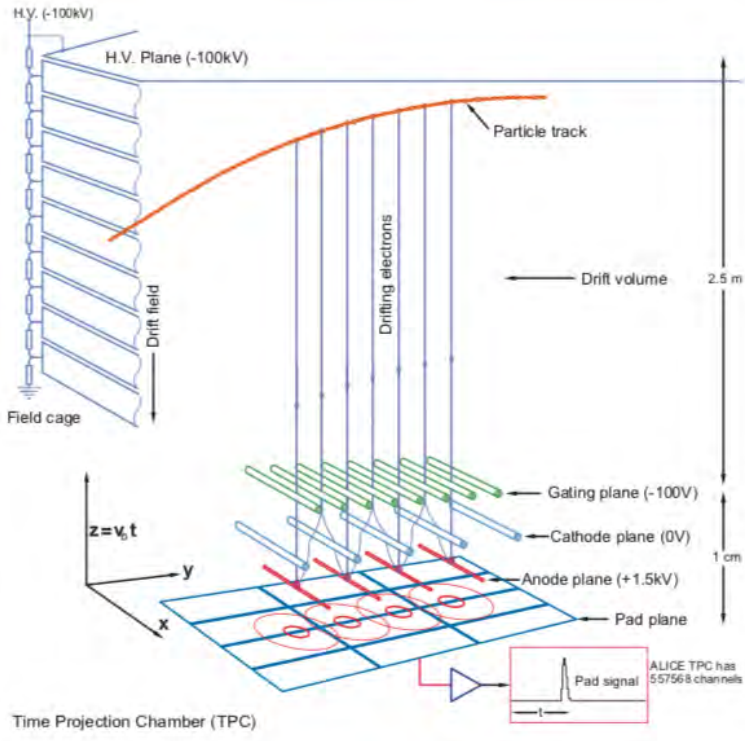

FIGURE 3.8: An illustration of track reconstruction of a charged particle passing TPC. See the text for details. Figure taken from [92].

3.2.3 Time-Of-Flight (TOF)

As the name suggests, TOF [81, 93] provides time information about particles arriving at the detector. When compared to a reference time in which the collision occurs, such time-of-flight measure is used for determining the velocity of the produced particle. Combined with the knowledge of the particle momentum provided by tracking detectors, a mass of the particle and therefore its species can be determined. The PID performance of the TOF detector is illustrated in Fig. 3.9 where a distribution of particle velocity β as a function of its momentum p is extracted using time-of-flight information measured in Pb-Pb collisions at $\sqrt{s_{\mathrm{NN}}} = 2.76$ TeV.

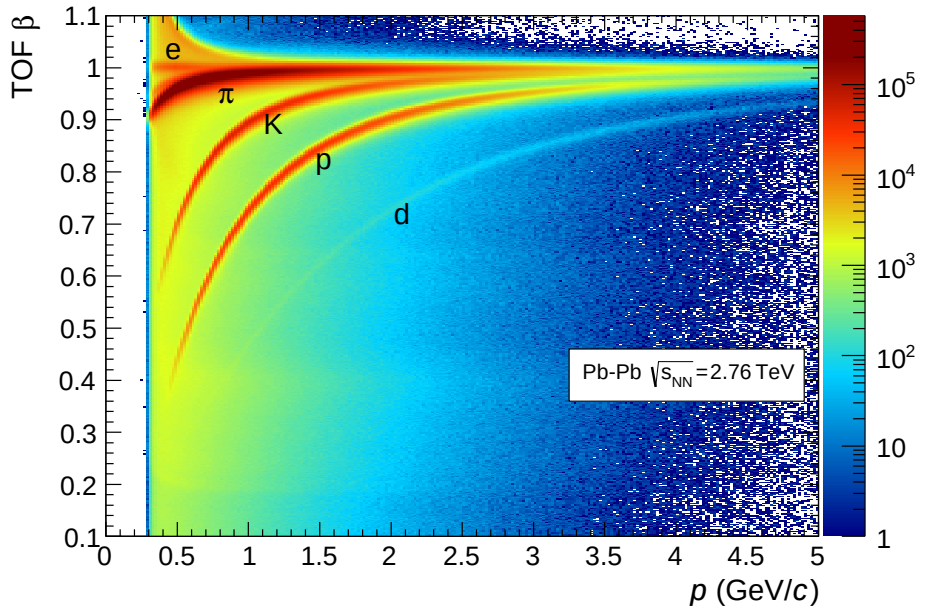

FIGURE 3.9: PID performance of TOF detector illustrated by distribution of measured particle velocity using time-of-flight information as a function of particle momentum p in Pb-Pb collision at $\sqrt{s_{\mathrm{NN}}} = 2.76$ TeV with an indication of the observed detector response to various particle species. Figure taken from [88].

TOF is a cylindrical shell with its an inner and outer radius from the beam axis of 370 cm and 399 cm, respectively. It is segmented into 18 azimuthally distributed supermodules, each further divided into five modules in the z-direction. In total, TOF consists of 90 modules. Each module contains 10-gap double-stack Multi-gap Resistive-Plate Chamber (MRPC) strips. A scheme of TOF detector is shown in Fig. 3.10.

The main advantage of MRPC compared to other gaseous detectors is that it generates a very high electrostatic field uniform over the whole sensitive volume. When a charged particle passes such a field, the products of the subsequent ionisation immediately start an avalanche which is collected by the electrodes in their proximity, producing a signal. Consequently, there is almost no drift time associated with interaction of the traversing particle with the detector volume, and therefore minimal time delay, providing a time resolution below 40 ps. The total response left by the passage of a single particle is given by a sum from each gap. Therefore the detector efficiency increases with the number of gaps used. The principle of MRPC operation is illustrated in Fig. 3.11 on one of the first designs using three gaps.

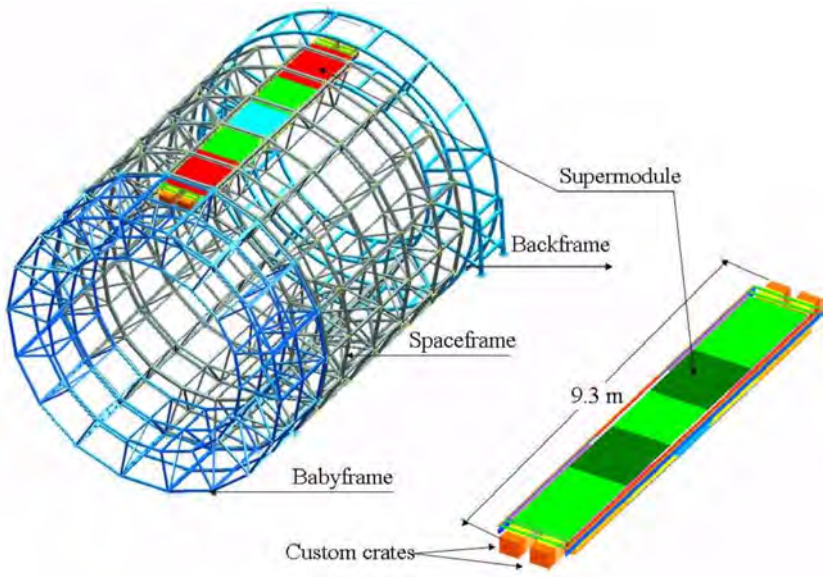

FIGURE 3.10: A 3D-cross-section of TOF detector including the supporting frame structure and a single super-module. Figure taken from [81].

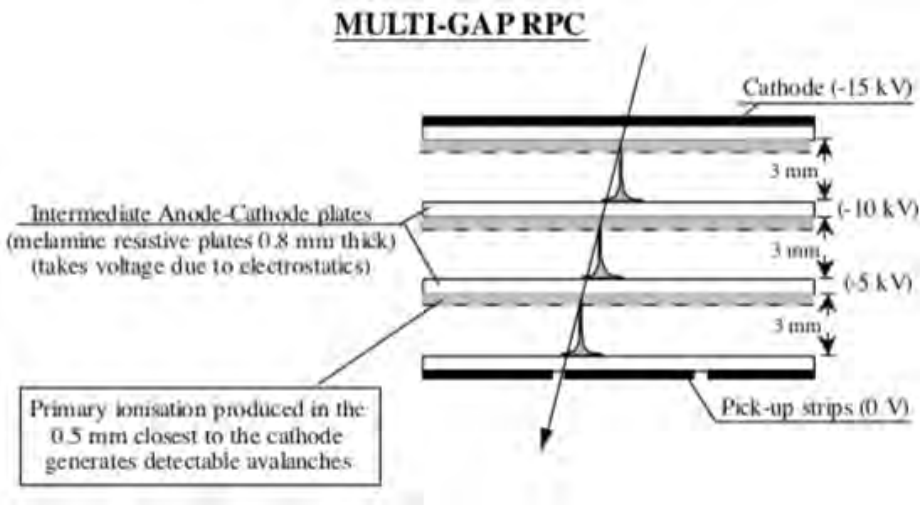

FIGURE 3.11: Principle of operation illustrated on 3-gap MRPC. This is not the final design is used for TOF of ALICE. See the text for details. Figure taken from [94].

3.2.4 T0 detector

As mentioned in the previous Section, PID is determined from time-of-flight information obtained as a difference between arrival time measured by TOF and the time when the collision occurs. Thus, one needs access to the reference starting time. In ALICE, such a quantity is provided by T0 detector [81, 95].

T0 consists of two arrays of 12 Cherenkov counters each located on both sides of the central barrel. Each counter is made out of a fine-mesh of Photo-Multiplier Tube (PMT) with dimensions of 30 mm in diameter and 45 mm long and a quartz radiator 20 mm in diameter and 20 mm long. T0-A is located at $z = 375$ cm covering $4.61 < \eta < 4.96$, while T0-C is located in front of the muon arm absorber at $z = -72.7$ cm and covers $-3.28 < \eta < -2.97$. In terms of radial distance, both arrays are located as close to the beam pipe as possible and covers full azimuth.

When a charged particle traverses a radiator with a velocity higher than the speed of light within such medium, the Cherenkov light is emitted and guided towards the PMT. There, the photon hits a cathode and throws out electrons by the photoelectric effect. Such an electron is accelerated and multiplied by a series of dynodes and collected at its end, producing a measurable signal.

The timing resolution of the T0 detector is approximately 50 ps. Besides providing starting time for T0F, it is also capable of identifying the position of the primary vertex based on a difference in arrival time to T0-A and T0-C with a precision of ± 1.5 cm. In addition, it provides one of the earliest input for the lowest (denoted as L0) trigger level, and it is capable of discriminating undesired beam-gas interactions.

3.2.5 V0 detector

The V0 detector [81, 95] has multiple applications within ALICE apparatus such as triggering, event characterisation, pile-up event veto, and luminosity monitoring.

Similarly to T0, V0 is composed of two arrays located on both sides of the central barrel, but this time these are plastic scintillator counters. Each array consists of 4 rings further divided into 8 radial segments, each connected to a single PMT. V0-C is located right in front of the absorber at $z = -90$ cm covering $-3.7 < \eta < -1.7$ acceptance and V0-A is located on opposite side at $z = 340$ cm covering forward region of $2.8 < \eta < 5.1$. Both arrays are located as close to the beam pipe as possible and have circular geometry covering full azimuth with a diameter of 100 cm and 76 cm for V0-A and V0-C, respectively.

When a charged particle passes through the sensitive volume, it loses energy by exciting the scintillator molecules. Their subsequent de-excitation emits light which is collected and guided through the optical cables to the PMT. There it is multiplied and

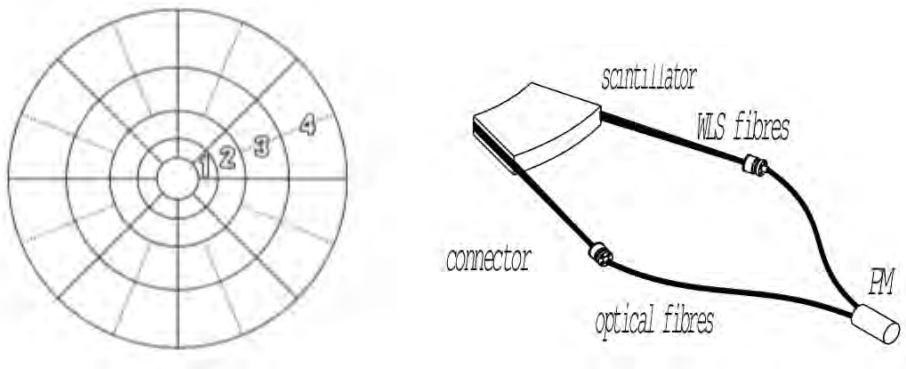

FIGURE 3.12: A scheme of V0 detector. V0 segmentation into 4 rings (left) with additional sectors of V0-C in rings 3 and 4 (depicted by dashed lines). Scheme of optical read-out of each sector (right). Figures taken from [95].

collected, producing a measurable signal as described in the case of T0 detector in the previous section.

One of the main advantages of plastic scintillators is that the output signal is proportional to the number of interacting particles. Therefore, by summing the signals measured by each V0 segment, one can determine the total number of particles reaching a detector and thus gain information about total charged-particle multiplicity. Moreover, this dependency between V0 signal and the number of passing particles is monotone. It can be used for the centrality determination and also as rough centrality trigger.

In addition, due to short relaxation times, V0 has a time resolution of $\sim$ 1 ns. Consequently, it can be used as a low-level Minimum-Bias (MB) trigger. It can work in two modes: as a logical AND requiring signal in both arrays, or logical OR when at least one signal from either side is needed. It can also be used to filter beam-gas interactions and pile-up collisions.

3.3 Data processing & reconstruction

3.3.1 Triggering

Even though ALICE was designed and optimised to cope with a very high interaction rate of Pb-Pb collisions at the LHC reaching up to 8 kHz, in reality, not every collision can be processed and recorded. This is due to various technical limitations in the form of read-out rates and response times of different detectors, processing speed, and even

overall file storage capacity. The situation became even more dire in the case of pp collisions, where the collision rate increases up to 200 kHz. Therefore a trigger system [81, 96] was developed for careful event selection in order to utilise most of ALICE potential.

The main part of the ALICE trigger system is the Central Trigger Processor (CTP) which is responsible for making a decision whether to accept or reject a given collision based on the trigger inputs collected from various detectors. Also, in case of a positive decision, it distributes a signal back to the individual detectors to commence with the read-out process of the currently occurring collision. The ALICE trigger system is divided into three trigger levels based on the swiftness of their reaction.

The first response of the trigger system to the detectors has to be fast enough to prevent losing too much information. To achieve that, there are two levels of "fast" triggers: L0 reaching detectors within 1.2 μs(which is however by design too fast, so it does not have enough time to collect inputs from all detectors), while slower L1 providing feedback within 6.5 μs based on all remaining "fast" inputs.

The slower L2 trigger level collects all inputs and provides a decision within 88 μs given by TPC, which presents a limiting factor due to its long read-out time. In addition, the L2 trigger includes so-called past-future protection. This continuous check prevents reconstruction of pile-up events, i.e. mixing information from various collisions occurring close to the actual triggered event. For instance, all particles passing through TPC are assigned to a single event, even though the particles are created in two or more subsequent Pb-Pb collisions happening within one TPC read-out window. In this particular example, such a triggered event would be vetoed by past-future protection.

Not to be limited by the TPC read-out rate, various detectors with similar read-out interval are grouped together into detector clusters. These clusters read out at a higher rate in order to increase the number of recorded events useful for studying certain physical phenomena (whenever it makes sense). A combination of different trigger inputs and detector clusters forms a trigger class, such as MB trigger, high-multiplicity trigger, etc.

While CTP decides whether or not an event should be recorded on the hardware level of detector inputs, HLT serves as a more sophisticated trigger layer. HLT inputs are based on (at least partially) reconstructed data, e.g. a presence of high-p_{T} particle, or a jet with energy above a threshold.

Once all trigger inputs are properly processed by CTP and the decision is made to accept the event, output data read out by the individual detectors are propagated to the Data-Acquisition (DAQ) system which is responsible for their further processing and compression. This results in fully reconstructed events which are then stored into permanent storage and consequently used for the actual analysis.

3.3.2 Track & vertex reconstruction

Track reconstruction (tracking) [81, 88] is a complex process in which the raw signals measured by individual detectors are transformed into complete trajectories representing the path left by physical particles passing through the ALICE apparatus. The main tracking detectors of ALICE are TPC providing a large portion of the overall sensitive volume, and ITS being the closest detector to the beam pipe. In addition, there is also TRD, and forward arm spectrometer which applicability is however limited primarily to muons.

The whole procedure starts by digitalisation of raw output signals from individual detectors (unless already providing digital signal) into digits. Then, the digits which are adjacent in space (and possibly also in time) are converted into clusters. During the next step, space-points (also referred to as hits) providing the coordinates where a particle likely passed through the detector are reconstructed. These are usually determined as centroids of each cluster.

Before the actual track finding commences, the preliminary estimation of collision point (PV) position is performed. This is based on hits provided by the two innermost (SPD) layers of ITS. In this step, each hit from the first layer is combined with each hit in the second layer into a so-called "tracklets" [98, 97] (an initial approximation of final tracks) by linear extrapolation. Determination of PV itself is done by finding the common point of origin (or crossing point) for most of the tracklets by method of the least-squares.

At this point, everything is ready for the track reconstruction process illustrated in Fig. 3.13. It starts from seeds created from the two outermost hits in TPC serving as a starting point for a track propagation towards the preliminary PV. The reconstruction is done using a Kalman filter method [99, 100]. In this iterative algorithm, a new hit (one pad closer to PV) is added, and the track parameters are updated accordingly in each step. This is repeated until the inner wall of TPC is reached. Then, the current track is extrapolated towards the outer wall of ITS. From there, the process continues again until all available hits are included all the way towards preliminary PV estimation.

During the second pass, the whole procedure is repeated however in reverse direction starting at the inner ITS walls using the last point reconstructed in the previous step (denoted as "ITSin" in Fig. 3.13) as a seed for propagating outward. This stage is finished beyond TPC outer wall by including additional points from TRD and TOF in a similar fashion.

Finally, the third pass of the Kalman filter is repeated. This time in the original direction, starting from the last hit on TOF outer wall (denoted as "TOFout" in Fig. 3.13) towards PV. In this step, global tracks obtained in the previous stage are fitted again using hits from individual detectors to obtain additional reference points on the inner

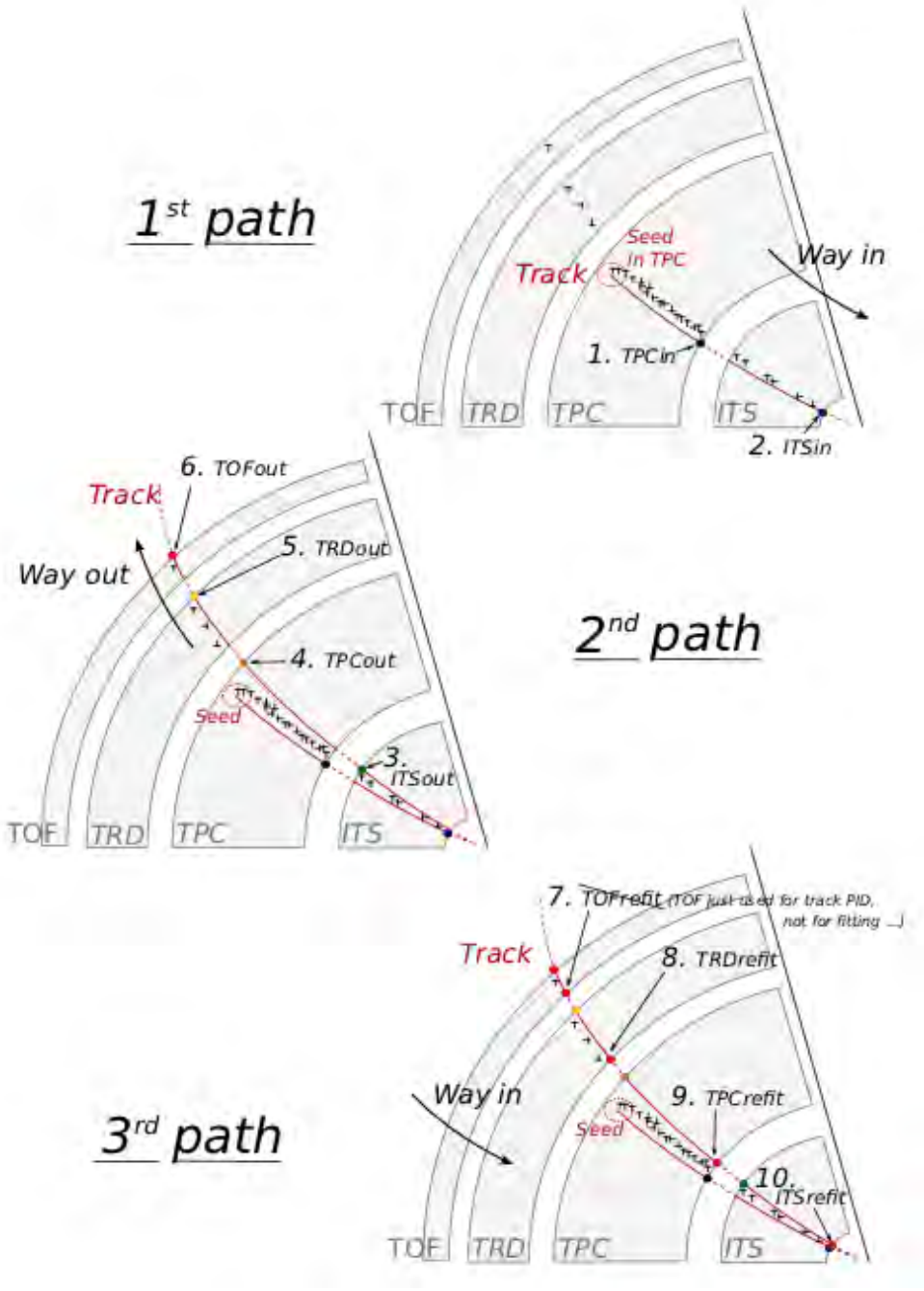

FIGURE 3.13: An illustration of track reconstruction process as performed in ALICE. See the text for details. Figure taken from [97].

walls of a given detector (referred to as ITS-refit, TPC-refit, etc.). This is done to ensure the most precise estimation of the track parameters at PV. Once the final re-fitting procedure is finished, the position of PV is re-evaluated using newly-reconstructed full tracks.

The above-mentioned procedure is illustrated in the case of primary tracks, i.e. trajectories left by relatively long-lived particles created directly in (or within a very short time period after) the collision. However, there is also an additional component of the whole sample of reconstructed tracks (generally called secondary tracks) left by decay products of relatively weakly-decaying particles, such as K^0_S and $\Lambda(\bar{\Lambda})$. These two constituents can be distinguished during the track finding procedure by looking at the impact parameter, i.e. the closest distance between the reconstructed track propagated towards PV, and the PV estimation itself. If its impact parameter is larger than a specific threshold, the track is considered secondary and does not contribute to the PV re-evaluation. Instead, it is kept for later as described below.

When the tracking is finished, a set of all secondary tracks is used for reconstruction of secondary vertices (SVs). These serve as potential candidates for space-points where above-mentioned short-lived particles undergo their decay. The secondary vertex finding is done by combining all pairs of reconstructed secondary tracks with opposite charges (determined from the orientation of track curvature). If the impact parameter between the two secondary tracks is small enough, the corresponding SV found in between them on the line of their closest approach is recorded as a potential candidate for a weak decay vertex.

3.3.3 Centrality determination

Generally speaking, the dynamics of heavy-ion collision is driven by the initial geometry given by overlapping region (and thus interaction volume) of the two colliding nuclei. It seems natural to quantify the level of overlap by an impact parameter b, the distance in transverse xy-plane between geometrical centres of the two nuclei.

Besides the impact parameter, there are additional quantities related to the geometry of the collision: the number of binary collisions N_{col} between the nucleons of the two projectiles, and the number of participants N_{part}. As mentioned in Section 1.2, participants are those nucleons which undergo at least one nucleon-nucleon collision, while those that avoid other nucleons and endure the collision untouched are called spectators (as illustrated in Fig. 3.14).

Customarily, collisions are characterised by the centrality (or centrality class) expressed in terms of percentile [101]. For example, perfectly aligned collisions when the two nuclei are fully overlapped, i.e. $b \approx 0$, are referred to as "most central" denoted as 0%. As the overlapping region is getting smaller, and the impact parameter increases,

one talk about "semi-central" collisions. In case that the impact parameter approaches the sum of the two radii, the collision is referred to as "peripheral", and its percentage representation gets close to 100%. However, neither impact parameter itself nor above-mentioned geometrical quantities are directly accessible experimentally.

One way to quantify the centrality of a given collision is by looking at the overall signal registered in the forward region. For that purpose, V0 detector serves as a suitable centrality estimator due to the proportionally between the magnitude of the measured signal and number of interacting particles (and its monotonous evolution) as already advertised in Section 3.2.5. The distribution of measured total V0 amplitude (given by the sum of both V0 arrays) can be fitted with a Glauber model, as shown in the top plot of Fig. 3.15 for Pb-Pb collisions at $\sqrt{s_{\mathrm{NN}}} = 2.76$ TeV [101].

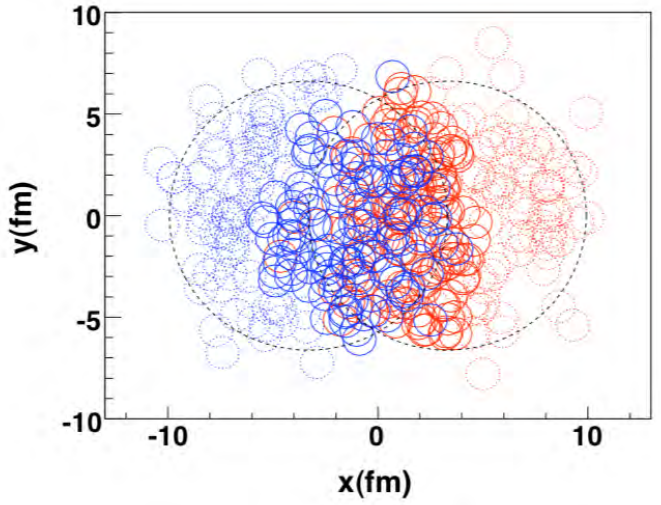

FIGURE 3.14: Glauber MC simulation of Pb-Pb collision at the LHC energy. Each circle represents a nucleon from one of the projectiles (distinguished by colours): participant (solid line) or spectator (dotted line). Figure taken from [102].

This is typically done by performing Monte Carlo Glauber simulation [102, 103] in which an exact position for each nucleon is generated for both projectiles. As the nuclei are Lorentz-contracted, only the transverse plane is considered. Each nucleon is modelled using a modified Wood-Saxon potential. Illustration of a single Pb-Pb collision is shown in Fig. 3.14. Knowing the distribution of all nucleons in both nuclei, one can extract the average values of N_{col} and N_{part} for any given impact parameter. Subsequently, these obtained values can be used as inputs for particle production model to evaluate more sophisticated observables, such as multiplicity of produced particles. In addition,

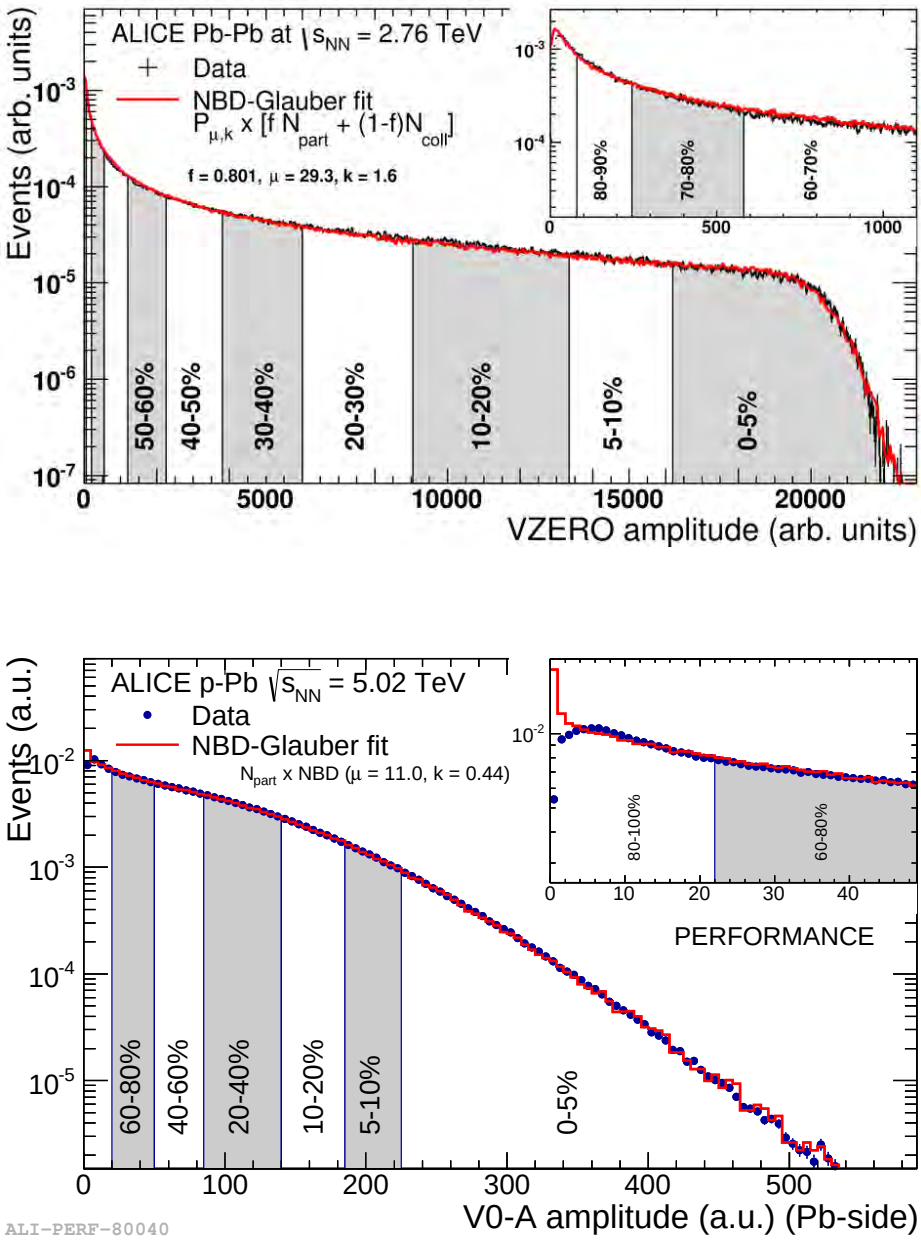

FIGURE 3.15: Distribution of amplitude measured by V0 detector in Pb-Pb collisions at $\sqrt{s_{NN}} = 2.76$ TeV [101] (top) and p-Pb collisions at $\sqrt{s_{NN}} = 5.02$ TeV (bottom). Shaded areas indicate corresponding centrality classes. See the text for details.

a negative-binomial distribution (NBD) is used to obtain the multiplicity distribution compatible with experimental data [104].

In the case of p-Pb collisions, the centrality determination procedure is applied as described above with the only difference being that instead of the sum of both V0 arrays, only the V0-A signal is used. Being situated in Pb-going direction, it is more sensitive to fragmentation of the heavy nucleus. It should, however, be noted that there is no firm connection between centrality and initial geometry established as introduced in the case of Pb-Pb collisions. The distribution of V0-A amplitude as measured in p-Pb collisions at $\sqrt{s_{\mathrm{NN}}} = 5.02$ TeV is shown by the bottom plot in Fig 3.15.

4 Analysis procedure

The full procedure involved in the measurement of p_{T}-differential anisotropic flow coefficients using correlations of inclusive and identified hadrons presented in this thesis is complex. The individual steps and the related technical aspects are described in detail in the following sections of this chapter.

For a concise overview, the flow of the whole analysis is summarised by a diagram shown in Fig. 4.1. The individual components (depicted in blue), their outcome (in green)m and also a dependency among them (indicated by pointing arrows) are presented. As discussed in Chapter 2, the final observables of interest, the anisotropic flow coefficients, are obtained from single-event quantities (i.e. correlations) averaged over many events. Therefore, the analysis is done on an event-by-event basis. The process is illustrated for a single event with entry and exit points (in red) of the event loop, and it is repeated for each analysed event. The whole process can be classified into the following distinct categories: event selection, particle filtering, and calculation of the correlations.

Firstly, only those events stored in the input data files which pass the event selection are used for the subsequent processing. On the other hand, if an event does not fulfil all required criteria, it is skipped entirely and does not affect the measurement. In this step, the event properties, such as event class based on centrality or multiplicity percentiles, are determined.

Secondly, the particle filtering is performed, resulting in samples of selected particles for each considered species; starting with a track selection that is used to filter well-reconstructed trajectories left by charged particles. These are used in multiple ways: for both reference (integrated) and differential correlations, as well as an input sample of candidates for the identification of $\pi^{\pm}$, $\mathrm{K}^{\pm}$, and $\mathrm{p}(\bar{\mathrm{p}})$. Then, the ensemble of identified $\mathrm{K}^{\pm}$ is used for the combinatorial reconstruction of ϕ meson candidates. Meanwhile, the samples of selected $\mathrm{K}^{0}_{\mathrm{S}}$ and $\Lambda(\bar{\Lambda})$ candidates are selected from a pre-filtered collection stored in the input data files.

Once the particle filtering is finished, corresponding flow vectors are constructed from the selected particles, and all desired single-event correlations of all orders and all combinations of harmonics are extracted. That is done for integrated, as well as differential correlations for each particle species serving as POIs separately.

The analysis of the given event is concluded at this point. The exit point of the event loop is reached, and the whole process is repeated with a new input event.

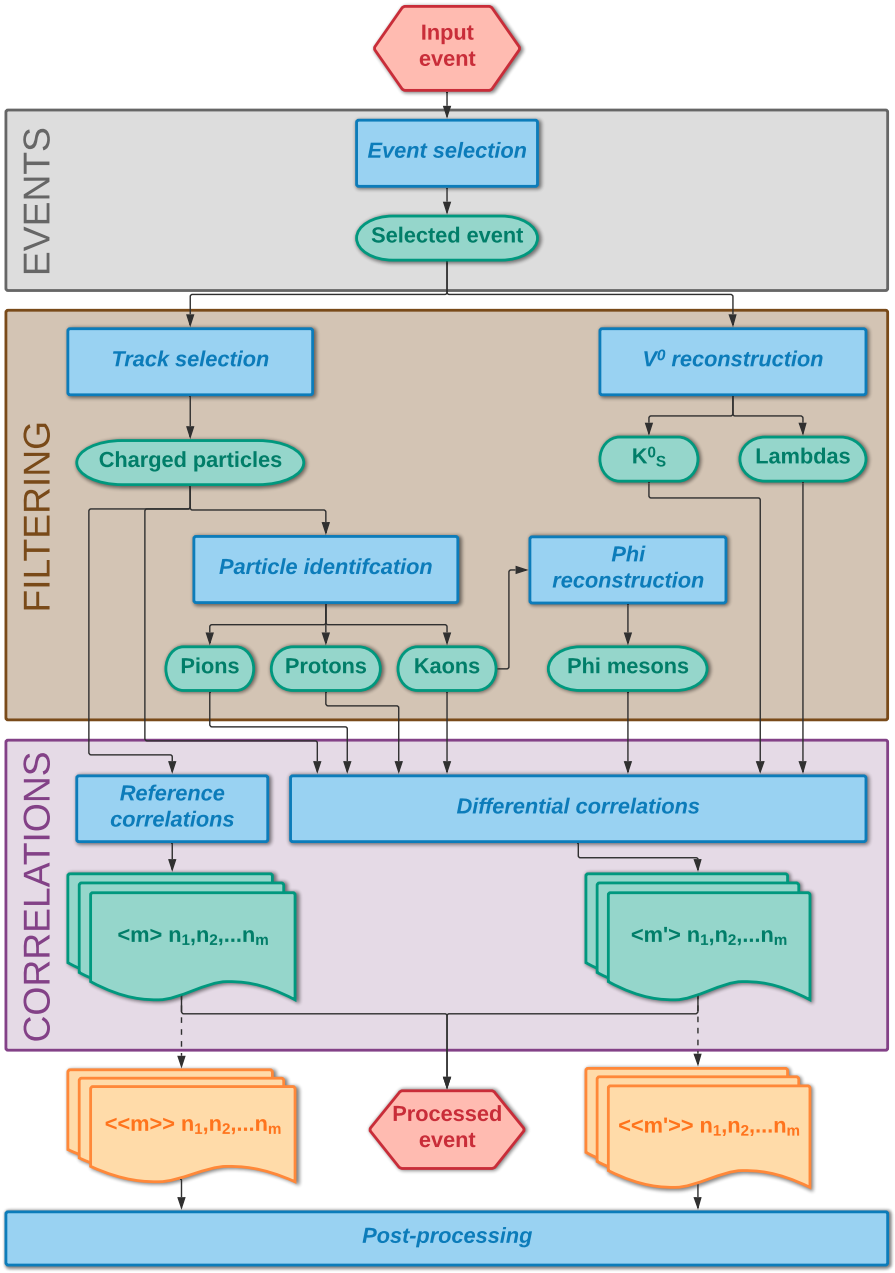

FIGURE 4.1: Diagram illustrating the overall flow of the analysis done on an event-by-event basis with entry and exit points (red), including individual steps (blue) and their output (green). the final outcome in terms of event-averaged correlations (orange) serving as input for subsequent post-processing outside the event loop is shown. See the text for further description.

As the final output of this procedure, the event-averaged correlations (depicted by orange) are obtained by sequential averaging of the corresponding single-event quantities[1]. These are then used for obtaining the final observables of interest, e.g. anisotropic flow v_n coefficients. A set of calculations and processes involved is generally referred to as post-processing since it does not require the analysis of input data and can be therefore calculated offline, i.e. without necessarily accessing the world-wide LHC grid.

Nota bene, the procedure described within this chapter is, in general, universal for all colliding systems. However, the environment of heavy-ion collisions differs dramatically from that of small collision systems, and so does the performance of some detectors. Therefore, this requires a slight modification of some selection criteria in some cases (especially in the case of V^0 reconstruction) to optimise the outcome of the selection procedure. The actual cuts are used for all analysed samples of Pb-Pb, p-Pb, and pp collisions unless stated otherwise. In that case, in addition to the values used for Pb-Pb by default, values used for p-Pb (and pp) are also provided in brackets.

4.1 Analysis code

The analysis is primarily performed by `AliAnalysisTaskUniFlow`, which is a so-called analysis task represented by an object-oriented class written in C++ utilising ROOT framework [105]. The analysis task is included in AliPhysics, the official ALICE software library available in the GitHub repository [106]. In addition, a complete codebase (for brevity referred to simply as UniFlow in the following), also including macros used in the post-processing, is available on the personal GitHub repository [107].

The UniFlow is implemented by the already described scheme presented in Fig. 4.1. It is designed with an aspect of modularity in mind, as indicated by the three encapsulating boxes representing event selection, particle filtering, and correlation calculation. Each of these major parts is isolated from the others. Their input and output present the only links between them For example, for the correlation calculation, it does not matter how the selection of individual particles is technically implemented as long as the resulting sample is provided in an anticipated format. The great benefit is that it allows to extend the analysis by including additional (or replacing no longer needed) species.

In general, correlation measurements are highly demanding in terms of the number of CPU operations required (and thus the overall CPU time spent). This is especially true in the case of multi-particle correlations. Therefore, a great deal of effort went into making the code more efficient even at the expense of increased complexity of the implementation. A rather simple example of this consideration is that the particle selection

[1] Within this analysis, mentioned event-averaging is technically done via `TProfile` objects implemented in ROOT framework for such purposes.

is performed only once per event. Once selected, all subsequent correlation calculations take into account (i.e. iterate over) only already filtered particles without the need to re-apply all preceding selection criteria and requirements for each candidate repeatedly for each correlation. This is particularly crucial due to the numerous calculations of flow vectors (i.e. Q_n, p_n, and s_n) needed during single correlation estimation since each flow vector built represents one pass over all corresponding particles within each event. For example, 2-particle p_{T}-differential correlation for a given harmonics requires more than three flow vectors per particle species and p_{T} interval to be constructed within a single event. In the case of 4-particle correlations, the total number of flow vectors needed grows to more than 15 for each species and p_{T} bin[2].

In order to fully utilise the Generic Framework notation as discussed in Section 2.2.2, a determination of which combinations of n_i harmonics are obtained is neither hard-coded within the task nor requires any modification of the code itself. Instead, it can be conveniently selected within a configuration macro, which is commonly used to customise the task parameters for a specific run. Therefore, one can extract only those correlations of interest without spending any additional CPU time on undesired combinations.

Altogether, this allows all the measurements presented in this thesis to be obtained using only a single analysis task class described here, in a consistent and resource-efficient way for all considered particle species.

4.2 Data sample

In the analysis presented in this thesis, the data samples of Pb-Pb, p-Pb, and pp collisions recorded by the ALICE detector and used here are summarised in Table 4.1. These collisions were collected during the LHC Run 2 data-taking campaign in the years 2015 and 2016.

System	Centre-of-mass energy	Data-taking periods	Sample size
Pb-Pb	$\sqrt{s_{\mathrm{NN}}} = 5.02$ TeV	LHC15o	50 M
p-Pb	$\sqrt{s_{\mathrm{NN}}} = 5.02$ TeV	LHC16q,t	600 M
pp	$\sqrt{s} = 13$ TeV	LHC16k,l	166 M

TABLE 4.1: Overview of minimum-bias data samples used in this analysis of Pb-Pb, p-Pb, and pp collisions together with the corresponding centre-of-mass energy, data-taking periods and overall number of collisions passing event selection procedure.

[2]For completeness, in case of particle species reconstructed via its decay products (as will be discussed further in this chapter) this number needs to be additionally multiplied by a number of invariant mass bins.

Since the main focus of this analysis relies on high-quality tracking and accurate particle identification, only those data runs are used during which all essential central barrel detectors responsible for the related aspects, i.e. ITS, TPC, and TOF, were working correctly. This information is assessed during quality assurance (QA) analysis by detector experts based on offline analysis of reconstructed events.

Moreover, only the so-called minimum-bias (MB) events are selected. Those represent the least biased sample technically possible where only a few requirements are imposed to select valid collisions to be recorded. This is necessary since not every collision which occurs can be processed because the collisional rate is generally much higher than the actual read-out capacity of the detectors. Namely, the MB trigger, internally referred to as INT7 or V0AND, requires at least one hit on both V0A and V0C detector arrays [81].

4.3 Event selection

During the data collection, not all recorded events necessarily originate only from the interactions of the colliding beams of particles that are of interest. The remaining undesired component, which causes mixing particles produced via different mechanisms (or collision) within the single reconstructed event, can be generally categorised into two groups: background processes and pile-up. Removal of such events from the sample is critical in general, but even more so in case of pp and p-Pb collisions, where such interactions are more likely due to a higher number of particles within the beam bunches. In order to remove such contamination, further criteria described below need to be applied during the event selection[3].

Background processes, such as the interaction of one of the colliding beams with the residual gas present in the beam pipe or with the pipe itself, typically occur far from the primary collision point in the centre of the detector. The products from these processes fly towards the detector at a rather low angle (almost parallel) with respect to the beam. In case they are detected, this results in a large number of hits within the tracking detectors (especially the ITS) while the actual number of tracks (or tracklets) reconstructed during the following data processing is rather low. Consequently, events contaminated with such processes are removed by imposing a cut on a correlation between these the number of hits and tracks. Similarly, the correlation between the low number of clusters in mid-rapidity seen by ITS and high activity in a forward region detected by V0 detectors can be used to reject such events.

[3] The criteria described in this section are implemented as the common `AliPhysicsSelection` and `AliEventSelection` task classes available in AliPhysics framework.

On the other hand, several beam-beam interactions may occur in a very narrow time window. When the interval is shorter than the integration time of the detectors, products of such interaction are referred to as pile-up. If this happens between the particles within the time interval of a single bunch crossing, then the collisions also occur very close to each other in space. Therefore this in-bunch pile-up is resolved by rejecting events with more than one reconstructed collision points.

In case there is an interaction between particles from a bunch different from the triggered one, it is described as an out-of-bunch pile-up. These can be identified by comparing online and offline signals from the SPD and V0 detectors. The former are fast signals serving as inputs for the first layer of detector triggers, while the latter contain full information that requires more time to be processed. Moreover, due to its short read-out time, the V0 detector can record not only the information during the currently triggered bunch crossing but also in several adjacent ones, both before and after the triggered bunch. Therefore checking the activity in the vicinity of the triggered crossing o This is known as past-future protection, with which one can reject out-of-bunch pile-up events by checking the activity in the vicinity of the triggered crossing.

Last but not least, only those events with properly assigned single PV are selected. The primary vertex is determined from reconstructed trajectories of detected particles by looking for a common point of origin. This is achieved in two ways: by using tracks reconstructed utilising the full potential of both ITS and TPC detectors and by using the SPD detector alone. The advantage of the latter is its better spatial resolution since it is located close to the beam pipe (and therefore to the interaction point) at the expense of having an only limited number of space-points available, especially compared to the tracking capability of TPC. When multiple vertices are found, the one with the highest number of contributors (i.e. associated tracks) is considered.

In an ideal case of accuraterly estimated primary vertex, the vertices obtained from both approaches should be available, and their position should be identical. Therefore, only those events should be selected whose distance between the two estimates is not too large. In practice, a PV is considered as well-reconstructed if at least one estimate is provided. When only SPD-reconstructed vertex is available, its spacial resolution along the beam axis has to be better than $|z^{\mathrm{SPD}}| < 0.25$ cm. Finally, to achieve good detector coverage by the majority of central barrel detectors, only PV within a region along the beam axis of $|z_{\mathrm{PV}}| < 10$ cm is selected.

4.4 Inclusive charged track selection

In general, not all reconstructed tracks obtained during the data processing as described in Section 3.3.2 are suitable for analysis. Only those tracks passing the selection criteria

listed in this section are used for the subsequent calculation.

This is done to ensure that only well-reconstructed tracks providing a good approximation for real trajectories of charged particles are selected. At the same time, the fake tracks present due to detector imperfections (e.g. track splitting) and the ones originating from interaction with the detectors themselves are rejected.

For this analysis, only tracks tagged (officially within ALICE Collaboration) as global are accepted. These are high-quality tracks reconstructed utilising response from both ITS and TPC detectors as opposed to using only the information from ITS or TPC alone. This is achieved by requiring a high-enough number of SPD hits and TPC clusters and efficiently good Kalman filter fit in terms of χ^2. Moreover, the successful re-fitting of available TPC hits is required.

To increase the quality of the track sample even further, a global pseudorapidity acceptance of $|\eta| < 0.8$ is imposed on the selected tracks. In this region, the availability of all TPC rows for each track is ensured and the tracks reconstructed around the edges of the detector are removed from the sample.

By measuring the azimuthal correlation, one is primarily interested in learning about the dynamics of the collisions. Therefore only particles created directly in the collision referred to as primary should be used in the analysis. Secondary particles, such as products of weekly decaying hadrons, are typically displaced from the primary vertex. In order to reduce the amount of such contamination in the selected sample, cuts on the distance of the closest approach (DCA) to the primary vertex (PV) are introduced. One is along the beam direction, DCA_z, and the other is in the transverse plane, DCA_{xy}, while the later is typically p_T-dependent. As the name suggests, DCA is the shortest distance between the PV and the track itself, which is evaluated at a line going through the PV perpendicular to the tangent of track curvature.

The full list of all applied selection criteria described above consists of the following:

- at least one hit in the SPD detector,
- Kalman filter fit quality per ITS cluster of $\chi^2 / N_\mathrm{ITS} < 36$,
- at least 70 TPC clusters included in the Kalman filter fit
- Kalman filter fit quality per TPC cluster of $\chi^2 / N_\mathrm{TPC} < 4$,
- successful re-fit using TPC space-points
  (flagged as `AliAODTrack::kTPCrefit`),
- maximal DCA in beam direction $|\mathrm{DCA}_z| < 2$ cm,
- maximal DCA in transverse plane $|\mathrm{DCA}_{xy}| < 0.0182 + 0.0350 \cdot (p_\mathrm{T}[\mathrm{GeV}/c])^{-1.1}$,
- pseudorapidity acceptance $|\eta| < 0.8$.

4.5 Particle identification

Once the sample of inclusive charged particles passing the conditions described in the previous section is selected, it undergoes a particle identification (PID) process. When finished, each particle is either rejected, if requirements are not met for any of the species, or it is considered as identified.

For the purpose of this analysis, identification of charged pions, kaons, and (anti-)protons is performed. Due to the composition of the ALICE apparatus (as described in Section 3.2), combined information from TPC and TOF detectors provides a significant tool of how to separate and thus identified these above-mentioned species.

Within ALICE Collaboration, there are two approaches commonly used for the identification of directly measurable charged particles. Namely, the so-called n-sigma method and the Bayesian approach.

4.5.1 n-sigma method

The n-sigma (n_σ) approach is the most common method used for particle identification. This approach compares an expected detector response for a given track under a specific particle species hypothesis with the actually measured one. Such comparison is expressed in terms of a difference between the measurement and the expectation.

In order to account for the finite detector resolution, the relative difference is expressed in terms of width σ of the measured response, rather than its absolute value. Thus the name n-sigma approach. This can be formulated as follows:

$$n_\sigma^i(S) = \frac{R^i_{\text{meas}} - \left\langle R_{\text{exp}} \right\rangle^i (S)}{\sigma^i(S)}, \tag{4.1}$$

where R^i_{meas} and $\left\langle R_{\text{exp}} \right\rangle^i$ represent measured and mean expected response for a given detector i, respectively, while S denotes the particle species hypothesis used in the expectation.

When assuming a Gaussian distribution, the difference can be then interpreted as a probability value that a given reconstructed track belongs to a specific particle species. Therefore, among all considered species, the smaller the $n_\sigma(S)$ value is, the more likely the particle can be identified as such species. Consequently, the particle identification is performed in such a way, that only those particles with $n_\sigma(S)$ below a specific limit are selected as belonging to this species.

Obviously, this method is highly efficient if the responses for various species are well-separated, i.e. when $\left\langle R_{\text{exp}} \right\rangle$ and therefore corresponding n_σ values are quite different among themselves. In the opposite case, when the particle species overlap (meaning

that n_σ values are similar), the situation became less clear, and more sophisticated and complex methods have to be used to make a firm verdict. An illustration of separation using responses from TPC and TOF detectors between charged π, K and p($\bar{\text{p}}$) expressed as an absolute difference between the measured and expected signal is shown in Fig. 4.2 for 0–10% most central Pb-Pb collisions at $\sqrt{s_{\text{NN}}} = 2.76$ TeV. There, the separation can be simply visualised as a distance between local maxima or peaks (approximately indicated by letters denoting each particle species). As one can see in this particular range of p_{T}, there is a good separation between protons and other particle species. On the other hand, the situation is less clear for pions and kaons as the two regions start to overlap.

As the different types of detectors exhibit different sensitivity to various species, information from multiple detectors is typically combined to achieve better particle identification. This is done by obtaining n_σ^i individually from each detector and then combined

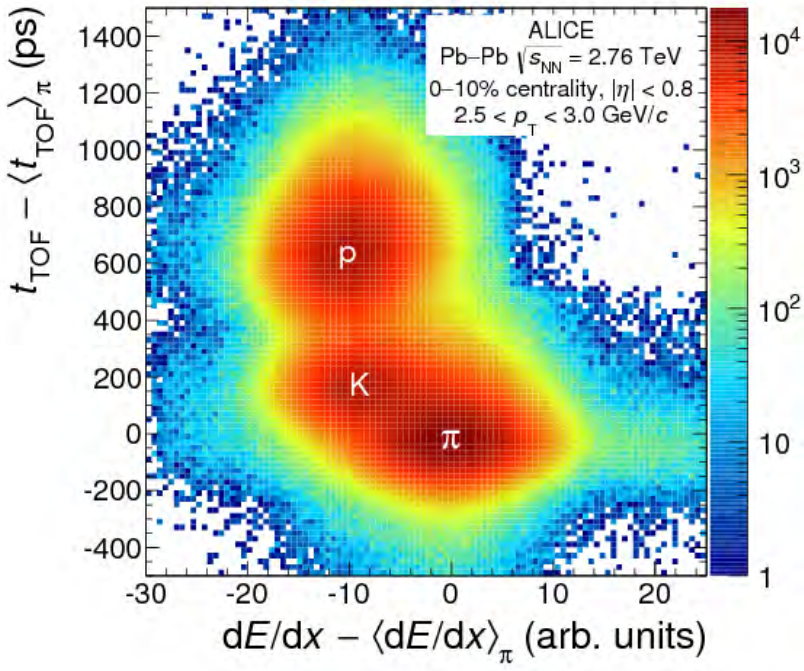

FIGURE 4.2: Combined response from TPC and TOF detectors expressed as absolute difference between measured and expected signal for π of charged particles within $2.5 < p_{\text{T}} < 3$ GeV/c in 0–10% most central Pb-Pb collisions at $\sqrt{s_{\text{NN}}} = 2.76$ TeV. Responses to π, K, and p is indicated for clarity. Figure taken from [108].

together into a single value. In this specific analysis, the final n_σ is obtained utilising responses from TPC and TOF detectors combined as follows:

$$n_\sigma = \sqrt{(n_\sigma^{\mathrm{TPC}})^2 + (n_\sigma^{\mathrm{TOF}})^2}. \tag{4.2}$$

However, as the separation generally deteriorates with increasing momentum of the particles and various species overlap more and more, the PID utilising n_σ approach is typically strongly p_{T}-dependent. To its disadvantage, the applied criteria and cuts might then differ considerably even within a narrow momentum range. Consequently, careful treatment is required.

4.5.2 Bayesian approach

The Bayesian PID approach is a more recently developed method as an alternative to the previously described n-sigma method. The motivation is that the efficiency of the identification based on responses from individual detectors is rather limited and does not exploit the full potential of ALICE detector with combined responses [108], which is illustrated in Fig. 4.2.

As discussed in the previous section, the standard n-sigma approach is based on the knowledge that the particle of certain species S produces an expected response R in a given detector. Assuming Gaussian distribution, this can be expressed as a conditional probability $P(R|S)$ given by the following relation:

$$P(R|S) = \frac{1}{\sigma\sqrt{2\pi}} e^{-\frac{1}{2}n_\sigma^2} = \frac{1}{\sigma\sqrt{2\pi}} e^{-\frac{(R_{\mathrm{meas}} - \langle R_{\mathrm{exp}} \rangle)^2}{2\sigma^2}}. \tag{4.3}$$

However, from the experimental point of view, the principal observable of interest is the particle species S itself. As the result of the PID process, one is therefore interested in the probability that a particle is of species S given that the observed response is R, i.e. the conditional probability $P(S|R)$.

As the name suggests, the relation between the two probabilities can be expressed by applying the well-known Bayes' theorem [109] as follows:

$$P(S|R) = \frac{P(R|S) \cdot P(S)}{P(R)} = \frac{P(R|S) \cdot P(S)}{\sum_j P(R|S_j) \cdot P(S_j)}, \tag{4.4}$$

where the prior $P(S)$ corresponds to the probability of measuring a specific species S and the $P(R)$ is the marginal probability of observing the measured response R. The latter can be expressed as the sum of the probabilities of all considered species (denoted

by index j) and provides an overall normalisation. For more details about this method, see [108] where a test of its validity together with its performance is reported.

The priors represent the estimation of per-event yields of the corresponding particles. When adequately calibrated using Monte Carlo simulation (utilising so-called "tuning on data"), the resulting posterior probability $P(S|R)$ can be interpreted as a purity of the selected sample. In practice, the particle identification is performed by imposing a criterion on the minimal posterior probability, and only those particle above such a threshold are considered as belonging to a particular species.

4.5.3 Performance of particle identification

In order to compare the capabilities of the two above-described PID methods, the following study is performed. In general, the performance of a PID technique is described in terms of the purity and the efficiency of the selected sample.

The purity is the fraction of correctly identified particles of a given species (i.e. those belonging to the same species as tagged) among all tagged ones corresponding to that species. It can also be interpreted as a probability that a given selected particle is appropriately identified as one of a particular species. Alternatively, its complement to unity gives a fraction of misidentified particles present in the tagged sample (or misidentification probability).

The efficiency denotes the relative amount of particles which were identified as a given species compared to the actually produced particles of that species (i.e. those which should have been tagged). However, in this evaluation, it does not matter whether the tagged particle is identified correctly (i.e. if it really belongs to the given species) or not. As a result, the efficiency can be hypothetically larger than one and cannot be simply interpreted as a corresponding probability. In contrast, one could consider only correctly identified particles in the nominator, but in that case, the efficiency would be correlated with purity. If below unity, its complement illustrates an approximate fraction of produced particles left out (i.e. not tagged as of given species) by the PID process.

From the provided description, it is clear that in order to evaluate either attribute, one has to possess the information about all created particles and their species in each collision. In reality, this is not possible. If it were the case, the whole PID procedure would be no longer necessary. Therefore, a collection of simulated Monte Carlo events is used to estimate purity and efficiency. The involved generators are compared and subsequently calibrated to (technically referred to as anchored to) the real sample of analysed collisions.

The performance of the two techniques in p-Pb collisions at $\sqrt{s_{\mathrm{NN}}} = 5.02$ TeV is shown as a function of particle p_{T} in Fig. 4.3: the Bayesian approach with a threshold of $p > 0.9$ (top row) and the n-sigma method with a commonly used cut of 3σ (bottom

row). When compared to the n-sigma method, the Bayesian PID performs much better in terms of the purity of the resulting sample. It is consistently above 95% for pions and protons over the whole studied p_{T} region, while it slowly decreases to approximately 80% for high-p_{T} kaons. On the other hand, the purity of the selected samples using n-sigma method is significantly lower than the previously discussed one, especially for kaons and protons for which it drops rapidly down to approximately 75–80%. Such decrease arises as the responses to different species observed in TPC and TOF detectors start to overlap as illustrated by Fig. 4.2. When looking at the PID efficiency, the Bayesian approach tags significantly smaller portion of kaons and protons with p_{T} above 3 GeV/c but almost twice as many pions in whole p_{T} when compared to the n-sigma method.

In summary, a typical trade-off between quality and quantity also applies in the case of particle identification. The Bayesian approach selects a high-purity sample of particles at the expense of its size mainly in intermediate and high momentum region, while the n-sigma method tags a higher number of created particles but with an overall higher probability of misidentification.

The primary interest of the project described in this thesis lies in the analysis of identified particles and the ability to distinguish between different species. Therefore high purity is crucial to prevent their mixing due to contamination caused by misidentification. Moreover, when measuring the v_n coefficients motivated by studying common collective behaviour, one is, in general, particularly interested in low momentum particles rather than products of hard processes dominating the high p_{T} region. The Bayesian approach is used as a primary method for the identification of charged pions, kaons, and protons based on the provided arguments.

4.5.4 Selection of $\pi^{\pm}$, $\mathrm{K}^{\pm}$, and $\mathrm{p}(\bar{\mathrm{p}})$

The selection of $\pi^{\pm}$, $\mathrm{K}^{\pm}$, and $\mathrm{p}(\bar{\mathrm{p}})$ samples is performed by applying the PID methods described in this section as well as imposing additional requirements on a sample of selected inclusive charged tracks passing criteria described in Section 4.4.

In the analysis reported in this thesis, the Bayesian approach is used as the default method for particle identification over the whole momentum region based on conclusions of the PID performance study discussed in the previous section. For the PID process, only the following particle species are considered: e, μ, π, K, and p; and the posterior probability for each of them is obtained while using the default calibration for the corresponding priors (for more details, see [108]).

The species with the highest probability is considered for the selection to prevent double-counting of candidates. Therefore, every candidate can be either rejected (when not fulfilling requirements for any of the species) or identified as belonging to exactly

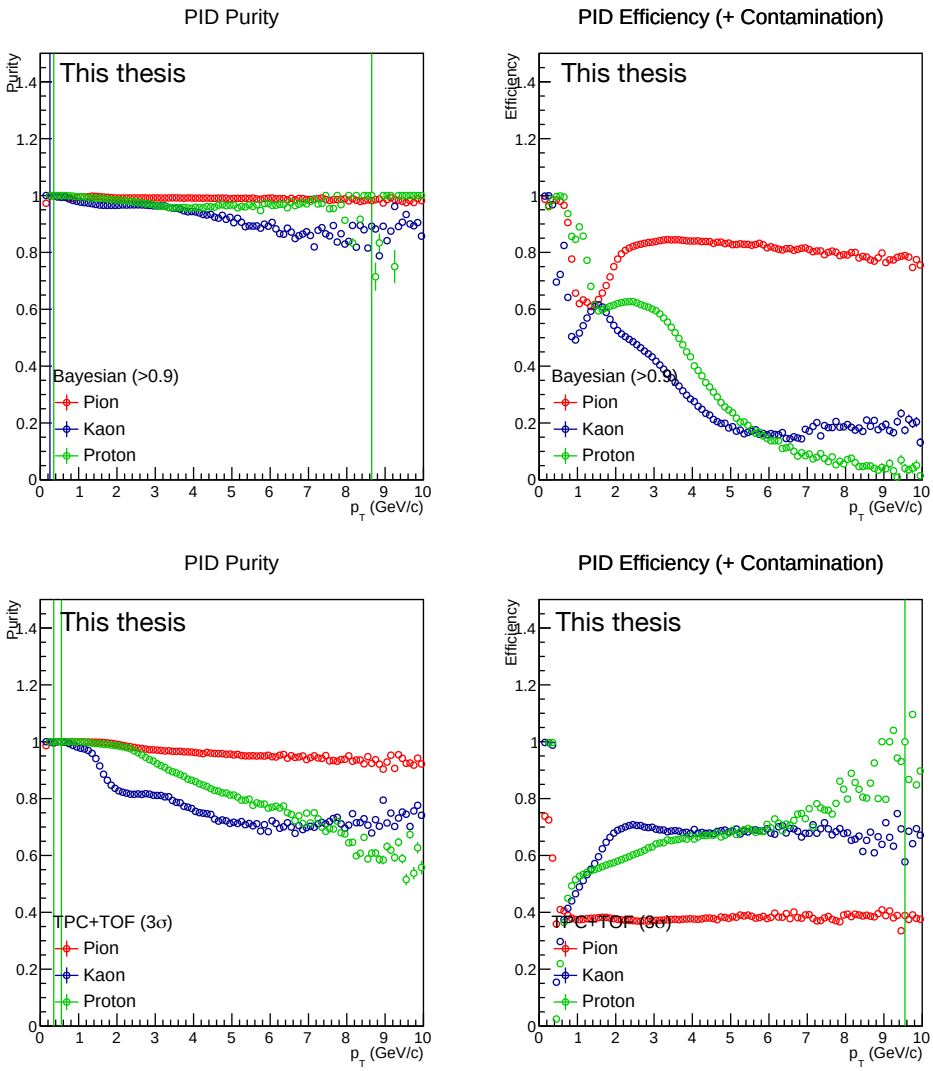

FIGURE 4.3: Comparison of performance of PID techniques used for $\pi^{\pm}$, $K^{\pm}$, and $p(\bar{p})$ identification in terms of purity (left) and efficiency (right): Bayesian approach with threshold $p > 0.9$ (top) and n-sigma method with 3σ cut (bottom) in p-Pb collisions at $\sqrt{s_{NN}} = 5.02$ TeV. See the text for details.

one particle species. Moreover, such a particle is considered as identified only when its probability is above the minimum threshold for a given species.

To remove potential outliers caused by miscalibration, the candidates which deviate by more than 3-sigma from the corresponding expectation of TPC and TOF (when available) response are rejected.

Overall, the full list of selection criteria[4] is listed below:

- passing selection requirements for inclusive charged hadrons (listed in Section 4.4),
- being identified using Bayesian approach with default calibrated priors,
- having the highest posterior probability among e, μ, π, K, and p:
  - above 95% for $\pi^{\pm}$ [above 80%],
  - above 90% for $\mathrm{K}^{\pm}$ [above 80%],
  - above 90% for $\mathrm{p}(\bar{\mathrm{p}})$ [above 80%],
- being within 3-sigma of the expected PID response using TPC and TOF (if available) detectors [not applied in pp and p-Pb].

4.6 Reconstruction of neutral hadrons

Unlike the selection of charged particles discussed in the previous sections, hadrons with no electric charge cannot be reconstructed directly. Due to lack of electromagnetic interaction, neutral particles do not deposit energy within the detectors as they pass through them, and therefore, there is no record of the interaction. It should be noted that while this is generally true, there is a special type of detector that is capable of recording a presence of electrically neutral particles, e.g. hadronic calorimeters. These detectors use various physical processed to measure such particles indirectly. However, as these are not involved in this particular analysis, they are not discussed in this thesis further.

Alternatively, a process has to be utilised in which the given particle of interest, here referred to as the mother, undergoes a decay into a number of products, referred to as the daughters. Such a specific process with its final particle composition and its characteristic probability (referred to as the branching ratio) is called decay channel. This approach can be best used when the products of a specific decay channel can be measured themselves.

In the rest of this section, indirect reconstruction and subsequent selection of the neutral hadron via its decay products is discussed. Namely, fully hadronic decay channels

[4] NB: The listed criteria are used by default for Pb-Pb, while those listed in brackets are used for p-Pb (and pp).

Hadron	Mass [MeV/c^2]	Lifetime ($c\tau$)	Decay channel	B.R. [%]
ϕ	1019.461 ± 0.016	45 fm	$\phi \longrightarrow K^+ + K^-$	49.2 ± 0.5
K^0_S	497.611 ± 0.013	2.68 cm	$K^0_S \longrightarrow \pi^+ + \pi^-$	69.20 ± 0.05
Λ	1115.683 ± 0.006	7.89 cm	$\Lambda \longrightarrow p + \pi^-$	63.9 ± 0.5

TABLE 4.2: Overview of reconstructed neutral hadron species with their masses, lifetimes, decay channels and corresponding branching ratios [110].

of ϕ and K^0_S mesons and $\Lambda(\bar{\Lambda})$ baryon where mother particle decays into a pair of daughters with opposite charges are measured as listed in Table 4.2.

4.6.1 Reconstruction of ϕ meson candidates

For the reconstruction of the ϕ meson, all candidates for decay products according to the selected decay channel (see Table 4.2), i.e. charged kaons, are first selected from the selected charged tracks. To be selected among the valid daughters, a track has to fulfil the following criteria:

- passing criteria for inclusive charged particles (listed in Section 4.4),
- being identified as kaon (described in detail in Section 4.5),
- having invariant mass under corresponding decay channel hypothesis within $0.99 - 1.07$ GeV/c^2 window,
- pseudorapidity acceptance $|\eta| < 0.8$.

Once all kaon candidates are selected, all possible pairs of non-identical kaons are combined into ϕ meson candidates. This is done on an event-by-event basis by summing the 4-momenta and electric charges of the corresponding daughters.

The resulting particles are divided into two independent samples based on their net electric charge: a) those with a charge of 0 (from opposite- or unlike-sign kaon pairs); and b) those with a charge of ± 2 (from like-sign kaon pairs). The former set represents a sample consisting of both candidates combined from a pair of kaons coming from true ϕ decays (i.e. true ϕ mesons) and ones combined from a pair of kaons originating from different physical processes and not produced by ϕ meson decays (combinatorial background). The later contains a set of nonphysical states representing a combinatorial background only. This sample is later used for a better evaluation of the background shape in the opposite-sign kaon pair sample. This will be discussed later in this section.

4.6.2 Reconstruction of K^0_S and $\Lambda(\bar{\Lambda})$ candidates

Contrary to the strong decay of ϕ mesons, both K^0_S and $\Lambda(\bar{\Lambda})$ decay via the weak interactions. Since their lifetimes are much longer compared to the one of ϕ, the decays happen further from the collision point. Therefore, a secondary vertex of such decay is displaced with respect to the PV, as seen in Table 4.2. Together with the fact that oppositely charged particles are bent in opposite directions in an external magnetic field (such as one within ALICE solenoid) due to Lorentz force, the K^0_S and $\Lambda(\bar{\Lambda})$ decays exhibit a characteristic V-shaped topology. Because of that, these particles are historically commonly referred to as V^0 particles.

Given this well-distinguishable topology, potential candidates for such weak decays of V^0 particles are pre-selected within track reconstruction procedure during data processing and stored in the data files, similarly to charged tracks, as mentioned in Section 3.3.2. However, the pre-selected sample of V^0 candidates contains not only the true decays of K^0_S and $\Lambda(\bar{\Lambda})$ but also the combinatorial background. Therefore a set of reconstruction criteria and topological cuts described in the following and illustrated in Fig. 4.4 is imposed to reduce the amount of this background [111, 112].

The Secondary Vertex (SV) representing the position where the decay occurs is evaluated on the line of the closest distance between each pair of oppositely charged daughter

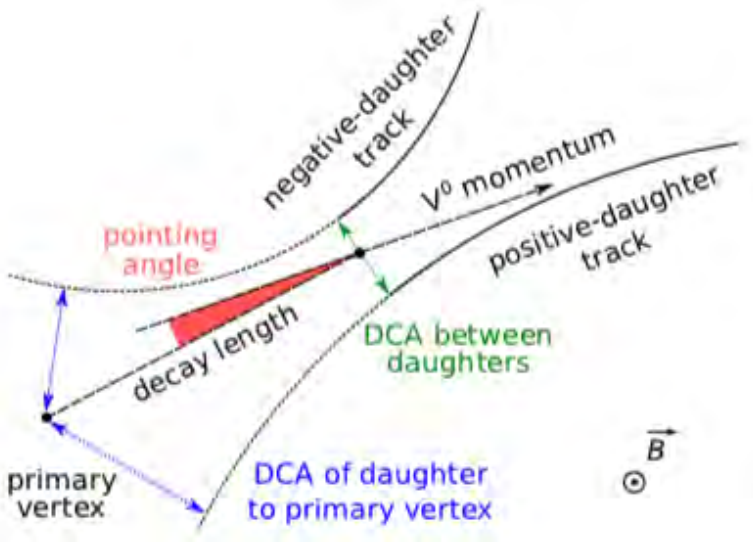

FIGURE 4.4: Illustration of the characteristic topology of V^0 particles decaying in a presence of homogenous magnetic field together with its parametrisation used for reducing the level of combinatorial background. See the text for detailed description. Figure taken from [113].

tracks. Therefore only those candidates with small enough DCA are selected. In addition, SV outside considered fiducial conical volume parallel to beam direction defined in terms of minimal and maximal radius from the PV are rejected. To prevent potential bias, a pseudorapidity window of $|\eta| < 0.8$ is required for selected V^0 candidates as for other particles of interests.

To reduce the number of non-prompt V^0 candidates (i.e. those coming from decays of heavier particles), the following criterion based on the cosine of pointing angle (CPA) is imposed. A pointing angle is defined as the angle between the reconstructed momentum vector $\vec{p}$ of the mother candidate and the direction connecting primary and secondary vertex. In an ideal case, the V^0 momentum vector should lie on this connecting line, and therefore, the angle should be close to zero and its cosine close to unity.

Similarly to inclusive track selection, only candidates with well-reconstructed daughter tracks passing through the whole TPC volume (thus limited within pseudorapidity window of $|\eta| < 0.8$) are selected. The tracking quality is given by the overall number of crossed pad-rows in the TPC, number of TPC clusters available for the tracking taking into account dead zones of the detector (referred to as findable clusters), and number of TPC clusters actually used for Kalman filter fit. Moreover, a successful final step of tracking procedure when the track is re-fitted using TPC space-points in inwards direction towards PV is also important.

On the other side, unlike the directly measured charged particles, in the case of daughter particles, one is by definition interested in the secondary tracks instead of primary ones. Therefore only those candidates whose daughters are well-separated from the primary vertex in terms of high-enough DCA are accepted.

The particle identification criteria are applied to both daughter particles according to related decay channels using the $n\sigma$-approach across the whole daughter p_{T} region, as discussed in Section 4.5. Even though slightly loose criteria are used, it substantially helps with reducing the background, especially by identifying the (anti-)protons from $\Lambda(\bar{\Lambda})$ decays.

In order to distinguish K^0_S from $\Lambda(\bar{\Lambda})$, a selection cut is performed using Armenteros-Podolaski parametrisation [114]. In this parametrisation for 2-particle decays, each mother particle is represented by a point in $(q_{\mathrm{T}}^{\mathrm{Arm}}, \alpha^{\mathrm{Arm}})$ phase-space given by:

$$q_{\mathrm{T}}^{\mathrm{Arm}} \equiv p_{\mathrm{T}}^{0}, \tag{4.5}$$

$$\alpha^{\mathrm{Arm}} \equiv \frac{p_{\mathrm{L}}^{+} - p_{\mathrm{L}}^{-}}{p_{\mathrm{L}}^{+} + p_{\mathrm{L}}^{-}}, \tag{4.6}$$

where $p_{\mathrm{L}}^{+}(p_{\mathrm{L}}^{-})$ is the longitudinal component of the projection of positively (negatively) charged daughter momentum along the mother momentum and p_{T}^{0} is the transverse

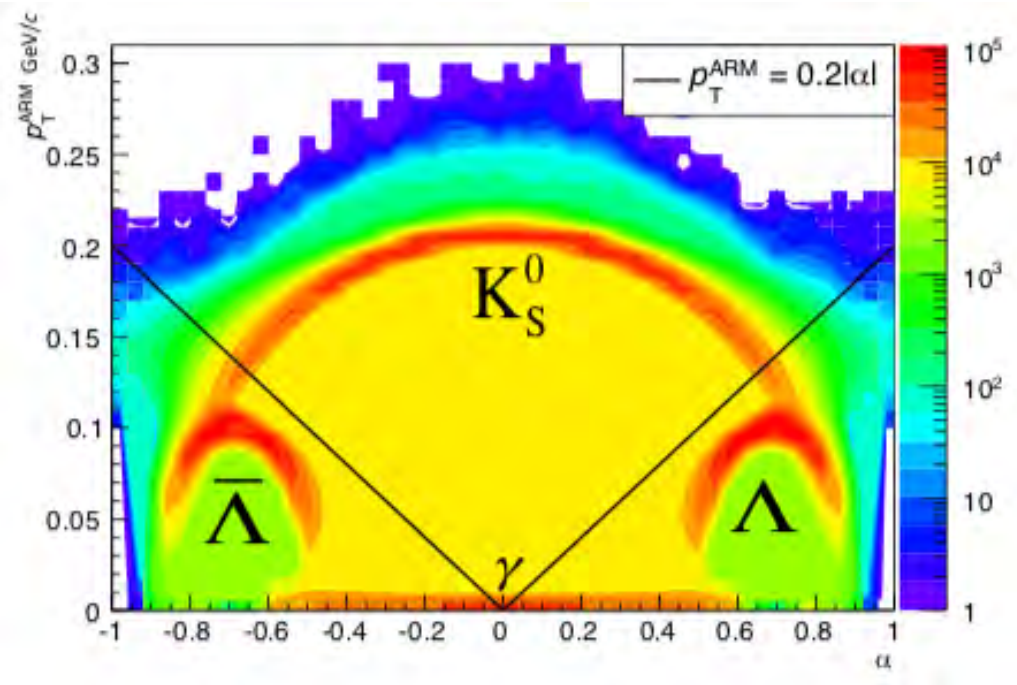

FIGURE 4.5: Illustration of observed response of V^0 particles according to Armenteros-Podolanski parametrisation shown in $(q_T^{Arm}, \alpha^{Arm})$ phase-space (here denoted as p_T^{ARM} and α, respectively). See the text for description. In addition, $\gamma \to e^+ + e^-$ conversion not discussed in the text is shown here. Figure taken from [115].

component of the mother momentum.

To further reduce potential misidentification and prevent potential double-counting of the V^0 candidates, so-called competing invariant mass cut is used. This criterion rejects a candidate under a specific hypothesis in case that this particular candidate lies in a vicinity of the rest mass of the other species. For example, a V^0 candidate passes all the criteria for K_S^0 selection but its invariant mass under a Λ hypothesis is close to real Λ rest mass within few MeV is not accepted as a K_S^0.

The complete set of all criteria[5] imposed on V^0 candidates (or individual species specified in parentheses) during the K_S^0 and $\Lambda(\bar{\Lambda})$ selection is:

- at least 70 TPC clusters included in the Kalman filter fit,
- at least 70 crossed TPC pad-rows N_{cross},
- at least 1 findable TPC cluster N_{find},

[5]NB: The listed criteria are used by default for Pb-Pb, while those listed in brackets are used for p-Pb (and pp).

- ratio of crossed pad-rows to findable clusters in TPC $N_{\text{cross}}/N_{\text{find}} > 0.8$,
- successful refit TPC space-points
  (flagged as `AliAODTrack::kTPCrefit`),
- rejecting so-called kink vertices (not flagged as `AliAODVertex::kKink`),
- V^0 candidates pre-selected during offline processing,
- mother candidate within η acceptance $|\eta_{\text{mother}}| < 0.8$,
- both daughters within η acceptance $|\eta_{\text{daughter}}| < 0.8$,
- fiducial volume radius $5 < r < 100$ cm [$0.5 < r < 200$ cm],
- DCA to PV of both daughters $\text{DCA}_{\text{PV}} > 0.1$ cm [> 0.06 cm],
- DCA among the two daughters $\text{DCA}_{\text{daughters}} < 0.5$ cm [< 1 cm],
- cosine of pointing angle CPA > 0.998 [$> 0.97(\text{K}^0_\text{S})$, > 0.995 (Λ)],
- at least 70 TPC clusters used for PID,
- both daughters correctly identified using TPC n-sigma method $n_\sigma^{\text{TPC}} < 3$ [< 5],
- K^0_S satisfying Armenteros-Podolanski parametrisation $q_\text{T}^{\text{Arm}} > 0.2|\alpha^{\text{Arm}}|$,
- K^0_S candidate within inv. mass window $0.4 < \text{M}_{\text{inv}}^{\text{K}^0_\text{S}} < 0.6\ \text{GeV}/c^2$,
- $\Lambda(\bar{\Lambda})$ candidate inv. mass window $1.08 < \text{M}_{\text{inv}}^{\Lambda(\bar{\Lambda})} < 1.16\ \text{GeV}/c^2$,
- K^0_S competing inv. mass rejection $|\Delta M_{\text{inv}}^{\text{K}^0_\text{S}}| < 5\ \text{MeV}/c^2$,
- $\Lambda(\bar{\Lambda})$ competing inv. mass rejection $|\Delta M_{\text{inv}}^{\Lambda(\bar{\Lambda})}| < 10\ \text{MeV}/c^2$.

Note, that selected Λ and $\bar{\Lambda}$ particles are treated in exactly the same way from the point-of-view of this analysis. Therefore, in the remainder of this thesis, both Λ and $\bar{\Lambda}$ particles are labelled simply as Λ, unless explicitly specified otherwise.

4.7 Azimuthal correlations

At this point, all the relevant particles in the given event are appropriately filtered according to the considered species, as reported in this section. In the following steps, these represent the particles of interest (POIs).

The next step is to evaluate all correlations necessary for further processing and analysis depending on the ultimate observable of interest. Within the project reported in this

thesis, the azimuthal correlations are obtained using Generic framework implementation of the Q-cumulant method described in detail in Section 2.2.2.

The process of evaluating desired correlations starts by filling appropriate flow vectors needed for evaluation both the numerator and the denominator terms as prescribed by (2.34) and corresponding relations for all combinations of harmonics involved.

Besides the above-mentioned POIs, the RFPs are used for the construction of reference flow vector Q_n. In the context of this analysis, those are all particles from the sample of selected inclusive charged hadrons within the kinematic region of $0.2 < p_{\mathrm{T}} < 3$ GeV/c. The lower bound is imposed in order to remove reconstructed tracks within a region where the tracking performance drops significantly. The upper cut then removes the high-p_{T} particles, which are generally created as the results of so-called hard processes (e.g. jet production) unrelated to the global collectivity and that the correlation measurement.

Similarly, the differential flow vectors, p_n and s_n (in case of overlap among POIs and RFPs) are constructed using the azimuthal angle of the POIs as given by (2.38) and (2.39), respectively. However, contrary to reference correlations, these are used for evaluation of differential correlation (denoted by the asterisk in the relevant expressions) within a rather small region of interest commonly referred to as a bin. In the case of p_{T}-differential correlations, this region is represented by a narrow p_{T} interval. Therefore, only those POIs which are within this interval are used for the construction of the corresponding flow vectors.

Then, once all Q_n, p_n and s_n vectors are prepared, the corresponding correlations are evaluated. The differential correlations are estimated for one bin at a time, while the reference correlations being integrated over the whole region of interest are assessed only once (per event).

The whole procedure is performed for each identified particle species representing the POIs separately, while the RFPs are kept unchanged, being the subset of selected inclusive charged hadrons sample. When all necessary correlation calculations are evaluated for all p_{T} intervals and particle species, the analysis of a given event is concluded.

4.7.1 Non-uniform acceptance correction

As discussed in Section 1.3, measurements of anisotropic correlations are sensitive to the shape of the azimuthal distribution of the correlated particles. In an ideal situation, such distribution should be perfectly flat. In reality, the tracking efficiency is not uniform over the whole acceptance area. This is generally caused by worn-out sectors and imperfections of the detectors resulting in regions with non-trivial shape of the particle distribution. The effect of the aforementioned flaws is shown in left sub-plots in Fig. 4.6 where

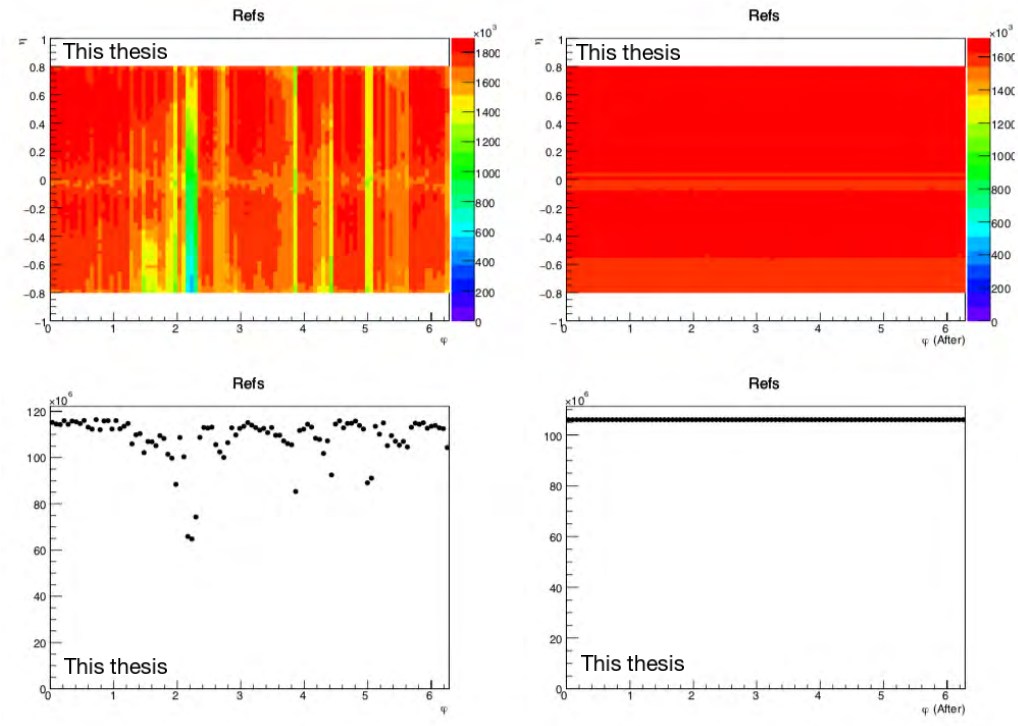

FIGURE 4.6: Distribution of RFPs in (φ, η) space (top row) and the corresponding projection into φ (bottom row) prior acceptance correction (left column) and after applying non-uniform correction (right column).

both the 2-dimensional distribution in (φ, η) space as well as its corresponding projection into φ are presented for the selected RFPs. Consequently, such non-uniformities impose bias on the correlation measurement.

In order to eliminate any potential bias from these detector effects, so-called non-uniform acceptance (NUA) correction is performed. The Generic framework offers an elegant way of applying any relevant correction [53]. This is done by including a single particle weight w_i when the relevant flow vectors are constructed according to (2.37), (2.38), and (2.39).

In this analysis, the NUA correction is done in the following way. First, the (η, φ) distribution of correlated particles are obtained (Fig. 4.6). Then, the particle weight is estimated as follows:

$$w_i(\eta, \varphi) = \frac{N^{\max}(\eta)}{N(\eta, \varphi)}, \tag{4.7}$$

where N is the number of correlated particles and $N^{\max}$ represents the maximal number

of particles present within a narrow η interval of the original (η, φ) distribution[6]. By doing so, the η dependence of the original distribution is mapped onto the corrected one while the distortions in φ are remedied. Finally, the extracted weights are applied on a track-by-track basis during the flow vector construction as already mentioned. This is done for the sample of RFPs and each species of POIs separately.

Like any data-driven correction, this method requires a sufficiently large set of particles to be adequately precise. Therefore, this re-weighting technique cannot be applied on an event-by-event basis. For the NUA to be the most efficient, the corrected sample of particles should reflect the set of particles used for the preparation of weights as closely as possible. As a consequence, the proper estimation of the weights requires an independent run over the whole data set.

The result of this particle NUA correction can be seen in the right column of Fig. 4.6 where the re-weighted distribution of RFPs and its projection are presented. There, the original non-uniformities were compensated, and the corrected distribution is nicely flat.

4.7.2 v_n vs invariant mass method

The approach described above is generally valid for all particle species. However, in contrast to the charged hadrons, i.e. $\mathrm{h}^{\pm}$, $\pi^{\pm}$, $\mathrm{K}^{\pm}$, and $\mathrm{p}(\bar{\mathrm{p}})$, neutral hadrons such as ϕ, $\mathrm{K}^0_{\mathrm{S}}$, and $\Lambda(\bar{\Lambda})$ cannot be measured directly. Instead, they are reconstructed through their decay products, as discussed in Sections 4.6.1 and 4.6.2.

Since the selection is performed stochastically by imposing requirements on pre-filtered set of candidates, the resulting particle sample contains both true particles of interest (commonly referred to as the signal) as well as random combinatorial background. While the latter represents misidentified particles or even fake unphysical states, the former contains true physical hadrons which decayed through the considered channel. Hypothetically, if one could separate the two components, only the signal particles would be used for the constructing the p_n and s_n flow vectors, and the single-event correlations would be then evaluated in the identical fashion as for other particle species.

However, this is not the case in reality, and therefore alteration of this procedure is required for the reconstructed species. As the composition of the sample is not a priori known, one does not extract the information about the true signal particles only but rather the sample as a whole when evaluating the correlations.

In this case, the so-called v_n vs invariant mass (m_{inv}) method based on the additivity of the v_n coefficients. The v_n of the whole sample is equal to the sum of the v_n of the individual components weighted by the respective fractions, assuming that v_n of the

[6] In principle, the numerator serves only as a reference value which is rather arbitrary as long as it contains the corresponding η dependence of the sample. However, it should be chosen with reason to prevent potential undesired issues such as numerical instability.

background component is a relatively smooth function of m_{inv} [116, 117]. This can be formulated by the following expression:

$$v_n^{\text{T}}(m_{\text{inv}}) = f^{\text{S}}(m_{\text{inv}})v_n^{\text{S}} + f^{\text{B}}(m_{\text{inv}})v_n^{\text{B}}(m_{\text{inv}}), \tag{4.8}$$

where v_n^{T} represents the anisotropic flow coefficients of the whole sample (which is effectively being measured) and v_n^{S}, v_n^{B} the one of the signal and background component, respectively. The f^{S} and f^{B} terms designate the corresponding fractions given simply as ratios:

$$\begin{aligned} f^{\text{S}} &= \frac{N^{\text{S}}}{N^{\text{S}} + N^{\text{B}}}, \\ f^{\text{B}} &= \frac{N^{\text{B}}}{N^{\text{S}} + N^{\text{B}}}, \end{aligned} \tag{4.9}$$

in which N^{S} and N^{B} denotes the actual number of signal and background particles in the given sample, respectively. The sum of the fraction is normalised to unity since the two being the only considered components of the whole sample, which can be expressed as follows:

$$f^{\text{S}} + f^{\text{B}} = 1. \tag{4.10}$$

For the sake of brevity and context of this section, only the dependence on m_{inv} is indicated in (4.8) and related expressions. However, keep in mind that all terms in this relation are also dependent on other observables considered in this analysis such as p_{T} of POIs and event characterisation (i.e. multiplicity or centrality class) unless explicitly stated otherwise. Moreover, it should also be stressed out that the v_n^{S} is the only variable in (4.8) considered to be constant with respect to the m_{inv}, which will be further discussed later.

The entire procedure can be factorised into two distinct steps: determination of signal and background fractions, and extraction of the v_n^{S} coefficient of the signal particles. Both of which are done by fitting corresponding observables using the m_{inv}-dependent functions. This is described in detail in the following.

In the first part, the f^{S} and f^{B} fractions are extracted. Actually, as the two components are linked via the overall normalisation expressed by (4.10), it suffices to determine only one of them. To achieve that, the invariant mass distributions of all candidates within each p_{T} interval are obtained. For the ϕ meson, distribution of like-sign kaon pair is extracted in addition to the one from opposite-sign candidates as already mentioned in Section 4.6.1. The fractions of signal and background particles present in the subset (corresponding to the given p_{T} bin) are then extracted by fitting the invariant mass distribution by a sum of two functions representing $N^{\text{S}}(m_{\text{inv}})$ and $N^{\text{B}}(m_{\text{inv}})$ terms. For illustration, the invariant mass distributions of ϕ, K^0_{S}, and $\Lambda(\bar{\Lambda})$ candidates are shown

in Fig. 4.7, 4.8 and 4.9, respectively, together with the results of the fitting procedure: the total fitted yield of all selected candidates (solid red line) as well as both signal (green dashed line) and background (blue dotted line) components separately. In the bottom panel, extracted fractions f^{S} and f^{B} are presented (denoted by the same colour code as above).

Since the evaluation of v_n is driven by the estimation of the particle fractions, it is

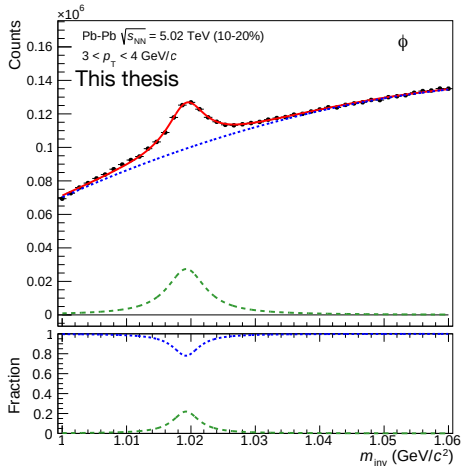

FIGURE 4.7: Invariant mass distribution of ϕ candidates together with fitted yields of signal and background particles (top) and the corresponding fractions (bottom) in Pb-Pb collisions. See the text for details.

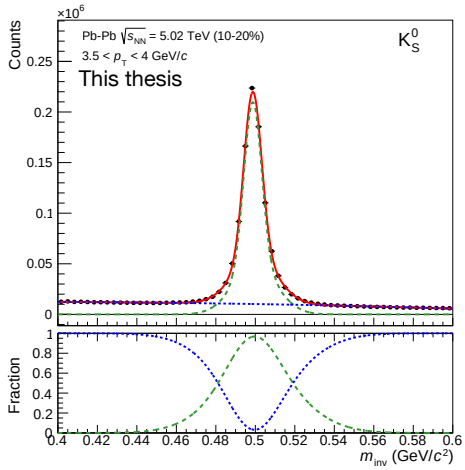

FIGURE 4.8: Invariant mass distribution of $\mathrm{K}^0_{\mathrm{S}}$ candidates together with fitted yields of signal and background particles (top) and the corresponding fractions (bottom) in Pb-Pb collisions. See the text for details.

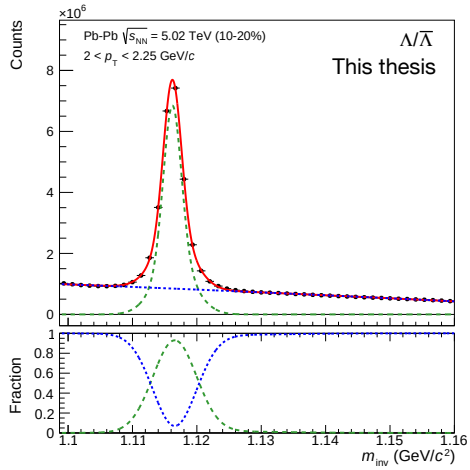

FIGURE 4.9: Invariant mass distribution of $\Lambda(\bar{\Lambda})$ candidates together with fitted yields of signal and background particles (top) and the corresponding fractions (bottom) in Pb-Pb collisions. See the text for details.

essential to determine the two components as accurately as possible. To do so, a species-dependent function is chosen for the signal yield. Namely, a relativistic Breit-Wigner distribution for ϕ meson and a sum of the two Gaussian distributions with the common mean value for the K^0_S and $\Lambda(\bar{\Lambda})$are used. The background term is represented by third-order polynomial for all three considered species.

In the second part of the procedure, the obtained fractions are used to determine the correlations of the signal particles. As a result, the process of building the p_n and s_n flow vectors as well as evaluating all necessary correlations has to be conducted not only in p_T bins (as described in the previous section) but also in narrow intervals of m_{inv} of the candidates.

However, before moving forward, a bit of clarification is needed at this point. Traditionally, this technique is used to extract the information about the signal particles at the level of v_n coefficients [117, 118] as illustrated by (4.8). Hence the name v_n vs invariant mass method.

Nevertheless, as can be seen from expressions (2.25) and (2.23), the $v'_n\{2\}$ is proportional to $d_n\{2\}$ cumulant which is in turn equal to $\langle\langle 2' \rangle\rangle$ event-averaged correlation. Therefore, when using the Q-cumulant method of 2-particle correlations, for the reconstructed species, it does not matter whether this step is done at the level of flow coefficients, differential cumulants or correlations themselves[7]. However, for higher-order cumulants, this does not necessarily hold anymore as there are more differential (and

[7] For completeness, the differential cumulant, d_n, is scaled by a square root of reference cumulant, c_n, as seen in (2.25). However, as the latter quantity is independent of both p_T and (in this context more importantly) m_{inv} it can be treated as a constant factor unrelated to the fitting procedure.

thus m_{inv}-dependent) terms involved, such as $\langle\langle 2' \rangle\rangle$ and $\langle\langle 4' \rangle\rangle$ correlations present in case of 4-particle cumulant $d_n\{4\}$ given by (2.24). Therefore, one might observe a certain deviation among the results of this technique performed on the various levels due to possible interference arising from a non-zero correlation between individual correlation orders.

Consequently, to prevent such potential bias, the v_n vs invariant mass method is applied on correlation level[8] for each correlation order separately. To reflect this, the modified version of this method expressed by (4.8) is obtained by substituting v_n coefficients by general k-particle differential correlations as follows:

$$\langle\langle k' \rangle\rangle^{\text{T}}(m_{\text{inv}}) = f^{\text{S}}(m_{\text{inv}}) \langle\langle k' \rangle\rangle^{\text{S}} + f^{\text{B}}(m_{\text{inv}}) \langle\langle k' \rangle\rangle^{\text{B}}(m_{\text{inv}}). \tag{4.11}$$

This approach yields an additional advantage when a particular analysis does not involve cumulant calculation. A suitable example is the non-linear response measurement (also presented in this thesis) for which the correlations themselves serve as the observables of interests as discussed in Section 2.4. And even more so if compared to standard linear response obtained from the measurement of cumulants. In such a situation, the same method is utilised in both aforementioned measurements. Therefore the mutual consistency is ensured.

The measured differential correlation in a given p_{T} bin is fitted by the sum of two terms corresponding to signal and background component as indicated by (4.11). For the description of the correlation expression corresponding to the background $\langle\langle k' \rangle\rangle^{\text{B}}$, a second-order polynomial function is used. The correlation of the signal particles $\langle\langle k' \rangle\rangle^{\text{S}}$ is considered as a m_{inv}-independent constant factor for the given p_{T} bin as already pointed out. During the fitting, the functions representing f^{S} and f^{B} terms obtained in the previous step are kept as fixed parameters.

An illustration of the procedure is shown in Fig. 4.10 where $\langle\langle 2' \rangle\rangle$ and $\langle\langle 4' \rangle\rangle$ correlations extracted from 10–20% most central Pb-Pb collisions at $\sqrt{s_{\text{NN}}} = 5.02$ TeV are presented as a function of m_{inv} of K^0_{S}, $\Lambda(\bar{\Lambda})$, and ϕ candidates separately. In addition to the actual measurement (black circles), the fit representing the $\langle\langle k' \rangle\rangle^{\text{T}}$ (solid red line) is plotted together with the individual components of (4.11): signal (green dashed line) and background (blue dotted line) terms. Since the later part convoluted by the fraction extracted in the previous step, mass-dependent $\langle\langle k' \rangle\rangle^{\text{B}}$ term (brown dash-dotted line) is also shown for clarity.

Once all the correlations are fitted, the corresponding differential cumulants, as well as the v_n coefficients, are calculated for the given p_{T} interval using the relations and procedure described in Section 2.2.1.

[8] Although still being referred to as v_n vs inv. mass in the related context of this thesis.

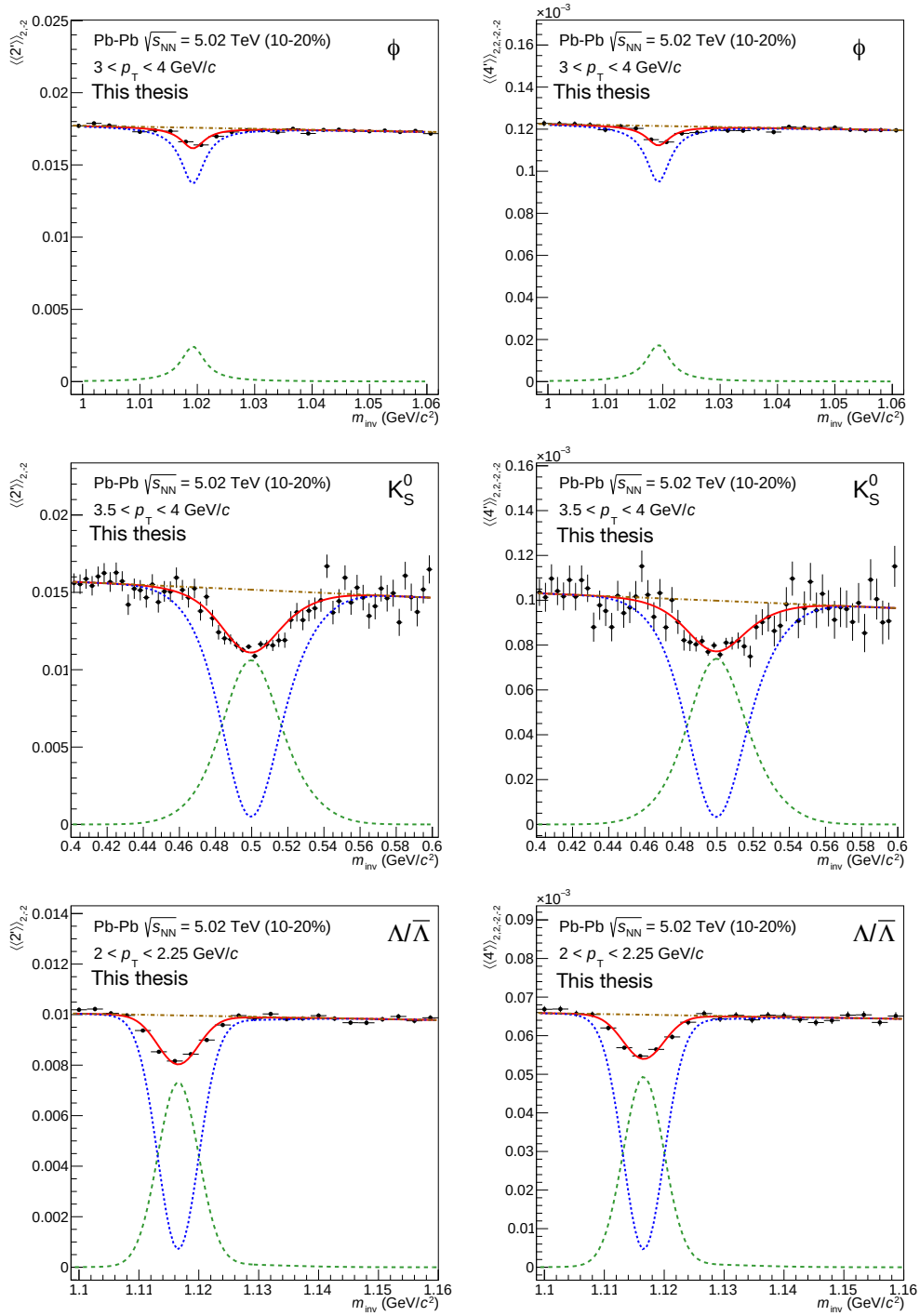

FIGURE 4.10: v_n vs inv. mass method for 2- (left column) and 4-particle (right column) correlations of ϕ (top row), K^0_S (middle row), abd $\Lambda(\bar{\Lambda})$ (bottom row) candidates in 10–20% most central Pb-Pb collisions at $\sqrt{s_{NN}} = 5.02$ TeV. See the text for details.

4.8 Systematic uncertainties

The selection criteria discussed in this chapter (and the corresponding values) are used as a default set of requirements imposed during the analysis. The variations of these criteria are made in order to evaluate the systematic uncertainties of the final observables.

This procedure can be summarised as follows. For each variation, only a single criterion is changed at the time, while the rest are kept fixed. Then, the whole analysis is performed using the modified set of criteria, as illustrated by a flowchart in Fig. 4.1. Afterwards, the final observables are obtained and compared to one corresponding to the default set of requirements. The absolute difference of the final observable between the varied and default configuration is assigned as a systematic uncertainty. Finally, the contributions from the different sources (parameters) are considered uncorrelated. Such components are summed in quadrature to obtain the final systematic uncertainty. In case that a single criterion was varied multiple times, only the largest difference is considered.

The systematic uncertainty is evaluated for each particle species separately, and only the relevant criteria are varied (e.g. variation of particle identification is not investigated for un-identified particles). In general, the p_{T}-dependence of the variation is taken into account. However, when the statistical precision is poor, p_{T}-integrated uncertainty is estimated, instead. This is the case for the measurement of non-linear flow mode coefficients, $v_{n,mk}$ or ϕ meson measurement.

The actual variations are based on the internal guidelines of ALICE Collaboration and motivated by consistency with previous measurements. In general, the criteria are changes to impose tighter constraints with respect to the default configurations (with a few exceptions). Consequently, the varied sample of is a sub-set of the default one.

In the following, the variations used for the evaluation of the systematic uncertainty in this analysis are listed[9].

- Event selection criteria (varied for all considered particle species):
  - event centrality percentile estimated based on number of particles observed in central barrel (CL1 estimator), [not applied in p-Pb]
  - accepted range of PV in z-direction within 8 cm.
- Charged track criteria (varied for $\mathrm{h}^{\pm}$, $\pi^{\pm}$, $\mathrm{K}^{\pm}$, and $\mathrm{p}(\bar{\mathrm{p}})$):
  - at least 90 TPC clusters included in the Kalman filter fit [at least 80 clusters],
  - track tagged as hybrid track (less constrained than global track).

[9] Similarly to selection criteria discussed in this Chapter, the conditions applied in Pb-Pb collisions are shown by default, while the ones applied in p-Pb collisions are indicated in brackets (if differ).

- Particle identification of charged hadrons (varied for $\pi^{\pm}$, $K^{\pm}$, and $p(\bar{p})$):
  - using n-sigma approach with the p_T-independent threshold $< 2\sigma$ [$< 3\sigma$],
  - using Bayesian approach with posterior probability above 90%.
- Reconstruction of K^0_S and $\Lambda(\bar{\Lambda})$:
  - at least 90 TPC clusters included in the Kalman filter fit,
  - ratio of crossed pad-rows to findable clusters in TPC $N_{\text{cross}}/N_{\text{find}} > 1$,
  - V^0 candidates pre-selected during online processing,
  - fiducial volume radius $r > 10$ cm [not varied in p-Pb],
  - fiducial volume radius $r > 1$ cm,
  - DCA to PV of both daughters $\text{DCA}_{\text{PV}} > 0.3$ cm,
  - DCA among the two daughters $\text{DCA}_{\text{daughters}} < 0.3$ cm [<0.75 cm]
  - cosine of pointing angle (not varied) [> 0.98 (K^0_S), > 0.997 (Λ)],
  - both daughters identified using TPC n-sigma method (not varied) [$n_\sigma^{\text{TPC}} < 3$],
  - $p_T > 0.2$ GeV/c for both daughters [not applied in p-Pb].

The summary of the total systematic uncertainty estimated is shown in Table 4.3 for illustration. The p_T-dependent systematic uncertainties for individual observables, event classes, ad particle species are presented in Appendix B.

Observable	%	$h^{\pm}$	$\pi^{\pm}$	$K^{\pm}$	$p(\bar{p})$	K^0_S	$\Lambda(\bar{\Lambda})$	ϕ
v_n (Pb-Pb)	0-10	1-2	2-9	4-6	3-15	8-11	7-20	13
	10-20	1	1-5	2-6	2-6	6	5-8	4
	20-30	1	1-5	1-6	2-6	3	3-5	3
	30-40	1	1-7	1-5	2-6	3	2-5	3
	40-50	1-2	1-6	1-6	2-4	7-10	2-3	4
	50-60	1-3	1-4	2-9	2-11	14-20	4-11	18
$v_{n,mk}$ (Pb-Pb)	0-5	-	-	-	-	10	4	-
	5-10					10	6	-
	10-20					11	8	5
	20-30					9	7	7
	30-40					9	5	6
	40-50					9	4	6
v_n (p-Pb)	0-20	2-13	3-13	5-15	5-12	9	9-10	9-12
	20-40	2-15	3-15	6-16	6-13	10	9-11	9-13
	40-60	2-18	3-18	7-19	8-16	14-15	14	11-14

TABLE 4.3: Overview of relative systematic uncertainties for individual observables, event classes, and particle species.

5 Results and discussion

5.1 Measurements of Pb-Pb collisions

In this section, the measurements of 2- and 4-particle cumulant method with the Generic Framework (GF) in minimum-bias Pb-Pb collisions at $\sqrt{s_{\mathrm{NN}}} = 5.02$ TeV are presented for various event classes based on V0M centrality percentiles in an overall range of 0-60%. The identified species, as well as inclusive charged hadrons, are selected within the pseudo-rapidity acceptance of $|\eta| < 0.8$ (i.e. mid-rapidity)

The measurements are compared to the theoretical calculations of iEBE-VISHNU model [119]. This event-by-event variation connects 2+1D viscous hydrodynamics of VISH2+1 model with UrQMD hadronic cascade model [120]. In addition, two sets of initial conditions are used for characterising the specific shear (η/s) and bulk (ξ/s) viscosity over entropy density, described by either AMPT [121] or T$_{\mathrm{R}}$ENTo [122] parametrisation. While the former uses constant values of $\eta/s = 0.08$ and $\xi/s = 0$, the later utilises temperature-dependent ones. For both configurations, a switching hadronisation temperature $T_{\mathrm{sw}} = 148$ MeV and relaxation time $\tau_0 = 0.6$ fm/c extracted from global Bayesian analysis [123] are used.

5.1.1 v_2 coefficients with 2- and 4-particle cumulants

The first step in cumulant-based correlation measurement is the estimation of reference flow, as discussed in Section 2.2. The p_{T}-integrated results using RFPs within $0.2 < p_{\mathrm{T}} < 3$ GeV/c are shown in Fig. 5.1. In the plot on the right, the v_2 coefficients using 2- and 4-particle cumulants with and without various pseudo-rapidity separations in terms of $|\Delta\eta|$ are presented as a function of V0M centrality percentile.

There, a typical v_n ordering is present. As a pseudo-rapidity separation increases, starting with none (i.e. no sub-event splitting) up to $|\Delta\eta| > 0.8$, the v_2 values steadily decrease. Such behaviour demonstrates the suppression of non-flow contamination in 2-particle cumulant measurement discussed in Section 2.5. Furthermore, values obtained from 2-particle cumulants are significantly higher compared to those of 4-particle cumulant measurement. In addition, no significant difference is observed between $v_2\{4\}$ and $v_2\{4, |\Delta\eta| > 0\}$. Such observed consistency between measurement with and without $|\Delta\eta|$ supports the statement that 4-particle cumulant measurements are insensitive

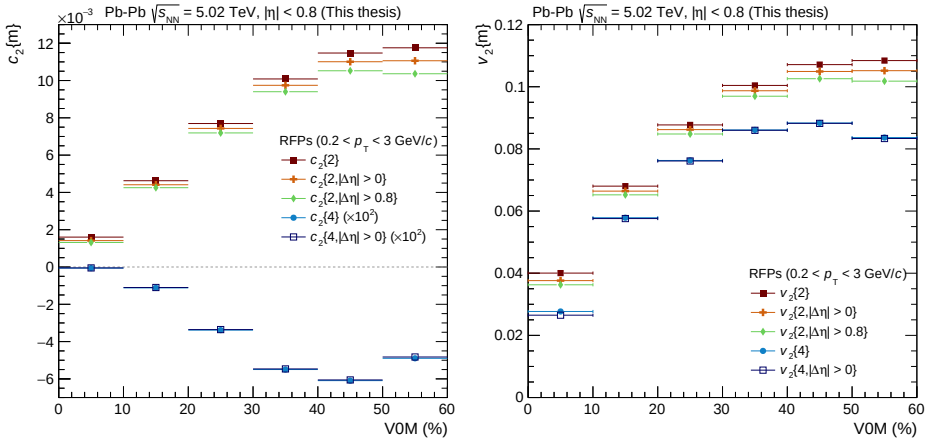

FIGURE 5.1: Measurement of $c_2\{m\}$ (left) and $v_2\{m\}$ (right) using 2- and 4-particle cumulants (with and without $|\Delta\eta|$) of RFPs within $0.2 < p_{\mathrm{T}} < 3$ GeV/c as a function of V0M percentile. Please note that $c_2\{4\}$ and $c_2\{4, |\Delta\eta| > 0\}$ are scaled by a factor of 10^2 for clarity.

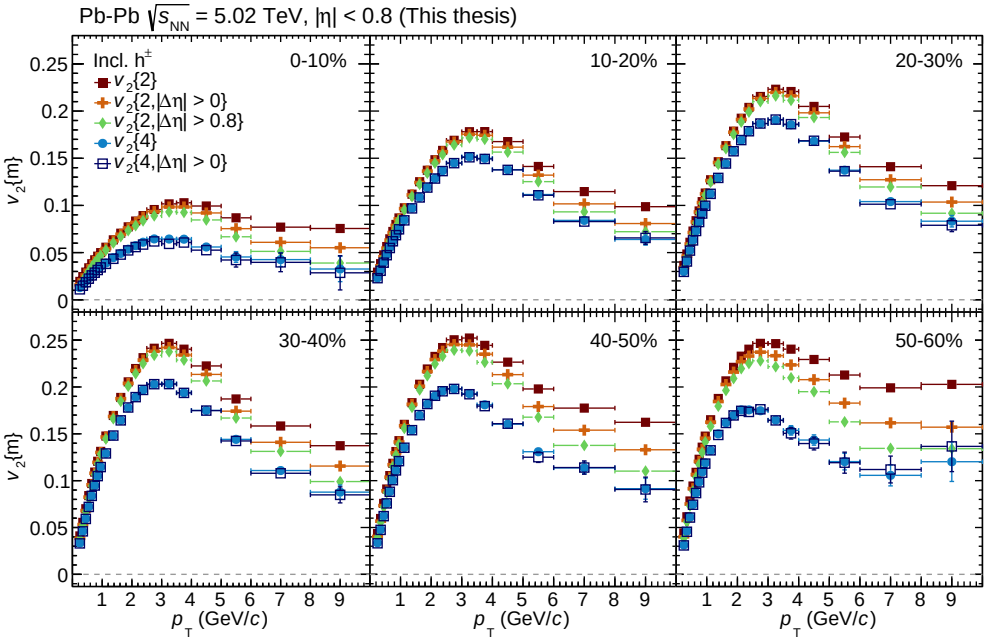

FIGURE 5.2: Measurement of p_{T}-differential v_2 of inclusive $\mathrm{h}^{\pm}$ using 2- and 4-particle cumulants (with and without $|\Delta\eta|$) for various centrality classes based on V0M percentile.

to the non-flow contribution in heavy-ion collisions, especially when compared to 2-particle cumulant. The observed difference between 4- and 2-particle cumulant (with $|\Delta\eta|$) is mainly attributed to the flow fluctuations as described in Section 2.3, which will be further examined in Section 5.1.3.

Another difference between the presented measurements lays in their centrality dependence. While values of $v_2\{2\}$ and $v_2\{2|\Delta\eta| > 0\}$ monotonically increase with increasing centrality percentiles, the values of 2-particle cumulants with considerably larger $|\Delta\eta|$ tends to saturate within 40-50% centrality bin. Such behaviour is driven by the initial eccentricity of the overlapping region, which is small in central collisions and increases with increasing centrality. In more peripheral collisions, the v_2 decreases as the number of interaction is small to fully transfer the initial eccentricity into final-state particle anisotropy. The same trend is observed for $v_2\{4\}$ values, even though the decrease is much more pronounced.

For completeness, the corresponding reference cumulants c_2 are presented in the left plot of Fig. 5.1. Please note that the values of c_2 using 4-particle cumulants are scaled for clarity. It should be pointed out that contrary to 2-particle cumulants, $c_n\{4\}$ values are negative across the whole investigated centrality range. Since this allows extraction of real (i.e. non-imaginary) values of v_n coefficients as expressed by (2.16), it often serves as an indication of collective behaviour present in the system. For more information about this topic, please refer to a study of collectivity investigation across various collision systems described in detail in [65].

Moving from the reference flow, a similar measurement of v_2 as a function of p_{T} of inclusive charged hadrons using 2- and 4-particle cumulants with various sub-event configurations are presented in Fig. 5.2 for individual centrality classes. Besides the features already observed in the case of reference measurements, the p_{T}-differential v_2 coefficient also exhibits the following p_{T} evolution. At first, the v_2 values rapidly increase with increasing p_{T}. Then it reaches a maximum around 3 GeV/c (also referred to as "the peak" in the following). Afterwards, it slowly decreases in a high-p_{T} region.

Considering the sensitivity to non-flow, the difference between 2- and 4-particle cumulants is increasing with increasing p_{T} until it reaches the peak v_2 value where it seems to be pronounced the most. Furthermore, the pseudo-rapidity separation dependence of $v_2\{2\}$ is relatively weak up to this point. On the other hand, the deviation between various $v_2\{2, |\Delta\eta|\}$ is more apparent for $p_{\mathrm{T}} > 3$ GeV/c. In this intermediate p_{T} region, the difference between 2- and 4-particle results becomes smaller as the η-separation increases. Based on such behaviour, the v_2 measurement with the largest separation available, i.e. $v_2\{2, |\Delta\eta| > 0.8\}$, is considered as the least affected by non-flow contamination. Consequently, only $v_2\{2, |\Delta\eta| > 0.8\}$ measurement is presented together with $v_2\{4\}$ for the comparison and the following discussion.

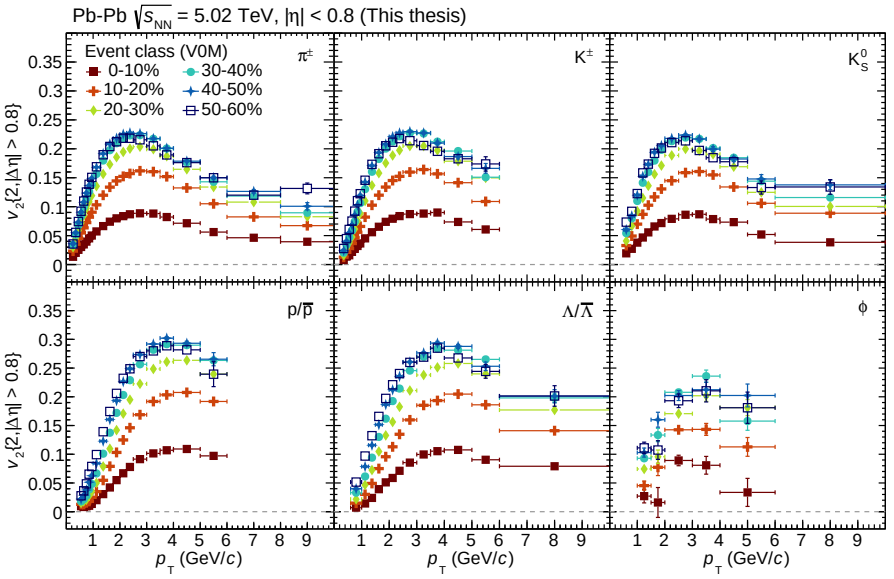

FIGURE 5.3: Measurement of $v_2\{2, |\Delta\eta| > 0.8\}$ of $\pi^{\pm}$, $K^{\pm}$, K^0_S, $p(\bar{p})$, $\Lambda(\bar{\Lambda})$, and ϕ as a function of p_T for various centrality classes based on V0M percentile.

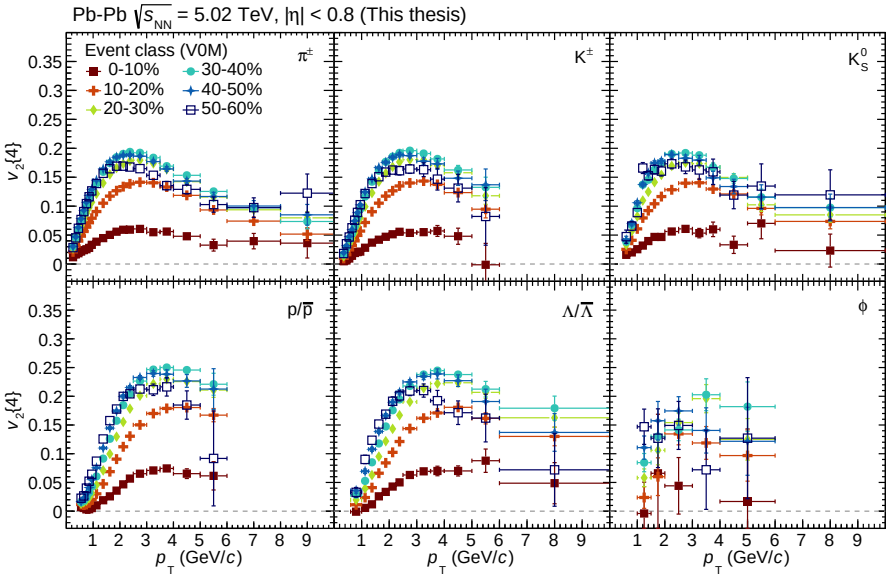

FIGURE 5.4: Measurement of $v_2\{4\}$ of $\pi^{\pm}$, $K^{\pm}$, K^0_S, $p(\bar{p})$, $\Lambda(\bar{\Lambda})$, and ϕ as a function of p_T for various centrality classes based on V0M percentile.

Shifting the focus towards identified species, the results of p_{T}-differential v_2 coefficients of $\pi^{\pm}$, $\mathrm{K}^{\pm}$, $\mathrm{K}^0_{\mathrm{S}}$, $\mathrm{p}(\bar{\mathrm{p}})$, $\Lambda(\bar{\Lambda})$, and ϕ using 2-particle cumulants with $|\Delta\eta| > 0.8$, and 4-particle cumulants are presented in Fig. 5.3 and 5.4, respectively, for various event classes based on V0M centrality percentile. As can be seen from these figures, all considered particle species share very similar features with inclusive unidentified charged hadrons, i.e. centrality and p_{T} dependence.

The main advantage of studying the v_n coefficients using the identified species is the possibility to probe their mass dependence and subsequently get insights about collision dynamics as well as particle production from a unique perspective. One way how to achieve that is to compare the v_n of individual species (presented in sub-plots of Fig. 5.3 and 5.4) within the same event sample (or centrality class). Such comparison can be seen in Fig. 5.5 and 5.6 for p_{T}-differential $v_2\{2, |\Delta\eta| > 0.8\}$ and $v_2\{4\}$, respectively. Based on these figures, rather than being aligned to a single p_{T} value, a clear shifting in the position of the peak is apparent. This feature results in a somewhat non-trivial trend.

Firstly, in the low p_{T} region, an explicit mass ordering of v_2 coefficients is observed: as particle mass increases, v_2 decreases for a given p_{T} value. Alternatively, this can be described that more massive particle reaches the given v_2 value at higher momenta. Such push of v_2 values of heavier particle towards higher p_{T} is consistent with a picture of a medium expanding with a single velocity common for all particles in a radial direction (in the transverse plane). Simply speaking, as a medium is expanding, it carries the particles with it, and if the "drifting" velocity is the same, more massive particles "feel smaller kick". This clear mass ordering is therefore addressed to so-called radial flow [124, 125].

Secondly, as the peak v_2 value is reached at different p_{T} for various species, a crossing point among the corresponding datasets appears at $p_{\mathrm{T}} \approx 3$ GeV/c. In the region with p_{T} above the crossing point, v_2 of $\pi^{\pm}$, $\mathrm{K}^{\pm}$, $\mathrm{K}^0_{\mathrm{S}}$ and ϕ tends to be consistent among themselves forming a mesonic band. The same is observed for the studied baryons, i.e. $\mathrm{p}(\bar{\mathrm{p}})$ and $\Lambda(\bar{\Lambda})$, as well. In addition, v_2 of baryons are significantly higher than those of mesons.

At this point, the importance of ϕ role should be stressed out. Without the measurements of v_2 of ϕ, one might hypothetically argue that the peak occurs at higher p_{T} as particle mass increases. Therefore, the observed splitting is yet another manifestation related to various masses. However, even though the precision of ϕ is limited compared to other species, it tends to follow other mesons while having a mass close to $\Lambda(\bar{\Lambda})$ and $\mathrm{p}(\bar{\mathrm{p}})$. Consequently, such apparent splitting is likely not related to the mass of the particle but preferably its composition, and it is commonly associated with parton coalescence or recombination mechanism of hadron production [126, 127].

Both measurements are compared to iEBE-VISHNU calculations to constrain the theoretical model and subsequently learn more about the initial conditions as well as QGP

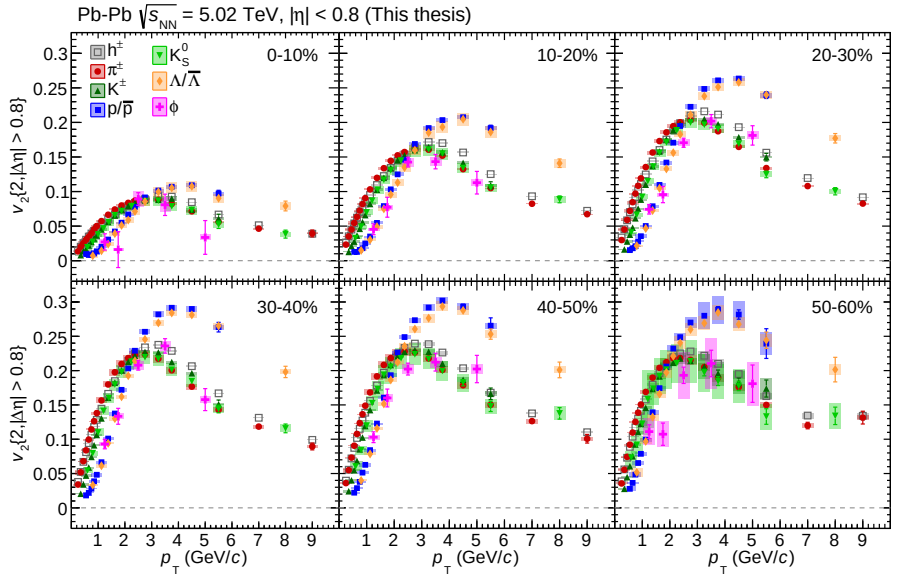

FIGURE 5.5: Comparison of p_T-differential $v_2\{2, |\Delta\eta| > 0.8\}$ of $h^{\pm}$, $\pi^{\pm}$, $K^{\pm}$, K^0_S, $p(\bar{p})$, $\Lambda(\bar{\Lambda})$, and ϕ within individual V0M centrality classes.

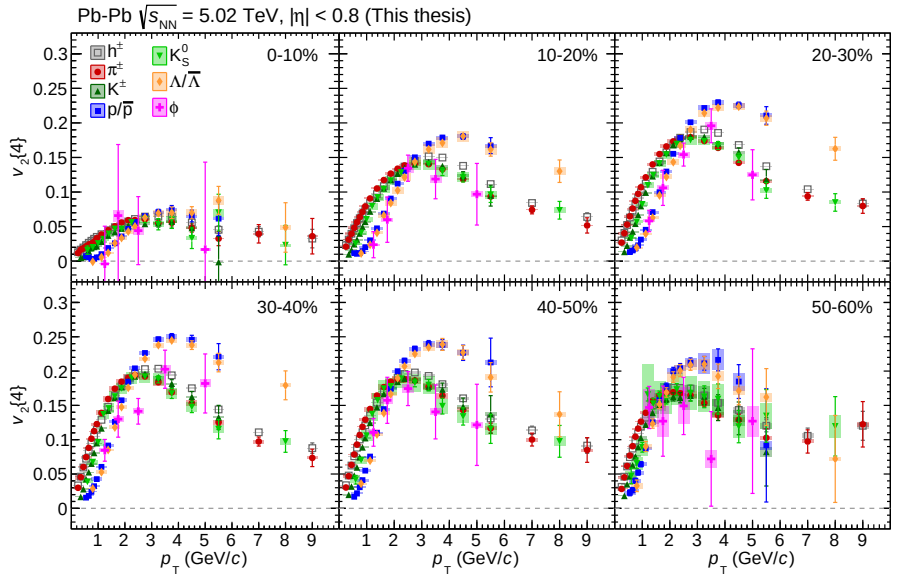

FIGURE 5.6: Comparison of p_T-differential $v_2\{4\}$ of $h^{\pm}$, $\pi^{\pm}$, $K^{\pm}$, K^0_S, $p(\bar{p})$, $\Lambda(\bar{\Lambda})$, and ϕ within individual V0M centrality classes.

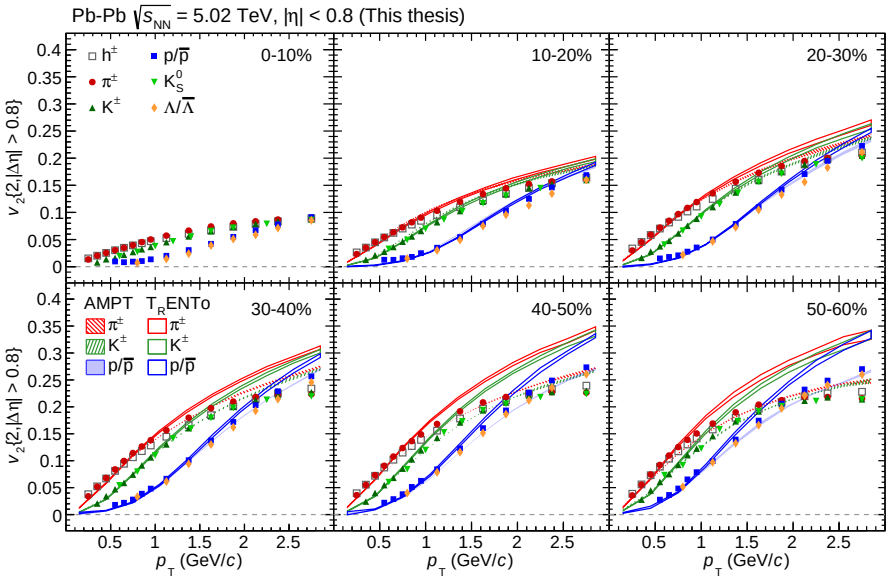

FIGURE 5.7: Comparison of p_T-differential $v_2\{2, |\Delta\eta| > 0.8\}$ measurement (low p_T zoom-in of Fig. 5.5) with iEBE-VISHNU calculations using AMPT and T$_R$ENTo initial conditions.

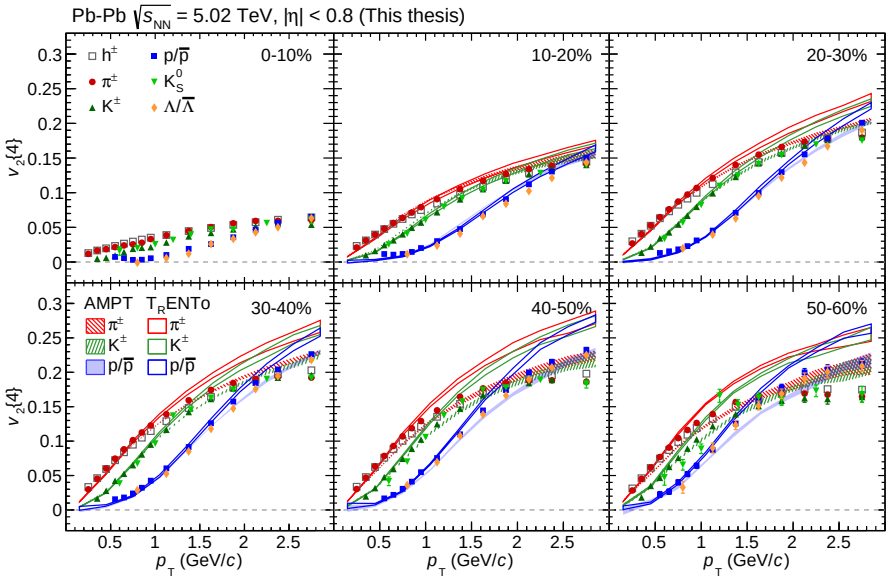

FIGURE 5.8: Comparison of p_T-differential $v_2\{4\}$ measurement (low p_T zoom-in of Fig. 5.6) with iEBE-VISHNU calculations using AMPT and T$_R$ENTo initial conditions.

properties. The results of both AMPT and T$_{\mathrm{R}}$ENTo initial conditions for $\pi^{\pm}$, K$^{\pm}$, and p($\bar{\mathrm{p}}$) are shown in Fig. 5.7 and 5.8 for 2- and 4-particle cumulant, respectively. For clarity, the p_{T} range of the measurements is matched with those provided by theoretical calculation. As can be seen from the Figures, both parameterisations are in good agreement with the measurements, even though AMPT reproduce the data more accurately. Specifically, AMPT quantitatively describes all three species, except for $p_{\mathrm{T}} > 2$ GeV/c where it slightly overestimates $\pi^{\pm}$and K$^{\pm}$. On the other hand, T$_{\mathrm{R}}$ENTo start to deviate from the measurement in a slightly lower p_{T} around $1 - 1.5$ GeV/c in the case of $\pi^{\pm}$and K$^{\pm}$, and also for p($\bar{\mathrm{p}}$) at a slightly higher p_{T}. Towards the upper limit of the studied region, it overestimates the experimental results significantly, especially in peripheral collisions. Based on this comparison, the measurement seems to favour the constant value of η/s (and $\xi/s = 0$) while the temperature dependence might play a role for very soft particles.

5.1.2 Scaling properties

To further study and quantify the scaling properties of p_{T}-differential v_n measurements, a so-called Number of Constituent Quark (NCQ) scaling introduced in [128] is performed. In this exercise, both measured v_n and p_{T} are scaled by a corresponding number of valence (constituent) quarks, n_q, i.e. two for mesons or three in the case of baryons.

The examination of NCQ scaling is presented in Fig. 5.9 and 5.10 for $v_2\{2, |\Delta\eta| > 0.8\}$ and $v_2\{4\}$, respectively. Although the difference between the magnitudes of baryons and mesons is small, the slitting between the two groups is still apparent for both $v_2\{2, |\Delta\eta| > 0.8\}$ and $v_2\{4\}$. Therefore, the observed scaling is only approximate across whole studied range of p_{T}. Such observation is in agreement with previous ALICE results obtained for 2-particle correlation using Scalar Product (SP) method [118, 38] as well as earlier measurements at RHIC [128, 129].

It was proposed later in [130] that instead of scaling p_{T} directly, one can express the x-axis in terms of transverse kinetic energy KE_{T}, given by

$$KE_{\mathrm{T}} \equiv m_{\mathrm{T}} - m_0 = \sqrt{p_{\mathrm{T}}^2 + m_0^2} - m_0, \tag{5.1}$$

to remove a potential mass effect. Using such a representation, the v_2 measurements at RHIC form a single line common for both hadron types [130, 131]. However, PHENIX [132] later reported a deviation from this universal scaling.

At the LHC energies, even after applying KE_{T}, the reported scaling is still only approximate if any at all [118, 38]. The same conclusions hold for the measurement using 2- and 4-particle cumulants obtained in this analysis, as shown in Fig. 5.11 and 5.12, respectively.

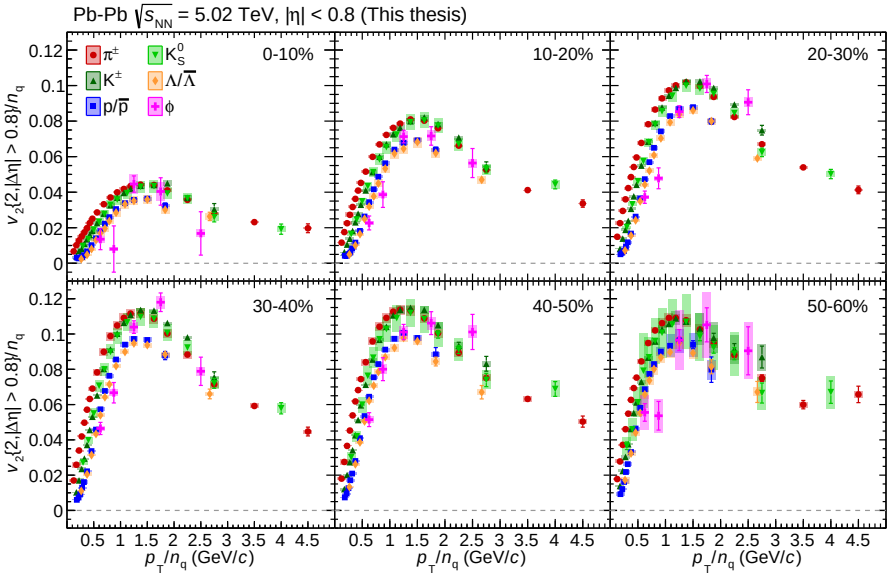

FIGURE 5.9: Measurement of $v_2\{2, |\Delta\eta| > 0.8\}$ scaled by number of valence quarks n_q of $\pi^{\pm}$, $K^{\pm}$, K^0_S, $p(\bar{p})$, $\Lambda(\bar{\Lambda})$, and ϕ as a function of p_T/n_q in various V0M centrality classes.

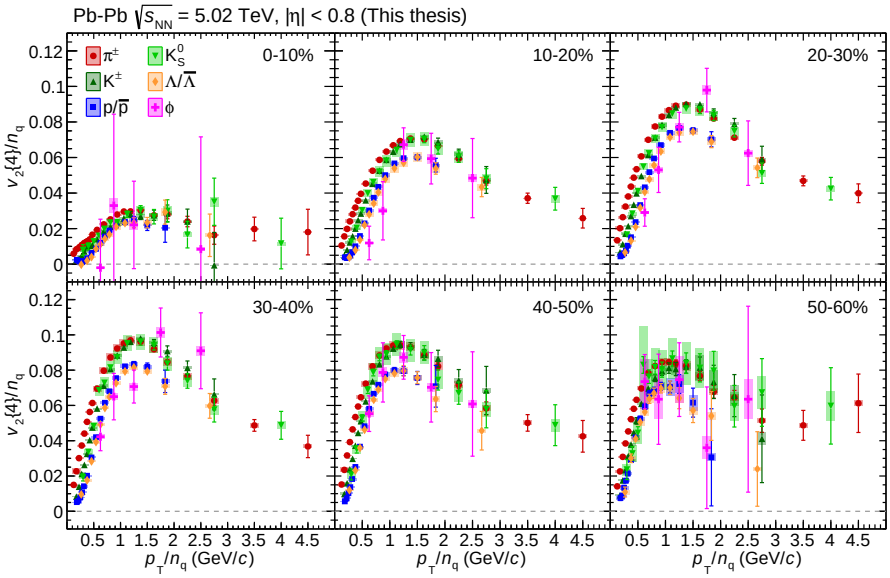

FIGURE 5.10: Measurement of $v_2\{4\}$ scaled by number of valence quarks n_q of $\pi^{\pm}$, $K^{\pm}$, K^0_S, $p(\bar{p})$, $\Lambda(\bar{\Lambda})$, and ϕ as a function of p_T/n_q in various V0M centrality classes.

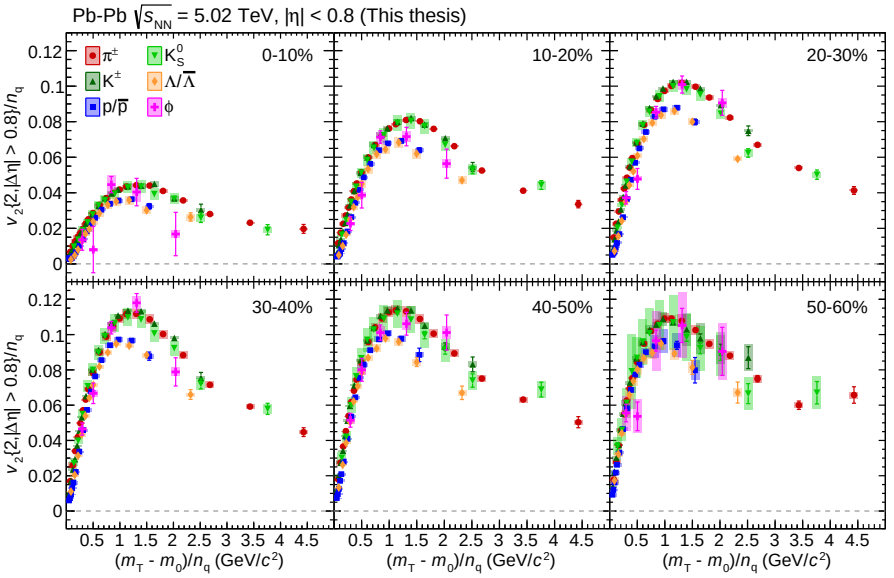

FIGURE 5.11: Measurement of $v_2\{2, |\Delta\eta| > 0.8\}$ scaled by number of valence quarks n_q of $\pi^{\pm}$, $K^{\pm}$, K^0_S, p($\bar{p}$), $\Lambda(\bar{\Lambda})$, and ϕ as a function of KE_T/n_q in various V0M centrality classes.

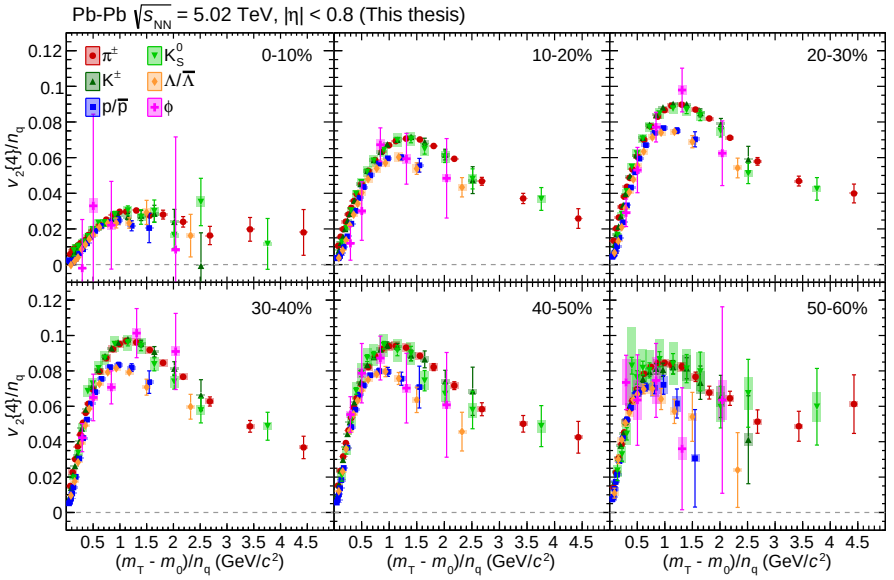

FIGURE 5.12: Measurement of $v_2\{4\}$ scaled by number of valence quarks n_q of $\pi^{\pm}$, $K^{\pm}$, K^0_S, p($\bar{p}$), $\Lambda(\bar{\Lambda})$, and ϕ as a function of KE_T/n_q within individual V0M centrality classes.

5.1.3 v_2 fluctuations

With access to both 2- and 4-particle cumulant measurement presented in this thesis, the effect of flow fluctuations can be investigated as described in Section 2.3. Please mind that both cumulants are assumed to be non-flow free in order to extract the related quantities properly. While $v_n\{4\}$ is insensitive to non-flow contamination by construction, it is not the case for the presented $v_n\{2\}$. The reported $v_2\{2, |\Delta\eta| > 0.8\}$ is used in this study as $|\Delta\eta| > 0.8$ is sufficiently large enough to suppress significant portion of non-flow. Consequently, the results presented in this Section might be potentially biased by residual non-flow.

The measurement of v_2 fluctuations, denoted by σ_2, and the $\langle v_2 \rangle$ magnitudes as a function of p_T for both inclusive charged hadrons and identified species in various centrality classes is presented in Fig. 5.14 and 5.15, respectively. Since these quantities are determined as either a sum or a difference of $v_2\{2\}$ and $v_2\{4\}$, they both exhibits generally very similar p_T and centrality dependence as discussed earlier in this Chapter.

A relative elliptic flow fluctuation $F(v_2)$ is determined as a simple ratio of σ_2 and $\langle v_2 \rangle$ to quantify better and compare the level of fluctuations. The results of this exercise are shown in Fig. 5.13, together with iEBE-VISHNU calculations for $\pi^{\pm}$, $K^{\pm}$, and $p(\bar{p})$. As

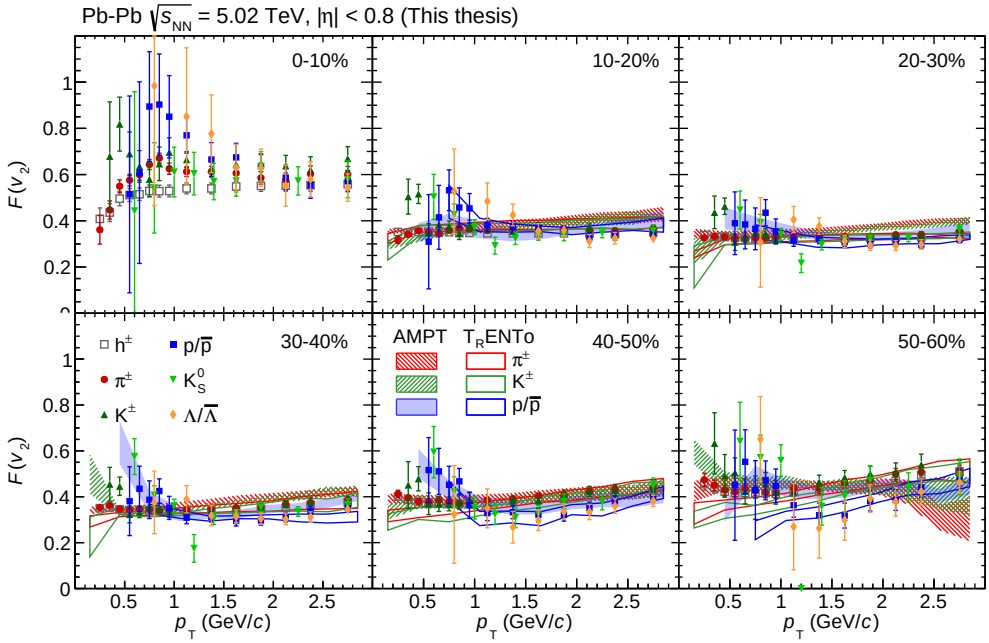

FIGURE 5.13: Relative elliptic flow fluctuations $F(v_2)$ of $h^{\pm}$, $\pi^{\pm}$, $K^{\pm}$, K^0_S, $p(\bar{p})$, and $\Lambda(\bar{\Lambda})$ as a function of p_T for various V0M centrality classes.

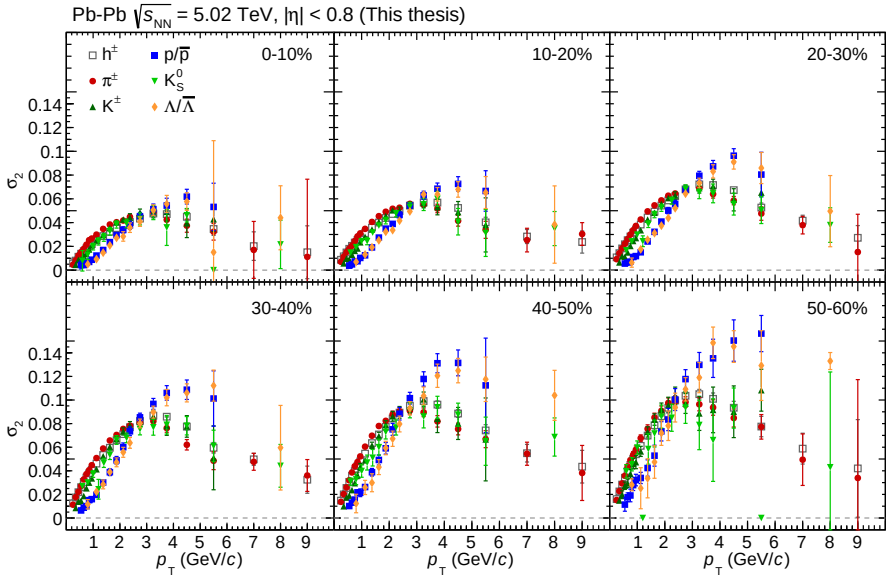

FIGURE 5.14: Measurement of elliptic flow fluctuations σ_2 of $h^{\pm}$, $\pi^{\pm}$, $K^{\pm}$, K^0_S, $p(\bar{p})$, and $\Lambda(\bar{\Lambda})$ as a function of p_T for various V0M centrality classes.

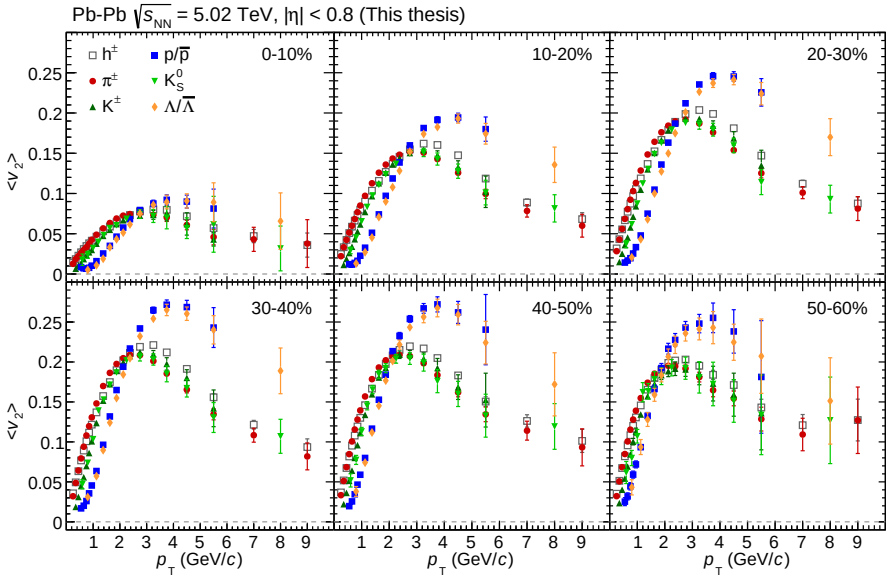

FIGURE 5.15: Magnitude of v_2 coefficients of $h^{\pm}$, $\pi^{\pm}$, $K^{\pm}$, K^0_S, $p(\bar{p})$, and $\Lambda(\bar{\Lambda})$ as a function of p_T for various V0M centrality classes.

can be seen from the Figure, all studied particle species are in a good agreement with each other. However, a hint of particle mass dependency emerges for $p_{\mathrm{T}} < 1$ GeV/c in 30-40%. Even though it seems to be present also in AMPT, due to the poor precision of the measurement as well as theoretical calculations, such observation is not conclusive.

Besides that, no significant p_{T}-dependence is present, except for most central collision where a slight decrease is present in $p_{\mathrm{T}} < 0.5$ GeV/c region. In terms of centrality evolution, the fluctuations are the largest in the most central 0-10% collisions, reaching a value of ≈ 0.6. This is consistent with the expectation since v_2 is driven by initial eccentricity, which is the smallest in such collisions as the overlapping region is almost perfectly circular. After a significant decrease, the fluctuations are constant with $F(v_2) \approx 0.4$ across semi-central collision, followed by a slight increase towards the peripheral 50-60% collisions.

5.1.4 Non-linear response

Besides studying the cumulants of v_n coefficients, the multi-particle correlation technique can be used for investigating even more intriguing aspects of azimuthal flow, such as non-linear flow mode. This observable quantifies the non-linear contribution of initial spatial anisotropies $\mathcal{E}_2$ and $\mathcal{E}_3$ to higher v_n harmonics ($n \geq 4$), as described in Section 2.4.

In the following, the p_{T}-differential non-linear flow modes $v_{4,22}$, $v_{5,32}$, and $v_{6,33}$ of identified $\pi^{\pm}$, $\mathrm{K}^{\pm}$, $\mathrm{K}^0_{\mathrm{S}}$, $\mathrm{p}(\bar{\mathrm{p}})$, $\Lambda(\bar{\Lambda})$, and ϕ in various V0M-based centrality classes in Pb-Pb collisions at $\sqrt{s_{\mathrm{NN}}} = 5.02$ TeV are presented. All measurements reported here are determined using the sub-event method with a pseudo-rapidity separation of $|\Delta\eta| > 0$ between the correlated particles. Note that only those centrality classes where the measurement can be performed with reasonable precision are presented.

It should be stressed out, that in this case of non-linear flow mode study presented in this section, my contributions consists of analysis of reconstructed species, namely $\mathrm{K}^0_{\mathrm{S}}$, $\Lambda(\bar{\Lambda})$, and ϕ, while results of $\pi^{\pm}$,$\mathrm{K}^{\pm}$, and $\mathrm{p}(\bar{\mathrm{p}})$ were obtained by my collaborator (main analyser and chair of the corresponding internal publication committee), Naghmeh Mohammadi.

Centrality dependence of all considered $v_{n,mk}\{|\Delta\eta| > 0\}(p_{\mathrm{T}})$ observables for individual species is presented in Fig 5.16. In the case of $v_{4,22}$ and $v_{5,32}$, the non-linear flow coefficients steeply increase with an increasing centrality starting at most-central collisions up to $\approx 30-40\%$. In more peripheral collisions, the $v_{n,mk}$ tends to decrease slightly. The $v_{6,33}$ tends to follow a similar behaviour, even though the observed centrality dependency seems less significant. Considering the p_{T}-dependency, the $v_{n,mk}$ increases with increasing p_{T}; then it reaches a maximum value at the intermediate region around $\approx 3-4$ GeV/c, depending on the particle species. However, the peak position shifts towards smaller p_{T} as the centrality percentile increases. Moreover, the magnitudes of

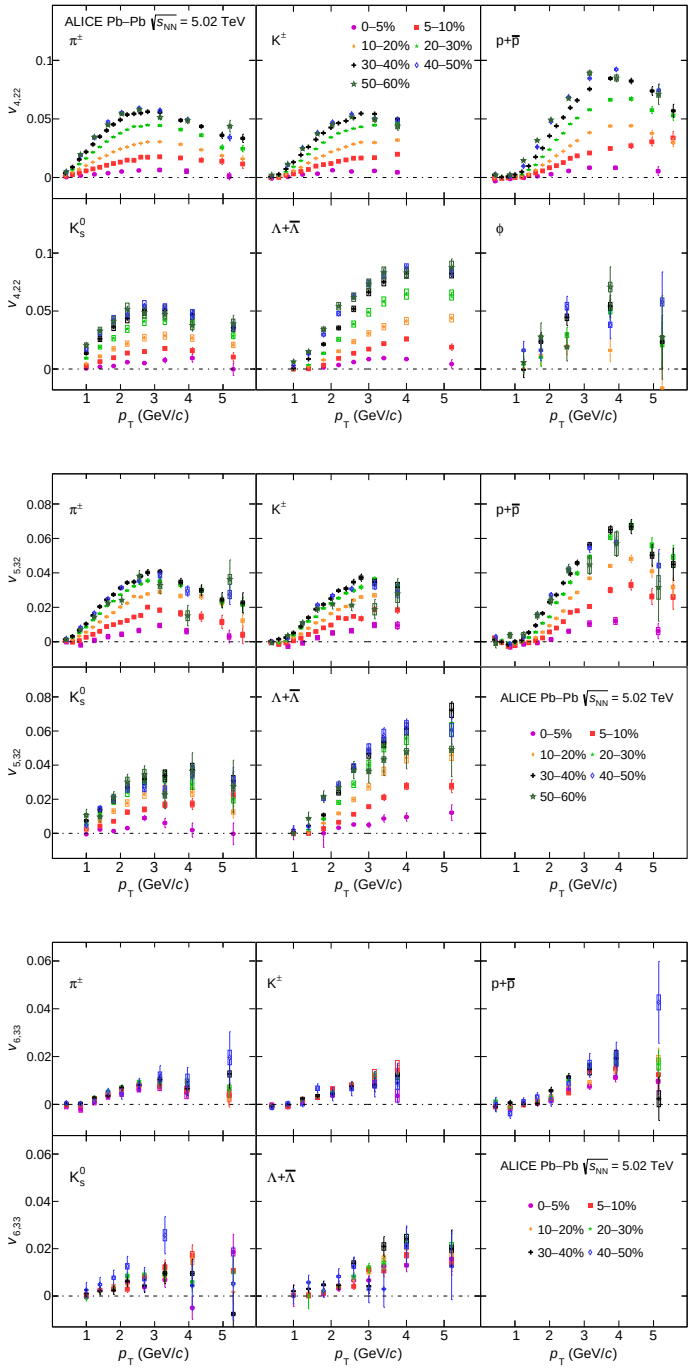

FIGURE 5.16: Centrality dependence of $v_{4,22}\{|\Delta\eta| > 0\}$ (top), $v_{5,32}\{|\Delta\eta| > 0\}$ (middle), and $v_{6,33}\{|\Delta\eta| > 0\}$ (bottom) of $\pi^{\pm}$, $K^{\pm}$, K^0_S, $p(\bar{p})$, $\Lambda(\bar{\Lambda})$, and ϕ as a function of p_T [133].

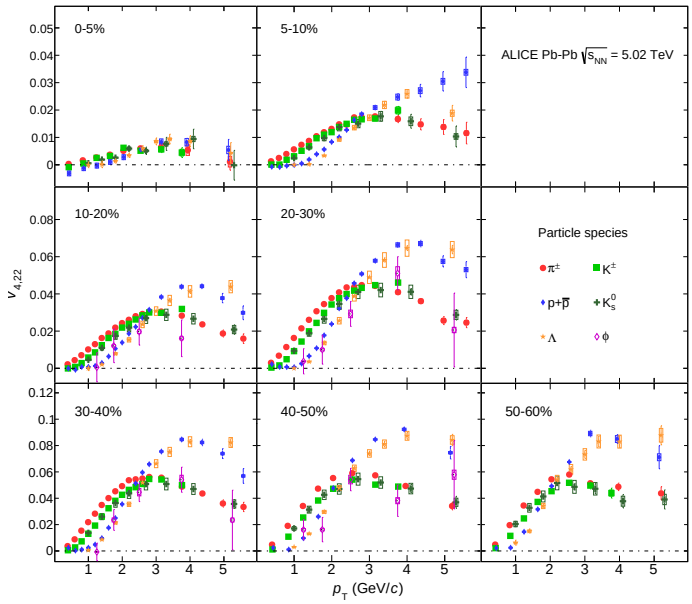

FIGURE 5.17: Measurement of p_T-differential $v_{4,22}\{|\Delta\eta| > 0\}$ of $\pi^{\pm}$, $K^{\pm}$, K^0_S, $p(\bar{p})$, $\Lambda(\bar{\Lambda})$, and ϕ in various V0M centrality classes [133].

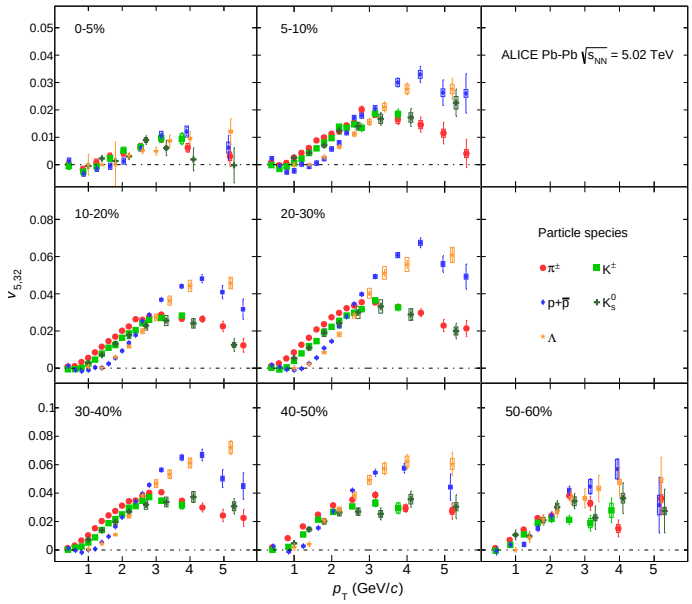

FIGURE 5.18: Measurement of p_T-differential $v_{5,32}\{|\Delta\eta| > 0\}$ of $\pi^{\pm}$, $K^{\pm}$, K^0_S, $p(\bar{p})$, $\Lambda(\bar{\Lambda})$, and ϕ in various V0M centrality classes [133].

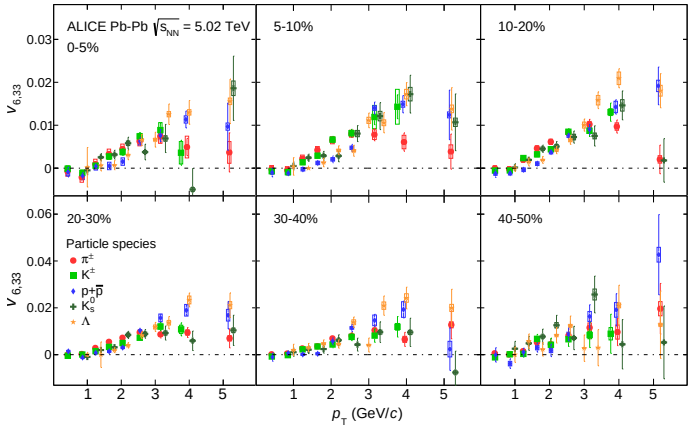

FIGURE 5.19: Measurement of p_{T}-differential $v_{6,33}\{|\Delta\eta| > 0\}$ of $\pi^{\pm}$, $\mathrm{K}^{\pm}$, $\mathrm{K}^0_{\mathrm{S}}$, $\mathrm{p}(\bar{\mathrm{p}})$, $\Lambda(\bar{\Lambda})$, and ϕ in various V0M centrality classes [133].

$v_{n,mk}$ coefficients exhibit a general $v_{4,22} < v_{5,32} < v_{6,33}$ ordering in the presented p_{T} range for all particle species.

In order to investigate the potential mass dependency, the results of $v_{4,22}$, $v_{5,32}$, and $v_{6,33}$ are plotted for all identified species together within individual centrality classes in Fig. 5.17, 5.18, and 5.19, respectively. As already seen in 2- and 4-particle cumulant measurements, both the mass ordering in low p_{T} region resulting into a crossing point of individual species at $p_{\mathrm{T}} \approx 2.5 - 3.5$ GeV/c, as well as a clear baryon/meson grouping, are apparent for all $v_{n,mk}$ coefficients. Although, it should be noted that the presence of mass ordering is less significant in the case of $v_{6,33}$, primarily due to its inedequate precision.

In order to investigate such features further, an investigation of scaling properties is performed following the study of v_n coefficients obtained with the cumulants. The n_q-scaled magnitudes of non-linear flow testing both NCQ and KE_{T} representations are shown in Fig. 5.20, 5.21, and 5.22 for $v_{4,22}$, $v_{5,32}$, and $v_{6,33}$, respectively. Based on these results, both NCQ and KE_{T} scaling of non-linear modes is only approximate within $\pm 20\%$ for $p_{\mathrm{T}} < 1$ GeV/c. Therefore, no obvious difference is observed for the non-linear and total contributions, as they are generally consistent.

In order to quantitatively compare the above-discussed features related to particle mass between standard (linear) v_n and non-linear $v_{n,mk}$ coefficients, the difference between $\pi^{\pm}$ and $\mathrm{p}(\bar{\mathrm{p}})$ results is investigated. The difference is normalised by corresponding reference (p_{T}-integrated) coefficients of inclusive charged hadrons to remove the discrepancy in different magnitudes of linear and non-linear contribution. The resulting measurement of such quantity is presented in Fig. 5.23, where $v_{4,22}$ measurement from

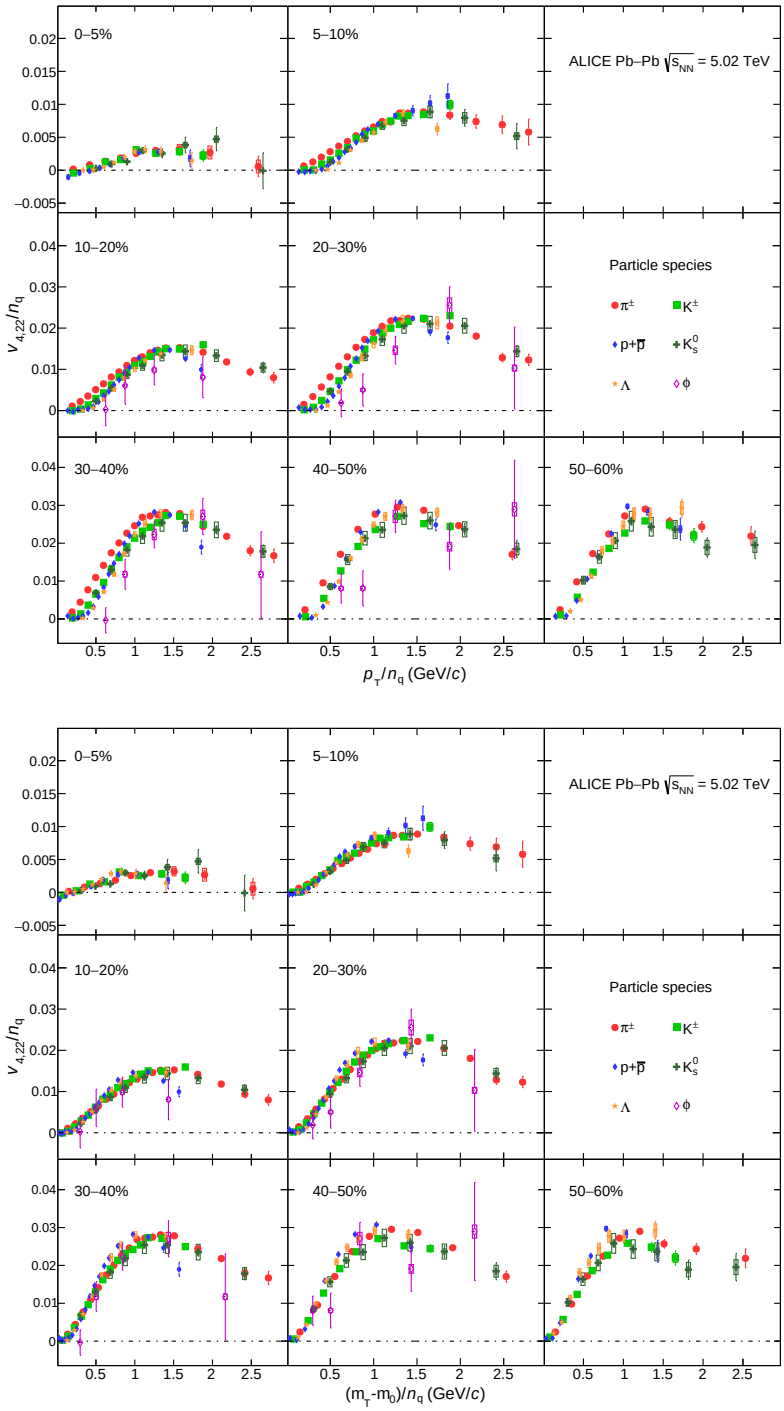

FIGURE 5.20: Measurement of $v_{4,22}\{|\Delta\eta| > 0\}$ scaled by number of valence quarks n_q of $\pi^{\pm}$, $K^{\pm}$, K^0_S, $p(\bar{p})$, $\Lambda(\bar{\Lambda})$, and ϕ as a function of p_T/n_q (top) and $(m_T - m_0)/n_q$ (bottom) in various V0M centrality classes [133].

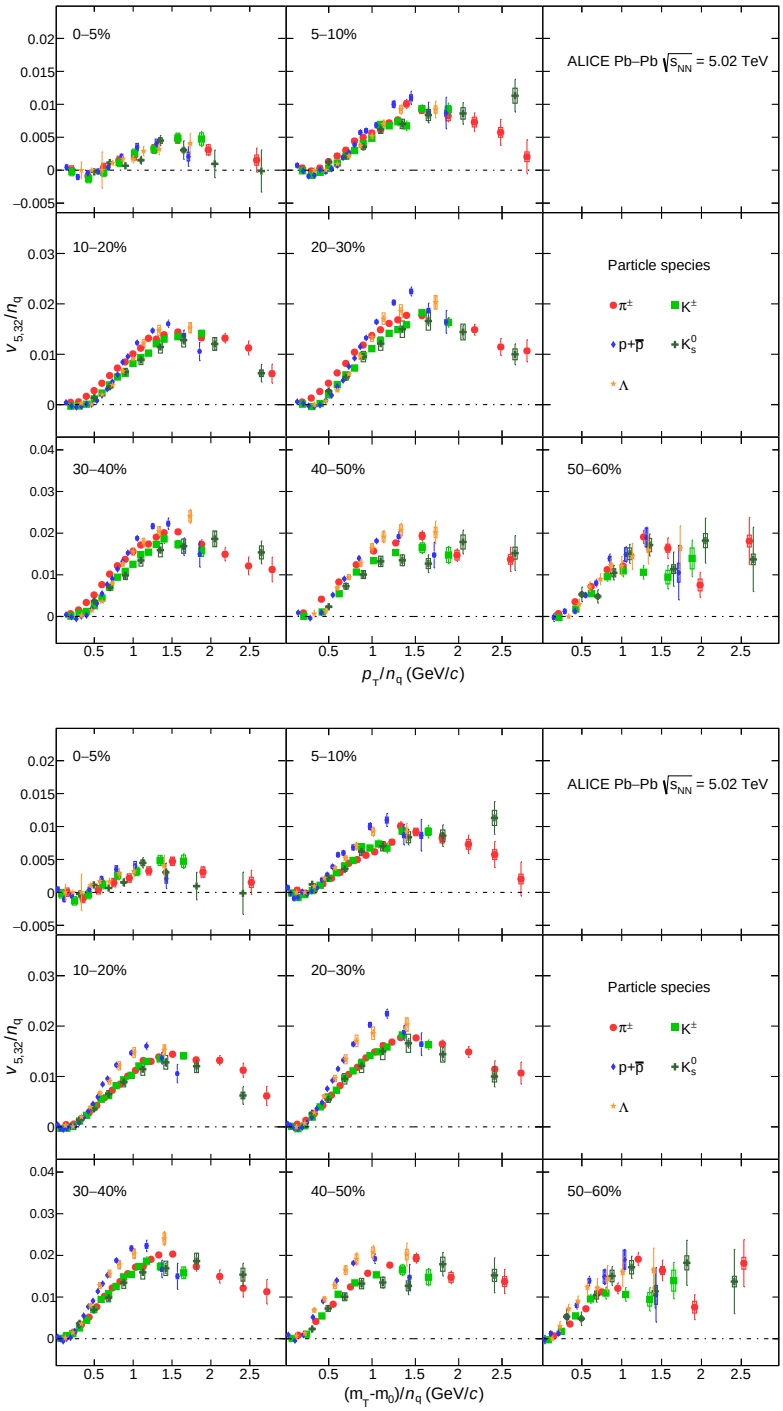

FIGURE 5.21: Measurement of $v_{5,32}\{|\Delta\eta| > 0\}$ scaled by number of valence quarks n_q of $\pi^{\pm}$, $K^{\pm}$, K^0_S, $p(\bar{p})$, $\Lambda(\bar{\Lambda})$, and ϕ as a function of p_T/n_q (top) and $(m_T - m_0)/n_q$ (bottom) in various V0M centrality classes [133].

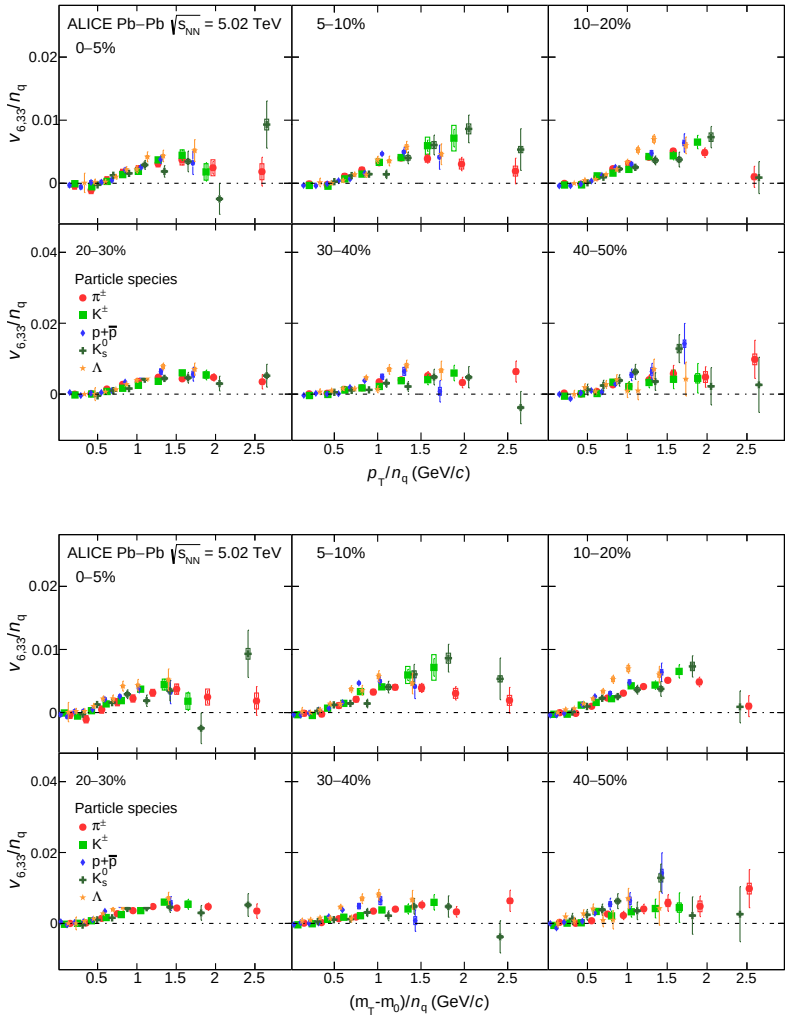

FIGURE 5.22: Measurement of $v_{6,33}\{|\Delta\eta| > 0\}$ scaled by number of valence quarks n_q of $\pi^{\pm}$, $K^{\pm}$, K^0_S, $p(\bar{p})$, $\Lambda(\bar{\Lambda})$, and ϕ as a function of p_T/n_q (top) and $(m_T - m_0)/n_q$ (bottom) in various V0M centrality classes [133].

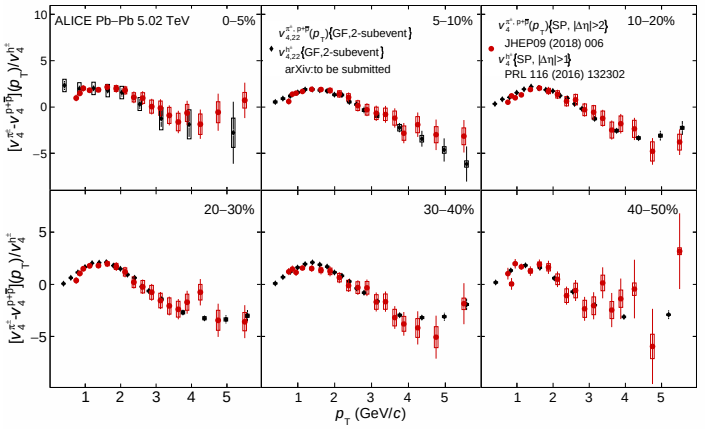

FIGURE 5.23: Difference between v_4 magnitude of $\pi^{\pm}$ and $\mathrm{p}(\bar{\mathrm{p}})$ normalised by corresponding reference flow in linear and non-linear contribution as a function of particle p_{T} [133].

this analysis is compared to p_{T}-differential v_4 coefficients from 2-particle correlations utilising SP method with separation of $|\Delta\eta| > 1$ from recent ALICE publications [36, 38].

Judging by this comparison, no significant difference is observed between linear and non-linear component in the region of $p_{\mathrm{T}} < 3 - 4$ GeV/c where the mass ordering takes place. Concerning the intermediate region of $p_{\mathrm{T}} > 3$ GeV/c, both measurements are in a good agreement (given their precision) indicating that potential quark coalescence similarly affects both observables.

Finally, the comparisons of $v_{n,mk}$ measurement and iEBE-VISHNU calculation are presented in Fig. 5.24, 5.25, and 5.26 for $v_{4,22}$, $v_{5,32}$, and $v_{6,33}$, respectively. For clarity, the comparisons of $\pi^{\pm}$, $\mathrm{K}^{\pm}$, $\mathrm{p}(\bar{\mathrm{p}})$, and $\mathrm{K}^0_{\mathrm{S}}$ and $\Lambda(\bar{\Lambda})$ are plotted separately. As can be seen, the difference between individual measurements and calculations varies widely depending on particle species, considered p_{T} range, as well as centrality class. Even though, both parameterisations achieve a fair agreement for $p_{\mathrm{T}} < 1$ GeV/c, AMPT is reproducing the measurements more accurately, especially at higher p_{T} region, where T$_{\mathrm{R}}$ENTo overestimates them significantly. Although, it should be noted that in this region, even AMPT shows a slight deviation from the measurement.

In summary, the non-linear flow modes $v_{n,mk}$ of identified particles exhibit very similar behaviour with the total v_n counterparts. Not only in terms of centrality and p_{T}

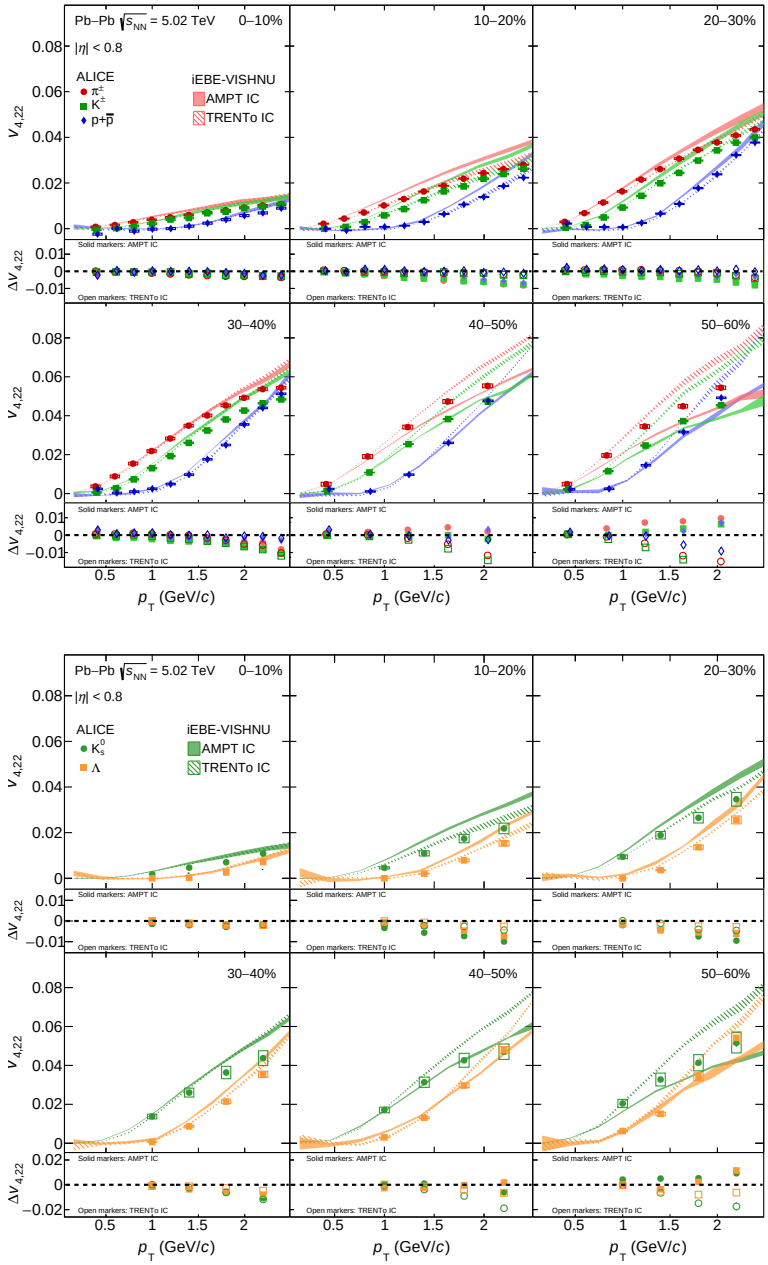

FIGURE 5.24: Comparison of p_T-differential $v_{4,22}$ measurement and iEBE-VISHNU calculation using AMPT and T$_R$ENTo initial conditions for identified $\pi^{\pm}$, $K^{\pm}$, and $p(\bar{p})$ (top) and K^0_S and $\Lambda(\bar{\Lambda})$ (bottom) [133].

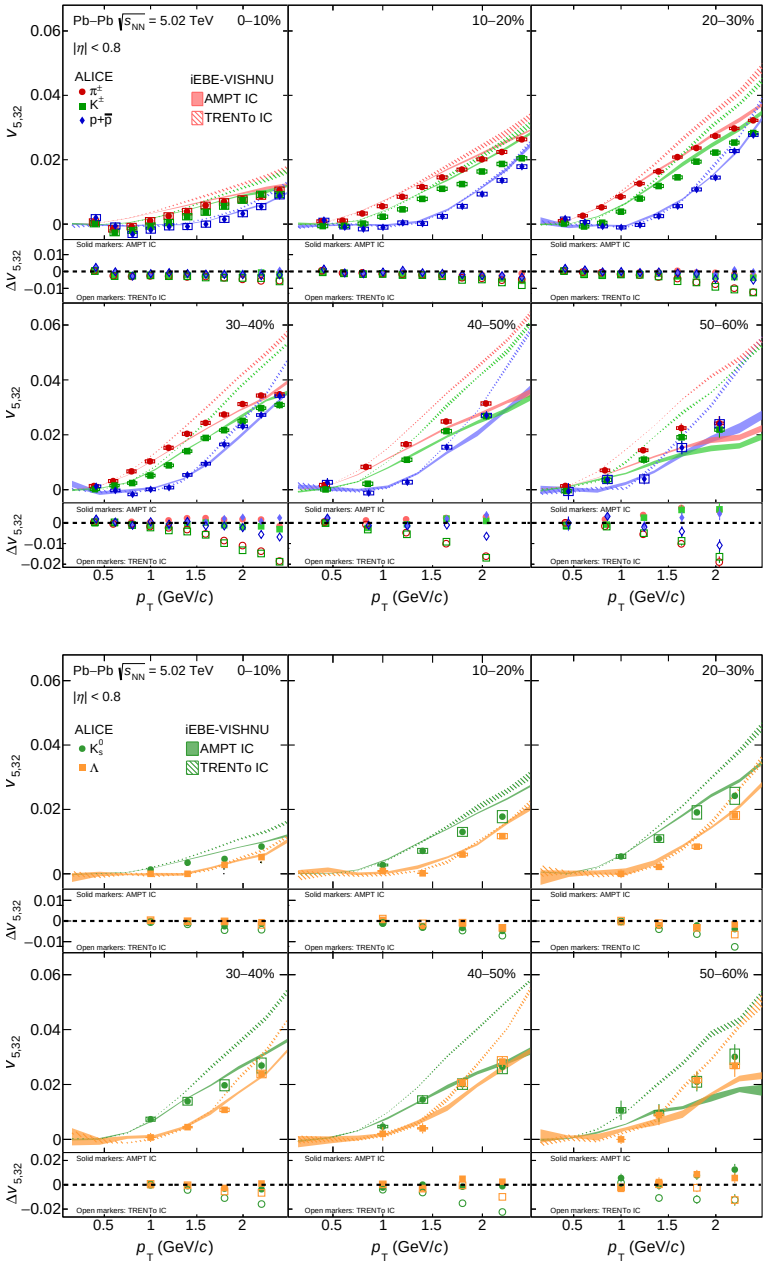

FIGURE 5.25: Comparison of p_{T}-differential $v_{5,32}$ measurement and iEBE-VISHNU calculation using AMPT and T$_{\mathrm{R}}$ENTo initial conditions for identified $\pi^{\pm}$, $\mathrm{K}^{\pm}$, and $\mathrm{p}(\bar{\mathrm{p}})$ (top) and $\mathrm{K}^0_{\mathrm{S}}$ and $\Lambda(\bar{\Lambda})$ (bottom) [133].

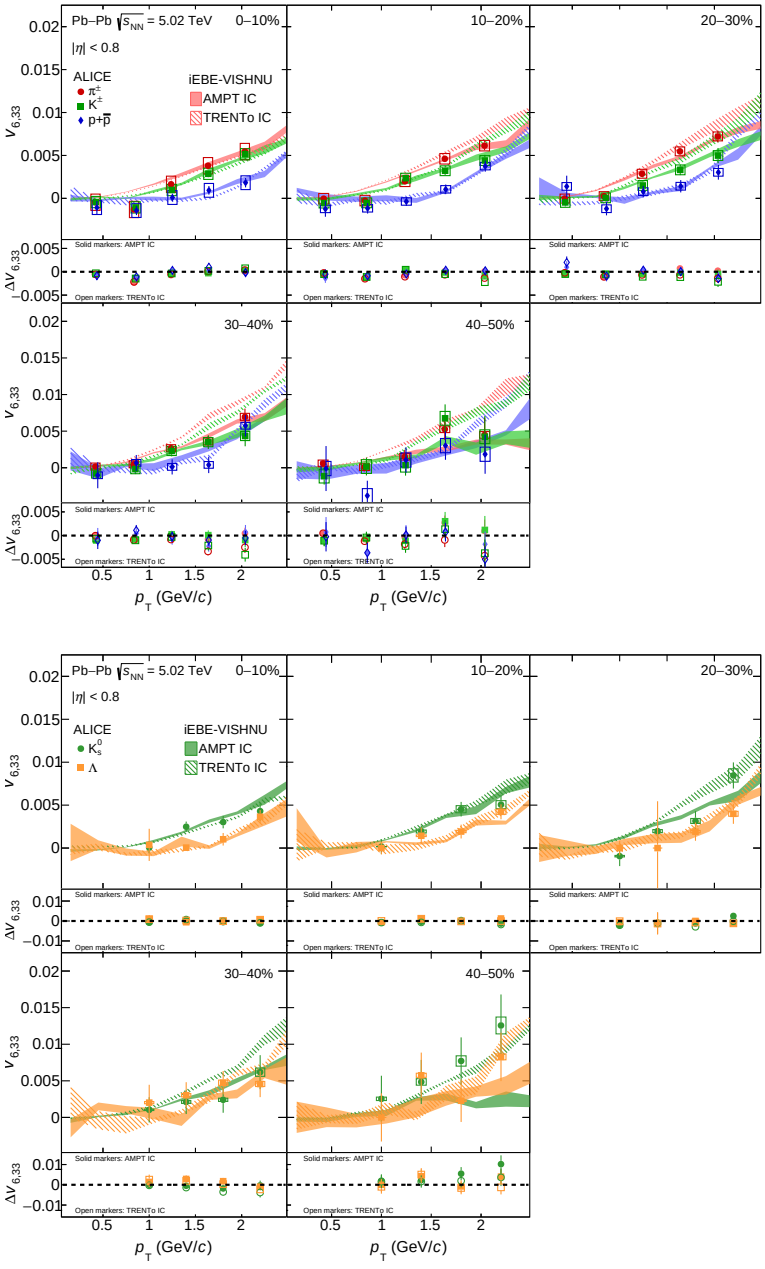

FIGURE 5.26: Comparison of p_T-differential $v_{6,33}$ measurement and iEBE-VISHNU calculation using AMPT and T$_R$ENTo initial conditions for identified $\pi^{\pm}$, $K^{\pm}$, and $p(\bar{p})$ (top) and K^0_S and $\Lambda(\bar{\Lambda})$ (bottom) [133].

dependence but also regarding the unique mass-related features, i.e. a clear mass ordering and significant baryon/meson grouping effect. This is supported by the test of the scaling properties with NCQ or KE_{T}. Considering the comparison among reported measurements and theoretical calculations as provided by iEBE-VISHNU hybrid model, neither of the currently available parametrisation is capable of precise quantitative description. Therefore, further effort is needed to include non-linear flow measurement while tuning the model parameters.

5.2 Measurements of p-Pb collisions

The measurement of p_{T}-differential v_2 coefficients in p-Pb collisions at a centre-of-mass energy of $\sqrt{s_{\mathrm{NN}}} = 5.02$ TeV separated into various event classes based on multiplicity percentiles provided by V0A detector are presented in this section. Similarly to the measurement in Pb-Pb collisions discussed in previous Section 5.1, the correlation analysis is conducted using the 2-particle cumulant method with GF implementation. Both the inclusive charged hadrons as well as the identified $\pi^{\pm}$, $\mathrm{K}^{\pm}$, $\mathrm{K}^0_{\mathrm{S}}$, $\mathrm{p}(\bar{\mathrm{p}})$, $\Lambda(\bar{\Lambda})$, and ϕ are selected in the consistent pseudorapidity window of $|\eta| < 0.8$.

Note that whilst being more accurately related to multiplicity, the event classes characterised by V0A percentiles are referred to as "centrality classes" (e.g. 0-20% most central collisions) throughout the text as well denoting the same property (sometimes interchangeably). The motivation for that is twofold. Firstly, the percentiles are determined in a similar fashion as in Pb-Pb case (though only using one of the two V0 arrays) where such term is commonly used. Secondly, to prevent potential confusion with a specially pre-selected collisions using (high-)multiplicity-based triggers (unless explicitly stated otherwise) as opposed to minimum-bias collisions reported here.

In contrast to heavy-ion collision, a formation of QGP-like medium is not expected in the case of small collision systems. Although, as discussed in Section 1.4, the results of various measurements of high-multiplicity p-Pb and pp collisions reported across all LHC experiments exhibit very similar features as those present in Pb-Pb collisions. Most notably the presence of long-range multi-particle collectivity. However, in the absence of expanding medium driving the rise of anisotropic flow, the non-flow is the dominating source of correlations biasing the extracted v_n coefficients in small collision systems. Consequently, a careful treatment in suppressing the non-flow contamination is essential to reduce the effects of such bias effectively.

To illustrate that, the measurement of p_{T}-differential $v_2\{2, |\Delta\eta| > 0.8\}$ coefficients[1] in 0-20% most-central p-Pb collisions is shown in Fig. 5.27. Besides the inclusive charged

[1] Please note that the label v_2^{unsub} is explicitly stated to stress out that no further subtraction of non-flow was done besides the pseudorapidy separation between the correlated particles.

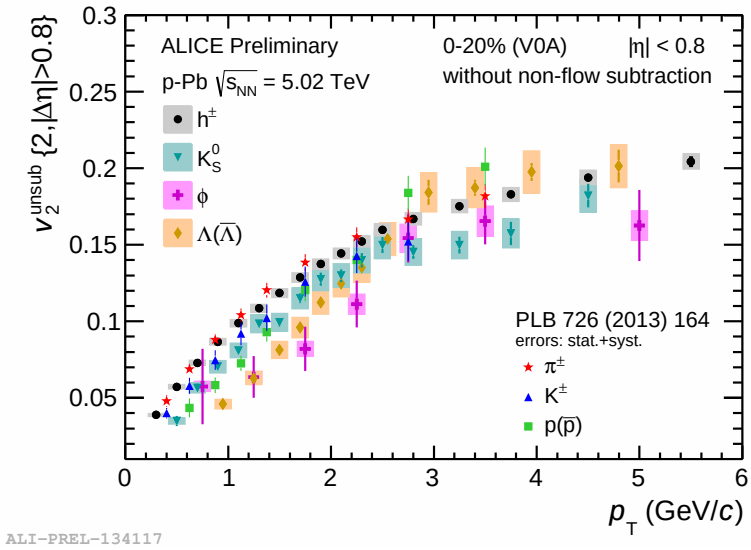

FIGURE 5.27: Measurement of p_T-differential $v_2\{|\Delta\eta| > 0.8\}$ of $h^{\pm}$, K^0_S, $\Lambda(\bar{\Lambda})$, and ϕ in 0-20% event class based on V0A percentile. In addition, earlier results of $\pi^{\pm}$, $K^{\pm}$, and $p(\bar{p})$ reported in [66] are included.

hadrons, the v_2 of K^0_S, $\Lambda(\bar{\Lambda})$ and ϕ is measured for the very first time in p-Pb collisions. In addition, this analysis extends the previous results of $\pi^{\pm}$, $K^{\pm}$, and $p(\bar{p})$ using 2-particle correlation with SP measured during the LHC Run 1 data-taking campaign. Due to the improved precision provided by larger data sample as well as by including additional particle species, a mass ordering at low p_T is observed, which is similar to what was reported in Pb-Pb collision at the same collision energy (see Fig. 5.5). In addition, a hint of particle type grouping is also present in a similar region of $p_T > 3$ GeV/c where the v_2 of both $p(\bar{p})$and $\Lambda(\bar{\Lambda})$ baryons are larger than that of K^0_S mesons.

However, looking at the measurement of inclusive $h^{\pm}$, the v_2 coefficient steadily increases even in the high-p_T region. Such an observation typically serves as a manifestation of a significant presence of non-flow contamination. Instead, a decrease of v_n is expected in this region [36]. Hence, this demonstrates that a simple two sub-event method, despite a relatively large separation of $|\Delta\eta| > 0.8$, is not enough to sufficiently suppress the non-flow contribution. Instead, a more sophisticated method such as non-flow subtraction (described in Section 2.5.2) is needed.

Besides the presence of significant non-flow contamination, a concern was raised, during the internal discussion, regarding the potential bias caused by the sensitivity of

the correlation technique to the multiplicity fluctuations. Therefore, this will be discussed in the following section before proceeding forward with the non-flow subtraction.

5.2.1 Study of sensitivity to multiplicity fluctuations

As discussed in Section 2.2, the cumulants are calculated from event-averaged correlations, $\langle\langle m \rangle\rangle$ as expressed by (2.9). These are obtained by averaging single-event correlations, $\langle m \rangle_e$, over many events within a specific collision class. Such event class is typically represented by intervals of centrality (or multiplicity) percentiles as described in Section 3.3.3. However, within each class, the number of measured particles (i.e. event multiplicity) is typically not fixed, but it varies from one collision to another.

One can imagine, that the precision (or the "quality") of the single-event correlation depends on the number of particles within single collision as it is estimated as an average over available correlation pairs (tuples), as can be seen in (2.7) for 2-particle correlation.

If the multiplicity fluctuations are small within the event class, the spread of the single-event correlations is narrow. Therefore, resulting $\langle\langle m \rangle\rangle$, obtained from such similar values provides a better estimate for average correlation than in case of large fluctuations as those values might have a wider spread. Simply speaking, mixing event with significantly different multiplicities may introduce bias into measured cumulants and subsequently even v_n coefficients. This is especially important for p-Pb and pp collisions, where the multiplicity fluctuations are relatively large compared to the overall event multiplicity.

In order to evaluate the sensitivity to the multiplicity fluctuations and the related potential bias, the following study is performed using inclusive charged hadrons in a sub-sample of p-Pb collisions. The p_{T}-differential v_2 coefficients are calculated using 2-particle correlations (with the sub-event method) utilising three different approaches related to event multiplicity. Specifically, the approaches differ in the presence (or absence) of particle and event weights when estimating the single-event correlation, $\langle m \rangle_e$, or event-averaged correlation, $\langle\langle m \rangle\rangle$, respectively, as follows[2]:

(A) standard approach for cumulants (as described in Section 2.2):

$$\langle 2 \rangle_e = \frac{(M-2)!}{M!} \sum_{i,j=1}^{M} e^{\mathrm{i}n(\varphi_i - \varphi_j)} \quad (i \neq j),$$

$$\langle\langle 2 \rangle\rangle \equiv \frac{\sum_{e=1}^{N} W_e^{\langle 2 \rangle} \langle 2 \rangle_e}{\sum_{e=1}^{N} W_e^{\langle 2 \rangle}},$$

[2]Note, that the approaches are illustrated here only for the reference correlations, but they are applied for differential correlations as well.

(B) same as (A), but all events are treated equally, i.e. $W_e^{\langle 2 \rangle} = 1 \ \ (\forall e)$,

(C) same as (B), but no weights are used for single-event correlations[3]:

$$\langle 2 \rangle_e = \sum_{i,j=1}^{M} e^{\mathrm{i}n(\varphi_i - \varphi_j)}, \ \ (i \neq j).$$

For a subset of p-Pb collisions corresponding to the 0-20% event class, the event-averaged correlations are calculated. However, the values are stored in multiplicity bins with variable bin width, in contrast to the standard procedure described in Section 2.2. Specifically, multiplicity bins of 1, 5, 10, 30, 50, 75 particles are used, in addition to the results integrated over the whole available multiplicity range. Therefore, each multiplicity bin represents a sample of collision with similar multiplicity (which spread is given by the bin width).

In the case of unit bins (width of 1), the event-averaged correlations are obtained from a sample of collisions with an identical number of particles. Therefore, in such a case, there are no multiplicity fluctuations permitted. As the bin width increases, the averaging over different multiplicities occurs, providing a ground for multiplicity fluctuations. Naively, the most significant effect is expected in a case of the widest bin covering whole available multiplicity range (which is typically reported as a representative of a given event class as illustrated by the results in Fig. 5.27).

Afterwards, the values from individual bins of a given binning are averaged, and the resulting p_{T}-differential v_2 is calculated. Finally, the results obtained using various bin width are compared in the form of a ratio with respect to the results from unit bins representing the un-biased measurement. This is done for each approach separately.

The results of this study are shown in Fig. 5.28 presenting the result of the p_{T}-differential $v_2\{2\}$ coefficients. The approach (A), i.e. standard cumulant-based correlation measurement, which is used throughout this thesis, is insensitive to the multiplicity fluctuations as it does not exhibit any significant dependence on the bin width. In case of the approach (B), in which all events are weighted equally independently of their multiplicity, a deviation at the level of $\approx 3\%$ is observed. However, the largest discrepancy reaching up to $\approx 13\%$ is present in the case of approach (C), in which no weights are used for both single-event and event-averaged correlations. In addition, a naively expected dependency is apparent as the level deviation grows with the increasing bin width. Even though the v_2 values obtained from bin width 5 and 10 seems to be smaller than the results from unit bins. This might be caused by the contribution of events with no particle

[3]This approach is motivated by a 2-particle correlation method called Scalar Product (SP) method [134, 135]. However, it should be noted, that the actual implementation of SP might differ from the approach used for the purpose of this study.

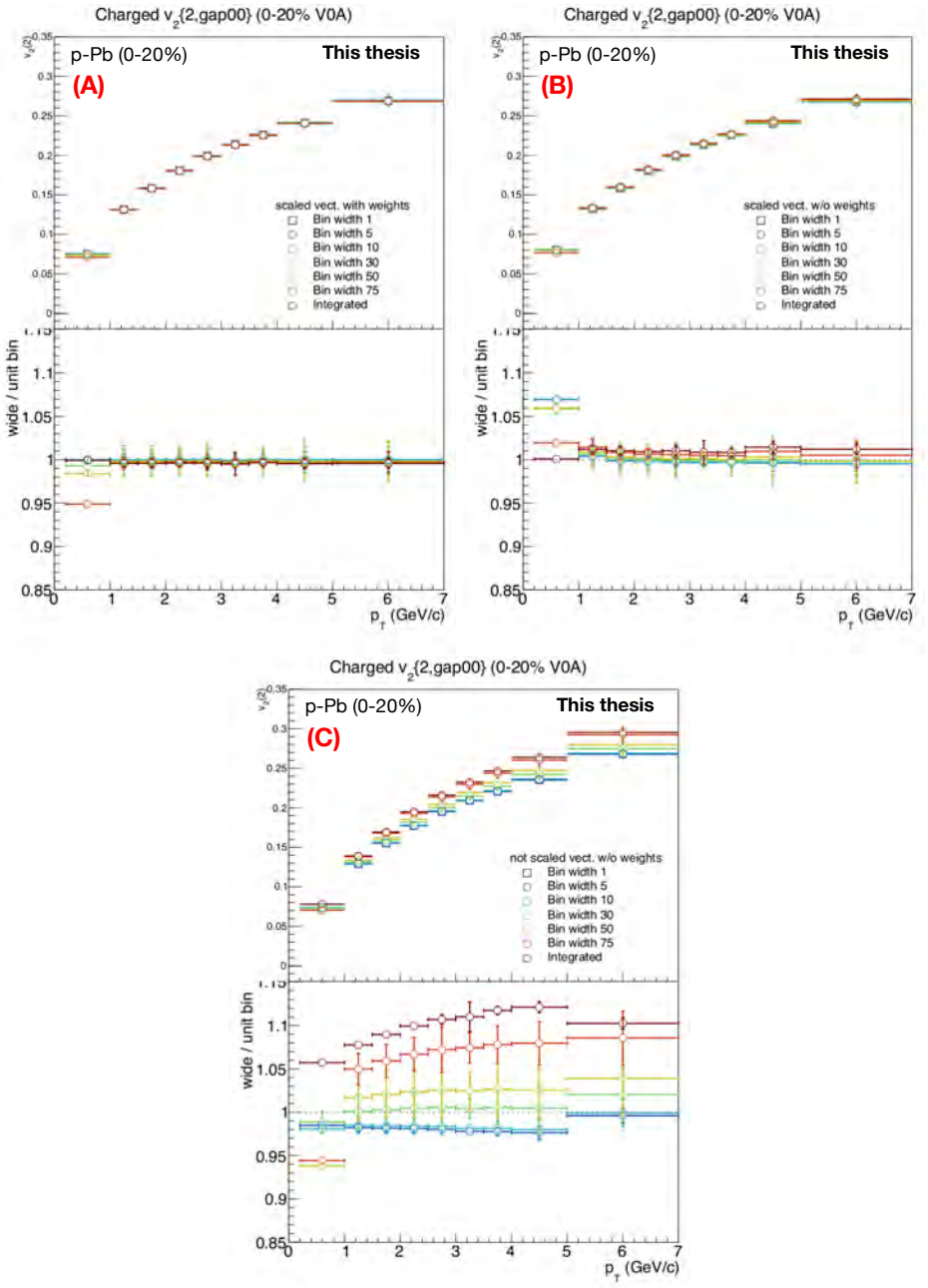

FIGURE 5.28: The measurements of $v_2\{2\}(p_{\mathrm{T}})$ of $h^{\pm}$ in 0-20% most central p-Pb collisions estimated in multiplicity bins with various widths (open circles) are shown (upper sub-plot) together with the ratios wrt. unit bin (open squares) results (lower sub-plot) for approach A (left), B (right), and C (bottom). See the text for details.

within the given p_{T} interval, which are typically excluded when the weights are used for $\langle m \rangle$.

Finally, the same exercise was performed in a case of the $v_2\{2, |\Delta\eta| > 0.8\}$ (see Fig. A.1 in Appendix A). When comparing the measurements with and without the η separation, no significant difference is observed, besides the generally higher values of v_n coefficients enhanced by the non-flow with smaller $|\Delta\eta|$. This indicates that bias arising from multiplicity fluctuations is not affected by the presence of the non-flow.

5.2.2 Non-flow subtraction using cumulants

When using cumulants in small collision systems, there is no well-established recipe commonly used for the non-flow subtraction. In fact, many aspects related to the procedure incorporated in this thesis represent a pioneering endeavour in this context.

Initially inspired by the angular correlation method, discussed in Section 2.5.2, the resulting v_n coefficients (after the non-flow subtraction is performed on the cumulant level as described above) can be expressed as follows:

$$v_n\{2\}^{\mathrm{sub}}(p_{\mathrm{T}}) \equiv \frac{d_n\{2\}^{\mathrm{sub}}}{\sqrt{c_n\{2\}^{\mathrm{sub}}}} = \frac{d_n\{2\} - k \cdot d_n\{2\}^{\mathrm{base}}}{\sqrt{c_n\{2\} - k \cdot c_n\{2\}^{\mathrm{base}}}}. \tag{5.2}$$

In this relation similar to (2.25), $d_n\{2\}$ and $c_n\{2\}$ are standard cumulants measured before the subtraction while $d_n\{2\}^{\mathrm{base}}$ and $c_n\{2\}^{\mathrm{base}}$ denote the cumulants obtained from a suitable sample representing the proxy of non-flow contribution discussed in the following section.

Based on the expectation that the non-flow approximately scales inversely with the number of correlated particles [135], the scaling factor k is present in (5.3) to account for different system sizes. It is given by

$$k = \frac{\langle M \rangle^{\mathrm{base}}}{\langle M \rangle}, \tag{5.3}$$

where the $\langle M \rangle$ denotes an average number of RFPs per event in the corresponding sample.

5.2.3 Study of various non-flow estimates

Before the subtraction can be applied, an initial study of various non-flow estimates summarised in this section was required before going to the actual subtraction. Correlation measurements obtained in the following collision types were selected as suitable candidates for the non-flow proxy based on a collection of previous studies where the

subtraction method was used (either in different collision systems or by using different correlation technique):

(A) peripheral p-Pb collisions (used in [66] as discussed in Section 2.5.2),

(B) integrated minimum-bias pp collisions (motivated by a measurement in Pb-Pb collisions [136]),

(C) pp collisions of similar event class as p-Pb.

It should be pointed out, that even though all three candidates are tested and discussed, (A) and (B) are the primary contenders. While (C) is motivated by subtracting correlations in events with a similar level of activity in terms of the number of produced particles, while the physics assumption is rather naive.

The dependence of subtracted v_n coefficients on η separation between the two correlated particles is tested to quantify the outcome of the subtraction procedure using above-listed estimates. This is motivated by the expectation, that if the correlation measurement is free of the non-flow contamination, the results should be insensitive to the imposed η separation. Moreover, the p_{T} behaviour of v_n is considered based on the empirical observation in heavy-ion collisions. There, after reaching a peak magnitude at $p_{\mathrm{T}} \approx 3 - 4$ GeV/c, v_n values slowly decrease as hard processes start to dominate over the soft production.

In this study, the representative subsets of the corresponding p-Pb and pp data samples, listed in Tab. 4.1, are analysed. To ensure the overall consistency, both p-Pb baseline as well as non-flow proxies, are analysed in exactly the same way as described in Chapter 4. Then, the subtraction is performed on the level of cumulants (which will be described specifically in the following section) expressed by (5.2) in Section 2.5.2 for each proxy. The results of this study are summarised in Fig. 5.29 showing p_{T}-differential $v_2\{2\}^{\mathrm{sub}}$ measurements with $|\Delta\eta|$ of 0, 0.2, and 0.8 in the various event classes.

Starting with method (A): peripheral p-Pb subtraction (top row of Fig. 5.29), the results after the subtraction are clearly dependent on the applied η separation. The value of $v_2\{2\}^{\mathrm{sub}}$ decreases with increasing $|\Delta\eta|$ imposed. Especially in the high-p_{T} region, where the dependency is more pronounced. Consequently, peripheral p-Pb collisions do not seem to provide a reliable non-flow estimate.

For the methods (B) and (C), the performance of the subtraction procedure using pp collisions looks much better, as the dependency on $|\Delta\eta|$ is less significant in the high-p_{T} region, compared to method (A). It also allows applying a smaller η separation, reducing the corresponding losses of correlated pairs and thus improving the statistical precision. However, a slightly reversed hierarchy is observed in the range of $1 < p_{\mathrm{T}} < 3$ GeV/c for 0-20% multiplicity class. When comparing the pp results, both using minimum-bias (B) and the same-event-class sample (C) are very similar. Although the difference lays

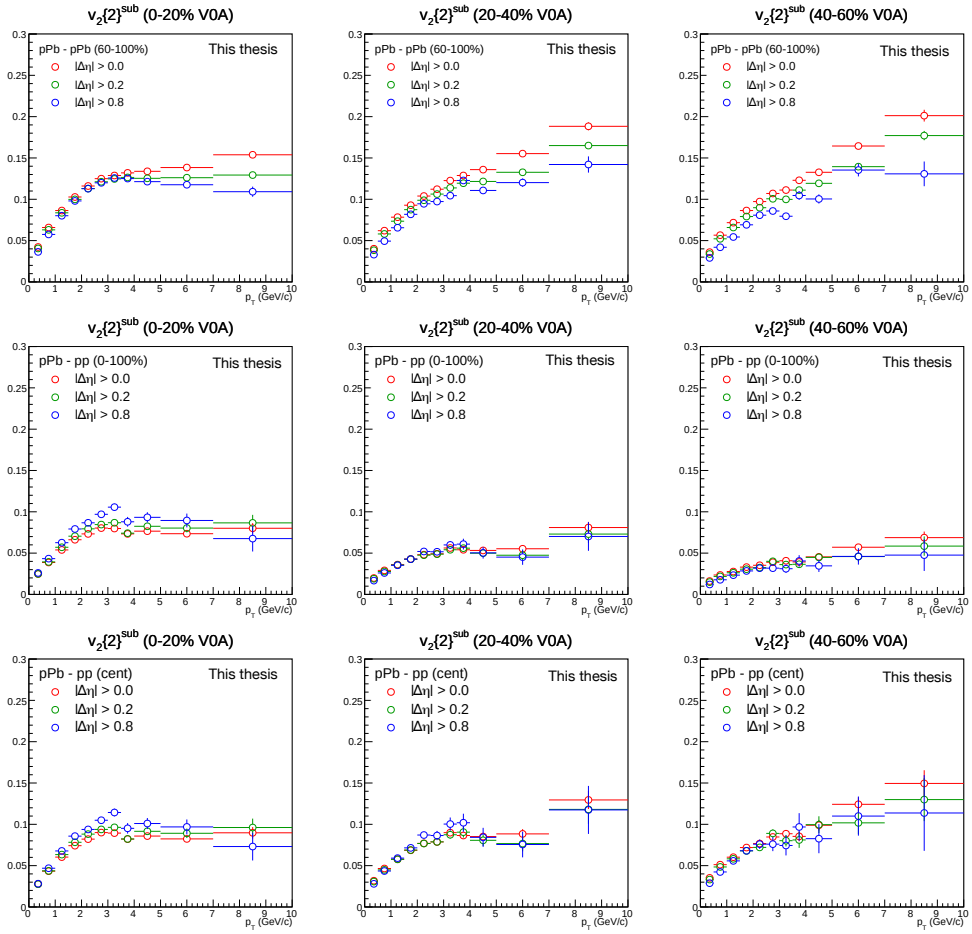

FIGURE 5.29: Comparison of subtracted p_{T}-differential $v_2\{2\}$ results using (A) peripheral p-Pb (top), (B) MB pp (middle), and (C) pp collisions from the same event class (bottom) in 0-20% (left), 20-40% (middle) and 40-60% (right) V0A classes using $|\Delta\eta|$ of 0 (red), 0.2 (green), and 0.8 (blue).

in the precision of the extracted $v_2\{2\}^{\mathrm{sub}}$ coefficients as the statistical uncertainty of the latter is considerably higher. This is due to the fact that the sample from the same event class as the p-Pb baseline is a strict subset of the used minimum-bias data.

Based on the results of this study, it was decided that the integrated minimum-bias pp collisions are the most suitable proxy of non-flow contamination in p-Pb collisions. As a result, the non-flow subtraction is performed on p-Pb collision as described in the following section using this estimate.

5.2.4 v_2 coefficients after non-flow subtraction

After a suitable non-flow proxy is selected, the next step is to estimate the appropriate scaling factor k as prescribed in (5.3). Therefore, the average number of the reference flow particles, $\langle M \rangle$, in both p-Pb and pp sample are extracted. This is done for each event class of p-Pb collisions individually. The extracted values of $\langle M \rangle$ and corresponding k factors are shown in Fig. 5.30.

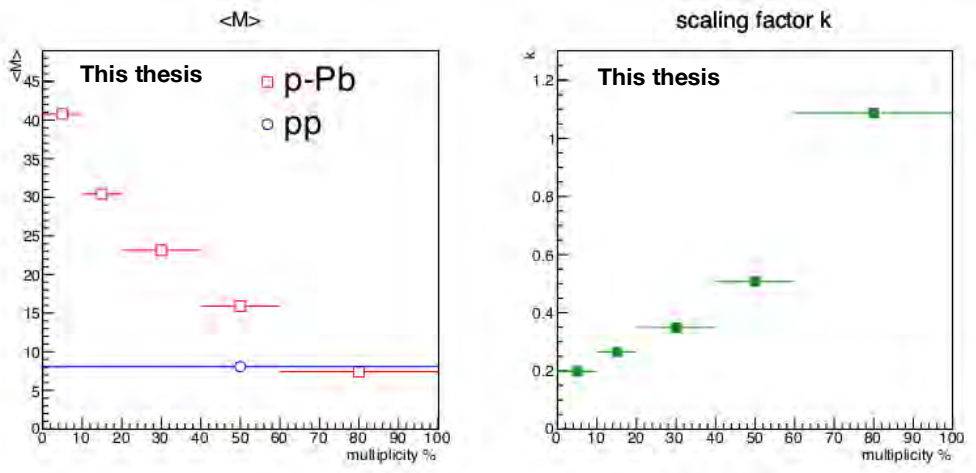

FIGURE 5.30: The average number of reference flow particles $\langle M \rangle$ of inclusive charged particles for p-Pb (red) and pp (blue) collisions (left) and the corresponding scaling factor k (right) for cumulants according to (5.2).

Afterwards, the subtraction is performed for the numerator and denominator of (5.2) separately. The procedure is illustrated in Fig. 5.31 and Fig. 5.32 for reference $c_2\{2\}$ and differential cumulant $d_2\{2\}$, respectively. Besides the final subtracted cumulants, all necessary components obtained in the process are also presented: original (un-subtracted) cumulants obtained in both p-Pb and pp collisions, both prior to and after scaling by a k factor.

Looking at Fig. 5.31, it should be noted that the value of $c_2\{2\}$ in 60-100% class of p-Pb collision is negative. In this particular case, the denominator of (5.2) is imaginary and therefore, the real value of $v_2\{2\}^{\text{sub}}$ cannot be extracted. One could admit that this is only due to the scaling factor. However, the values corresponding to pp prior to scaling (open blue markers) are almost exclusively higher (except for 60-100% bin) than p-Pb measurement (open red markers). Thus, without the presence of the scaling factor, only the single purely real value of $v_2\{2\}^{\text{sub}}$ could be extracted.

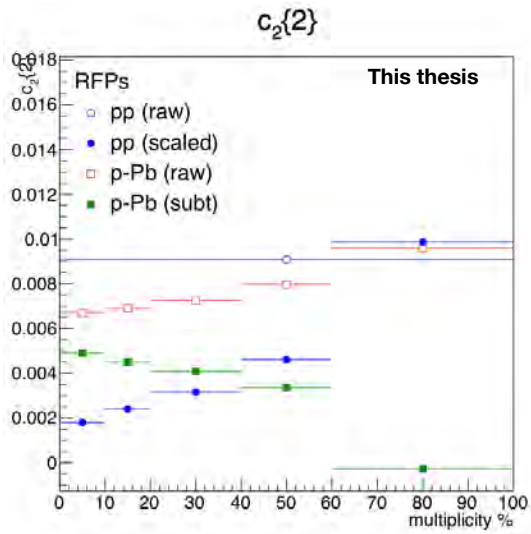

FIGURE 5.31: Result of the non-flow subtraction procedure of $c_2\{2\}$ (solid green) for various V0A classes of p-Pb collisions together with the original un-subtracted values (open red), and both scaled (solid blue) and un-scaled (open blue) pp measurements.

The final results of p_{T}-differential $v_2\{2, |\Delta\eta| > 0.4\}$ of inclusive $\mathrm{h}^{\pm}$ and identified $\pi^{\pm}$, $\mathrm{K}^{\pm}$, $\mathrm{K}^0_{\mathrm{S}}$, $\Lambda(\bar{\Lambda})$, and ϕ in p-Pb collisions at $\sqrt{s_{\mathrm{NN}}} = 5.02$ TeV after subtraction by centrality integrated minimum-bias pp collisions at $\sqrt{s} = 13$ TeV are presented in Fig. 5.33.

After the subtraction, the 0-20% event class of p-Pb collisions exhibit all characteristic features of flow measurements of identified hadrons in Pb-Pb collisions, as discussed in Section 5.1.1. The mass ordering is clearly presented in the low p_{T} region, then the crossing point appears around $p_{\mathrm{T}} \approx 3$ GeV/c, followed by a significant baryon/meson grouping. Both these mass-related features are more pronounced when compared to initially un-subtracted results shown in Fig 5.27. Judging by the results of the charged hadrons, the v_2 values no longer increase towards higher p_{T}, but reach a plateau for $p_{\mathrm{T}} > 3.5$ GeV/c, instead. However, when moving toward more peripheral collisions, the v_2 values start to linearly increase with increasing p_{T} and difference between individual species is slowly vanishing.

Similarly to Pb-Pb collisions, a test of scaling properties of the subtracted v_2 coefficients is performed. The results of NCQ and KE_{T} scaling are presented in Fig. 5.34. In the case of NCQ in 0-20% event class, v_2/n_q shows only an approximate scaling for $p_{\mathrm{T}} > 1.5$ GeV/c, while still manifesting an apparent residual mass-ordering in low p_{T} region. On the other hand, the difference between individual species is suppressed significantly when KE_{T} scaling is applied instead. In event classes with higher percentiles, neither of the scaling representation seems to work despite large uncertainties since the

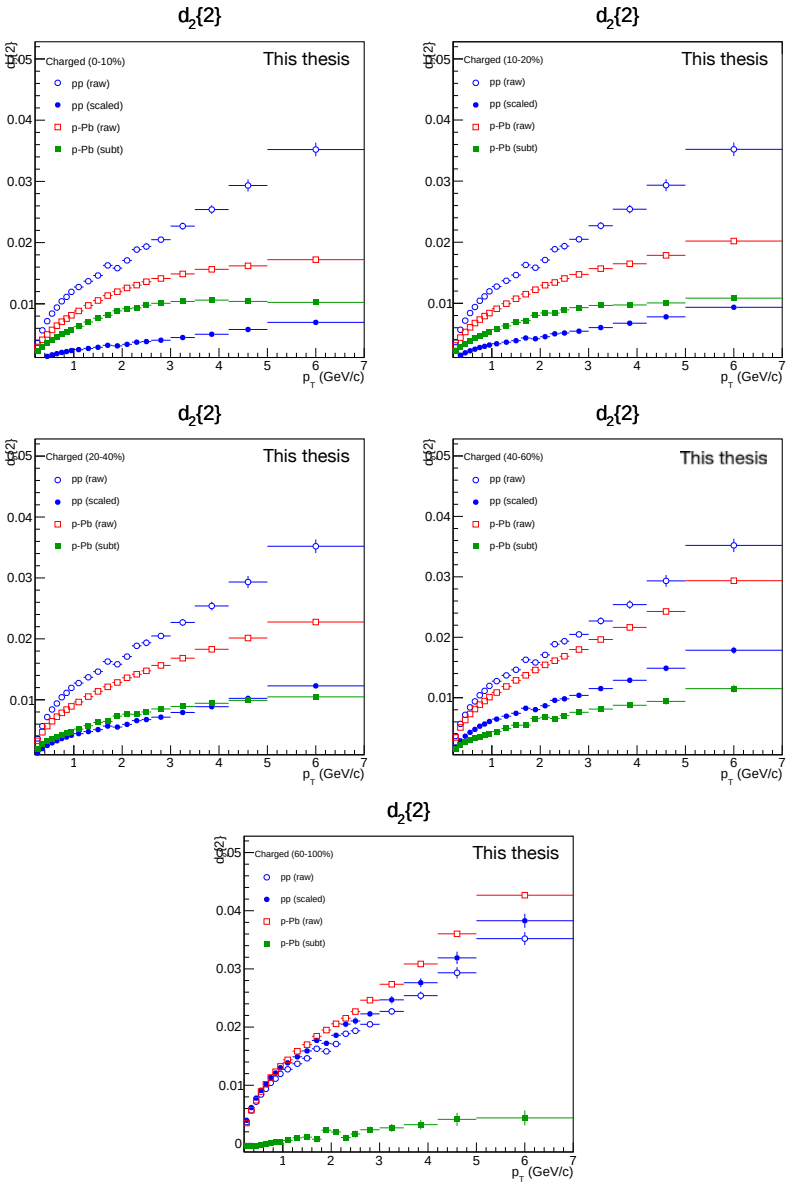

FIGURE 5.32: Results of the non-flow subtraction procedure of $d_2\{2\}$ (solid green) of the inclusive charged hadrons in various V0A classes of p-Pb collisions together with the original un-subtracted values (open red), and both scaled (solid blue) and un-scaled (open blue) pp measurements.

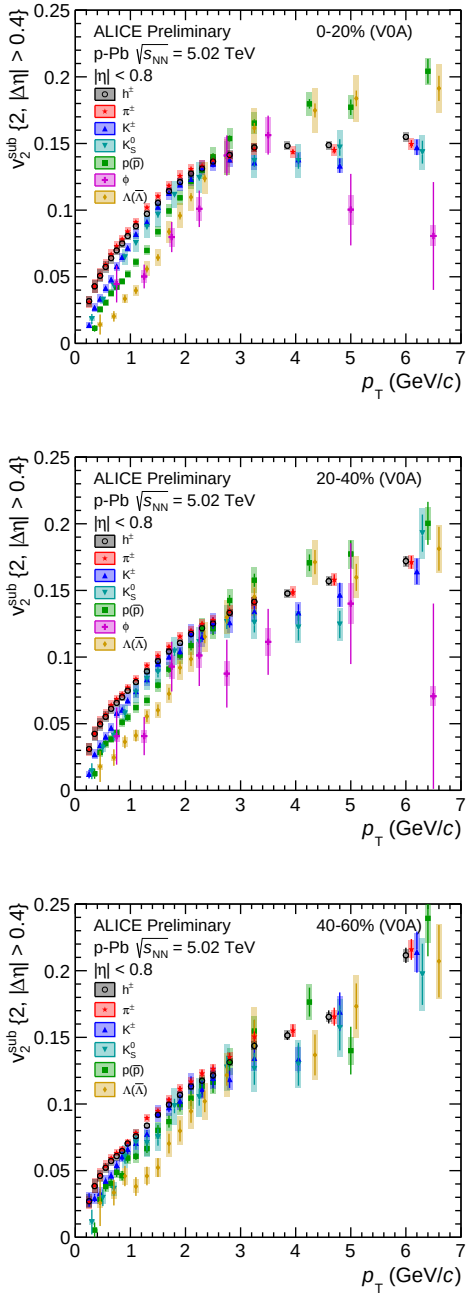

FIGURE 5.33: Measurement of p_T-differential $v_2\{2, |\Delta\eta| > 0.4\}$ of $h^{\pm}$, $\pi^{\pm}$, $K^{\pm}$, K^0_S, $\Lambda(\bar{\Lambda})$, and ϕ in p-Pb collision after non-flow subtraction by integrated pp collisions at $\sqrt{s} = 13$ TeV for various V0A event classes.

linear rise in the high-p_{T} region clearly remains.

5.2.5 v_2 coefficients with 4-particle cumulants

The first measurement of v_n coefficients with 4-particle cumulant of identified hadrons in Pb-Pb collisions (presented in Section 5.1.1) created a new opportunity to better suppress the non-flow contamination in small collision systems. For reconstructed particle species, i.e. $\mathrm{K}^0_{\mathrm{S}}$, $\Lambda(\bar{\Lambda})$, and ϕ, the flow extraction has not been done before for 4-particle cumulants. Once the methodology was tested on a rather "familiar grounds" of heavy-ion collisions, it can be applied in a more challenging environment such as the small collision systems. A first attempt of measuring the p_{T}-differential $v_2\{4\}$ coefficients of identified hadrons in p-Pb collisions is summarised in this section.

Before moving to the actual p_{T}-differential measurement, one has to start by looking at the cumulant of the reference (integrated) flow. The measurement of $c_2\{4\}$ using RFPs within $0.2 < p_{\mathrm{T}} < 3$ GeV/c is presented in Fig. 5.35 as a function of V0A percentile. While the $c_2\{4\}$ cumulant increases with increasing V0A percentiles, its values are negative up to percentile of 20%. Consequently, this region is used for the further analysis, because of the extraction of real (i.e. non-imaginary) $v_2\{4\}$ values is possible according to (2.16) in Section 2.2, i.e. $v_n\{4\} = \sqrt[4]{-c_n\{4\}}$.

The measurements of p_{T}-differential $v_2\{4\}$ of both inclusive and identified hadrons in 0-20% event-class of p-Pb collisions is presented in Fig. 5.36. Even though these results exhibit a similar behaviour as the measurement of 2-particle cumulants which has been discussed previously, there are some obvious differences presented as well. Considering the mass-related features, a significant baryon/meson grouping persists at the intermediate p_{T} region of $2-4$ GeV/c. However, previously observed clear mass ordering is suppressed, and individual particle species are consistent among each other.

For a better comparison, the measurement of v_2 coefficients using 2- and 4-particle cumulants without pseudo-rapidity separation as well as subtracted results with $|\Delta\eta| > 0.4$ are displayed together in Fig. 5.37 for individual species. The $v_2\{4\}$ increases with increasing p_{T} up to $2-3$ GeV/c (depending on the particle species) where a maximum value is reached. In the higher-p_{T} region, it decreases significantly. Such behaviour is consistent with the naive expectation based on the measurements of Pb-Pb collisions discussed in Section 5.1.1. This might serve as an indication for the absence of the non-flow contamination when using 4-particle cumulants. On the other hand, v_2 of $\mathrm{h}^{\pm}$, for which the measurement is accurate enough to extend its range, decreases linearly, and eventually, it turns into negative values. This evolution is completely unexpected, as there is no clear explanation for such observation.

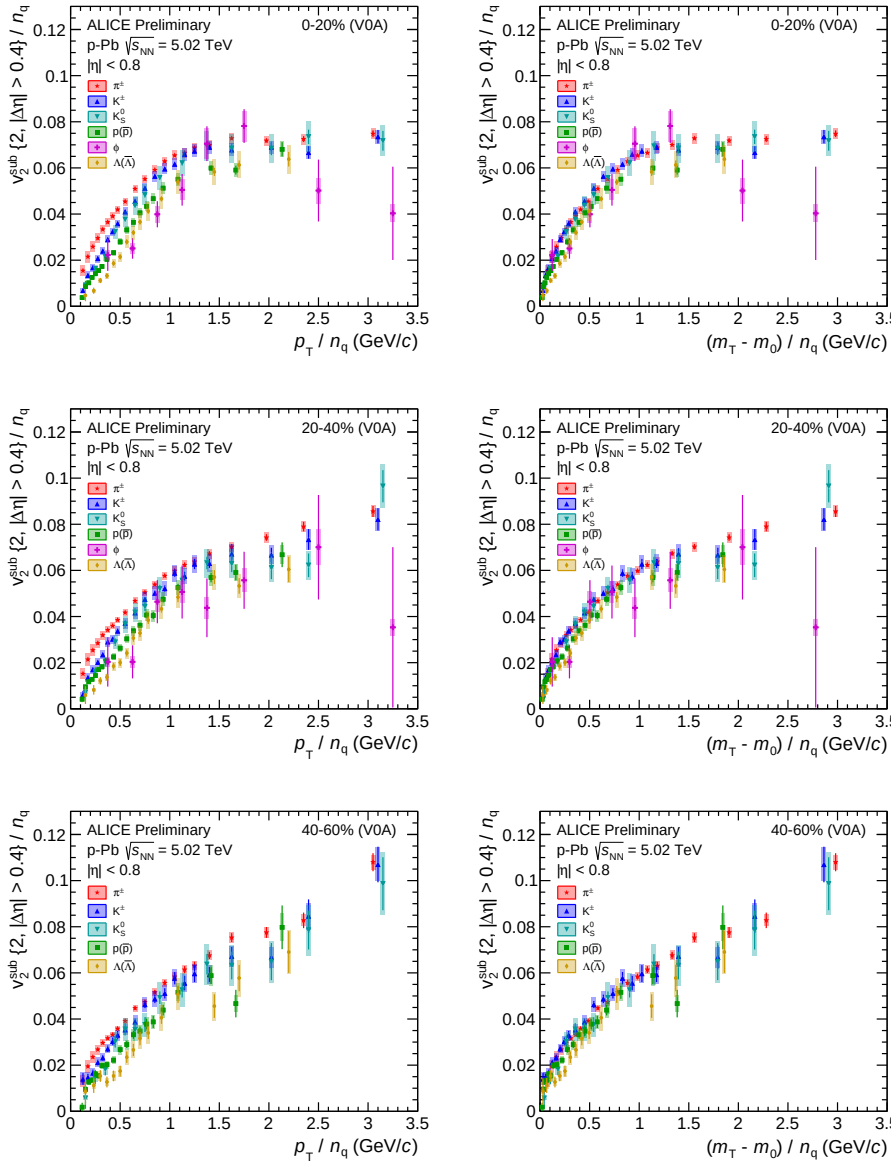

FIGURE 5.34: Results of subtracted $v_2\{2, |\Delta\eta| > 0.4\}$ scaled by number of valence quarks n_q as a function of p_T/n_q (left) or $(m_T - m_0)/n_q$ (right) for various V0A event classes.

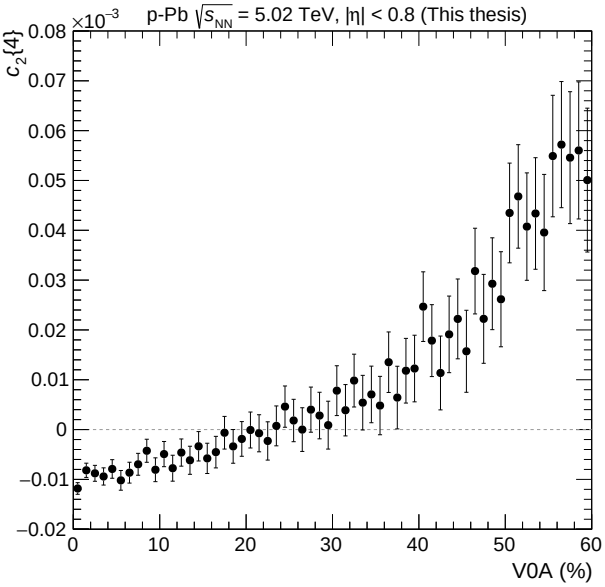

FIGURE 5.35: Measurement of $c_2\{4\}$ in p-Pb collisions as a function of V0A percentile.

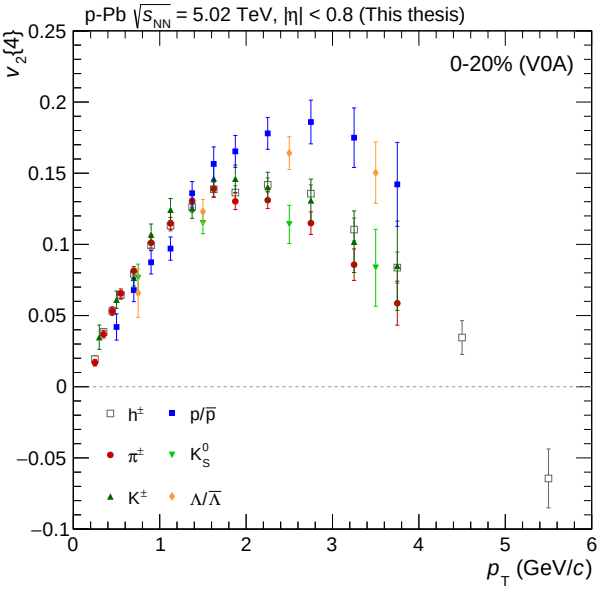

FIGURE 5.36: Results of $v_2\{4\}$ of identified species as a function of p_T in 0-20% V0A event class of p-Pb collisions.

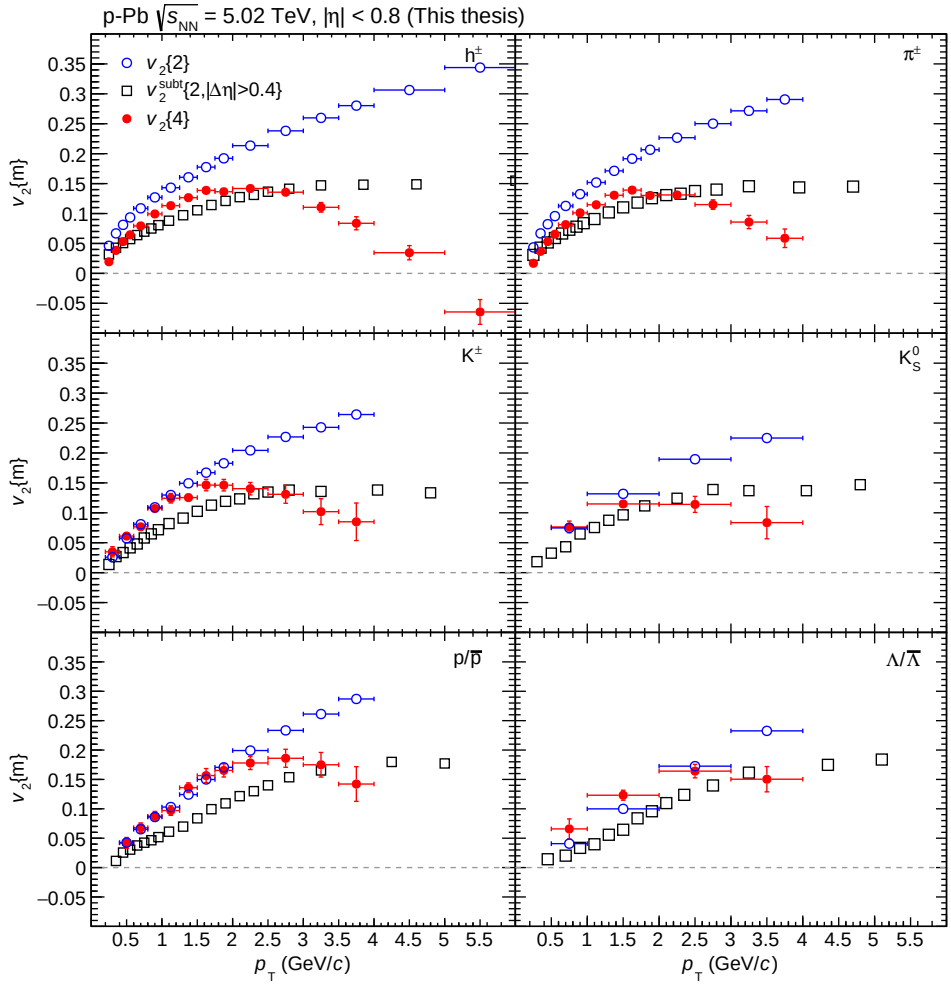

FIGURE 5.37: Comparison of $v_2\{4\}$, $v_2\{2\}$ and $v_2\{2\}^{\text{sub}}$ as a function of p_{T} for various identified particle species.

In summary, the initial measurement of $v_2\{2, |\Delta\eta| > 0.8\}$ of identified species in events with highest multiplicities (Fig. 5.27) revealed a similar feature typically appearing in heavy-ion collisions, which are associated with the common expansion of created medium (QGP). However, it is known that the non-flow contamination is a dominant source of correlations in collisions of small systems. Therefore, in contrast to the well-established 2-sub-event method, a more sophisticated (and thus less straightforward procedures) procedures are needed. By performing a non-flow subtraction, both characteristic aspects of v_n measurements of identified hadrons are more explicit (as can be seen

in Fig. 5.33). With the most recent measurements of 4-particle cumulants, a clear non-zero $v_2\{4\}$ is observed. Such observation provides yet another argument supporting the presence of collective behaviour even in collisions of small systems. On the other hand, the observation of $v_2\{4\}$ being larger than $v_2\{2\}^{\text{sub}}$, and the negative $v_2\{4\}$ of inclusive charged hadrons, presented in the high p_{T} region, is very puzzling. Further investigation will undoubtedly deepen the current understanding of the collective phenomena and potentially brings a fresh perspective on a small collision systems.

6 Summary

Extensive research of ultra-relativistic heavy-ion collisions aims to study the physics of extremely hot and dense nuclear matter, the QGP. Among many interesting observations, we have learned that this collectively-expanding medium behaves as an almost perfect liquid by studying the anisotropy in the azimuthal distribution of created particles. This has been shown in (for example) Pb-Pb and Xe-Xe collisions.

On the other hand, the pp and p-Pb collisions were typically considered as a baseline for the heavy-ion measurements due to an absence of QGP-related effects. However, recent observations of collective features in two-particle correlations in these small collision systems present a paradigm shift in our understanding of the collision dynamics. Since then, it became clear that further examination is essential to understand the mechanism behind the collective nature of small collision systems.

The analysis, reported in this thesis, is similarly motivated. It aims to study the collectivity by measuring the anisotropic flow v_n coefficients of identified particles in the collisions of small nucleonic systems. Besides providing tighter constraints for the theoretical calculations, the analysis of individual particle species allows studying the particle production mechanisms from a unique perspective.

At the very beginning, it started with a very brief study of pp collisions[1] Nevertheless, the focus changed to p-Pb collisions at $\sqrt{s_{\mathrm{NN}}} = 5.02$ TeV when a new data-taking campaign took place at the LHC in 2016. This new larger data sample allowed extending the previous study by measuring the pt-differential (unsubtracted) v_2 using the 2-particle cumulant method and by including additional particle species, such as K0s, Lambdas, and Phis, for the first time in p-Pbcollisions. Already there, a clear mass ordering is apparent at low p_{T} similar to the observation in Pb-Pb collisions, where it is typically associated with the radial flow of the expanding medium. However, small collision systems are dominated by non-flow (e.g. resonance decays, jet fragmentation). Therefore, a non-flow subtraction was proposed in addition to the sub-event method. Afterwards, the extensive study was done testing various approaches and multiple non-flow estimates.

Moreover, the effect of multiplicity fluctuations on 2-particle correlation analysis in p-Pb collisions was studied by utilising different approaches to particle and event weights. The potential bias caused by such fluctuations was investigated by comparing the v_2

[1] Note, that in order to provide a context to the reader, the project is summarised here as a chronological series, and therefore it does not match the order in which the results are presented in Chapter 5.

measurement obtained from collisions with the fixed number of particles (i.e. unit multiplicity bins) with sub-samples of finite multiplicity ranges where the fluctuations occur. Based on this comparison, it was found out that the standard Generic Framework implementation is insensitive to the multiplicity fluctuations, while alternative approaches exhibit a significant deviation reaching up to 13%.

As a result, the non-flow subtraction was performed at the cumulant level while using the measurement in minimum-bias pp collisions at $\sqrt{s} = 13$ TeV as non-flow proxy. After the subtraction, the v_2 measurement in 0-20% event class is very similar to the results observed in Pb-Pb collisions. A clear mass ordering in low p_{T} is more pronounced when compared to unsubtracted results. Then a crossing point appears at 3 GeV/c followed by a baryon/meson grouping at high p_{T}, where v_2 of mesons are systematically higher than those of baryons. Similarly to Pb-Pb collisions, only an approximate scaling is observed for both NCQ and KE_{T} cases.

However, significantly high values of v_2 were observed at a high-p_{T} region, where a decrease is expected based on Pb-Pb collisions. This, together with a linearly increasing v_2 with pt observed in other event classes, indicates the residual non-flow prevailing in the measurement. Not satisfied by the performance of non-flow subtraction method in 2-particle correlation measurement, the focus shifted towards the heavy-ion collisions to test the possibility of using 4-particle cumulants. This initial study resulted in the very first measurement of p_{T}-differential v_2 of identified hadrons obtained using the 4-particle cumulant method. Moreover, the v_2 results of 2-particle cumulants with large pseudorapidity separation is presented. Both characteristic features reported in previous measurements, i.e. mass ordering in low p_{T} and particle-type grouping in high p_{T}, are present in case of 2- and 4-particle cumulants as well. Also, an approximate NCQ and KE_{T} scaling is observed, indicating no significant difference.

In addition, the elliptic flow fluctuations of the underlying PDF are studied thanks to access to both 2- and 4-particle correlations. A constant relative fluctuations of approximately 40% is observed for all particles within the investigated p_{T} region. Given the statistical precision, no conclusive mass dependence is observed.

Besides the cumulant-based measurement of v_2 coefficients, multi-particle correlations are used to measure more intriguing aspects of azimuthal anisotropy. The measurements of p_{T}-differential $v_{4,22}$, $v_{5,23}$, and $v_{6,33}$ coefficients of identified hadrons are presented. These coefficients quantify the non-linear flow response of low order initial spatial anisotropies to higher-order v_n harmonics. Even though these results are qualitatively similar to the total v_n measurements, they present a significant challenge in the theoretical model development.

The experimental results in Pb-Pb collisions are compared to the hydrodynamical

calculations using iEBE-VISHNU hybrid model with two sets of initial parameters characterising the transport properties: constant shear- (η/s) and zero bulk-viscosity (ζ/s) over entropy ratio (AMPT), and temperature-dependent ones (T_RENTo). Overall, the iEBE-VISHNU model with the AMPT initial condition achieves better agreement with the measurements favouring the constant value of η/s (and $\zeta/s = 0$), while the T_RENTo initial conditions generally overestimates them.

Finally, once the method of multi-particle cumulant was successfully tested in a more familiar environment of Pb-Pb collisions, the very first attempt for p_T-differential v_2 measurement using 4-particle cumulants in p-Pb was made.

After the initial increase in low p_T, the v_2 values are significantly lower at the intermediate p_T when compared to previous 2-particle correlation results. This might indicate the absence of the non-flow contamination in the 4-particle cumulant measurement based on the observation from Pb-Pb collisions. However, such decreasing trend seems to continue further as the v_2 of charged hadrons turn into negative values. Such behaviour is entirely unexpected, and further investigation beyond this initial study is needed for its explanation.

In conclusion, we have found that the various discussed measurements based on multi-particle correlations in both small and large collision systems exhibit similar characteristics. Besides the p_T-dependence, the mass-related features typically associated with the presence of expanding medium is present even in p-Pb where the QGP formation is not expected. These observations support the presence of collective behaviour in the collisions of small nuclear systems, even though its origin remains a puzzle, yet to be fully understood.

A Multiplicity fluctuations

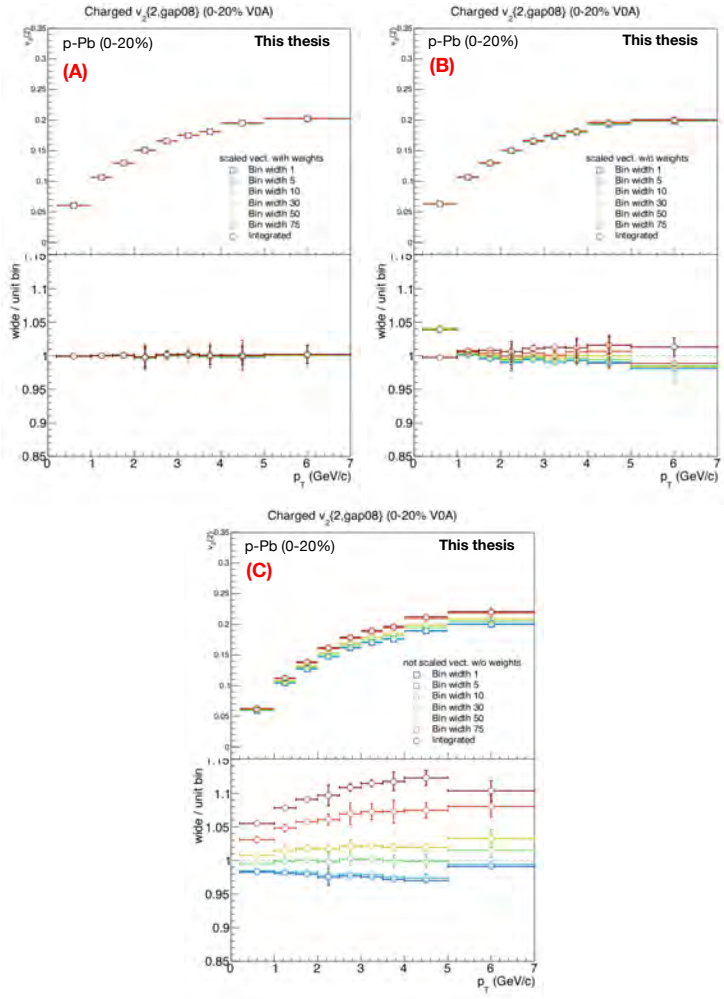

FIGURE A.1: The $v_2\{2, |\Delta\eta| > 0.8\}(p_T)$ of $h^{\pm}$ in 0-20% class of p-Pb collisions estimated in multiplicity bins with various widths (open circles) are shown (upper sub-plot) together with the ratios wrt. unit bin (open squares) results (lower sub-plot) for approach A (left), B (right), and C (bottom). See the text in Section 5.2.1 for details.

B Systematic uncertainties

B.1 Cumulants in Pb-Pb collisions

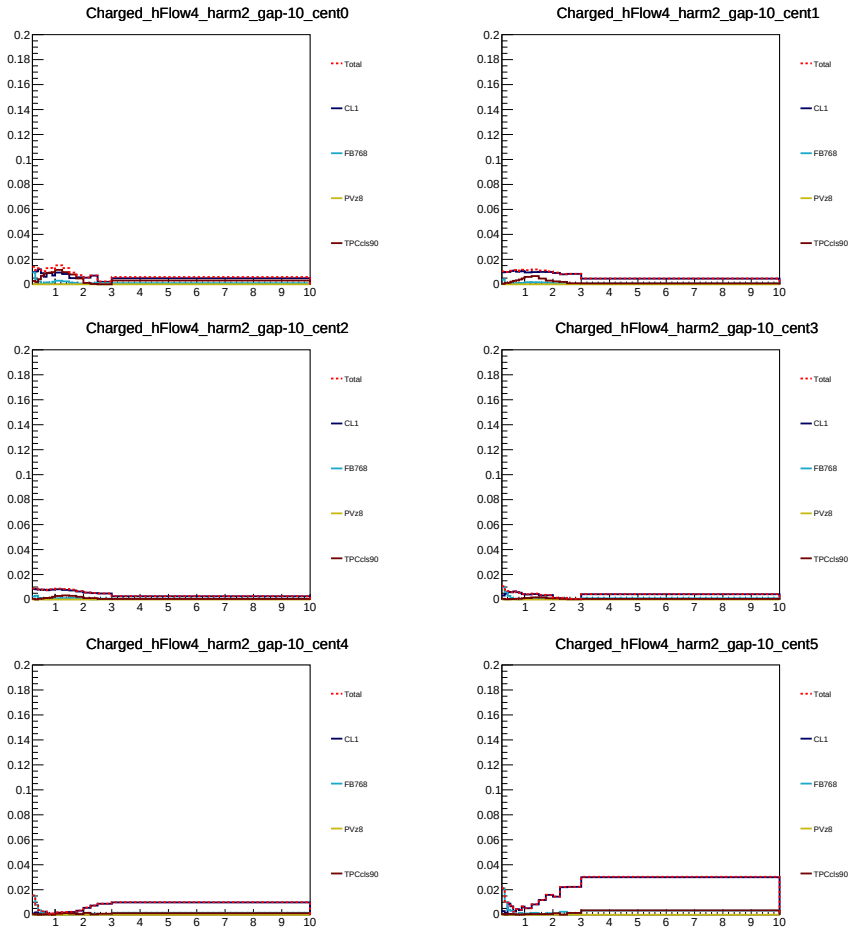

FIGURE B.1: Relative systematic uncertainty for v_n of $h^{\pm}$ in Pb-Pb collisions.

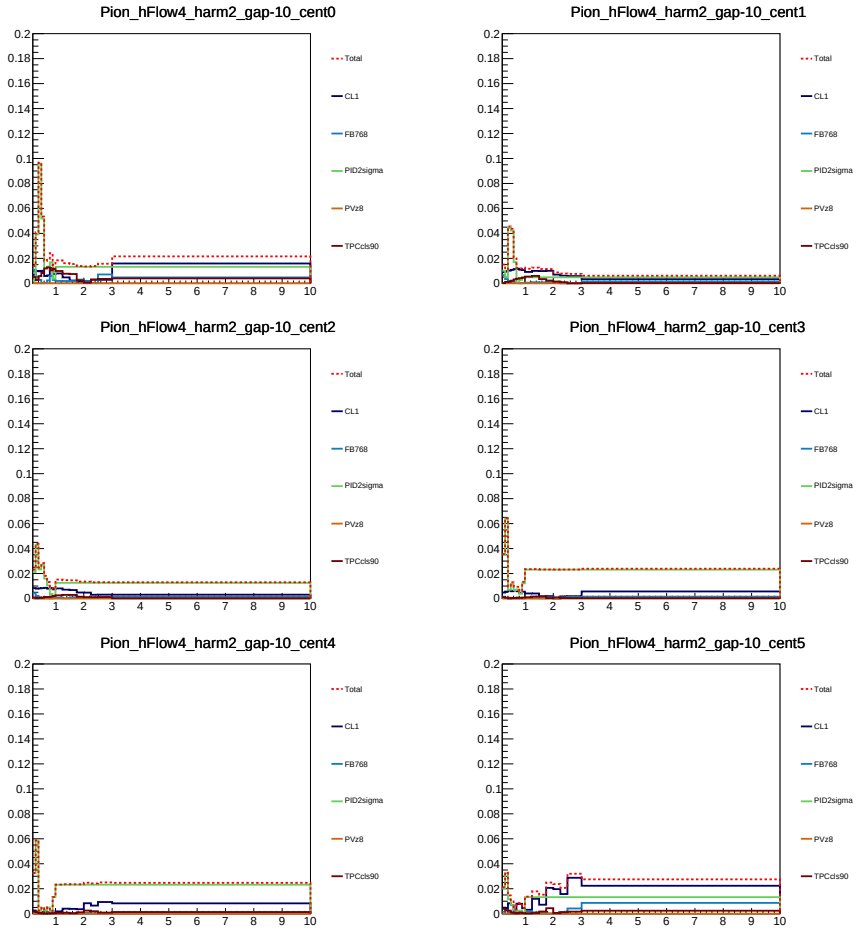

FIGURE B.2: Relative systematic uncertainty for v_n of $\pi^{\pm}$ in Pb-Pb collisions.

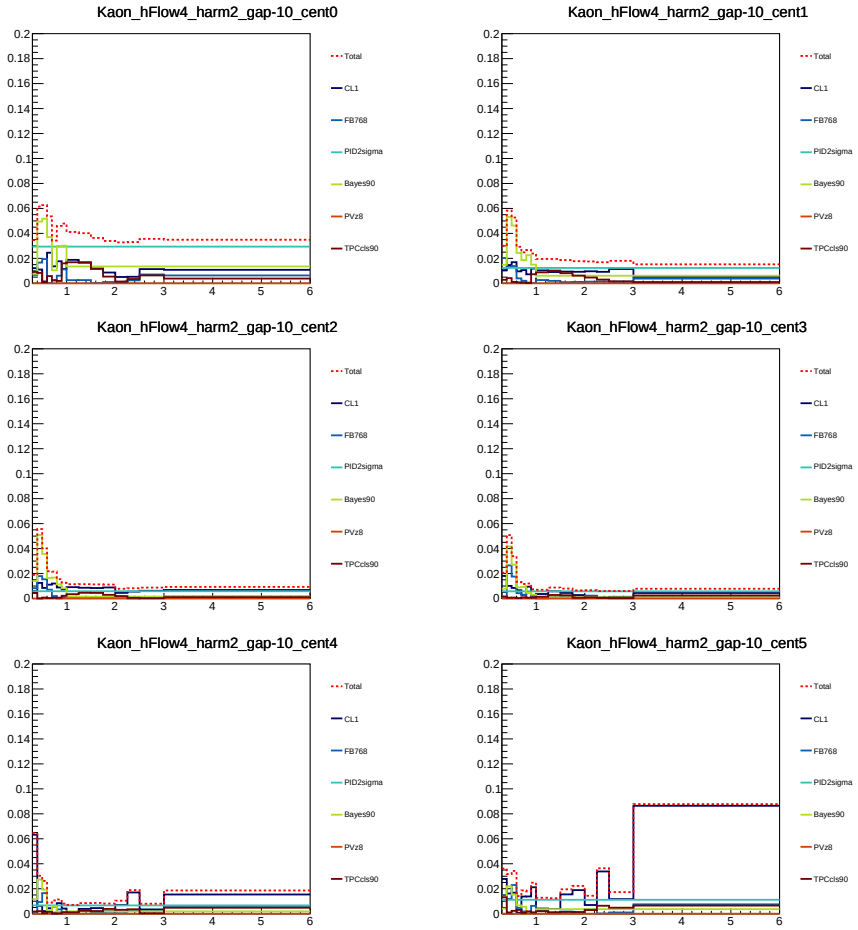

FIGURE B.3: Relative systematic uncertainty for v_n of $K^{\pm}$ in Pb-Pb collisions.

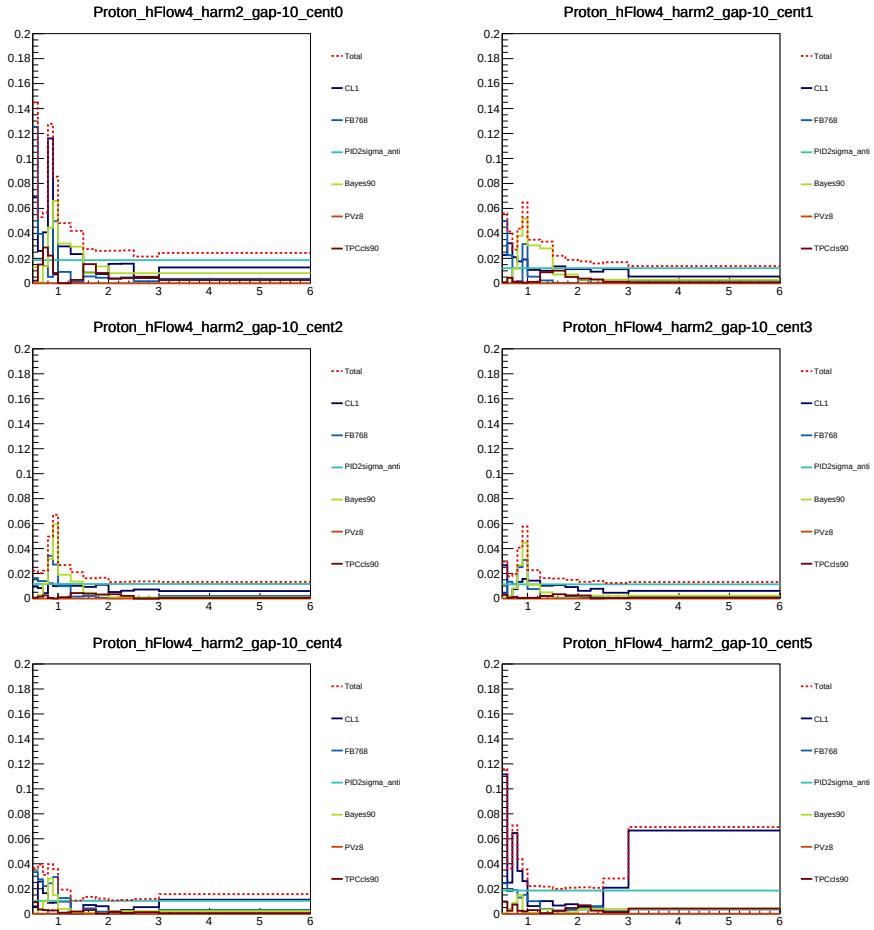

FIGURE B.4: Relative systematic uncertainty for v_n of $\mathrm{p}(\bar{\mathrm{p}})$ in Pb-Pb collisions.

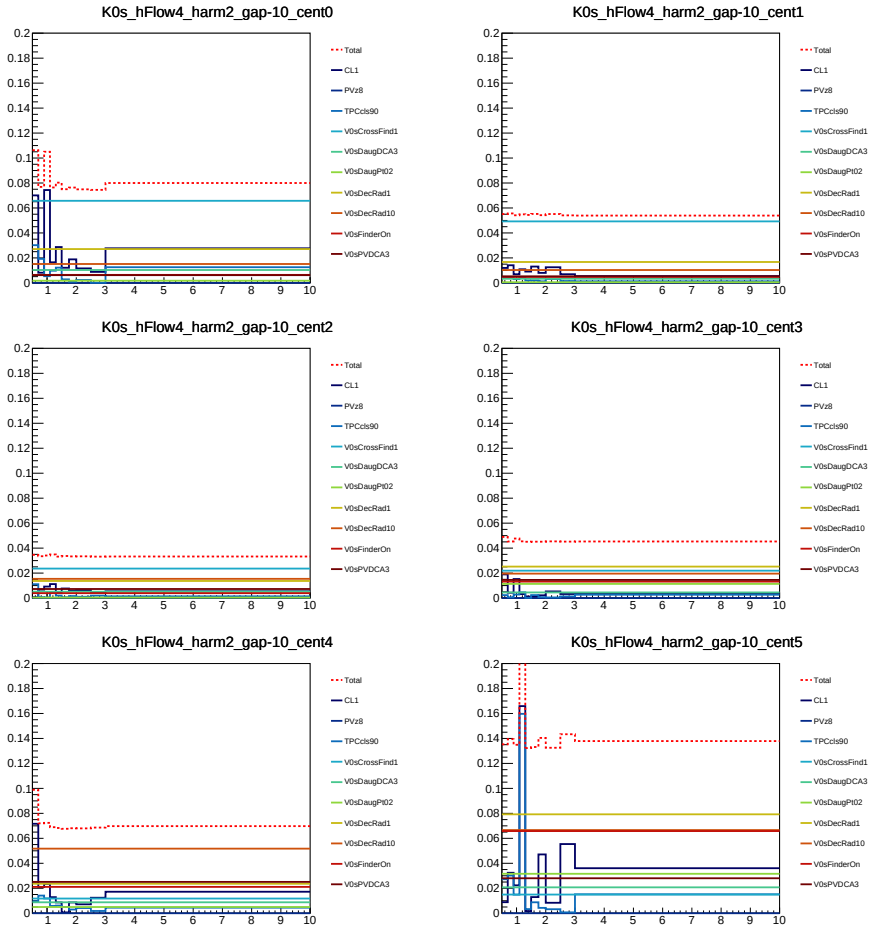

FIGURE B.5: Relative systematic uncertainty for v_n of K^0_S in Pb-Pb collisions.

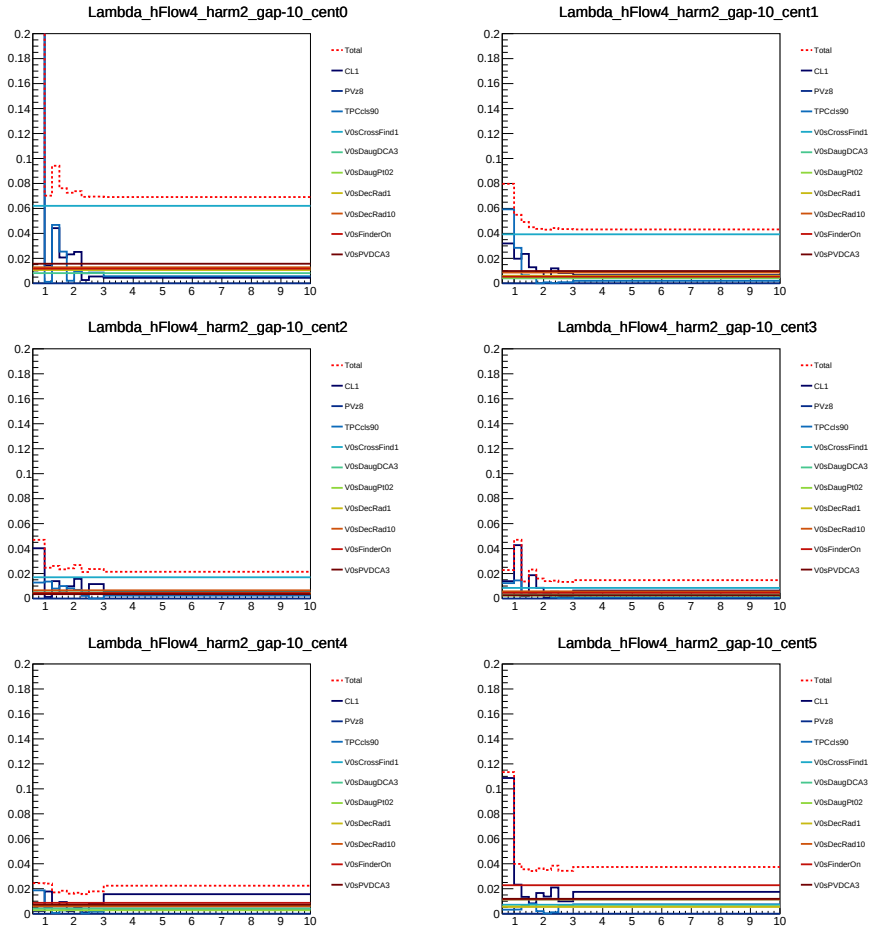

FIGURE B.6: Relative systematic uncertainty for v_n of $\Lambda(\bar{\Lambda})$ in Pb-Pb collisions.

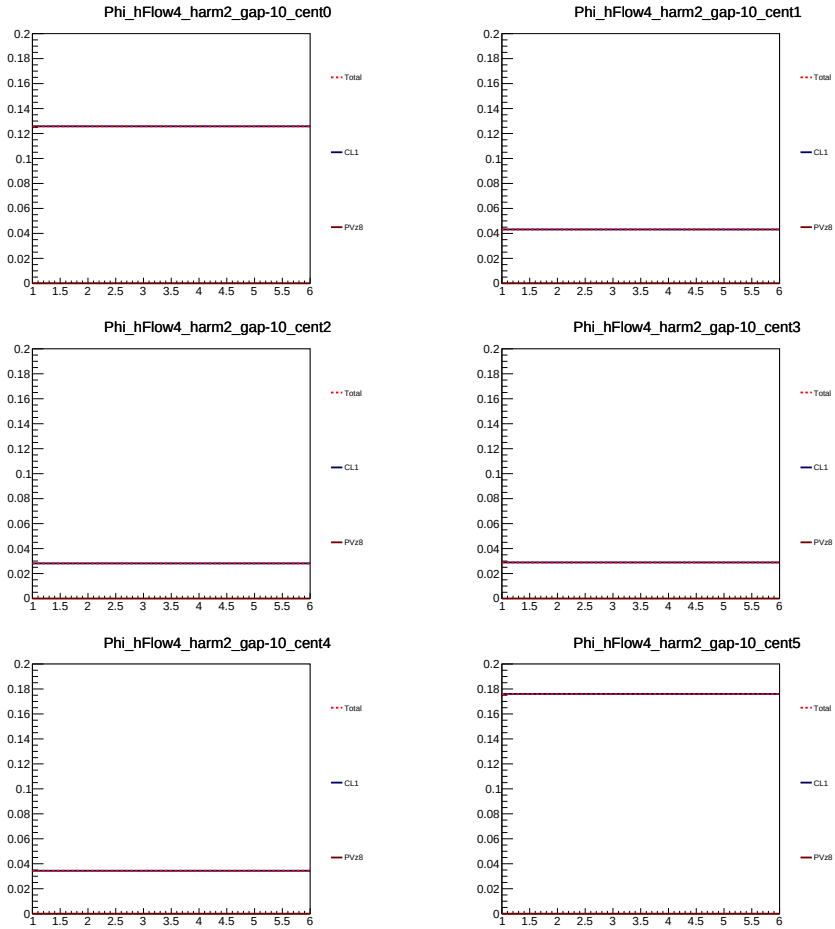

FIGURE B.7: Relative systematic uncertainty for v_n of ϕ in Pb-Pb collisions.

B.2 Non-linear flow modes in Pb-Pb collisions

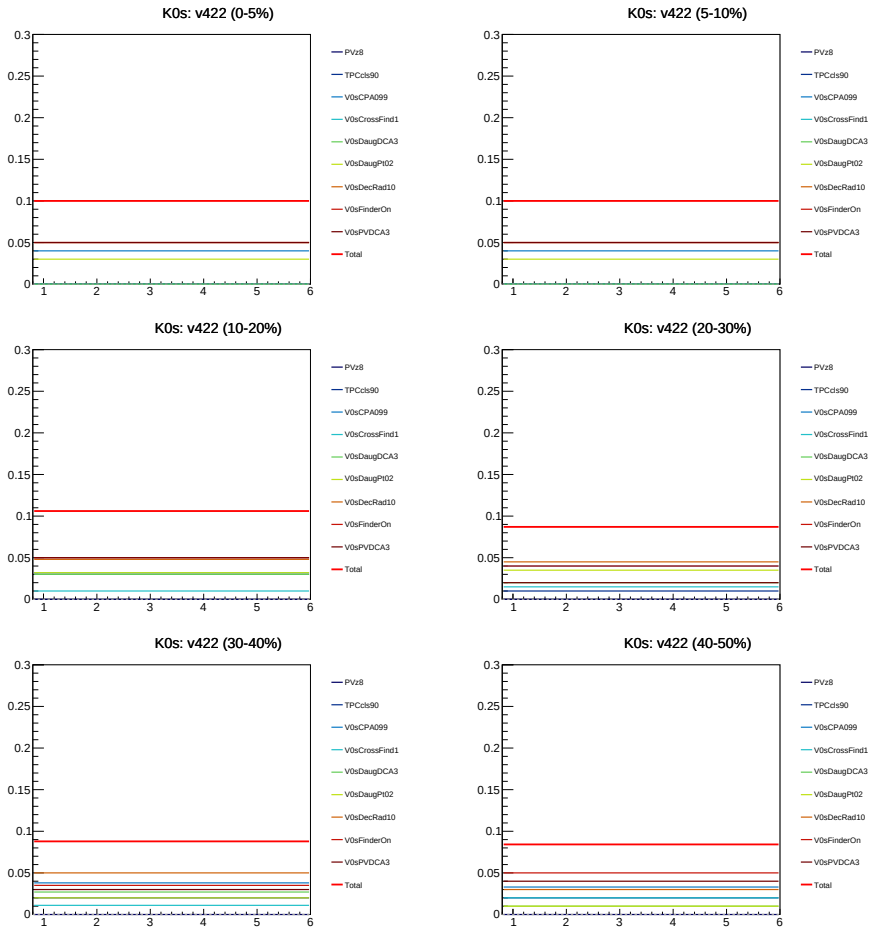

FIGURE B.8: Relative systematic uncertainty for non-linear flow modes of K^0_S in Pb-Pb collisions.

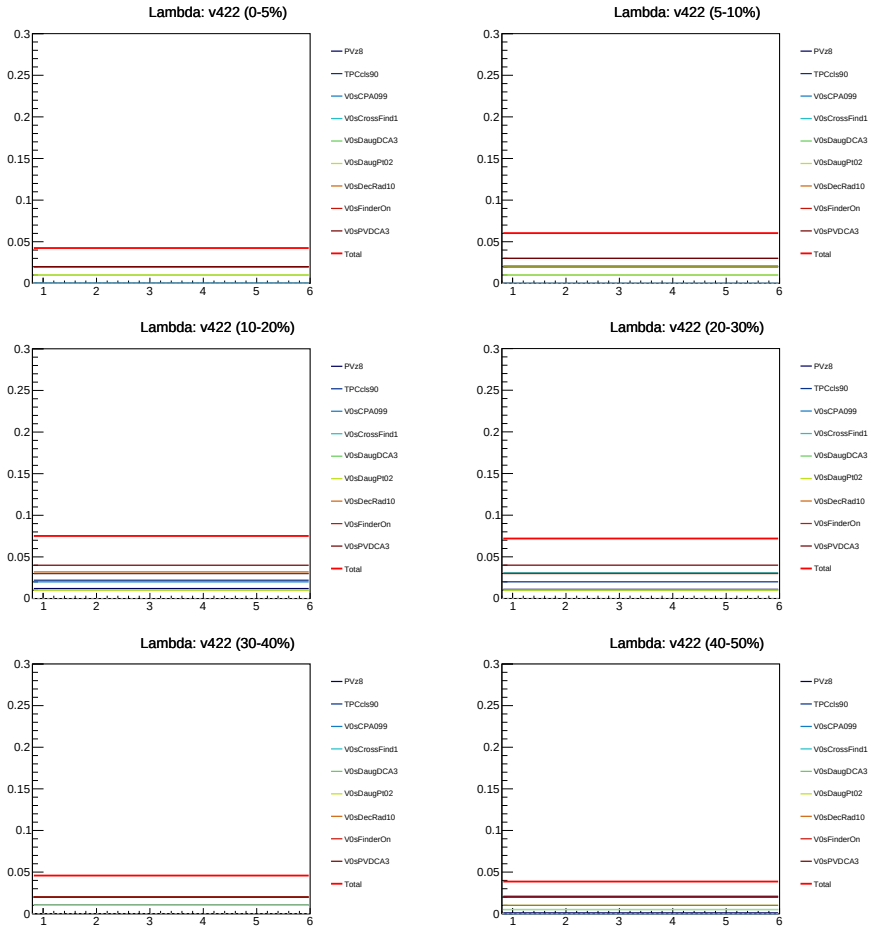

FIGURE B.9: Relative systematic uncertainty for non-linear flow modes of $\Lambda(\bar{\Lambda})$ in Pb-Pb collisions.

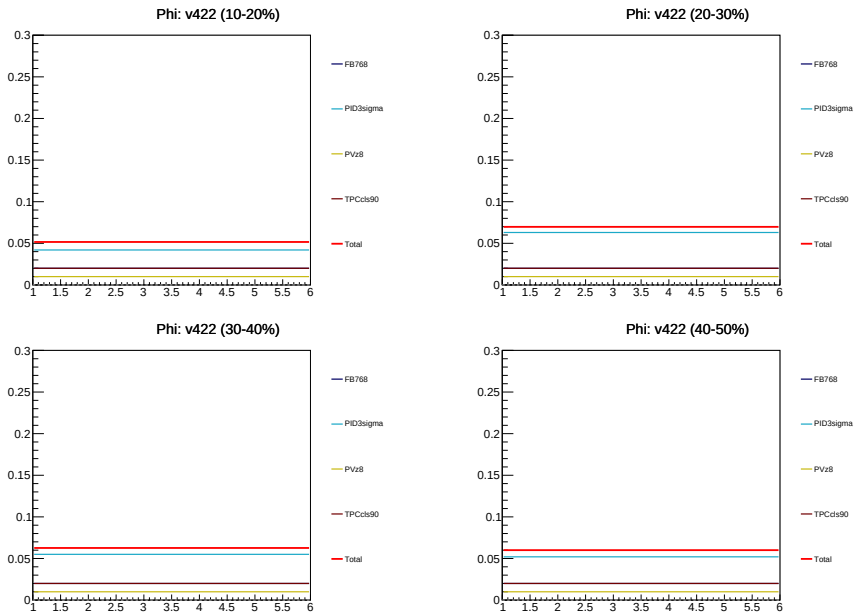

FIGURE B.10: Relative systematic uncertainty for non-linear flow modes of ϕ in Pb-Pb collisions.

B.3 Cumulants in p-Pb collisions

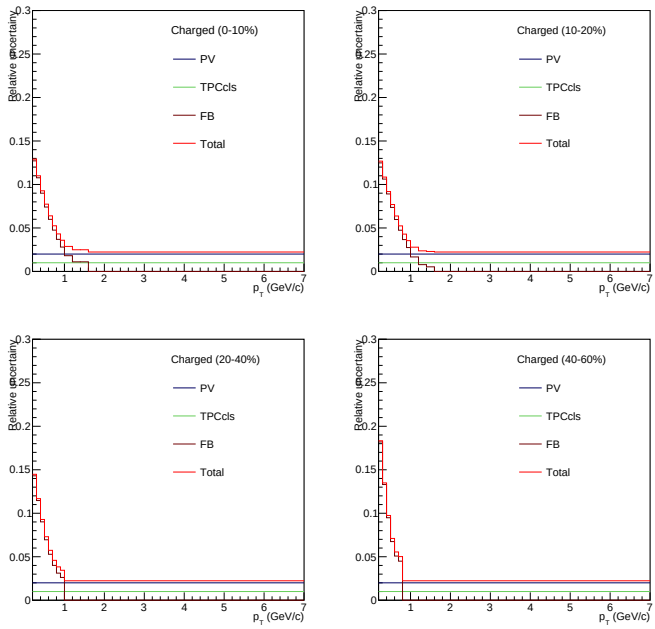

FIGURE B.11: Relative systematic uncertainty for v_n of $h^{\pm}$ in p-Pb collisions.

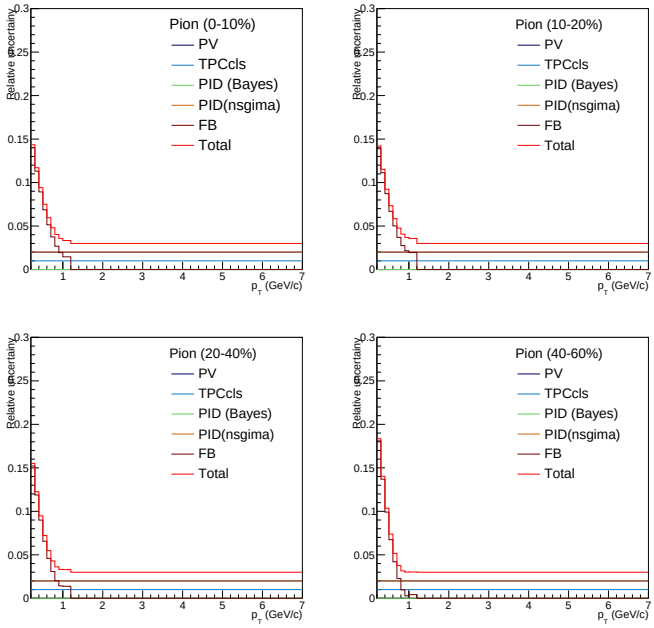

FIGURE B.12: Relative systematic uncertainty for v_n of $\pi^{\pm}$ in p-Pb collisions.

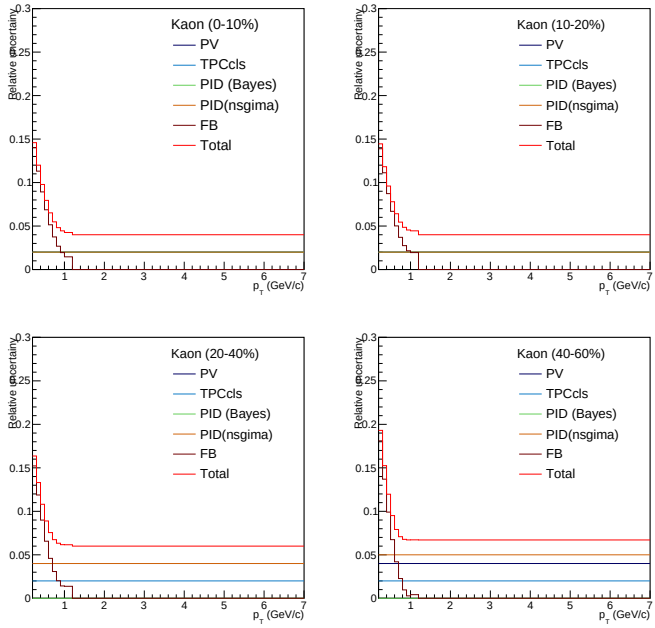

FIGURE B.13: Relative systematic uncertainty for v_n of $K^{\pm}$ in p-Pb collisions.

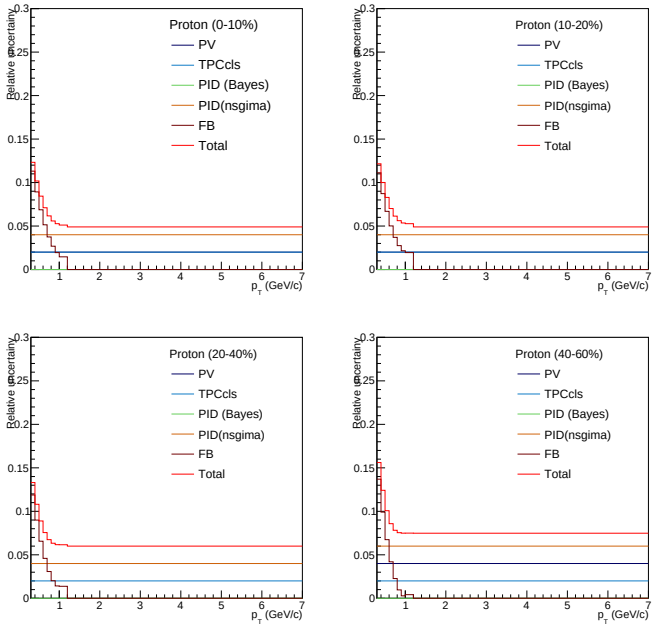

FIGURE B.14: Relative systematic uncertainty for v_n of $\mathrm{p}(\bar{\mathrm{p}})$ in p-Pb collisions.

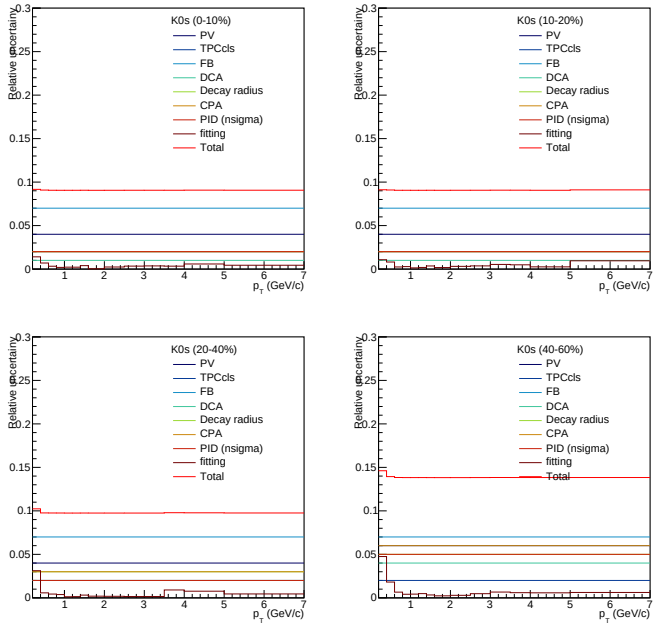

FIGURE B.15: Relative systematic uncertainty for v_n of K^0_S in p-Pb collisions.

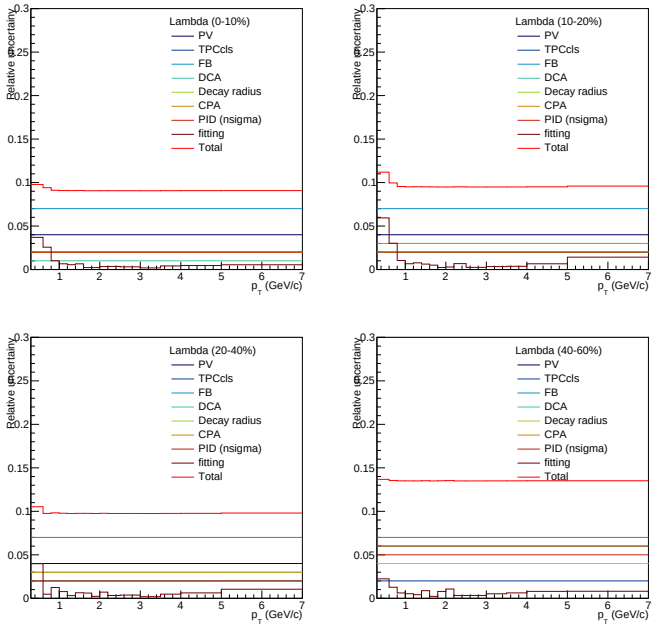

FIGURE B.16: Relative systematic uncertainty for v_n of $\Lambda(\bar{\Lambda})$ in p-Pb collisions.

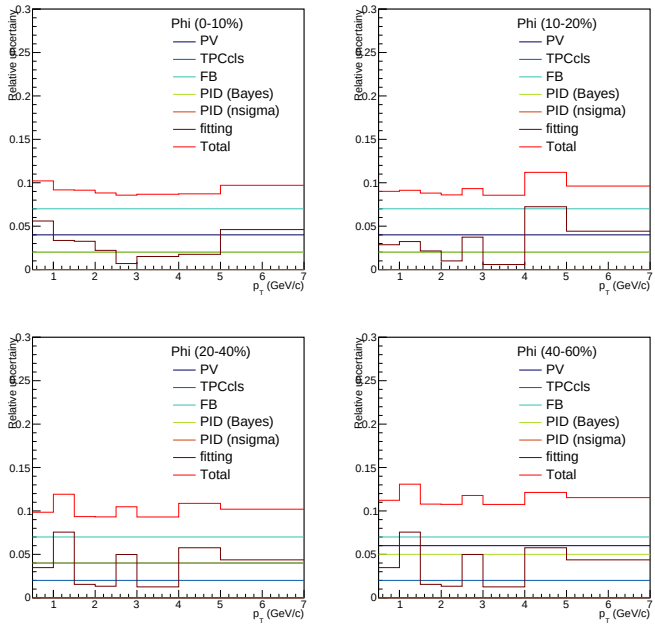

FIGURE B.17: Relative systematic uncertainty for v_n of ϕ in p-Pb collisions.

Bibliography

[1] Wikipedia contributors. *Standard Model — Wikipedia, The Free Encyclopedia*. [Online; accessed November 11, 2019]. 2019. URL: https://en.wikipedia.org/w/index.php?title=Standard_Model&oldid=928956838.

[2] C. Patrignani et al. "Review of Particle Physics". In: *Chin. Phys.* C40.10 (2016), p. 100001. DOI: 10.1088/1674-1137/40/10/100001.

[3] C. Montag and A. Fedotov. "Beam-beam effects in space charge dominated ion beams". In: *Proceedings, ICFA Mini-Workshop on Beam-Beam Effects in Hadron Colliders (BB2013): CERN, Geneva, Switzerland, March 18-22 2013*. 2014, pp. 63–68. DOI: 10.5170/CERN-2014-004.63. arXiv: 1410.4076.

[4] C. Bernard et al. "QCD thermodynamics with three flavors of improved staggered quarks". In: *Phys. Rev.* D71 (2005), p. 034504. DOI: 10.1103/PhysRevD.71.034504. arXiv: hep-lat/0405029 [hep-lat].

[5] L. P. Csernai, J. I. Kapusta, and L. D. McLerran. "On the Strongly-Interacting Low-Viscosity Matter Created in Relativistic Nuclear Collisions". In: *Phys. Rev. Lett.* 97 (2006), p. 152303. DOI: 10.1103/PhysRevLett.97.152303. arXiv: nucl-th/0604032 [nucl-th].

[6] Patrick Steinbrecher. "The QCD crossover at zero and non-zero baryon densities from Lattice QCD". In: *Nucl. Phys.* A982 (2019), pp. 847–850. DOI: 10.1016/j.nuclphysa.2018.08.025. arXiv: 1807.05607 [hep-lat].

[7] A. Bazavov et al. "Equation of state in (2+1)-flavor QCD". In: *Phys. Rev.* D90 (2014), p. 094503. DOI: 10.1103/PhysRevD.90.094503. arXiv: 1407.6387 [hep-lat].

[8] J. Berges and K. Rajagopal. "Color superconductivity and chiral symmetry restoration at nonzero baryon density and temperature". In: *Nucl. Phys.* B538 (1999), pp. 215–232. DOI: 10.1016/S0550-3213(98)00620-8. arXiv: hep-ph/9804233 [hep-ph].

[9] M. A. Stephanov, K. Rajagopal, and E. V. Shuryak. "Signatures of the tricritical point in QCD". In: *Phys. Rev. Lett.* 81 (1998), pp. 4816–4819. DOI: 10.1103/PhysRevLett.81.4816. arXiv: hep-ph/9806219 [hep-ph].

[10] Z. Fodor and S. D. Katz. "Critical point of QCD at finite T and mu, lattice results for physical quark masses". In: *JHEP* 04 (2004), p. 050. DOI: 10.1088/1126-6708/2004/04/050. arXiv: hep-lat/0402006 [hep-lat].

[11] Grazyna Odyniec. "Beam Energy Scan Program at RHIC (BES I and BES II) – Probing QCD Phase Diagram with Heavy-Ion Collisions". In: *PoS* CORFU2018 (2019), p. 151. DOI: 10.22323/1.347.0151.

[12] Jurgen Schukraft. "Little bang at big accelerators: Heavy ion physics from AGS to LHC". In: *AIP Conf. Proc.* 531.1 (2000), pp. 3–15. DOI: 10.1063/1.1315029.

[13] Raimond Snellings. "Elliptic Flow: A Brief Review". In: *New J. Phys.* 13 (2011), p. 055008. DOI: 10.1088/1367-2630/13/5/055008. arXiv: 1102.3010 [nucl-ex].

[14] Particles and friends. *Evolution of collisions and QGP*. [Online; accessed December 8, 2019]. 2019. URL: https://particlesandfriends.wordpress.com/2016/10/14/evolution-of-collisions-and-qgp/.

[15] Edmond Iancu. "QCD in heavy ion collisions". In: *Proceedings, 2011 European School of High-Energy Physics (ESHEP 2011): Cheile Gradistei, Romania, September 7-20, 2011*. 2014, pp. 197–266. DOI: 10.5170/CERN-2014-003.197. arXiv: 1205.0579 [hep-ph].

[16] Larry McLerran. "A Brief Introduction to the Color Glass Condensate and the Glasma". In: *Proceedings, 38th International Symposium on Multiparticle Dynamics (ISMD 2008): Hamburg, Germany, September 15-20, 2008*. 2009, pp. 3–18. DOI: 10.3204/DESY-PROC-2009-01/26. arXiv: 0812.4989 [hep-ph].

[17] F. Gelis et al. "The Color Glass Condensate". In: *Ann. Rev. Nucl. Part. Sci.* 60 (2010), pp. 463–489. DOI: 10.1146/annurev.nucl.010909.083629. arXiv: 1002.0333 [hep-ph].

[18] F. D. Aaron et al. "Combined Measurement and QCD Analysis of the Inclusive e+-p Scattering Cross Sections at HERA". In: *JHEP* 01 (2010), p. 109. DOI: 10.1007/JHEP01(2010)109. arXiv: 0911.0884 [hep-ex].

[19] Peter F. Kolb and Ulrich W. Heinz. "Hydrodynamic description of ultrarelativistic heavy ion collisions". In: (2003), pp. 634–714. arXiv: nucl-th/0305084 [nucl-th].

[20] Jean-Yves Ollitrault. "Relativistic hydrodynamics for heavy-ion collisions". In: *Eur. J. Phys.* 29 (2008), pp. 275–302. DOI: 10.1088/0143-0807/29/2/010. arXiv: 0708.2433 [nucl-th].

[21] Bo Andersson. "THE LUND STRING MODEL". In: *7th European Symposium on Antiproton Interactions: From LEAR to the Collider and Beyond Durham, England, July 9-13, 1984*. 1986, pp. 447–462.

[22] M. Connors et al. "Jet measurements in heavy ion physics". In: *Rev. Mod. Phys.* 90 (2018), p. 025005. DOI: 10.1103/RevModPhys.90.025005. arXiv: 1705.01974 [nucl-ex].

[23] S. Voloshin and Y. Zhang. "Flow study in relativistic nuclear collisions by Fourier expansion of Azimuthal particle distributions". In: *Z. Phys.* C70 (1996), pp. 665–672. DOI: 10.1007/s002880050141. arXiv: hep-ph/9407282 [hep-ph].

[24] B. Alver and G. Roland. "Collision geometry fluctuations and triangular flow in heavy-ion collisions". In: *Phys. Rev.* C81 (2010). [Erratum: Phys. Rev.C82, 039903 (2010)], p. 054905. DOI: 10.1103/PhysRevC.82.039903,10.1103/PhysRevC.81.054905. arXiv: 1003.0194 [nucl-th].

[25] B. V. Jacak and B. Muller. "The exploration of hot nuclear matter". In: *Science* 337 (2012), pp. 310–314. DOI: 10.1126/science.1215901.

[26] S. Acharya et al. "Investigations of Anisotropic Flow Using Multiparticle Azimuthal Correlations in pp, p-Pb, Xe-Xe, and Pb-Pb Collisions at the LHC". In: *Phys. Rev. Lett.* 123.14 (2019), p. 142301. DOI: 10.1103/PhysRevLett.123.142301. arXiv: 1903.01790 [nucl-ex].

[27] K. Aamodt et al. "Harmonic decomposition of two-particle angular correlations in Pb-Pb collisions at $\sqrt{s_{NN}} = 2.76$ TeV". In: *Phys. Lett.* B708 (2012), pp. 249–264. DOI: 10.1016/j.physletb.2012.01.060. arXiv: 1109.2501 [nucl-ex].

[28] V. Khachatryan et al. "Observation of Long-Range Near-Side Angular Correlations in Proton-Proton Collisions at the LHC". In: *JHEP* 09 (2010), p. 091. DOI: 10.1007/JHEP09(2010)091. arXiv: 1009.4122 [hep-ex].

[29] S. Chatrchyan et al. "Observation of Long-Range Near-Side Angular Correlations in Proton-Lead Collisions at the LHC". In: *Phys. Lett.* B718 (2013), pp. 795–814. DOI: 10.1016/j.physletb.2012.11.025. arXiv: 1210.5482 [nucl-ex].

[30] G. Aad et al. "Observation of Long-Range Elliptic Azimuthal Anisotropies in $\sqrt{s}$ =13 and 2.76 TeV pp Collisions with the ATLAS Detector". In: *Phys. Rev. Lett.* 116.17 (2016), p. 172301. DOI: 10.1103/PhysRevLett.116.172301. arXiv: 1509.04776 [hep-ex].

[31] C. Gale, S. Jeon, and B. Schenke. "Hydrodynamic Modeling of Heavy-Ion Collisions". In: *Int. J. Mod. Phys.* A28 (2013), p. 1340011. DOI: 10.1142/S0217751X13400113. arXiv: 1301.5893 [nucl-th].

[32] P. Kovtun, D. T. Son, and A. O. Starinets. "Viscosity in strongly interacting quantum field theories from black hole physics". In: *Phys. Rev. Lett.* 94 (2005), p. 111601. DOI: 10.1103/PhysRevLett.94.111601. arXiv: hep-th/0405231 [hep-th].

[33] R. Nouicer. "New State of Nuclear Matter: Nearly Perfect Fluid of Quarks and Gluons in Heavy Ion Collisions at RHIC Energies". In: *Eur. Phys. J. Plus* 131.3 (2016), p. 70. DOI: 10.1140/epjp/i2016-16070-2. arXiv: 1512.08993 [nucl-ex].

[34] J. Noronha-Hostler, M. Luzum, and J-Y. Ollitrault. "Hydrodynamic predictions for 5.02 TeV Pb-Pb collisions". In: *Phys. Rev.* C93.3 (2016), p. 034912. DOI: 10.1103/PhysRevC.93.034912. arXiv: 1511.06289 [nucl-th].

[35] H. Niemi et al. "Predictions for 5.023 TeV Pb + Pb collisions at the CERN Large Hadron Collider". In: *Phys. Rev.* C93.1 (2016), p. 014912. DOI: 10.1103/PhysRevC.93.014912. arXiv: 1511.04296 [hep-ph].

[36] J. Adam et al. "Anisotropic flow of charged particles in Pb-Pb collisions at $\sqrt{s_{\mathrm{NN}}} = 5.02$ TeV". In: *Phys. Rev. Lett.* 116.13 (2016), p. 132302. DOI: 10.1103/PhysRevLett.116.132302. arXiv: 1602.01119 [nucl-ex].

[37] S. Acharya et al. "Energy dependence and fluctuations of anisotropic flow in Pb-Pb collisions at $\sqrt{s_{\mathrm{NN}}} = 5.02$ and 2.76 TeV". In: *JHEP* 07 (2018), p. 103. DOI: 10.1007/JHEP07(2018)103. arXiv: 1804.02944 [nucl-ex].

[38] S. Acharya et al. "Anisotropic flow of identified particles in Pb-Pb collisions at $\sqrt{s_{\mathrm{NN}}} = 5.02$ TeV". In: *JHEP* 09 (2018), p. 006. DOI: 10.1007/JHEP09(2018)006. arXiv: 1805.04390 [nucl-ex].

[39] B. B. Abelev et al. "Long-range angular correlations on the near and away side in p-Pb collisions at $\sqrt{s_{NN}} = 5.02$ TeV". In: *Phys. Lett.* B719 (2013), pp. 29–41. DOI: 10.1016/j.physletb.2013.01.012. arXiv: 1212.2001 [nucl-ex].

[40] B. B. Abelev et al. "Multiparticle azimuthal correlations in p -Pb and Pb-Pb collisions at the CERN Large Hadron Collider". In: *Phys. Rev.* C90.5 (2014), p. 054901. DOI: 10.1103/PhysRevC.90.054901. arXiv: 1406.2474 [nucl-ex].

[41] V. Khachatryan et al. "Evidence for Collective Multiparticle Correlations in p-Pb Collisions". In: *Phys. Rev. Lett.* 115.1 (2015), p. 012301. DOI: 10.1103/PhysRevLett.115.012301. arXiv: 1502.05382 [nucl-ex].

[42] V. Khachatryan et al. "Evidence for collectivity in pp collisions at the LHC". In: *Phys. Lett.* B765 (2017), pp. 193–220. DOI: 10.1016/j.physletb.2016.12.009. arXiv: 1606.06198 [nucl-ex].

[43] M. Aaboud et al. "Measurement of multi-particle azimuthal correlations in pp, p+Pb and low-multiplicity Pb+Pb collisions with the ATLAS detector". In: *Eur. Phys. J.* C77.6 (2017), p. 428. DOI: 10.1140/epjc/s10052-017-4988-1. arXiv: 1705.04176 [hep-ex].

[44] T. Sjöstrand et al. "An Introduction to PYTHIA 8.2". In: *Comput. Phys. Commun.* 191 (2015), pp. 159–177. DOI: 10.1016/j.cpc.2015.01.024. arXiv: 1410.3012 [hep-ph].

[45] Z. Citron et al. "Future physics opportunities for high-density QCD at the LHC with heavy-ion and proton beams". In: *HL/HE-LHC Workshop: Workshop on the Physics of HL-LHC, and Perspectives at HE-LHC Geneva, Switzerland, June 18-20, 2018*. 2018. arXiv: 1812.06772 [hep-ph].

[46] A. M. Poskanzer and S. A. Voloshin. "Methods for analyzing anisotropic flow in relativistic nuclear collisions". In: *Phys. Rev.* C58 (1998), pp. 1671–1678. DOI: 10.1103/PhysRevC.58.1671. arXiv: nucl-ex/9805001 [nucl-ex].

[47] B. Alver et al. "Importance of correlations and fluctuations on the initial source eccentricity in high-energy nucleus-nucleus collisions". In: *Phys. Rev.* C77 (2008), p. 014906. DOI: 10.1103/PhysRevC.77.014906. arXiv: 0711.3724 [nucl-ex].

[48] A. Bilandzic, R. Snellings, and S. Voloshin. "Flow analysis with cumulants: Direct calculations". In: *Phys. Rev.* C83 (2011), p. 044913. DOI: 10.1103/PhysRevC.83.044913. arXiv: 1010.0233 [nucl-ex].

[49] You Zhou. "Anisotropic flow and flow fluctuations at the large hadron collider". PhD thesis. Utrecht U., 2016. URL: https://cds.cern.ch/record/2127503.

[50] N. Borghini, P. M. Dinh, and J-Y. Ollitrault. "Flow analysis from multiparticle azimuthal correlations". In: *Phys. Rev.* C64 (2001), p. 054901. DOI: 10.1103/PhysRevC.64.054901. arXiv: nucl-th/0105040 [nucl-th].

[51] M. Cacciari and G. P. Salam. "Dispelling the N^3 myth for the k_t jet-finder". In: *Phys. Lett.* B641 (2006), pp. 57–61. DOI: 10.1016/j.physletb.2006.08.037. arXiv: hep-ph/0512210 [hep-ph].

[52] N. Borghini, P. M. Dinh, and J-Y. Ollitrault. "A New method for measuring azimuthal distributions in nucleus-nucleus collisions". In: *Phys. Rev.* C63 (2001), p. 054906. DOI: 10.1103/PhysRevC.63.054906. arXiv: nucl-th/0007063 [nucl-th].

[53] A. Bilandzic et al. "Generic framework for anisotropic flow analyses with multiparticle azimuthal correlations". In: *Phys. Rev.* C89.6 (2014), p. 064904. DOI: 10.1103/PhysRevC.89.064904. arXiv: 1312.3572 [nucl-ex].

[54] R. S. Bhalerao, J-Y. Ollitrault, and S. Pal. "Characterizing flow fluctuations with moments". In: *Phys. Lett.* B742 (2015), pp. 94–98. DOI: 10.1016/j.physletb.2015.01.019. arXiv: 1411.5160 [nucl-th].

[55] H. Heiselberg and A-M. Levy. "Elliptic flow and HBT in noncentral nuclear collisions". In: *Phys. Rev.* C59 (1999), pp. 2716–2727. DOI: 10.1103/PhysRevC.59.2716. arXiv: nucl-th/9812034 [nucl-th].

[56] S. A. Voloshin and A. M. Poskanzer. "The Physics of the centrality dependence of elliptic flow". In: *Phys. Lett.* B474 (2000), pp. 27–32. DOI: 10.1016/S0370-2693(00)00017-4. arXiv: nucl-th/9906075 [nucl-th].

[57] M. Miller and R. Snellings. "Eccentricity fluctuations and its possible effect on elliptic flow measurements". In: (2003). arXiv: nucl-ex/0312008 [nucl-ex].

[58] S. A. Voloshin et al. "Elliptic flow in the Gaussian model of eccentricity fluctuations". In: *Phys. Lett.* B659 (2008), pp. 537–541. DOI: 10.1016/j.physletb.2007.11.043. arXiv: 0708.0800 [nucl-th].

[59] J-Y. Ollitrault, A. M. Poskanzer, and S. A. Voloshin. "Effect of flow fluctuations and nonflow on elliptic flow methods". In: *Phys. Rev.* C80 (2009), p. 014904. DOI: 10.1103/PhysRevC.80.014904. arXiv: 0904.2315 [nucl-ex].

[60] K. Aamodt et al. "Higher harmonic anisotropic flow measurements of charged particles in Pb-Pb collisions at $\sqrt{s_{NN}}$=2.76 TeV". In: *Phys. Rev. Lett.* 107 (2011), p. 032301. DOI: 10.1103/PhysRevLett.107.032301. arXiv: 1105.3865 [nucl-ex].

[61] D. Teaney and L. Yan. "Event-plane correlations and hydrodynamic simulations of heavy ion collisions". In: *Phys. Rev.* C90.2 (2014), p. 024902. DOI: 10.1103/PhysRevC.90.024902. arXiv: 1312.3689 [nucl-th].

[62] J. Qian et al. "Differential flow correlations in relativistic heavy-ion collisions". In: *Phys. Rev.* C95.5 (2017), p. 054908. DOI: 10.1103/PhysRevC.95.054908. arXiv: 1703.04077 [nucl-th].

[63] L. Yan and J-Y. Ollitrault. "v_4, v_5, v_6, v_7: nonlinear hydrodynamic response versus LHC data". In: *Phys. Lett.* B744 (2015), pp. 82–87. DOI: 10.1016/j.physletb.2015.03.040. arXiv: 1502.02502 [nucl-th].

[64] S. Acharya et al. "Linear and non-linear flow modes in Pb-Pb collisions at $\sqrt{s_{\mathrm{NN}}} =$ 2.76 TeV". In: *Phys. Lett.* B773 (2017), pp. 68–80. DOI: 10.1016/j.physletb.2017.07.060. arXiv: 1705.04377 [nucl-ex].

[65] Katarina Gajdosova. "Investigations of collectivity in small and large collision systems at the LHC with ALICE". Presented 23 Aug 2018. PhD thesis. Copehagen U., 2018. URL: https://cds.cern.ch/record/2644253.

[66] B. B. Abelev et al. "Long-range angular correlations of ß, K and p in p-Pb collisions at $\sqrt{s_{\mathrm{NN}}}$ = 5.02 TeV". In: *Phys. Lett.* B726 (2013), pp. 164–177. DOI: 10.1016/j.physletb.2013.08.024. arXiv: 1307.3237 [nucl-ex].

[67] L. R. Evans and P. Bryant. "LHC Machine". In: *JINST* 3 (2008). This report is an abridged version of the LHC Design Report (CERN-2004-003), S08001. 164 p. DOI: 10.1088/1748-0221/3/08/S08001. URL: http://cds.cern.ch/record/1129806.

[68] CERN. *The Large Hadron Collider*. 2019. URL: https://home.cern/science/accelerators/large-hadron-collider (visited on 10/05/2019).

[69] CERN. *LHC report: xenon in action*. 2017. URL: https://home.cern/news/news/accelerators/lhc-report-xenon-action (visited on 10/07/2019).

[70] CERN. *How much does it cost?* 2007. URL: https://web.archive.org/web/20110807103920/http://askanexpert.web.cern.ch/AskAnExpert/en/Accelerators/LHCgeneral-en.html#3 (visited on 10/05/2019).

[71] CERN. *Beams back in the LHC*. 2019. URL: https://home.cern/science/engineering/cryogenics-low-temperatures-high-performance (visited on 10/08/2019).

[72] D. Brandt et al. "Accelerator physics at LEP". In: *Rept. Prog. Phys.* 63 (2000), pp. 939–1000. DOI: 10.1088/0034-4885/63/6/203.

[73] S. Chatrchyan et al. "Observation of a New Boson at a Mass of 125 GeV with the CMS Experiment at the LHC". In: *Phys. Lett.* B716 (2012), pp. 30–61. DOI: 10.1016/j.physletb.2012.08.021. arXiv: 1207.7235 [hep-ex].

[74] G. Aad et al. "Observation of a new particle in the search for the Standard Model Higgs boson with the ATLAS detector at the LHC". In: *Phys. Lett.* B716 (2012), pp. 1–29. DOI: 10.1016/j.physletb.2012.08.020. arXiv: 1207.7214 [hep-ex].

[75] CERN. *Pulling together: Superconducting electromagnets*. 2019. URL: https://home.cern/science/engineering/pulling-together-superconducting-electromagnets (visited on 10/05/2019).

[76] Jean-Luc Caron. *Cross section of LHC dipole.* 1998. URL: https://cds.cern.ch/record/841539 (visited on 10/05/2019).

[77] CERN. *Cryogenics: Low temperatures, high performance*. 2019. URL: https://home.cern/science/engineering/cryogenics-low-temperatures-high-performance (visited on 10/05/2019).

[78] CERN. *Accelerating: Radiofrequency cavities*. 2019. URL: https://home.cern/science/engineering/accelerating-radiofrequency-cavities (visited on 10/05/2019).

[79] Esma Mobs. *The CERN accelerator complex.* 2016. URL: https://cds.cern.ch/record/2197559 (visited on 10/05/2019).

[80] CERN. *A vacuum as empty as interstellar space*. 2019. URL: https://home.cern/science/engineering/vacuum-empty-interstellar-space (visited on 10/05/2019).

[81] K. Aamodt et al. "The ALICE experiment at the CERN LHC". In: *JINST* 3 (2008), S08002. 259 p. DOI: 10.1088/1748-0221/3/08/S08002. URL: https://cds.cern.ch/record/1129812.

[82] ALICE Collaboration. *ALICE Collaboration*. 2019. URL: http://alice-collaboration.web.cern.ch (visited on 10/06/2019).

[83] J. Adam et al. "Centrality dependence of the charged-particle multiplicity density at midrapidity in Pb-Pb collisions at $\sqrt{s_{NN}}$ = 5.02 TeV". In: *Phys. Rev. Lett.* 116.22 (2016), p. 222302. DOI: 10.1103/PhysRevLett.116.222302. arXiv: 1512.06104 [nucl-ex].

[84] Arturo Tauro. *3D ALICE Schematic RUN2 - with Description*. 2017. URL: https://alice-figure.web.cern.ch/node/11218 (visited on 10/05/2019).

[85] L. Betev and P. Chochula. *Definition of the ALICE Coordinate System and Basic Rules for Sub-detector Components Numbering*. ALICE internal note (ALICE-INT-2003-038). 2003.

[86] G. Dellacasa et al. "ALICE technical design report of the inner tracking system (ITS)". In: (1999).

[87] Paul. Kuijer. "The inner tracking system of the Alice experiment". In: *Nucl. Instrum. Meth.* A530 (2004), pp. 28–32. DOI: 10.1016/j.nima.2004.05.042.

[88] B. B. Abelev et al. "Performance of the ALICE Experiment at the CERN LHC". In: *Int. J. Mod. Phys.* A29 (2014), p. 1430044. DOI: 10.1142/S0217751X14300440. arXiv: 1402.4476 [nucl-ex].

[89] G. Dellacasa et al. "ALICE: Technical design report of the time projection chamber". In: (2000).

[90] J. Alme et al. "The ALICE TPC, a large 3-dimensional tracking device with fast readout for ultra-high multiplicity events". In: *Nucl. Instrum. Meth.* A622 (2010), pp. 316–367. DOI: 10.1016/j.nima.2010.04.042. arXiv: 1001.1950 [physics.ins-det].

[91] G. Renault et al. "The Laser of the ALICE Time Projection Chamber". In: *Int. J. Mod. Phys.* E16 (2007), pp. 2413–2418. DOI: 10.1142/S0218301307008021. arXiv: nucl-ex/0703042 [NUCL-EX].

[92] Alexander Kalweit. "Production of light flavor hadrons and anti-nuclei at the LHC". PhD thesis. 2012. URL: https://cds.cern.ch/record/2119440.

[93] *ALICE Time-Of-Flight system (TOF): Technical Design Report*. Technical Design Report ALICE. Geneva: CERN, 2000. URL: http://cds.cern.ch/record/430132.

[94] E. Cerron Zeballos et al. "A New type of resistive plate chamber: The Multigap RPC". In: *Nucl. Instrum. Meth.* A374 (1996), pp. 132–136. DOI: 10.1016/0168-9002(96)00158-1.

[95] P. Cortese et al. "ALICE technical design report on forward detectors: FMD, T0 and V0". In: (2004).

[96] C. W. Fabjan et al. *ALICE trigger data-acquisition high-level trigger and control system: Technical Design Report*. Technical Design Report ALICE. Geneva: CERN, 2004. URL: https://cds.cern.ch/record/684651.

[97] Antonin Maire. "Production des baryons multi-étranges au LHC dans les collisions proton-proton avec l'expérience ALICE". PhD thesis. Strasbourg U., 2011. URL: https://cds.cern.ch/record/1490315.

[98] K. Aamodt et al. "First proton-proton collisions at the LHC as observed with the ALICE detector: Measurement of the charged particle pseudorapidity density at s**(1/2) = 900-GeV". In: *Eur. Phys. J.* C65 (2010), pp. 111–125. DOI: 10.1140/epjc/s10052-009-1227-4. arXiv: 0911.5430 [hep-ex].

[99] R. E. Kalman. "A new approach to linear filtering and prediction problems" transaction of the asme journal of basic". In: 1960.

[100] Pierre Billoir. "Track Fitting With Multiple Scattering: A New Method". In: *Nucl. Instrum. Meth.* A225 (1984), pp. 352–366. DOI: 10.1016/0167-5087(84)90274-6.

[101] B. B. Abelev et al. "Centrality determination of Pb-Pb collisions at $\sqrt{s_{NN}}$ = 2.76 TeV with ALICE". In: *Phys. Rev.* C88.4 (2013), p. 044909. DOI: 10.1103/PhysRevC.88.044909. arXiv: 1301.4361 [nucl-ex].

[102] B. Alver et al. "The PHOBOS Glauber Monte Carlo". In: (2008). arXiv: 0805.4411 [nucl-ex].

[103] C. Loizides, J. Nagle, and P. Steinberg. "Improved version of the PHOBOS Glauber Monte Carlo". In: (2014). [SoftwareX1-2,13(2015)]. DOI: 10.1016/j.softx.2015.05.001. arXiv: 1408.2549 [nucl-ex].

[104] K. Aamodt et al. "Charged-particle multiplicity measurement in proton-proton collisions at $\sqrt{s} = 0.9$ and 2.36 TeV with ALICE at LHC". In: *Eur. Phys. J.* C68 (2010), pp. 89–108. DOI: 10.1140/epjc/s10052-010-1339-x. arXiv: 1004.3034 [hep-ex].

[105] R. Brun and F. Rademakers. "ROOT: An object oriented data analysis framework". In: *Nucl. Instrum. Meth.* A389 (1997), pp. 81–86. DOI: 10.1016/S0168-9002(97)00048-X.

[106] ALICE Collaboration. *AliPhysics*. https://github.com/alisw/aliphysics.

[107] Vojtech Pacik. *UniFlow*. https://github.com/vpacik/uniflow.

[108] J. Adam et al. "Particle identification in ALICE: a Bayesian approach". In: *Eur. Phys. J. Plus* 131.5 (2016), p. 168. DOI: 10.1140/epjp/i2016-16168-5. arXiv: 1602.01392 [physics.data-an].

[109] Phil Gregory. *Bayesian Logical Data Analysis for the Physical Sciences*. New York, NY, USA: Cambridge University Press, 2005. ISBN: 052184150X.

[110] M. Tanabashi et al. "Review of Particle Physics". In: *Phys. Rev.* D98.3 (2018), p. 030001. DOI: 10.1103/PhysRevD.98.030001.

[111] K. Aamodt et al. "Strange particle production in proton-proton collisions at sqrt(s) = 0.9 TeV with ALICE at the LHC". In: *Eur. Phys. J.* C71 (2011), p. 1594. DOI: 10.1140/epjc/s10052-011-1594-5. arXiv: 1012.3257 [hep-ex].

[112] B. B. Abelev et al. "K^0_S and Λ production in Pb-Pb collisions at $\sqrt{s_{NN}}$ = 2.76 TeV". In: *Phys. Rev. Lett.* 111 (2013), p. 222301. DOI: 10.1103/PhysRevLett.111.222301. arXiv: 1307.5530 [nucl-ex].

[113] Vit Kucera. "Study of strange particle production in jets with the ALICE experiment at the LHC". Presented 15 Nov 2016. PhD thesis. Aug. 2016. URL: https://cds.cern.ch/record/2239143.

[114] J. Podolanski and R. Armenteros. "III. Analysis of V-events". In: *The London, Edinburgh, and Dublin Philosophical Magazine and Journal of Science* 45.360 (1954), pp. 13–30. DOI: 10.1080/14786440108520416.

[115] Luke Hanratty. "Λ and K^0_S production in Pb-Pb and pp collisions with ALICE at the LHC". Presented 15 Aug 2014. PhD thesis. June 2014. URL: https://cds.cern.ch/record/1753431.

[116] N. Borghini and J-Y. Ollitrault. "Azimuthally sensitive correlations in nucleus-nucleus collisions". In: *Phys. Rev.* C70 (2004), p. 064905. DOI: 10.1103/PhysRevC.70.064905. arXiv: nucl-th/0407041 [nucl-th].

[117] B. I. Abelev et al. "Centrality dependence of charged hadron and strange hadron elliptic flow from s(NN)**(1/2) = 200-GeV Au + Au collisions". In: *Phys. Rev.* C77 (2008), p. 054901. DOI: 10.1103/PhysRevC.77.054901. arXiv: 0801.3466 [nucl-ex].

[118] B. B. Abelev et al. "Elliptic flow of identified hadrons in Pb-Pb collisions at $\sqrt{s_{\mathrm{NN}}}$ = 2.76 TeV". In: *JHEP* 06 (2015), p. 190. DOI: 10.1007/JHEP06(2015)190. arXiv: 1405.4632 [nucl-ex].

[119] C. Shen et al. "The iEBE-VISHNU code package for relativistic heavy-ion collisions". In: *Comput. Phys. Commun.* 199 (2016), pp. 61–85. DOI: 10.1016/j.cpc.2015.08.039. arXiv: 1409.8164 [nucl-th].

[120] H. Song, S. A. Bass, and U. Heinz. "Viscous QCD matter in a hybrid hydrodynamic+Boltzmann approach". In: *Phys. Rev.* C83 (2011), p. 024912. DOI: 10.1103/PhysRevC.83.024912. arXiv: 1012.0555 [nucl-th].

[121] Z-W. Lin et al. "A Multi-phase transport model for relativistic heavy ion collisions". In: *Phys. Rev.* C72 (2005), p. 064901. DOI: 10.1103/PhysRevC.72.064901. arXiv: nucl-th/0411110 [nucl-th].

[122] J. S. Moreland, J. E. Bernhard, and S. A. Bass. "Alternative ansatz to wounded nucleon and binary collision scaling in high-energy nuclear collisions". In: *Phys. Rev.* C92.1 (2015), p. 011901. DOI: 10.1103/PhysRevC.92.011901. arXiv: 1412.4708 [nucl-th].

[123] J. E. Bernhard et al. "Applying Bayesian parameter estimation to relativistic heavy-ion collisions: simultaneous characterization of the initial state and quark-gluon plasma medium". In: *Phys. Rev.* C94.2 (2016), p. 024907. DOI: 10.1103/PhysRevC.94.024907. arXiv: 1605.03954 [nucl-th].

[124] S. A. Voloshin. "Transverse radial expansion and directed flow". In: *Phys. Rev.* C55 (1997), R1630–R1632. DOI: 10.1103/PhysRevC.55.R1630. arXiv: nucl-th/9611038 [nucl-th].

[125] P. Huovinen et al. "Radial and elliptic flow at RHIC: Further predictions". In: *Phys. Lett.* B503 (2001), pp. 58–64. DOI: 10.1016/S0370-2693(01)00219-2. arXiv: hep-ph/0101136 [hep-ph].

[126] D. Molnar and S. A. Voloshin. "Elliptic flow at large transverse momenta from quark coalescence". In: *Phys. Rev. Lett.* 91 (2003), p. 092301. DOI: 10.1103/PhysRevLett.91.092301. arXiv: nucl-th/0302014 [nucl-th].

[127] R. C. Hwa and C. B. Yang. "Scaling distributions of quarks, mesons and proton for all p(T), energy and centrality". In: *Phys. Rev.* C67 (2003), p. 064902. DOI: 10.1103/PhysRevC.67.064902. arXiv: nucl-th/0302006 [nucl-th].

[128] S. S. Adler et al. "Elliptic flow of identified hadrons in Au+Au collisions at s(NN)**(1/2) = 200-GeV". In: *Phys. Rev. Lett.* 91 (2003), p. 182301. DOI: 10.1103/PhysRevLett.91.182301. arXiv: nucl-ex/0305013 [nucl-ex].

[129] J. Adams et al. "Azimuthal anisotropy in Au+Au collisions at s(NN)**(1/2) = 200-GeV". In: *Phys. Rev.* C72 (2005), p. 014904. DOI: 10.1103/PhysRevC.72.014904. arXiv: nucl-ex/0409033 [nucl-ex].

[130] Michael Issah and Arkadij Taranenko. "Scaling Characteristics of Azimuthal Anisotropy at RHIC". In: *22nd Winter Workshop on Nuclear Dynamics (WWND 2006) La Jolla, California, March 11-19, 2006*. 2006. arXiv: nucl-ex/0604011 [nucl-ex].

[131] A. Adare et al. "Scaling properties of azimuthal anisotropy in Au+Au and Cu+Cu collisions at s(NN) = 200-GeV". In: *Phys. Rev. Lett.* 98 (2007), p. 162301. DOI: 10.1103/PhysRevLett.98.162301. arXiv: nucl-ex/0608033 [nucl-ex].

[132] A. Adare et al. "Deviation from quark-number scaling of the anisotropy parameter v_2 of pions, kaons, and protons in Au+Au collisions at $\sqrt{s_{NN}} = 200$ GeV". In: *Phys. Rev.* C85 (2012), p. 064914. DOI: 10.1103/PhysRevC.85.064914. arXiv: 1203.2644 [nucl-ex].

[133] S. Acharya et al. "Non-linear flow modes of identified particles in Pb-Pb collisions at $\sqrt{s_{\mathrm{NN}}}$ = 5.02 TeV". In: (2019). arXiv: 1912.00740 [nucl-ex].

[134] C. Adler et al. "Elliptic flow from two and four particle correlations in Au+Au collisions at s(NN)**(1/2) = 130-GeV". In: *Phys. Rev.* C66 (2002), p. 034904. DOI: 10.1103/PhysRevC.66.034904. arXiv: nucl-ex/0206001 [nucl-ex].

[135] S. A. Voloshin, A. M. Poskanzer, and R. Snellings. "Collective phenomena in non-central nuclear collisions". In: *Landolt-Bornstein* 23 (2010), pp. 293–333. DOI: 10.1007/978-3-642-01539-7_10. arXiv: 0809.2949 [nucl-ex].

[136] J. Adam et al. "Higher harmonic flow coefficients of identified hadrons in Pb-Pb collisions at $\sqrt{s_{\mathrm{NN}}}$ = 2.76 TeV". In: *JHEP* 09 (2016), p. 164. DOI: 10.1007/JHEP09(2016)164. arXiv: 1606.06057 [nucl-ex].

Acronyms

ACORDE ALICE Cosmic Ray Detector. 49

AD ALICE Diffractive detector. 49

ALICE A Large Ion Collider Experiment. 45

ATLAS A Toroidal LHC Apparatus. 45

CERN European Organization for Nuclear Research. 45

CGC Colour-Glass Condensate. 7

CMS Compact Muon Solenoid. 45

CNM Cold Nuclear Matter. 13

CPV Charged-Particle Veto. 49

CTP Central Trigger Processor. 60

DAQ Data-Acquisition. 60

DCal Di-jet Calorimeter. 49

EM electromagnetic. 2

EMCal Electromagnetic Calorimeter. 49

FMD Forward Multiplicity Detector. 49

GF Generic Framework. 31

HLT High-Level Trigger. 53

HMPID High-Momentum Particle Identification Detector. 49

IP Interaction Point. 49

ITS Inner Tracking System. 49

LEP Large Electron-Positron Collider. 45

LHC Large Hadron Collider. 45

LHCb Large Hadron Collider beauty. 45

lQCD lattice QCD. 4

MB Minimum-Bias. 59

MRPC Multi-gap Resistive-Plate Chamber. 56

NBD negative-binomial distribution. 66

NCQ Number of Constituent Quark. 104

PDF Probability Density Function. 35

PHOS Photon Spectrometer. 49

PID particle identification. 48

PMT Photo-Multiplier Tube. 58

pQCD perturbative QCD. 4

PV Primary Vertex. 49

QCD Quantum Chromodynamics. 2

QED Quantum Electrodynamics. 2

QGP Quark-Gluon Plasma. 4

SDD Silicon Drift Detector. 49

SP Scalar Product. 104

SPD Silicon Pixel Detector. 49

SSD Silicon Strip Detector. 49

SV Secondary Vertex. 82

TOF Time-Of-Flight. 49

TPC Time-Projection Chamber. 49

TRD Transition Radiation Detector. 49

ZDC Zero Degree Calorimeter. 49